NASA/CR—2000-209957

Measurements in a Transitional Boundary Layer Under Low-Pressure Turbine Airfoil Conditions

Terrence W. Simon, Songgang Qiu, and Kebiao Yuan
University of Minnesota, Minneapolis, Minnesota

March 2000

The NASA STI Program Office . . . in Profile

Since its founding, NASA has been dedicated to the advancement of aeronautics and space science. The NASA Scientific and Technical Information (STI) Program Office plays a key part in helping NASA maintain this important role.

The NASA STI Program Office is operated by Langley Research Center, the Lead Center for NASA's scientific and technical information. The NASA STI Program Office provides access to the NASA STI Database, the largest collection of aeronautical and space science STI in the world. The Program Office is also NASA's institutional mechanism for disseminating the results of its research and development activities. These results are published by NASA in the NASA STI Report Series, which includes the following report types:

- TECHNICAL PUBLICATION. Reports of completed research or a major significant phase of research that present the results of NASA programs and include extensive data or theoretical analysis. Includes compilations of significant scientific and technical data and information deemed to be of continuing reference value. NASA's counterpart of peer-reviewed formal professional papers but has less stringent limitations on manuscript length and extent of graphic presentations.

- TECHNICAL MEMORANDUM. Scientific and technical findings that are preliminary or of specialized interest, e.g., quick release reports, working papers, and bibliographies that contain minimal annotation. Does not contain extensive analysis.

- CONTRACTOR REPORT. Scientific and technical findings by NASA-sponsored contractors and grantees.

- CONFERENCE PUBLICATION. Collected papers from scientific and technical conferences, symposia, seminars, or other meetings sponsored or cosponsored by NASA.

- SPECIAL PUBLICATION. Scientific, technical, or historical information from NASA programs, projects, and missions, often concerned with subjects having substantial public interest.

- TECHNICAL TRANSLATION. English-language translations of foreign scientific and technical material pertinent to NASA's mission.

Specialized services that complement the STI Program Office's diverse offerings include creating custom thesauri, building customized data bases, organizing and publishing research results . . . even providing videos.

For more information about the NASA STI Program Office, see the following:

- Access the NASA STI Program Home Page at ***http://www.sti.nasa.gov***

- E-mail your question via the Internet to help@sti.nasa.gov

- Fax your question to the NASA Access Help Desk at (301) 621-0134

- Telephone the NASA Access Help Desk at (301) 621-0390

- Write to:
  NASA Access Help Desk
  NASA Center for AeroSpace Information
  7121 Standard Drive
  Hanover, MD 21076

NASA/CR—2000-209957

Measurements in a Transitional Boundary Layer Under Low-Pressure Turbine Airfoil Conditions

Terrence W. Simon, Songgang Qiu, and Kebiao Yuan
University of Minnesota, Minneapolis, Minnesota

Prepared under Grant NAG3–1249

National Aeronautics and
Space Administration

Glenn Research Center

March 2000

Acknowledgments

This project was supported by NASA-Glenn Research Center. The contract monitors were David Ashpis and Fred Simon. Their guidance is greatly appreciated. The authors particularly appreciate the thorough review of the final manuscript by David Ashpis. The authors would like to also thank Mr. Bob Nelson and Mr. Pat Nelsen at the Mechanical Engineering Department Research Shop for their excellent help with fabrication of the test facility.

Trade names or manufacturers' names are used in this report for identification only. This usage does not constitute an official endorsement, either expressed or implied, by the National Aeronautics and Space Administration.

Available from

NASA Center for Aerospace Information
7121 Standard Drive
Hanover, MD 21076
Price Code: A10

National Technical Information Service
5285 Port Royal Road
Springfield, VA 22100
Price Code: A10

TABLE OF CONTENTS

		Page
Nomenclature		vi
Chapter One	**Introduction**	1
	Objectives	4
	Review of Past Research	4
	Experimental Studies on Transition	4
	Numerical Analyses and Modeling	7
	Past Research at the Heat Transfer Laboratory at the University of Minnesota	9
Chapter two	**Facilities and Instrumentation**	12
	Setup and Techniques	13
	Turbulence Generator	19
	Cascade Simulator	21
	Instrumentation	26
	Hot-Wire Probes	26
	Calibration	28
	Pressure Transducer	29
	Intermittency Circuit	30
	Digitizer	31

	Low-Pass Filter	32
	Flow Visualization Setup and Techniques	32
Chapter Three	**Data Processing**	35
	Single-Wire Data	35
	Cross-Wire Data	35
	Triple-Sensor Data	38
	Near-Wall Correction on Hot-Wire data	39
	Shear Stress	40
	Intermittency	41
	Power Spectra	41
	Integral Length Scales	44
	Energy Scales and Turbulence Dissipation	46
	Measurements	47
Chapter Four	**Results**	50
4.1	**Inlet Conditions**	50
	Inlet Velocity and Turbulence	51
	One-Dimensional Power Spectra	53
	Energy and Integral Length Scales	54
4.2	**Pressure Profiles**	67
4.3	**Flow Visualization**	71
4.4	**Velocity Profiles**	74

Low Turbulence Flow, FSTI=0.5% 74
Moderate Turbulence Flow, FSTI=2.5% 111
High Turbulence Flow, FSTI=10% 147
4.5 Separated Flow Transition Models 177

Chapter Five Conclusions 184

References 197

Appendix A Shear Stress Direction Visualization A-1

NOMENCLATURE

Symbol	Units	Explanation
c, c_p	W/°C	specific heat at constant pressure
$C_p = 2(p_t - p)/\rho U_\infty^2$		static pressure coefficient
$C_f = 2\tau_w / \rho U_\infty^2$		skin friction coefficient
d_s	m	sensor diameter
Eu	m^2/sec	power spectral density function of u′
Ev	m^2/sec	power spectral density function of v′
Ew	m^2/sec	power spectral density function of w′
f	1/sec	frequency
FSTI		free stream turbulence intensity
H		pitch correction coefficient for triple-wire sensor
k	W/m°C	fluid conductivity
k_t		correction factor for tangential cooling of cross-wire sensor
k_w		a constant in the Wills correction
K		yaw correction coefficient for triple-wire sensor or acceleration parameter, $K = \frac{\nu}{U_\infty^2}\frac{dU_\infty}{dx}$
l	m	distance along true chord
l_s	m	sensor length
L	m	true chord length
L_x	m	axial chord length

L_{ss}	m	suction surface length
$LR = s_r - s_s$	m	separation length
$LT = s_{te} - s_{ts}$	m	transition length
Lu, Lv, Lw	m	energy scales based upon u, v, and w
N		number of points in sample
p, p_s	Pa	static pressure or pressure tap location
p_t	Pa	total pressure
PSD		power spectral density, Eu, Ev, or Ew
q	W/m^2	heat flux
Q_u	m^2/sec^2	auto-correlation of u′
$Re = L_{ss} u_e / \nu$		Reynolds number based on suction surface length and exit velocity
Re_{LT}		Reynolds number based on transition length
$Re_{s_{st}}$		Reynolds number based on the distance between separation point and start of transition
$Re_{s_{ts}}$		local Reynolds number at the start of transition
$Re_{s_{te}}$		local Reynolds number at the end of transition
$Re_{\delta_2} = \delta_2 U_\infty / \nu$		momentum thickness Reynolds number
$Re_{2_{ts}}$		momentum thickness Reynolds number at the start of transition
s	m	distance along suction surface
s_r	m	s at reattachment
s_s	m	s at separation

s_{st}	m	distance between separation point and start of transition
s_{te}	m	s at end of transition
s_{ts}	m	s at start of transition
$St = q / \rho\, c\, U_\infty \left(T_w - T_\infty\right)$		Stanton number
$Str = f\delta_2 / U_\infty$		Strouhal number
t'	°C	temperature fluctuation
T_w	°C	wall temperature
T_∞	°C	freestream temperature
$TI = u'/\bar{u}$		turbulence intensity
t	sec	time
u	m/sec	instantaneous fluid velocity
U	m/sec	velocities used in hot-wire calibration
u_e	m/sec	exit velocity
u_{in}	m/sec	inlet velocity
u'	m/sec	fluctuating component of velocity
u'_{rms}	m/sec	rms fluctuation velocity
$u^+ = u/u^*$		velocity in wall coordinates
$\bar{u}$	m/sec	time-averaged velocity
u^*	m/sec	friction velocity
U_∞, u_∞	m/sec	free-stream velocity, at edge of boundary layer
U_{eff}	m/sec	effective velocity in hot-wire calibration
$-\overline{u'v'}$	m^2/sec^2	turbulent shear stress
$\overline{uv}$	m^2/sec^2	velocity product, averaged
v	m/sec	instantaneous wall-normal velocity

v'	m/sec	fluctuating wall-normal velocity
$\bar{v}$	m/sec	mean wall-normal velocity
v'_{rms}	m/sec	rms of fluctuating wall-normal velocity
w	m/sec	instantaneous spanwise velocity
w'	m/sec	fluctuating component of w
$\bar{w}$	m/sec	mean spanwise velocity
w'_{rms}	m/sec	rms fluctuating component of w
x	m	axial (streamwise) position
y	m	normal distance from the wall
$y^+=yu*/\nu$		y, in wall coordinates
z	m	spanwise distance
$\delta, \delta_{99.5}$	m	boundary layer thickness
δ_2	m	momentum thickness
δ_{2s}	m	momentum thickness at separation
δ_{2ts}	m	momentum thickness at start of transition
δ^*	m	displacement thickness
δ^*_s	m	displacement thickness at separation
ε	m^2/sec^3	turbulence dissipation
γ		intermittency
λ		Taylor microscale
Λ_{ux}	m	integral length scale of u′ in streamwise direction
Λ_{vx}	m	integral length scale of v′ in streamwise direction
Λ_{wx}	m	integral length scale of w′ in streamwise direction

μ	N sec/m^2	dynamic viscosity
ν	m^2/sec	kinematic viscosity
ρ	kg/m^3	density
τ_w	Pa	shear stress

Superscripts

+	wall coordinates
′	fluctuating components

Subscripts

e, exit	quantity at the exit
eff	effective
i	index for data point number
in	quantity at the inlet
j	index for data point number
n	normal direction, or normal component
r	reattachment
s	separation or static quantities
te	end of transition
ts	start of transition
t	tangential direction (tangential component) or total (stagnation) quantity
w	quantity evaluated at the wall, except E_w, or for the wire
∞	at the edge of the boundary layer

CHAPTER ONE
INTRODUCTION

As the environment under which gas turbines must operate has become increasingly more severe, the gas turbine engine design and manufacturing community has implemented many innovative schemes for higher efficiency operation and improved cooling performance of critical engine components. Schemes utilizing innovations such as highly loaded turbine blades subject to strong pressure gradients, film cooling, internal flow cooling, protective ceramic coatings, superalloys, single-crystal metals, and composite materials have emerged. System efficiency is important to users of commercial aircraft for fuel represents an important expense item to carriers. System efficiency is important to military aircraft, particularly military transport aircraft, for inefficiency represents an important limitation on the flexibility of missions. In recent years, new demands for improved performance for applications such as turbomachinery for space use or the propulsion system of the national aerospace plane have driven the gas turbine industry to search for even more innovative techniques for cooling and for improved aerodynamic performance. Also, manufacturers of stationary gas turbines for electric power generation have seen an emerging international market and severe competition as the U.S. electric power supply industry strives to offer the most efficient, yet reliable, systems. This has driven them to implement or consider implementation of the advanced schemes that were derived for aerospace applications. In support of these objectives, efforts have been made to strengthen the understanding of heat and

momentum transport processes within the very complex flow regions of gas turbines.

Several difficulties regarding turbine and compressor design remain as a result of less than complete knowledge of the fundamental fluid mechanics and transport processes in an environment of increased loading and increased demand for higher efficiency and durability. Such understanding of the fundamentals of the flow and heat transfer has always been important, but as the engine designs have become more sophisticated and design margins have been reduced, the importance has grown. One concern is the lack of understanding about boundary layer stability, including transition and separation, within an environment which is representative of turbomachine airfoil passages. The inability, partially due to this lack of knowledge, to precisely predict flow separation is an important problem. The stability of a laminar boundary layer may be described in terms of its nearness to the onset of transition, a transitional boundary layer is often described in terms of its intermittency (the fraction of the flow that is turbulent-like or the fraction of the time the flow is turbulent-like), and a turbulent boundary layer is characterized in terms of its maturity, usually given as the momentum thickness Reynolds number. The description of these regimes is particularly difficult on the suction side of low-pressure turbine airfoils, where separation bubbles are believed to cause a significant degradation of engine efficiency, particularly at altitude and during off-design operation. The location and extent of these separation regions depend on the history of streamwise development of the boundary layer and the nature of the flow external to the separation bubble. Thus, the full history of the boundary layer must be known and its effect on the stability of a boundary layer which is

subjected to destabilizing effects must be assessed. The inability to accurately predict the skin friction and convective heat transfer coefficient distributions remains an important problem which is limited by an incomplete understanding of the stability of boundary layer flows. This is particularly true on low-pressure turbine blades, which, typically, are not film cooled. Traditional design practices using local momentum thickness Reynolds numbers and the local pressure gradients to determine the point of onset of transition and the length of the transition zone have been shown to be inadequate for complex flows. Computation through transition with k-ε modeling, though done with increasing frequency, is considered to be not entirely reliable and careful testing and expensive design change are usually required due to this lack of reliability. Experimental and computational results are being combined to describe the fundamental physics of the transition process within the engine and, with this knowledge, transition models are being developed. Thus, experimental support for understanding transition is needed. Present knowledge is insufficient to assess the many single and compound effects of the many influences on transition that exist within the engine. Much of this knowledge will be supplied by experimental evidence. Improved understanding will allow improved designs of the airfoil shape for more controlled diffusion and a better definition of the engine operating envelope for optimum performance and minimal separation and drag.

OBJECTIVES

The transition boundary layer flow study was initiated to address the need for improved performance of low-pressure turbine stages and better

understanding of flow transition and separation on the suction surface of a modern, low-pressure turbine airfoil under various free-stream disturbance levels and with curvature and acceleration effects.

Careful documentation will be made of (1) the development of the boundary layer which approaches the separated flow region (including transition from disturbed-laminar to turbulent flow and, possibly, reverse transition to laminar flow), (2) the free shear layer over the separation region, and (3) the reattached flow downstream of the separation bubble.

REVIEW OF PAST RESEARCH

Experimental Studies on Transition

Mayle (1991) did an excellent review and study on the laminar-to-turbulent transition phenomenon and its impact on gas turbine engine design. Mayle stated that a substantial fraction of the boundary layer on each side of a gas turbine airfoil may be transitional. He described various transition modes and their roles in gas turbine engines. Various correlation equations were then developed and suggested for each of the transition modes.

Of the various transition modes described by Mayle (1991), the first mode is natural transition. This transition mode begins with small disturbances in a laminar boundary layer. Such small disturbances arise by the boundary layer being receptive to small disturbances in the external flow and by small disturbances, such as roughness, at the wall. These unstable, weak disturbances develop to two-dimensional waves, Tollmien-Schlichting (TS) waves. The TS waves are then amplified to three-dimensional vortices due to secondary

instability. The transition then proceeds through vortex break-down, culminating in turbulent spots, and eventually, to fully-developed, turbulent flow. Tollmien and Schlichting (Schlichting 1979) were the first researchers to describe this transition with linear stability theory.

The turbulent spots in a transitional flow were first reported by Emmons (1951). He pointed out that transition is a three-dimensional, unsteady phenomenon. He observed the production, growth, and convection of turbulent spots in a water tunnel with flow visualization. Intermittent phenomena were observed as the turbulent spots pass .

The second mode of transition is bypass transition, following Morkovin (1969). In this transition mode, no Tollmien-Schlichting waves are visible and the linear stability mechanism seems to have been bypassed, as shown by Blair (1990) for transition in favorable pressure gradient flows. A characteristic of bypass transition is the sudden appearance of turbulent spots. In gas turbine flows, bypass transition is the transition mode due to high free-stream turbulence (Mayle, 1991). Several experiments on bypass transition were performed in actual gas turbine engines or turbine cascades. Much of these works prior to 1991 were reviewed by Mayle (1991) and Volino and Simon (1991).

Recently, Blair (1992a, 1992b) investigated moderately accelerated boundary layer flow with various levels of free-stream turbulence. All of his experimental test cases resulted in bypass transition. His data followed the bypass transition pattern described above.

Halstead et al. (1995a, 1995b, 1995c, 1995d) conducted a comprehensive experimental study of boundary layer flows on airfoil surfaces in compressors

and low-pressure turbines using a close simulation of an actual gas turbine engine. In their tests, surface measurements were done with surface-mounted, hot-film gauges and the free-stream velocities were measured with hot-wire probes. Their experiments showed large regions of laminar and transitional flow on the suction surface, with the boundary layer generally developing along two distinct, but coupled, paths -- under the wakes and between wakes. In their simulation of low-pressure turbines, FSTI between the wakes was 2.5-3% and FSTI within the wake was around 4.5%. They found that calmed regions, generated by the passage of turbulent spots produced by the wake paths, were effective in suppressing flow separation and delaying transition in the no-wake path which followed the wake path. They observed bypass transition and separated-flow transition on both suction and pressure surfaces.

The separated-flow transition observed in Halstead et al.'s experiments is another important transition mode in gas turbine flows. This mode of transition occurs in the free-shear-layer-like flow over a separated laminar boundary layer. Tollmien-Schlichting waves may or may not be involved in this transition mode (Mayle, 1991). Separated-flow transition often occurs in low-pressure turbines and compressors. As pointed out by Mayle (1991), understanding and utilizing separated-flow transition through separation bubbles can easily increase low-pressure turbine efficiency by several percentage points.

Pauley et al. (1990) presented a separation bubble bursting model based on their numerical results obtained by computing the separated laminar flows using a 2-D unsteady, incompressible, direct solution of the Navier-Stokes equations (DNS). They proposed that under certain conditions the separated shear layer becomes unstable and sheds spanwise vortices. The shedding

frequency can be represented by a Strouhal number, based on momentum thickness and free-stream velocity at the separation point, $Str = \frac{f\delta_{2_s}}{U_{\infty_s}}$. Their Strouhal number, 0.00686, compared favorably with Henk's (1990) experimental data.

Morin and Patrick (1991) performed an experimental study of laminar separation bubbles on a flat plate with adverse pressure gradients. No curvature effects were included in their study. They found that the transition process for laminar separation bubbles is different from that of attached boundary layers. The transition process in the shear layer over a separation bubble is more like that in a laminar free shear layer where discrete, spanwise vortices develop due to the Kelvin-Helmholtz instability and eventually break down to a fully-turbulent shear layer.

Work of Malkiel and Mayle (1995) showed that transition of laminar shear layers in separation bubbles possess both characteristics of attached boundary layers and free shear layers. They found that the intermittency development in separation bubbles can be modeled with correlations developed for attached boundary layer flows and Kelvin-Helmhotz vortex pairing exists in the transition region, similar to those in free shear layers.

Numerical Analyses and Modeling

Halstead et al. (1995d) explored using several existing codes with various turbulence models for computing flows in compressors and low-pressure turbines and compared their computational results to their experimental data (Halstead et al. 1995a, 1995b, and 1995c). In undisturbed, laminar flow and attached, turbulent flow, existing boundary layer codes with traditional

turbulence models can be used to compute skin friction coefficients, heat transfer rates and other general features. They were less successful in predicting the transition onset location, transition length, flow separation, and the reattachment point, however. In flows which have these events, the lack of knowledge about their fundamental behavior necessitates experimental observations as well as detailed direct computation (DNS). As more is learned, computational models which are reliable for design and affordable in the design setting can be developed. A possible alternative path to experimentation is complete reliance upon Navier-Stokes solutions, without modeling (DNS). Rai and Moin (1991) performed a DNS of a 3%-FSTI case on a flat wall. Pauley et al. (1990) conducted a DNS on separated laminar flows. Presently, DNS complements the experimental evidence nicely in that several terms that may be used by modelers, such as the pressure-strain term, are available by computation but cannot be found experimentally. The disadvantage of the DNS is that it is too costly, to be reasonable for design purposes when applied to engine flows and engine geometries in many practical cases, use of KNS is not possible at this time. Rai and Moin's DNS required nearly 1,000 hours of Cray YMP CPU time for a simple transitional boundary layer flow. Presently, such calculations are being made only in simple flows to gather information about transition behavior. Though they compute the Navier-Stokes equations without turbulence modeling, there are a number of other modeling choices that must be made in DNS simulation. Thus, even if the cost aspect were removed, continued experimental verification would be needed.

Volino and Simon (1991) reviewed the modeling efforts with one- and two-equation models and indicated a need to include more physics of transition

in the models. Volino and Simon (1995c) also recommended the use of a two-scale transition model for computing the effects of free-stream turbulence and near-wall bursting on production of the large-scale turbulence, the cascading of energy to the small scales, and the dissipation of energy at the small scales.

Past research at the Heat Transfer Laboratory at the University of Minnesota

The University of Minnesota program began with a study of the effects of three levels of free-stream disturbance (0.45%, 2.0%, and 8.6%) in transitional boundary layers (Kim et al. 1992). Complete documentation was done for two, low-FSTI cases. Kim et al. (1994) studied the combined effects of elevated free-stream disturbance and concave curvature on unaccelerated flows at two levels of disturbance, 0.6% and 8.6% FSTI, with the wall bent to a uniform radius of concave curvature of 97 cm. They showed that at 8% FSTI, transition occurred near the leading edge of the test wall and the flow was fully turbulent downstream. The entire data set of their experiments, complete with tabulated data, was presented in a NASA contractors report by Kim and Simon (1991). Volino and Simon (1994c) reprocessed the above data using the fluctuation values of the streamwise velocity, u′, the wall normal velocity, v′, and the temperature, t′, to segregate the signal into octants, according to the sign of each. Such octant segregation allowed describing the various events within the boundary layer, separately. Results from the Heat Transfer Laboratory comparing the octant decomposition in transitional and fully-turbulent flow showed a fundamental difference in structure between the two flows, with an increased importance of large scales in transitional flows compared to a wider distribution of important scales in the turbulent flow. Volino and Simon's

(1994c) octant analysis suggested the utility of incorporating multiple scales in transition models.

Volino and Simon (1994a, 1995a) measured mean velocity and temperature profiles, as well as skin friction and Stanton number values in a boundary layer flow with a relatively mild ($K=0.75\infty10^{-6}$) acceleration, which was more typical of the acceleration rates used in previous transitional and turbulent flow research. In the mild acceleration cases, transition was little influenced by acceleration. The cases for the flows in a boundary layer on a concave wall which experienced strong (maximum K of the order $10x10^{-6}$) acceleration rates were also reported by Volino and Simon (1995b, 1995c). The stronger acceleration had a significant effect in lengthening the transition zone. Also, at the beginning of the test section, where the acceleration was the strongest, some evidence of a reverse transition tendency was detected. This happened in spite of the high (~8%) inlet free-stream turbulence level to the test section. Two different regions of the transitional boundary layer were identified (distributed in both time and space). The first was a severely disturbed, non-turbulent flow characterized by high-amplitude unsteadiness, with energy distributed over a range of relatively low frequencies. Within this non-turbulent region, little turbulence was produced and the role of the wall (and, hence, the boundary layer) was to dampen and reduce the scales of free-stream turbulence. The second region was turbulent, possessing high-amplitude fluctuations having energy distributed over a wide range of scales, which included much higher frequencies than observed in the non-turbulent region.

Spectral measurements at several positions within the boundary layer were presented by Volino and Simon (1994b) for better documentation of the

nature of transition. Their spectral measurements proved valuable for determining the local state of the flow and for explaining the interaction between the boundary layer and free-stream disturbances. Their spectral analysis results complemented the original description of this flow which came from octant decomposition. The fundamental difference of flow "turbulence" scales between the transitional and fully-turbulent flow was clearly identified by their spectral data. Surface heat transfer measurements (Volino and Simon 1995c) were also made to describe this flow. Stanton numbers fell well below those seen in the unaccelerated flow on the concave wall under high free-stream turbulence conditions. In the zone which was declared to be intermittent (transitional flow), Stanton numbers fell below a correlation for low free-stream turbulence, fully-turbulent flow on a flat plate. Stanton number values rose to match this correlation as the flow became fully-turbulent. Through this region, the acceleration weakened and the free-stream turbulence level dropped. Skin friction values exhibited similar behavior but were generally higher than the Stanton number values, relative to an equivalent flat wall correlation. The Reynolds analogy factor, $2St/C_f$, dropped from about 1.15 in the unaccelerated flow to 0.8 in the accelerated flow case. The octant analysis (Volino and Simon 1995c) showed a lack of small-scale mixing in the transitional flow, as compared to scales associated with mixing in a fully-turbulent flow. All stations showed approximately the same octant distribution, indicating that even at the last measurement station, mature, fully-turbulent behavior was not achieved.

CHAPTER TWO
FACILITIES AND INSTRUMENTATION

In this study, all experiments were performed in the low-speed, open-return, blown-type wind tunnel shown in Fig. 2.1. This wind tunnel was initially designed and built by Wang (1984) and later modified by Kim (1990). The air is drawn into the tunnel by a New York Blower, model 224, centrifugal blower with a capacity of 5500 cfm. The fan is driven by a 3-phase, 230 V, 10 HP electric motor of Westinghouse model 680B103G37. A Louis-Allis Lancer Jr., VT, 10 HP variable frequency motor controller (model 92245) was employed for the control of motor and blower speed. The air drawn in by the blower goes through a filter box where particles larger than 5 μm, which could damage the hot-wire in the test section, are eliminated. Downstream of the blower are a series of grids and a honeycomb section for removal of the flow swirl and redistribution of the flow, improving flow uniformity. Flow is then redirected by an oblique header. A heat exchanger, immediately following the header, provides thermal uniformity of the flow within 0.1 ^{0}C spatially and temporally with a plumbing loop of circulating water through a 40 gallon storage tank, a 3/4 HP centrifugal pump (Dayton model 98K588), a cold water feed to the storage tank, and a drain for the discharge of excess water, as sketched in Fig. 2.1. The temperature of the tunnel flow is stabilized by adjusting the tap flow rate to the storage tank. Following the heat exchanger is a flow conditioning section consisting of a settling chamber and a screen pack for re-orientation of the flow and for reducing the free stream turbulence. A 10.7:1 contraction ratio nozzle is attached to the second settling chamber for increasing the flow velocity and for further reduction of the flow

turbulence. The inlet area of the nozzle is 0.914 m × 0.914 m. The nozzle has an exit area of 0.685 m × 0.114 m and an exit aspect ratio of 6:1, minimizing end-wall effects and insuring an ample two-dimensional region in the test wall and flow passage.

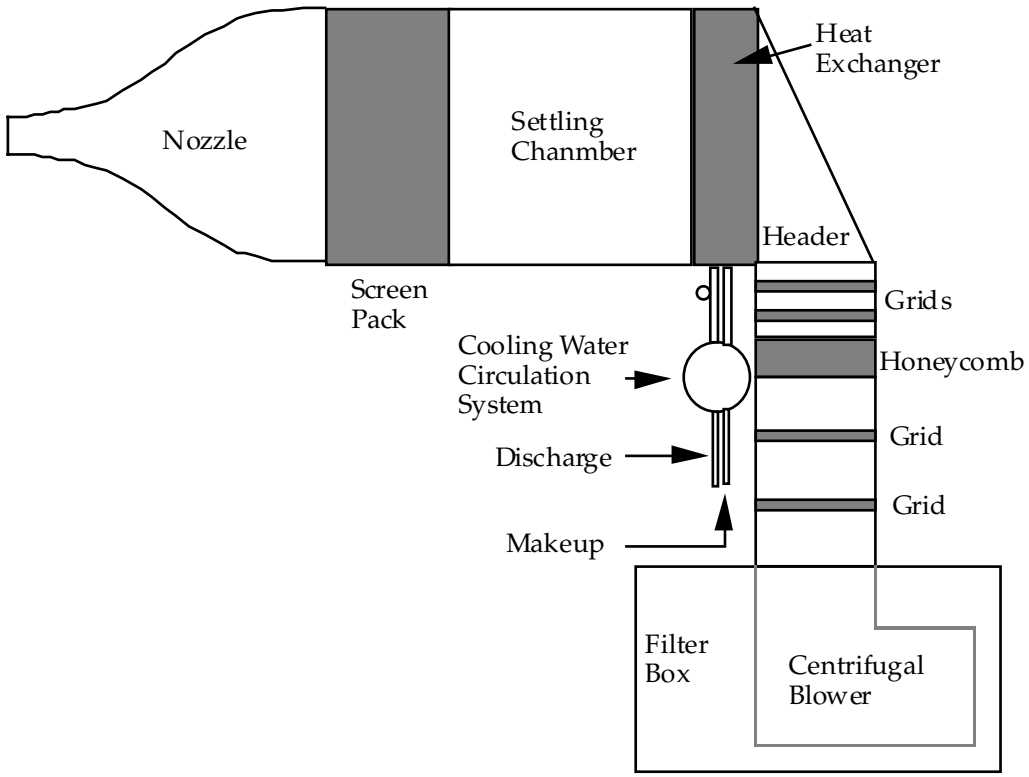

Fig. 2.1 Schematic diagram of the wind tunnel

SETUP AND TECHNIQUES

The wind tunnel exit is connected to a rectangular settling duct of the nozzle exit dimensions, followed by a test section (cascade simulator). A general layout of the test section and turbulence generation grids is given in Fig. 2.2. A

simplified top view is shown in Fig. 2.3. The settling duct is constructed of 9.5 mm (3/8 inch) Plexiglas sheet. In the present transitional boundary layer flow study, experiments were performed at three different turbulence levels of 0.5%, 2.5%, and 10% to investigate the free stream turbulence effects on flow transition and separation at low-pressure turbine conditions. In the 0.5% FSTI configuration, the rectangular settling duct is directly connected to the nozzle exit and no turbulence generation is presented. In the 2.5% FSTI configuration, a passive rod-grid is placed between the nozzle exit and the transition duct inlet. In the high-FSTI (10%) configuration, the rod-grid is replaced by a passive bar-grid and a high pressure jet grid is installed in the settling duct, as shown in Fig. 2.2. The jet grid is located 45.5 cm downstream of the duct inlet and 66.5 cm upstream of the blade leading edge. A high pressure manifold is hooked to the jet grid and high pressure air of 750 kPa (110 psi) is supplied to the manifold through a pressure regulator and a by-pass valve. The pressure of the supply air to the manifold can be adjusted by the pressure regulator and the by-pass valve. The jet grid issues high-velocity jets into the main flow at $\pm 60^0$ to the duct direction. The low pressure region in the vicinity of the high-velocity jets, combined with high pressure region at the impingement of adjacent grid jets, generates circulation zones of a moderate length scale immediately downstream of the jet grid. A change of the supplied air pressure by adjusting the pressure regulator and by-pass valve setting alters the jet velocity relative to the main flow; hence, the scales of the circulation zones and the turbulence level downstream are changed. The jet grid technique was initially designed by Sahm and Moffat (1992) and adapted and modified by the present authors for this study. This version of a jet grid, combined with a square bar grid, can generate

turbulence intensities of 20 % at the inlet of the test section. Higher turbulence levels can be obtained with this setup, but with excessive non-uniformity. The approach flow was tested and a suitably uniform flow was confirmed for up to 10% FSTI, as will be reported in a later chapter.

For adjusting the flow approaching the test section, one bleed section is clamped to each side of the approach duct. Adjustment is with screws located on the top and bottom end walls, Fig. 2.3. The bleeds are made of 2.54 mm (0.1 inch) thick Plexiglas that is flexible for easy adjustment but strong enough to sustain the pressure loads. The bleeds are used to adjust the direction of the approach flow.

In this study, a boundary layer type, single, tungsten, hot-wire of 4 μm diameter was used for near-wall flow measurements. A low-pressure transducer was applied to acquire total pressure data via a total pressure pitot tube. The same transducer was connected to a set of pressure taps on the suction wall for the measurements of static pressure distributions along the convex wall. Three columns of pressure taps are installed on the top end walls, immediately upstream of the test section. These taps are separated 1.27 cm (0.5 inch) both in streamwise direction and the cross-stream direction. One column of taps is located on the same endwall, over the exit region, with 1.27 cm (0.5 inch) interval. These taps and a single tuff were used for monitoring the approach flow and stagnation points on the leading edge while the two bleeds were being re-oriented, insuring that the approach flow moves in the proper direction, i.e. the streamlines meet the blade leading edges at the stagnation lines of the real turbine cascade. A two-dimensional region (constant static pressure region) could be found upstream of the test section. A constant pressure region, found

with the taps on the end wall, also exits downstream of the blade trailing edges. The static pressure data taken at these upstream and downstream regions, together with the total pressure measured with pitot tube in the core flow, can be used to calculate the inlet and exit flow velocities.

A boundary layer type, cross-hot-wire probe (TSI 1218) and a ninety degree bend, triple-hot-wire (TSI 1299BM) probe were used to document the free stream turbulence in the entrance region.

In all near-wall velocity measurements, a hot-wire probe was placed in the flow through the open slot on the concave wall. The probe cross-stream location was controlled by a stepping motor assembly. This assembly consists of system controller, Modulynx SCA 311, a controller card of type 10D010, a PDM155 driver, and a SLO-Syn, M063-LF-401, stepping motor, all from Superior Electric, Inc. The motor is capable of 400 half-steps per revolution, at 5 μm normal displacement for each half-step.

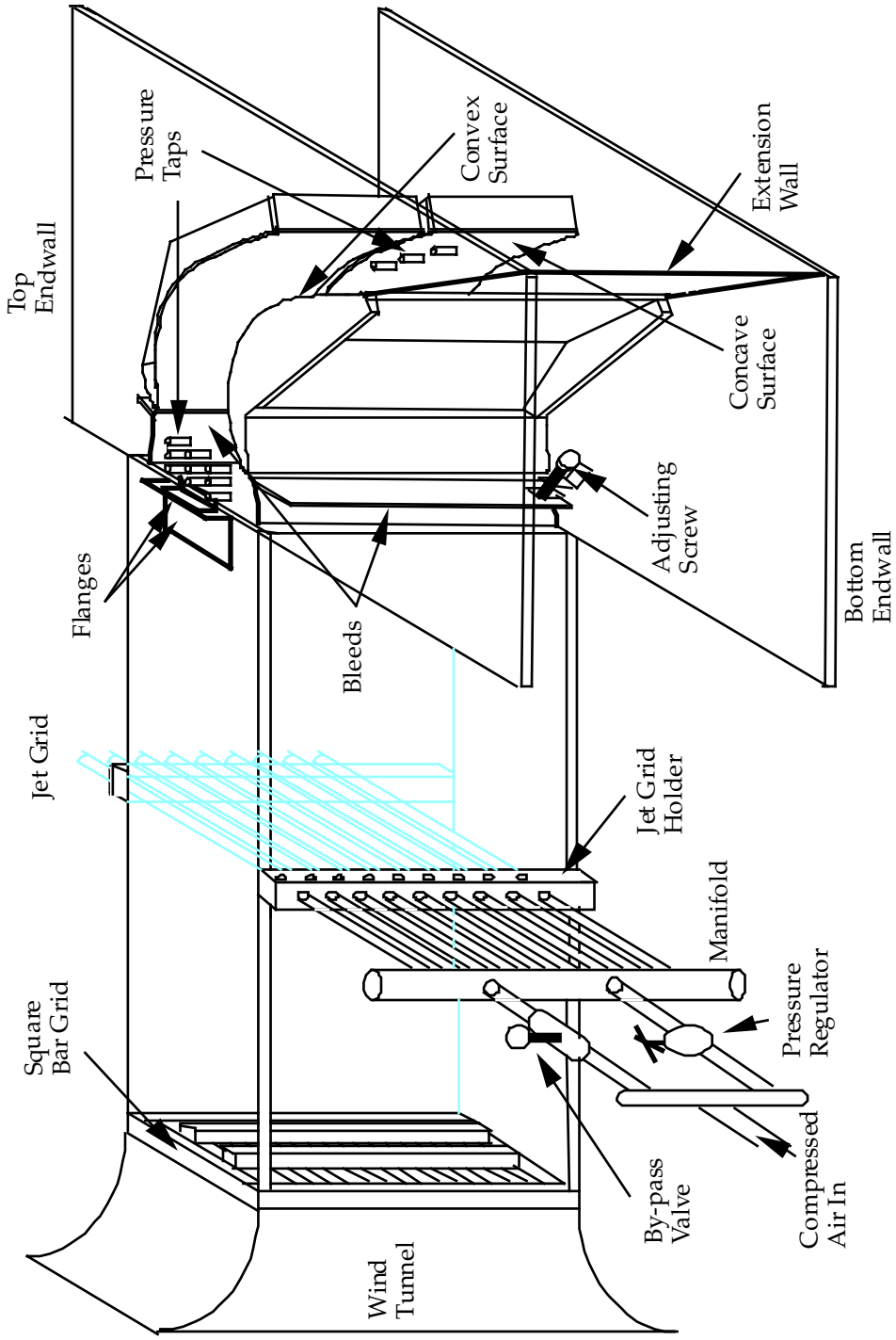

Fig. 2.2 Setup of the turbulence genarators and the test section

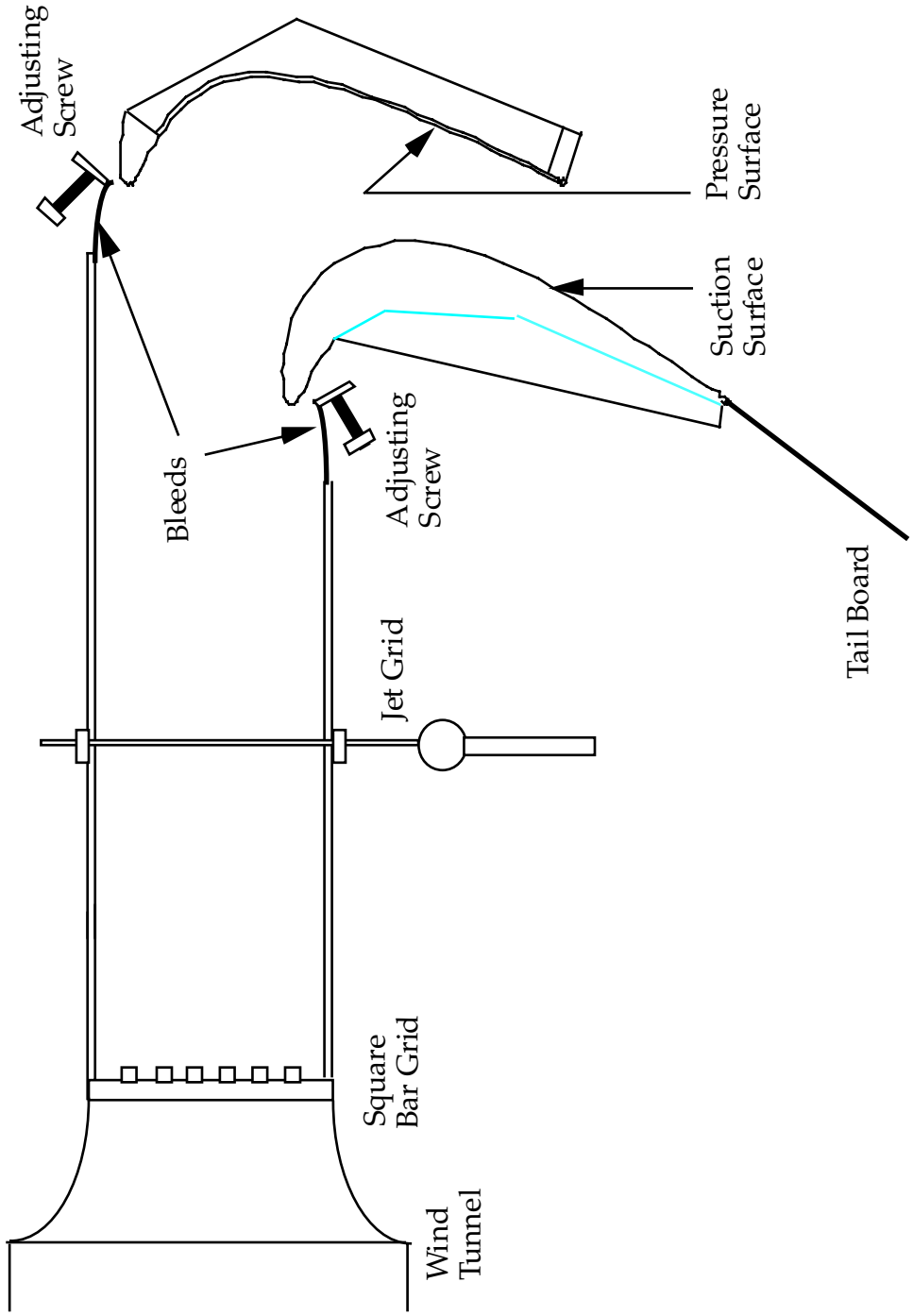

Fig. 2.3 A top view of turbulence generation and test section

Turbulence Generator

The turbulence generation grid used in the 2.5% FSTI configuration consists a wooden frame and thirteen steel rods of 4.76 mm (3/16 inch) diameter, see Fig. 2.4. Two of the thirteen rods are arranged in the vertical (spanwise) direction with 3.81 cm (1.5 inch) open spaces and the other eleven rods are placed in the horizontal (cross-stream) direction, separated by 5.72 cm (2.25 inches). The rods are held in position by the wooden frame.

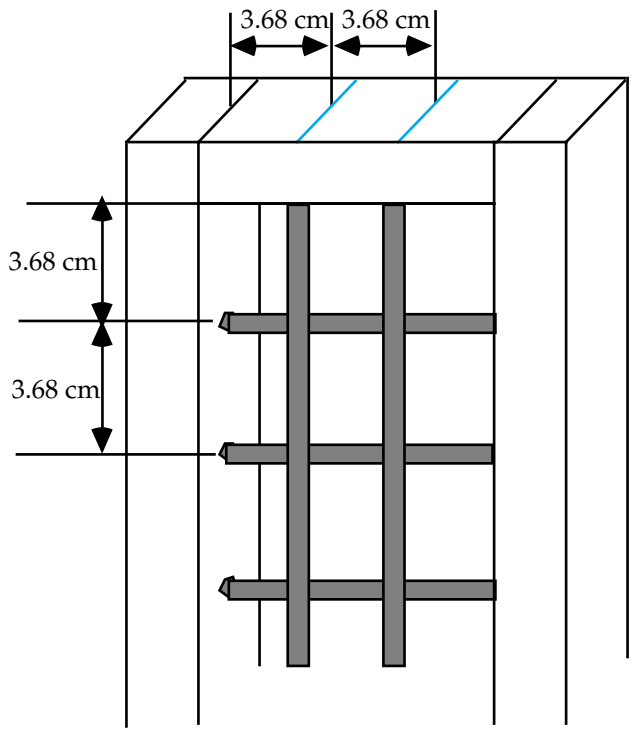

Fig. 2.4 Cylinder-bar grid

The bar-grid in the 10% FSTI configuration is made of a series of square wooden bars of 1.3 cm on a side, as shown in Fig. 2.5. The bars are arranged to form a mesh 2.5 cm ∞ 3.2 cm. The size of the bars, combined with the mesh size,

yields a blockage of 63%. The bar grid alone generates turbulence intensities of 6% 1.0 m (or about 31 mesh lengths) downstream.

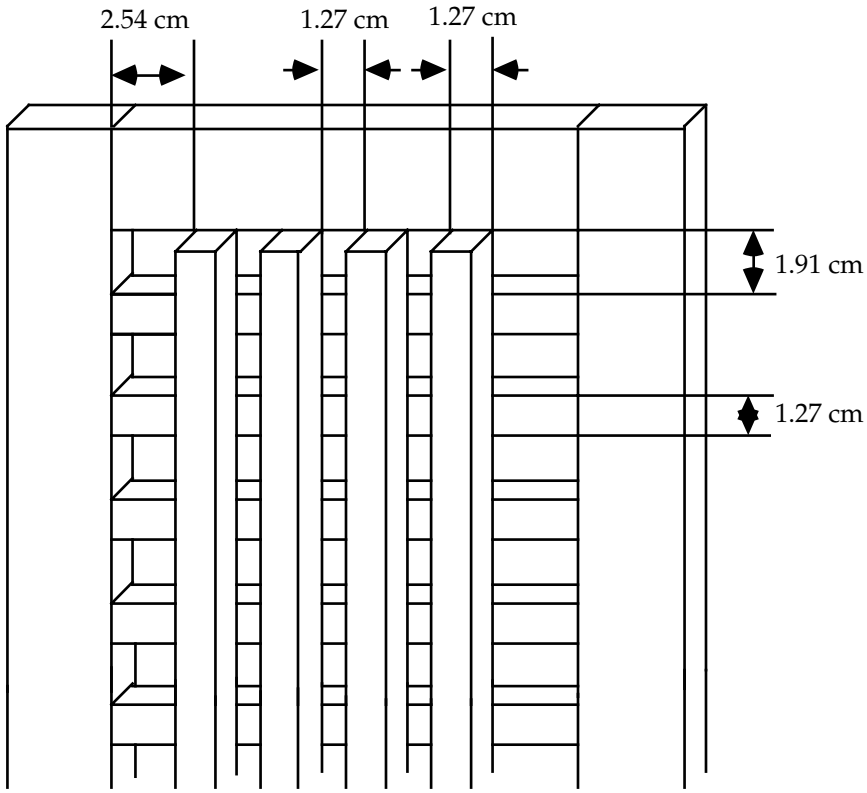

Fig. 2.5 Square-bar grid

The jet grid is composed of nine stainless steel tubes of 0.95 cm OD with five pairs of jet holes, angled at ± 60^0 to the downstream direction (Fig. 2.6). On each tube are five pairs of 0.8 mm diameter holes arranged symmetrically in the cross-span direction. Nine jet tubes are supported by two grid holders which are essentially 2.54 cm ∞ 2.54 cm Plexiglas ribs. Each holder has nine 9.53 mm (3/8 inch) diameter holes for the insertion of the jet tubes and nine threaded holes which hold set screws for holding the tubes in place, Fig. 2.2. Jet grid tubes

were inserted through these holes across the width of the duct, as shown. The tubes were aligned to insure that the index marks on the jet tubes appear at the center of the small, threaded holes. By this means, the jets produced by the grid are symmetric about the streamwise direction. Set screws were then applied through these threaded holes, holding the tubes in position.

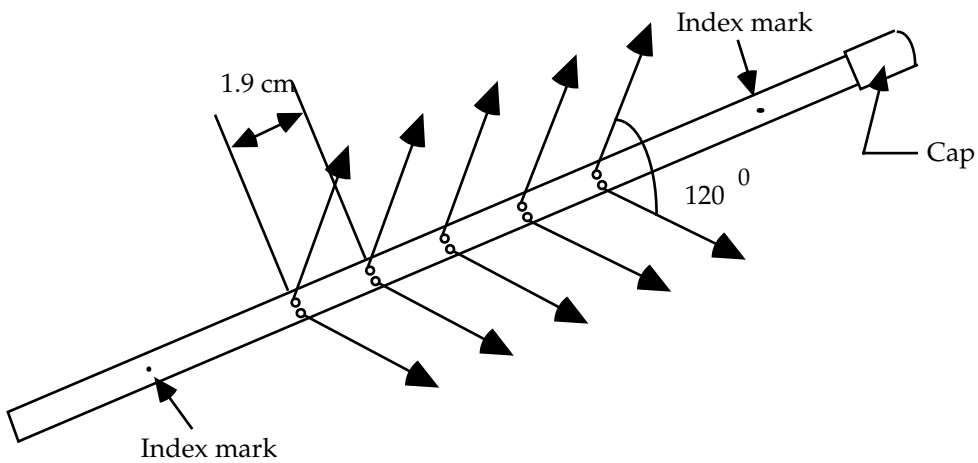

Fig. 2.6 Jet grid

Cascade Simulator

The cascade simulator is composed of two endwalls, a convex wall, and a concave wall. The bottom endwall is a 1.27 cm (0.5 inch) thick Plexiglas plate upon which the convex and concave walls are placed and bolted. Another Plexiglas sheet of the same size, but equipped with static pressure taps, as described before, serves as the top endwall. The convex wall is a machined piece of high-grade, reinforced, FR-4 fiberglass. The material was chosen for its excellent machining characteristics and its low thermal conductivity. Small values of thermal conductivity reduces hot-wire measurement error in the near-

wall region caused by thermal losses from the high temperature wire to the wall. Figure 2.7 is the sketch of the convex wall. The whole piece was machined from a block of 5.08 cm × 12.7 cm × 68.58 cm FR-4 fiberglass. The smoothly curved surface on the convex side and part of the concave side near the leading edge are fashioned in exactly the same shape as in a real turbine blade. This shape is identified as Pak B by Pratt and Whitney. The convex wall is bolted to the end walls through bolting holes on the top and bottom ends. The actual chord length is 11.4 cm (4.5 inch) and the span-to-chord aspect ratio of 6. The pitch-to-chord ratio (solidity) is 0.8 and turning is 95° (35° from the tangential direction of the engine to 30° from the tangential direction).

Thirteen static pressure taps are installed along the convex wall, staggered 22.86 cm and 24.13 cm from the bottom endwall. That configuration prevents any tap effect on the near-wall flow at the centerline (34.29cm from the endwall). Each pressure tap is configured with a 0.635 mm (25 mil) hole, drilled perpendicular to the convex surface, of 2.54 mm to 5.08 mm depth and a 3.175 mm diameter hole, drilled from the other side of the blade, forming a counter sink. A 3.175 mm OD copper tube of about 2 cm long is placed into the bigger hole and is sealed in position with epoxy.

The concave wall of the test section is shown in Fig. 2.8. A thin Lexan sheet constitutes most of the pressure surface. Several strengthening ribs, glued on the outer side of the Lexan sheet, are machined from Plexiglas. The leading edge region (pressure and suction sides) and the full pressure side reproduce the geometry of the turbine blade.

In designing the concave wall, concern was for easy access of the hot-wire probe through it for near-convex-wall measurements. Therefore, the concave

wall is divided into two pieces of the same height, 33.9 cm for each piece. One of them is bolted to the top endwall while the other is on the bottom end wall, leaving a 7.62 mm wide slit in the center which is open for access of the hot-wire probe. In the test run, the slit was sealed off by Mylar tape.

The geometry of each wall is two-dimensional, holding the same shape over its entire span.

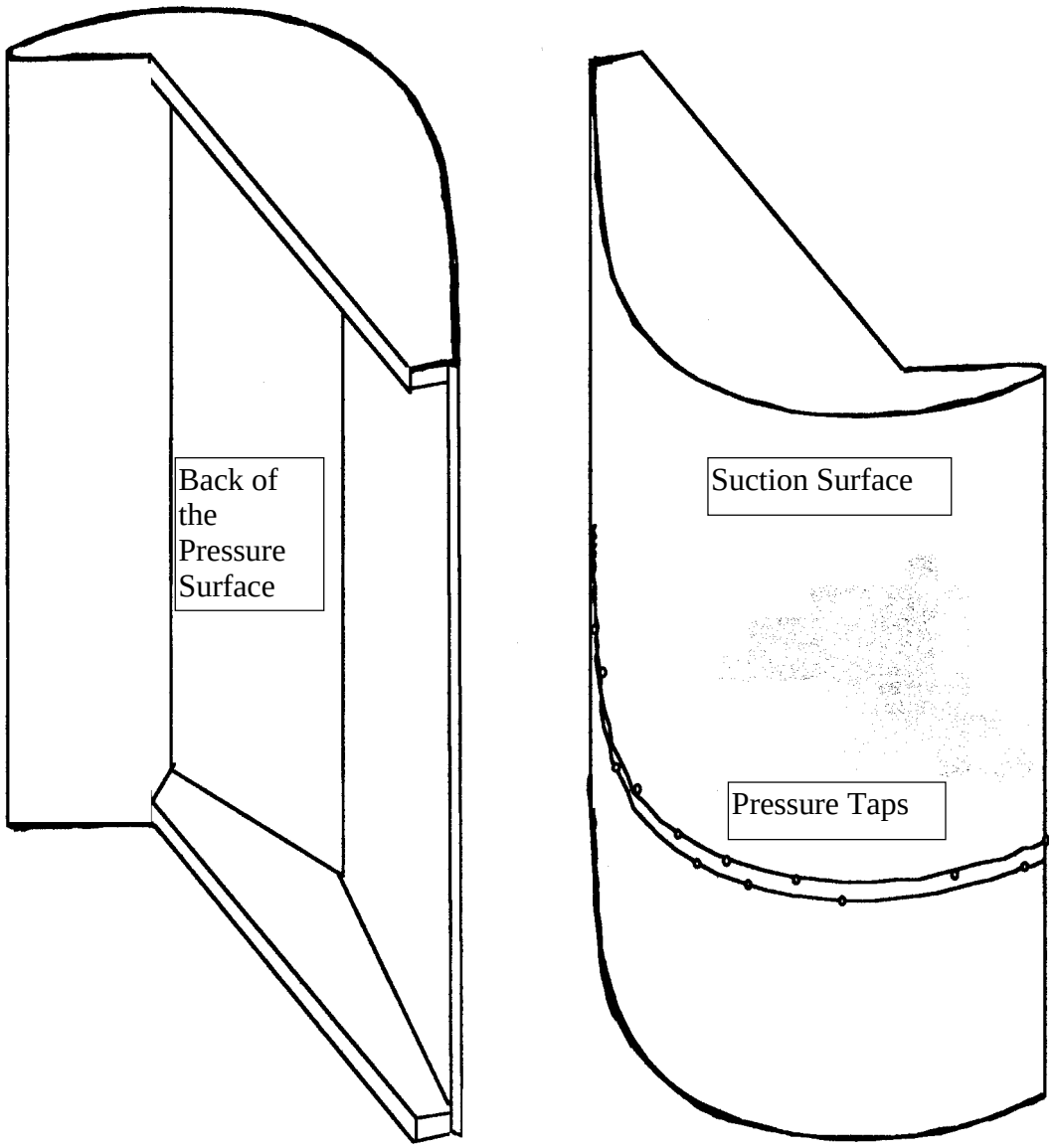

Fig. 2.7 Convex Wall

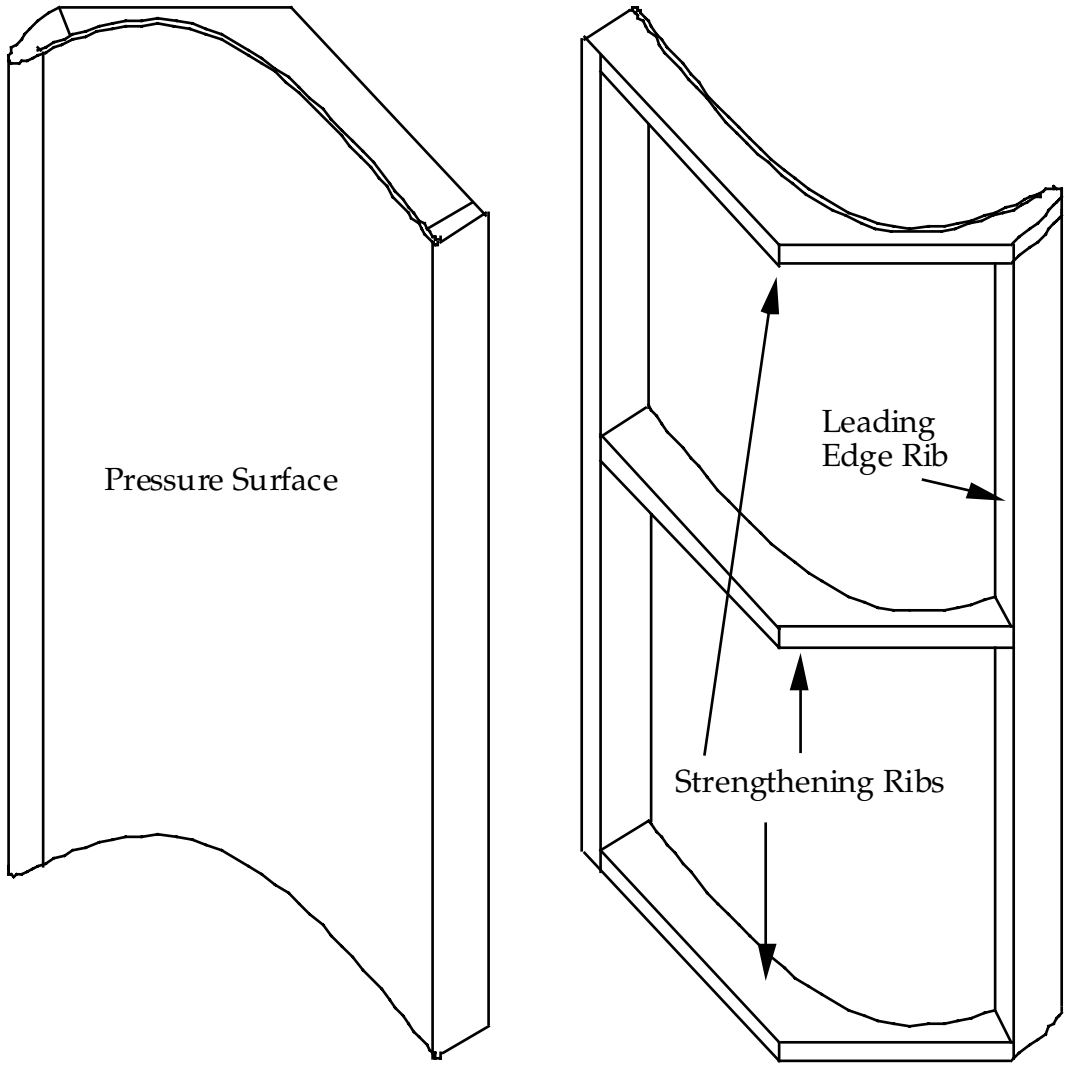

Fig. 2.8 Concave wall

INSTRUMENTATION

Hot-Wire Probes

In this study, hot-wire anemometry was used to measure the instantaneous and local velocities. Hot-wire anemometry mainly consists of using an electronic circuit to hold a wire placed in the stream to a pre-set temperature. Since the heat loss from the sensor to the surrounding fluid is velocity dependent, the circuit must alter the current to the wire in order to do so. The velocity is determined, through calibration, by measuring the instantaneous current supplied to the heated wire.

A boundary layer type probe (TSI model 1218) was used in this study for near-wall velocity measurements. This probe has the sensor approximately 12.7 mm (0.5 inch) upstream of the probe stem. By doing so, the influence of the probe and support on the flow is minimized. The prongs of the probe are curved upstream; measurements are to be taken in only one flow direction since the probe cannot distinguish reverse from forward flow. A tungsten wire of 4 μm diameter is mounted on the probe to be perpendicular to the stem and parallel to the wall.

A cross-wire probe (TSI 1243, T1.5) was employed to document the free stream turbulence. The prongs are curved at 12.7 mm (0.5 inch) radius, as in the single-wire probe. Tungsten wire of 4 μm diameter was used with this probe. Two wires are orthogonal to each other and are inclined 45^0 to the main flow, as depicted in Fig. 2.9. The two wires are separated by 1 mm in the spanwise direction.

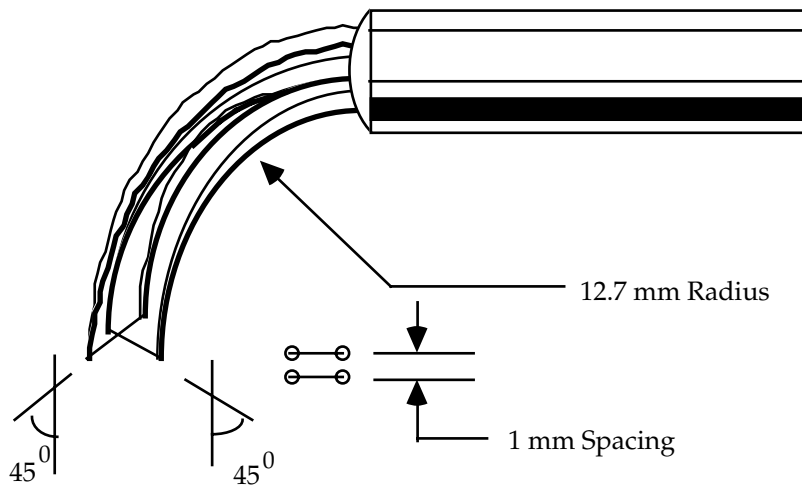

Fig. 2.9 Cross-wire probe

Figure 2.10 shows a triple-wire probe (TSI 1299BM) with six straight prongs bent so that the probe provides instantaneous measurements of the three principal components of velocity with minimal prong interference and with good spatial resolution. The probe holder is bent 90^0 for possible near-wall measurement. Three, 51-µm hot-film sensors are mounted on these prongs. In a perfectly-constructed probe, each of the sensors is perpendicular to the other two sensors. The hot-film sensor behaves similar to the hot wire but is constructed with a thin metal film on a quartz cylinder. Each sensor is inclined at 54.74^0 to the main flow and the azimuthal sensor-separation angle formed by each sensor with respect to the other sensors is 60^0. Russ and Simon (1990) demonstrated that for a slightly non-orthogonal probe (as the one used in present study), simple orthogonal probe equations can be used to process the signals with only slight error.

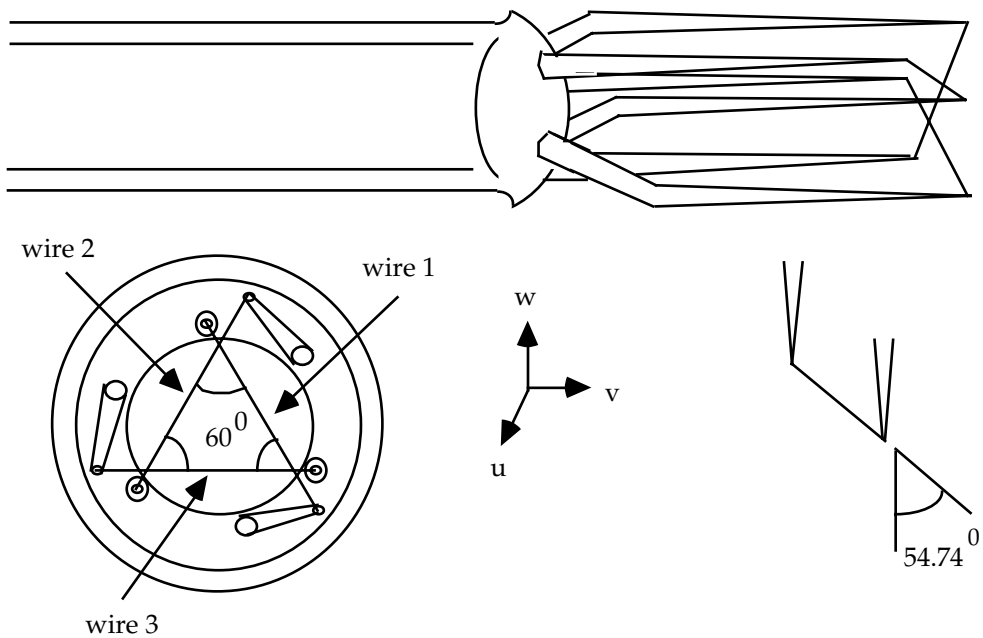

Fig. 2.10 Triple-wire probe

Calibration

The probes were calibrated in an air jet. The velocity through the jet was adjusted via a pressure regulator. The supply pressure was measured via a pressure transducer and the velocity at the exit plane of the jet issuing into the room was calculated. The hot-wire voltage reflected the cooling rate of the passing air stream on the wire because the energy generated by the electrical power in the wire was dissipated to the surrounding fluid by natural and forced convection. A King's law relationship between the hot-wire voltage and the jet velocity could be found by applying these physical laws and Collis and Williams (Wills 1962) empirical heat transfer model for a cylindrical wire. King's law used for calibration in this experiment could be expressed as:

$$(\text{Velocity})^n = A + B \cdot (\text{Voltage})^2 \qquad n = 0.435 \ldots 0.5 \qquad (2\text{-}1)$$

where the A and B are calibration constants. The value of n is found also by calibration, but will always be near 0.45.

The sensors of the cross-wire probe were calibrated in the calibration jet described above with the wires inclined at 45^0 to the jet flow (same position as was used in measurements). The velocity component normal to the sensor, [$U_{eff}=U_{jet}\cos(45^\circ)$], which is the effective velocity for wire cooling, was used as the calibration velocity. King's correlation, Eqn. (2-1), was applied to each of the two wires and the calibration constants were calculated.

In the calibration of the triple-wire probe, the sensors were inclined at 54.74° to the jet flow. Therefore, $U_{eff} = \sqrt{2.04 U_{jet}\cos(54.74^0)}$ was used as the calibration velocity. The coefficient 2.04 in the above equation is discussed in the next chapter. Equation (2-1) was employed to determine the calibration constants for each of the three sensors.

Pressure Transducer

A variable-reluctance type (Validyne DP45) pressure transducer was used for all pressure measurements. The diaphragm of the transducer was designed for a low pressure difference in the range 0 - 8.9 cm (3.5 inch water), with an accuracy of 0.5% of full scale. Calibration of the transducer was performed in the calibration jet with a micro-manometer. The same calibration was used for hot-wire calibration (to be discussed). Response of the transducer to the varying pressure is linear, so that the calibration constant can be obtained by a linear fit to the data. Drift of the calibration slope with time is negligible. The transducer zero-point is frequently reset.

The analog output of the pressure transducer is conditioned by a Validyne sine wave carrier demodulator of type CD-15. The output signal provided by the demodulator is stabilized and amplified. Gain and offset of the signal from the demodulator is adjustable. Once the gain is adjusted, no change is made. The offset is often adjusted to zero before use.

Intermittency Circuit

In all near-wall velocity measurements, an intermittency circuit was utilized to evaluate the local flow state of the flow (laminar, turbulent, or transitional). The circuit is based on the design of Kim et al. (1978). It takes the voltage across the hot-wire as an input and provides the larger of the first and second derivatives of the input signal. If either or both of the derivatives exceeds a threshold level, the circuit declares the flow turbulent and outputs a +5 V signal. Otherwise, it declares the flow non-turbulent and outputs a 0 V signal. The basic idea of the circuit is to separate the high-frequency, turbulent flow from the low-frequency, non-turbulent flow by judging on the first and second time derivatives of the flow signal. The second derivative in the circuit is included to prevent misinterpreting the flow state when the first derivative crosses zero.

The threshold levels for the derivatives were set for each flow. The tuning of the circuit in a simple flow is straightforward. But in a complex flow, such as in the present study, tuning of the circuit is significantly more difficult. Experience showed that when the flow is fully turbulent or fully non-turbulent, the intermittency is not very sensitive to the setting of the threshold levels and the circuit can judge flow state reasonably well. When the flow is transitional,

whether the circuit declares part of the flow as turbulent or non-turbulent is largely dependent on how the threshold levels are set. The same ambiguity would exist if the experimenters were to make such determination themselves from the velocity-time record. Despite some potential for uncertainty, the trends of intermittency with distance are reliable.

Verification of the threshold settings was done by comparisons of the hot-wire waveform and the intermittency function. Before taking the intermittency measurements, the instrument and the circuit were brought to a simple boundary layer flow. The hot-wire voltage waveform was then compared by eye against the intermittency function waveform to see whether the circuit interpreted the flow state (laminar, turbulent, or transitional) the same way as the experimenter would have interpreted it. By many such comparisons taken after the thresholds were set, an uncertainty of 10% was selected for the low-FSTI cases, rising to 15% for the higher FSTI cases.

Digitizer

A Fluke 8840A multimeter was used to convert the analog signals from the thermocouples and pressure transducers. The Fluke multimeter is a 16-bit-resolution digitizer with a variable range of 200 mV to 1000 V dc. It has an option of auto range. The sample speed can be set at three different rates, slow (2.5 Hz), medium (20 Hz), and fast (100 Hz). Thermocouples were used to establish and control the flow temperature.

A 12-bit Norland Prowler digital oscilloscope with a variable range of 100 mV to 20 V and a variable reading rate of 1 Hz to 100 kHz was used for high-speed recording. The oscilloscope has two channels with a 4096 reading buffer

for each channel. For triple-wire measurements, two oscilloscopes were linked in a master-slave mode for simultaneous recording of data on three channels. The digitizers (Fluke multimeter and Norland Prowler oscilloscope) were connected to a PC via IEEE cables for data transfer and instrument control.

Low-Pass Filter

A lowpass filter, Model SR650 from Stanford Research Systems, was employed for hot-wire data conditioning. It has two independent filter channels, one for the lowpass filter and the other for a highpass filter. In the mean velocity profile measurements, only the lowpass filter was used. The filter has a very sharp cutoff frequency of 115 dB/Octave rolloff. The cutoff frequency may be set between 1 Hz and 100 kHz with three digits of resolution. It has an adjustable gain of 0-60 dB with very low noise (less than $4\mu V/\sqrt{Hz}$).

FLOW VISUALIZATION SETUP AND TECHNIQUES

In conjunction with velocity and pressure measurements, flow separation measurements were made on the suction surface with a visualization technique. Surface static pressure measurements were limited to the locations of pre-mounted static pressure taps. Velocity profiles measured with the hot-wire, along with intermittency distributions are appropriate for detailed documentation of boundary layer development, flow transition, and reattachment of the flow. To locate the exact positions of the flow separation and reattachment points, which are important for modeling transition length and the length between separation and transition onset, such profile measurements were

found to be inadequate. Thus, a technique for measuring wall shear stress direction was developed. We found that the separation and reattachment points could be accurately identified with this simple, but versatile, technique.

The schematic of the apparatus for the visualization of flow separation on the suction surface is depicted in Fig. 2.11. The individual components of the facility are shown in the figure. For this study, a piece of contact paper marked with dots using Staedtler Lumocolor 317 marker pens was pasted on the surface before turning on the flow. The number density of the dots was adjusted as needed for the application. Too few gave too little information whereas too many dots generated a messy picture. In the present study, it was found that a spacing of 2.5 mm between dots in the lateral and 5 mm between dots in the vertical direction is appropriate. The solvent (99% pure isopropyl alcohol) was sprayed to the substrate (contact paper) after the blower was turned on and flow reached steady state. The sprayer consists of an automotive fuel pump, a reservoir for the solvent, an automotive fuel injector, and a needle valve. The solvent flow rate was adjustable with the bypass valve, which controls the solvent pressure. The period of solvent injection was regulated by the injector switch. The solvent put the ink into solution, allowing it to flow in the direction of the local wall shear stress for a few seconds until the surface dried. Spraying the solvent is an art which required time to develop.

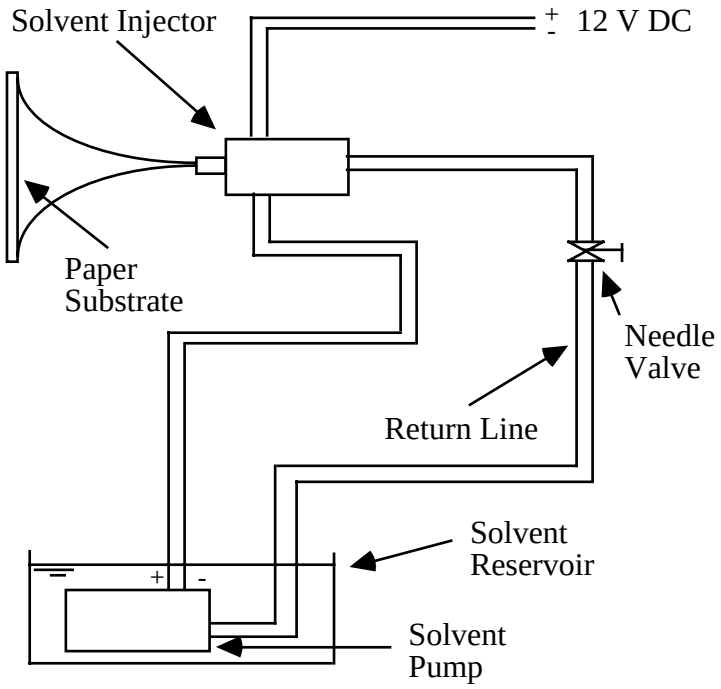

Fig. 2.11 Schematic of flow visualization setup

CHAPTER THREE
DATA PROCESSING

SINGLE-WIRE DATA

Ensemble means were computed by summing over 4096 samples. The sample rate was set at 100 Hz for most of the measurements. The corresponding sample time was more than 40 seconds, which usually eliminated small-sample and low-frequency unsteadiness effects. The digitizer had sample-hold capabilities so values were "frozen" in less than a micro second. Since statistical values such as mean and turbulence intensity were sought, a sampling rate of 100 Hz was suitable. The ensemble means and rms fluctuations were calculated from the following equations:

$$\bar{u}(x,y,z) = \frac{1}{N}\sum_{i=1}^{N} u_i(x,y,z) \tag{3-1}$$

$$u'_{rms}(x,y,z) = \sqrt{\frac{1}{N-1}\sum_{i=1}^{N}[u'_i(x,y,z)]^2} = \sqrt{\frac{1}{N-1}\sum_{i=1}^{N}[u_i(x,y,z) - \bar{u}(x,y,z)]^2}$$

$$= \sqrt{\frac{1}{N-1}\sum_{i=1}^{N} u_i^2(x,y,z) - \frac{1}{N(N-1)}[\sum_{i=1}^{N} u_i(x,y,z)]^2} \tag{3-2}$$

For boundary layer flow measurements, the uncertainty in both ensemble mean velocity and rms velocity fluctuation is 3%, which is mainly caused by calibration error and misalignment.

CROSS-WIRE DATA

In a two-dimensional or three-dimensional flow, effective velocities must be computed with the normal component of the velocity, U_n, and the tangential component of the velocity, U_t, with a tangential factor, k_t, as follows:

$$U_{eff1} = \sqrt{U_{n1}^2 + k_t^2 U_{t1}^2} \tag{3-3}$$

$$U_{eff2} = \sqrt{U_{n2}^2 + k_t^2 U_{t2}^2} \tag{3-4}$$

where $k_t = -5\times10^{-4}\frac{l_s}{d_s}$ + 0.3 (Wills, 1962) and $\frac{l_s}{d_s}$ is length-to-diameter ratio of the hot wire.

Instantaneous velocities, u and v, were calculated with equations (3-3) and (3-4), combined with following equations for U_n and U_t (see Fig. 3.1):

$$U_{n1} = u\sin(45^0) + v\cos(45^0) \tag{3-5}$$

$$U_{t1} = v\sin(45^0) - u\cos(45^0) \tag{3-6}$$

$$U_{n2} = u\sin(45^0) - v\cos(45^0) \tag{3-7}$$

$$U_{t2} = u\cos(45^0) + v\sin(45^0) \tag{3-8}$$

The cross-correlation of u'_{rms} and v'_{rms} , the turbulent shear stress, $\overline{u'v'}$, was calculated by

$$\overline{u'v'} = \overline{uv} - \overline{u}\,\overline{v} = \frac{1}{N}\sum_{i=1}^{N}(u_i v_i) - \frac{1}{N^2}\sum_{i=1}^{N}u_i \sum_{i=1}^{N}v_i \tag{3-9}$$

The non-linear equations (3-3) and (3-4) were solved by iteration for instantaneous velocities during the acquisition and the summations used for computing the ensemble-averaged velocities and rms velocity fluctuations were evaluated. The mean and rms fluctuation values were then computed and stored on the hard disk. Considerable hard disk space was saved by not recording all the instantaneous voltages from the hot-wire anemometer, or the instantaneous velocities, but some extra time was paid during the tests for solving of these non-linear equations.

Champagne et al. (1967a, 1967b) proposed a post-processing correction for normal velocity fluctuations, v'_{rms}, and turbulent shear stresses, $\overline{u'v'}$. The corrections on streamwise velocity, u, normal velocity, v, and streamwise velocity

fluctuations, u'_{rms}, are negligible. From Fig. 3.1, it can be noted that the effective cooling velocities (normal component of the velocities) of wire 1, U_{eff1} , and wire 2, U_{eff2}, can be related to the streamwise flow velocity, u, and normal velocity, v, by the following equations:

$$U_{eff1} = u\sin(45^0) + v\cos(45^0) \tag{3-10}$$

$$U_{eff2} = u\sin(45^0) - v\cos(45^0) \tag{3-11}$$

or

$$u = \frac{U_{eff1} + U_{eff2}}{2\sin(45^0)} \tag{3-12}$$

$$v = \frac{U_{eff1} - U_{eff2}}{2\cos(45^0)} \tag{3-13}$$

The corrections were then made to v'_{rms} and $\overline{u'v'}$ with the Champagne Correction

$$v'_{rms,corrected} = v'_{rms,measured}\sqrt{\frac{1-k_t^2}{1-3k_t^2+4k_t^4}} \tag{3-14}$$

$$\overline{u'v'}_{corrected} = \overline{u'v'}_{measured}\frac{1+k_t^2}{1-k_t^2} \tag{3-15}$$

The Champagne correction was tested against a direct correction of instantaneous velocity. The error resulting from the Champagne correction was less than 0.5% and the acquisition time was greatly reduced. The cross-wire mean velocities have a uncertainty of about 3%, mainly caused by calibration errors. The uncertainty in u'_{rms} is 3%, 4% in v'_{rms} and 5% in $\overline{u'v'}$ (Volino and Simon, 1995c).

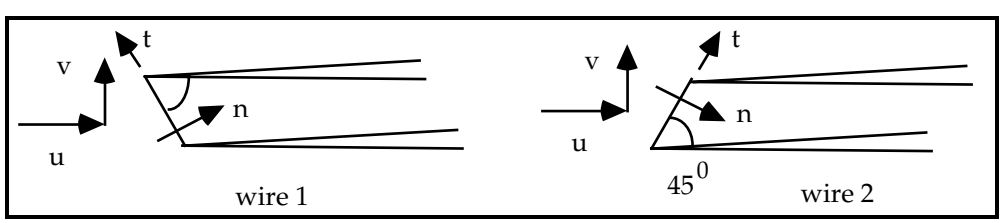

Fig. 3.1 Alignment of a cross-wire

TRIPLE-SENSOR DATA

For a triple-sensor probe described above, the equation that relates the effective cooling velocity to normal (U_n), tangential (U_t), and vertical (U_b) components of velocity to the sensors is:

$$U_{eff} = \sqrt{U_n^2 + K^2 U_t^2 + H^2 U_b^2} \tag{3-16}$$

Where K, the yaw coefficient, is 0.2 and H, the pitch coefficient, is 1.08 (Lekakis et al. 1989).

Applying the above equation to each of the three sensors results in three non-linear equations, one each for u, v, and w, in terms of U_{eff1}, U_{eff2}, and U_{eff3}, the three instantaneous cooling velocities. The cooling velocities are computed from voltage outputs by King's law. These equations are solved to yield the three instantaneous velocities u, v, and w. The solution, however, is very difficult. Fortunately, use of an orthogonal probe can significantly simplify the problem.

For a perfectly orthogonal probe, three non-linear equations can be approximated by following linear equations (Russ and Simon, 1990):

$$U_{eff1} = K^2 U_{t1}^2 + U_{t2}^2 + U_{t3}^2 \tag{3-17}$$

$$U_{eff2} = K^2 U_{t2}^2 + U_{t1}^2 + U_{t3}^2 \tag{3-18}$$

$$U_{eff3} = K^2 U_{t3}^2 + U_{t1}^2 + U_{t2}^2 \tag{3-19}$$

$$U_{t1} = u\sin(35.26^0) - (w\cos(60^0) + v\sin(60^0))\cos(35.26^0) \tag{3-20}$$

$$U_{t2} = u\sin(35.26^0) - (w\cos(60^0) - v\sin(60^0))\cos(35.26^0) \tag{3-21}$$

$$U_{t3} = u\sin(35.26^0) + w(35.26^0) \tag{3-22}$$

The errors incurred during the processing of mean velocities using the above equations are less than 2%, 2.5% for turbulence intensities (Russ and Simon

1990). The measurement errors, combined with processing errors, yield an uncertainty of 3.6% in mean velocities. The uncertainty in fluctuation components, u′, v′ and w′, is 4%.

NEAR-WALL CORRECTION ON HOT-WIRE DATA

Velocities at points very near the wall (y less than 0.4 mm) are affected by conduction between the hot-wire and the wall. This conduction causes extra heat loss from the wire to the surroundings and yields falsely high velocity readings. The discrepancies between the true value and measured value depend on the wire distance from the wall, shear velocity, and wall conductivity (Chew et al. 1995). An empirical scheme proposed by Wills (1962) was used to correct the near-wall velocities. Wills developed his correlation in laminar flow and proposed that half of the correction be used in turbulent boundary layer flows, though he did not give the reason. Kim (1990) calibrated the correction in a simple, unaccelerated, fully-turbulent boundary layer on a flat plate and found that 84% of the Wills correction was best. The Wills correction was used for laminar flows and Kim's correlation was used for turbulent flows. The correction scheme used in this study is as follows:

Laminar Flow:

$$u_{corrected} = [u_{uncorrected}^{0.45} - (\frac{\nu}{d_s})^{0.45} k_w]^{1/0.45} \tag{3-23}$$

$$k_w = 0.9 - 7.2\times10^{-2}\left(\frac{2y}{d_s}\right) + 2.89\times10^{-3}\left(\frac{2y}{d_s}\right)^2 - 6.15\times10^{-5}\left(\frac{2y}{d_s}\right)^3 + 6.51\times10^{-7}\left(\frac{2y}{d_s}\right)^4 \quad \text{when } 2y/d_s < 50$$

or

$$k_w = 0.54 - 2.42\times10^{-2}\left(\frac{2y}{d_s}\right) + 5.01\times10^{-4}\left(\frac{2y}{d_s}\right)^2 - 5.36\times10^{-6}\left(\frac{2y}{d_s}\right)^3$$

$$+ 2.85\times10^{-8}\left(\frac{2y}{d_s}\right)^4 \quad \text{when } 2y / d_s > 50$$

Where d_s, the sensor diameter is 4 μm for tungsten wire, or 5 μm for platinum wire.

Turbulent Flows:

$$u_{corrected} = 0.84[u_{uncorrected}^{0.45} - (\frac{\nu}{d_s})^{0.45} k_w]^{1/0.45} + 0.16u_{uncorrected} \quad (3\text{-}24)$$

Transitional flows are composed of laminar and turbulent flows. The above corrections were applied to their respective components.

SHEAR STRESS

The wall shear stress and friction coefficient were determined from the near-wall velocity profiles by casting them into wall coordinates (u^+, y^+) and fitting the transformed profiles to the "law of the wall" while iterating on the shear stress. In the process, the shear stress was first guessed and the u^+, y^+ based on the guessed shear stress was compared to the model (linear law in sublayer, and van Driest equation in the buffer layer). If the match between them was deemed not good enough, another shear stress was tried. The fitting process continued until a good agreement was found and the shear stress was so determined. The emphasis here was on the near-wall data, generally in the range of $1 < y^+ < 100$. This method results in an uncertainty in wall shear stress of about 7% - 8% in C_f.

INTERMITTENCY

The instantaneous voltage outputs from the intermittency circuit are either zero, indicating laminar-like flow, or five volts, implying turbulent-like flow. The intermittency was evaluated by counting the number of five-volt points over the 4096 samples. The circuit which establishes intermittency has adjustments which were made at the beginning of the test so that the intermittency function (the function that indicates the instantaneous state of the flow) agreed with the experimenter's interpretation of the state of the flow. This was done by viewing the hot-wire voltage waveform against the intermittency function waveform. To do this, both were digitized at 100 kHz to capture the waveform. This setting, once chosen, was used throughout the test program. The intermittency uncertainty is 10 % for the low FSTI cases, rising to 15% in the elevated FSTI cases.

POWER SPECTRA

In the present study, power spectra were measured on the velocity fluctuations in the free-stream. Data were acquired using the single, cross, and triple hot-sensor probes described above. During the acquisition, only the u'_{rms}, v'_{rms}, and w'_{rms} are recorded. For each spectrum, data were acquired in three sections at sampling rates of 1 kHz, 10 kHz and 100 kHz. The data were low-

pass filtered at 1/10th the sampling rate, i.e. 100 Hz, 1 kHz and 10 kHz for each section, respectively. Twenty sets of 4096 data points were acquired for each of the three sections. A Fast Fourier Transform (FFT) was performed for each set of 4096 sampling points to compute the power spectral density (PSD) of $u', Eu = u'^2_{rms}/df$; PSD of v', $Ev = v'^2_{rms}/df$; and PSD of w', $Ew = w'^2_{rms}/df$. Twenty spectra from each section were averaged and the three sections were then pieced together to form a full spectrum. The PSD from the first section of 1 kHz sampling rate (with 100 Hz low- pass filtering) provide the spectrum from 0 to 50 Hz. The PSD from the second section of 10 kHz sampling rate (with 1 kHz low-pass filtering) forms the middle part of the spectrum from 50 Hz to 500 Hz, while the PSD from the third section (100 kHz sampling rate and 10 kHz low-pass filtering) covers the final portion of the spectrum from 500 Hz to 5000 Hz. Acquiring spectra in sections provided better resolution over the whole spectrum for this particular flow and with the instruments used.

Figures 3.2 and 3.3 show typical free-stream power spectra at the inlet of the test section (Fig. 2.2), acquired with a single-wire and a cross-wire probe, respectively.

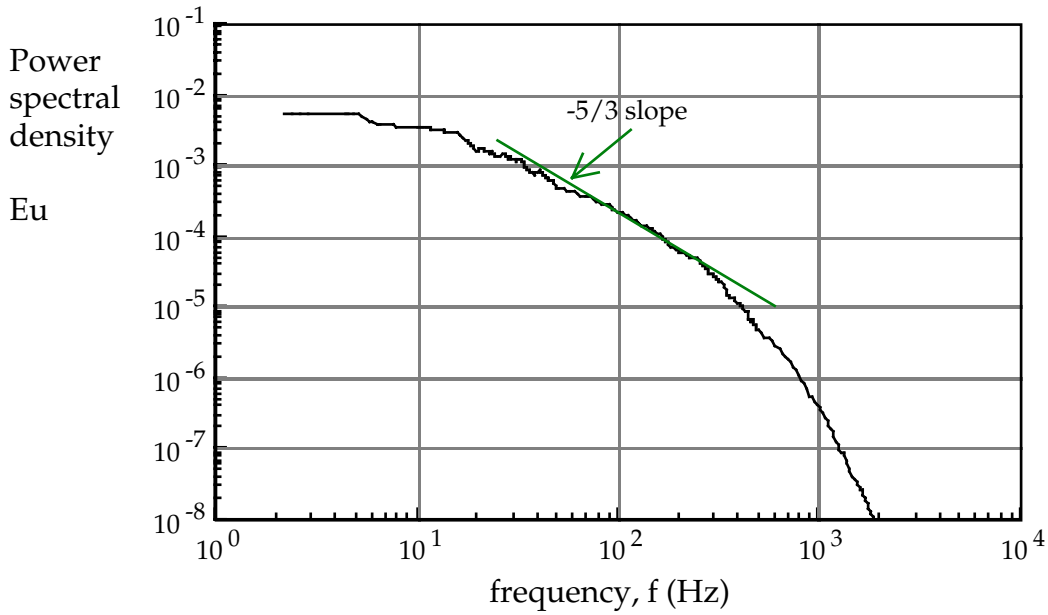

Fig. 3.2 Power spectrum of u′, u_{in}=3.4 m/sec, FSTI=10%, single-wire measurement

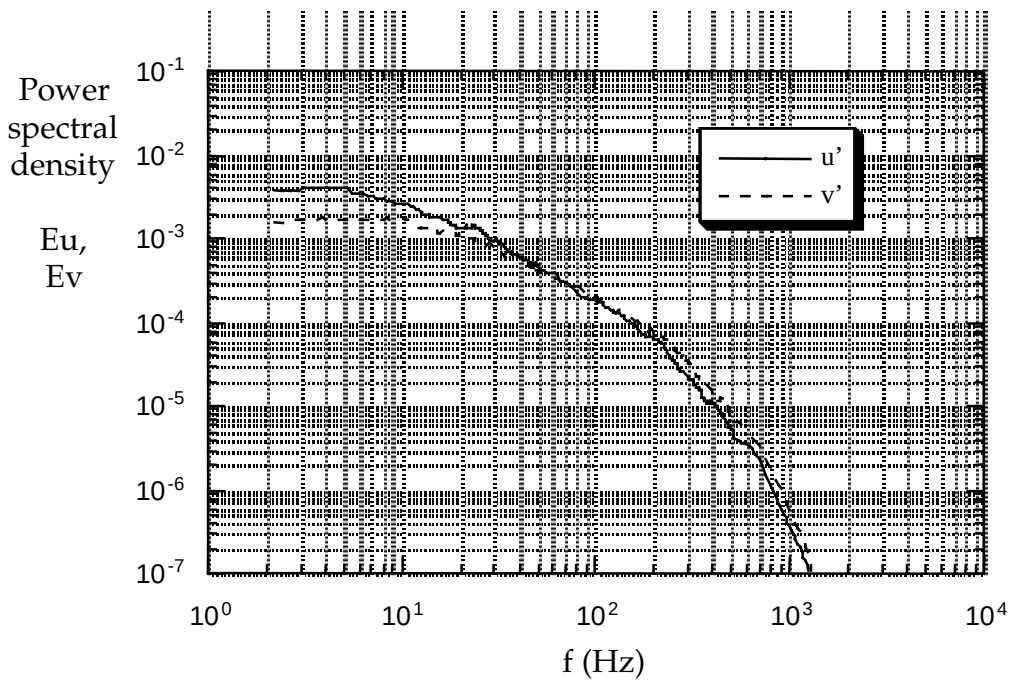

Fig. 3.3 Power spectra of u′ and v′, u_{in}=3.4 m/s TI=10%, Cross-wire measurement

INTEGRAL LENGTH SCALES

The integral length scales in the streamwise direction were computed using two different schemes. The first method is by using the auto-correlation of u′, v′ and w′ to compute the streamwise integral length scales, Λ_{ux}, Λ_{vx}, and Λ_{wx}. According to Hinze (1975), the equation that relates the integral length scale, Λ_{ux}, to the auto-correlation of u′, Q_u, is

$$\Lambda_{ux} = \frac{1}{u'^2_{rms}} \int_0^\infty Q_u(x)dx = \frac{\bar{u}}{u'^2_{rms}} \int_0^\infty Q_u(t)dt = \frac{\bar{u}}{u'^2_{rms}} \sum_{i=1}^{N} Q_{u,i} \,. \tag{3-25}$$

The auto-correlation of u′, Q_u, is computed from a data set of 4096 sampling points by the following equation

$$Q_{u,i} = \sum_{j=1}^{N-i} u_j u_{i+j} \Delta t \tag{3-26}$$

where Δt is the sampling interval, Δt=1/sampling frequency. A typical example of the auto-correlation of u′, the same data set of u′ as presented in Fig. 3.2, is shown in Fig. 3.4. Theoretically, the tail should decrease sharply to zero. Note in Fig. 3.4 a long wavy tail. This is due to a low-frequency unsteadiness which is typical of such flows. It represents large eddy scales and some tunnel unsteadiness. The range from t=0 to the first intersection with the $Q^2 = 0$ coordinate, $t = M\Delta t$, was used to calculate the integral length scale.

Combining equations (3-25) and (3-26) and considering that the auto-correlation is integrated from t=0 to first intersection, $t = M\Delta t$, results in a algebraic equation for the computation of Λ_{ux},

$$\Lambda_{ux} = \frac{\bar{u}\Delta t}{u'^2_{rms}} \sum_{i=1}^{M} \sum_{j=0}^{N-i} u_j u_{i+j} \tag{3-27}$$

Similarly, equations for Λ_{vx} and Λ_{wx} can be derived as

$$\Lambda_{vx} = \frac{\overline{v}\Delta t}{v'^2_{rms}} \sum_{i=1}^{M} \sum_{j=0}^{N-i} v_j v_{i+j} \tag{3-28}$$

$$\Lambda_{wx} = \frac{\overline{w}\Delta t}{w'^2_{rms}} \sum_{i=1}^{M} \sum_{j=0}^{N-i} w_j w_{i+j} \tag{3-29}$$

The integral length scales in the streamwise direction were also calculated by the second method, extrapolating PSD functions to zero frequency and applying the following formulas presented in Hinze (1975):

$$\Lambda_{ux} = \frac{\overline{u}E_u(f=0)}{4u'^2_{rms}} \tag{3-30}$$

$$\Lambda_{vx} = \frac{\overline{u}E_v(f=0)}{4v'^2_{rms}} \tag{3-31}$$

$$\Lambda_{wx} = \frac{\overline{u}E_w(f=0)}{4w'^2_{rms}} \tag{3-32}$$

where Eu(f=0), Ev(f=0), and Ew(f=0) are the values of PSD's at zero frequency. The integral length scale of u′ in the streamwise direction computed from the power spectrum shown in Fig. 3.2 is Λ_{ux}=3.57. The length scale estimated from the auto-correlation of u′ in Fig. 3.4 is Λ_{ux}=3.5, which is consistent with power spectrum calculation. The uncertainty in Λ_{ux} was 7%; 10% in Λ_{vx} and Λ_{wx}.

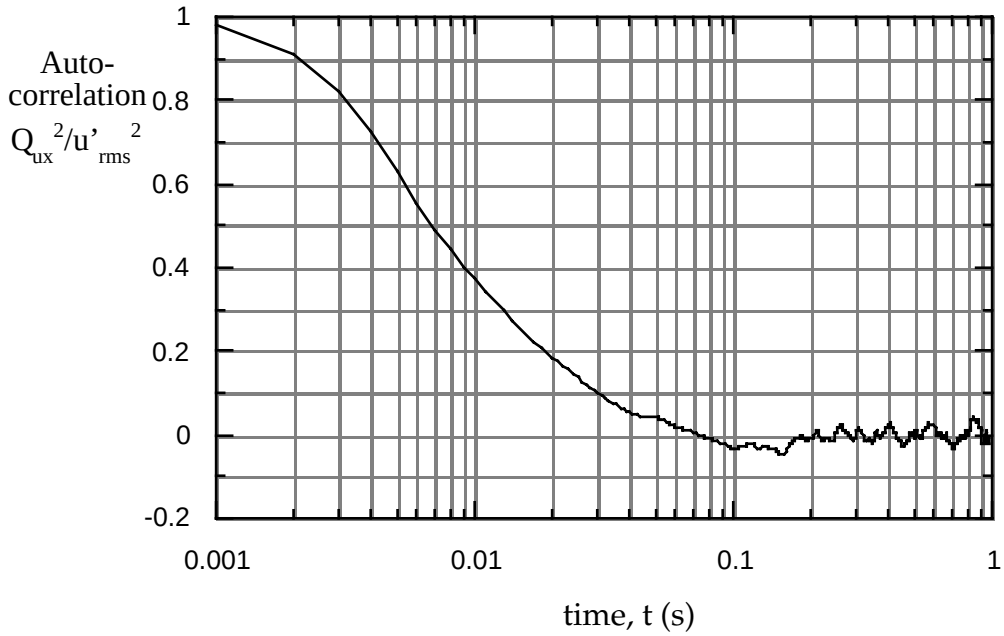

Fig. 3.4 Auto-correlation of u', u_{in}=3.4 m/sec, TI=10%

ENERGY SCALES AND TURBULENCE DISSIPATION

In the present study, energy scales were computed from the power spectra. As noted on Fig. 3.2, there is a -5/3 slope region, or inertial subrange of the spectrum (Hinze, 1975). The turbulence dissipation, ε, was evaluated by fitting the -5/3 slope line through the power spectrum in the inertial subrange region using the following Kolmogoroff spectrum law (Hinze 1975),

$$E_u(f) = 0.6545\pi^{-2/3}\varepsilon^{2/3}U_\infty^{2/3}(2f)^{-5/3} \tag{3-33}$$

The energy scale, Lu, and the Taylor microscale, λ, were calculated from the turbulence dissipation with the formula presented in Ames (1994):

$$Lu = 1.5 \, | u'_{rms} |^3 / \varepsilon \tag{3-34}$$

$$\lambda = (15 \nu u'^2_{rms} / \varepsilon)^{1/2} \tag{3-35}$$

The above equations show a clear relationship of power spectra with energy scale, Lu, and Taylor microscale, λ.

MEASUREMENTS

From run to run, slight variations in flow velocity for nominally the same case were recorded. This resulted in slight shifts in recorded velocities and chord Reynolds numbers from the nominal values but the non-dimensional quantities were normalized with the proper values and should not reflect these changes.

In the boundary layer flow study, the measurements would not be started without at least a half hour blower warm-up time.

Static pressure distributions on the suction surface were measured with pressure taps in the surface and a diaphragm-type pressure transducer. On the suction surface, there are thirteen pressure taps located according to Table 3.1.

The near-wall velocities were measured on the mid-plane of the test section, where the open slit on the concave wall allowed the insertion of a hot-wire probe into the flow. Though the test section was designed to facilitate velocity measurement at any streamwise position on the suction surface, focus was on the 13 stations of Table 3.1 At each measurement station, the wall position was first located and the probe was carefully brought to the wall. Usually, velocity profiles were acquired with 90 to 106 y-positions.

In the flow visualization study, contact paper, with adhesive backing and pre-marked ink dots on the front surface, was taped to the suction surface before

the test. After turning the experimental facility on and allowing flow to reach steady state, the solvent was sprayed to the substrate. Ink in solution then moved in the shear stress direction and, thus, left streak lines, indicating the shear stress direction.

TABLE 3.1. Pressure tap locations on the suction surface

Tap #	x	x/L_x	l	l/L	s	s/L_{ss}
	(cm)	(%)	(cm)	(%)	(cm)	(%)
p1	0.00	0.00	0.00	0.00	0.00	0.00
p2	0.41	3.98	0.07	0.65	0.69	4.49
p3	2.17	21.11	1.08	9.48	2.72	17.78
p4	3.89	37.78	2.48	21.71	4.42	28.97
p5	4.80	46.67	3.36	29.39	5.34	34.96
p6	5.66	55.06	4.28	37.45	6.25	40.92
p7	6.43	62.47	5.18	45.29	7.17	46.96
p8	7.09	68.89	6.04	52.82	8.08	52.89
p9	7.67	74.57	6.88	60.23	9.00	58.95
p10	8.41	81.73	8.05	70.40	10.37	67.93
p11	8.84	85.93	8.78	76.80	11.28	73.84
p12	9.37	91.11	9.73	85.09	12.54	82.14
p13	10.01	97.28	10.87	95.06	14.14	92.61

In the table, x=axial distance from the blade leading edge, l=distance along the true chord, s=distance along the suction surface, L_x=axial chord length, L=true chord length, L_{ss}=suction surface length (see Fig. 3.5).

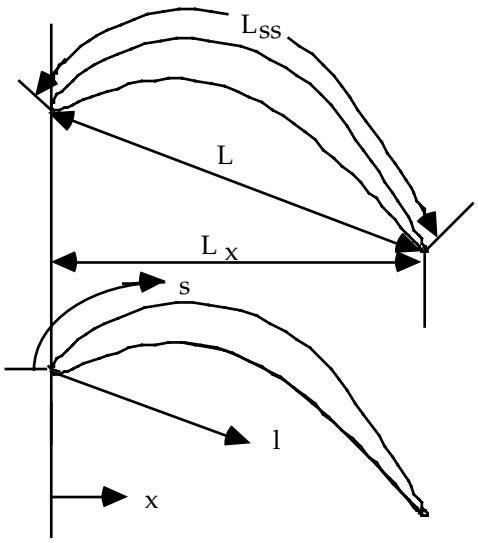

Fig. 3.5 Blades, with axial distance, x, chord distance, l, chord length, L, axial chord length, L_X, suction surface distance, s, and suction surface length, L_{SS}.

CHAPTER FOUR
RESULTS

4.1 INLET CONDITIONS

The test facility was designed to simulate the flow through a low-pressure turbine. Various turbulence generation schemes were employed for a wide range of free stream turbulence levels, as occur in a gas turbine. Three different turbulence levels were chosen to match the work done in industry, such as the GE low pressure turbine test (Halstead et al. 1995c), and to meet the requests of researchers engaged in modeling. Bar grids are commonly used for low and moderate turbulence generation while the jet grid is one of the few options for high turbulence generation. The jet grid can produce up to 50% turbulence intensity but the free stream uniformity is usually poor at these high levels. With some adjustments, uniform inlet flow turbulence was achieved for 10% FSTI. Detailed measurements of approach flow turbulence and boundary layer development were made for eleven cases. These cases are described in terms of four Reynolds number values; Re=50,000, 100,000, 200,000, and 300,000 and three levels of free stream turbulence intensity, 0.5%, 2.5% , and 10%. These Reynolds numbers are based upon the exit velocity and the suction surface length. The exit velocity is computed from the measured approach flow velocity and the channel geometry. The 0.5% FSTI case provides the base case, the 2.5% FSTI case is representative of low-pressure turbine approach flow conditions between wakes from the immediate upstream airfoil row and the 10% FSTI case is perhaps representative of the approach flow within the wakes from the upstream

airfoils. The 10% FSTI level is particularly relevant if the upstream airfoils have large regions of separated flow. Table 4.1 lists all the cases investigated.

TABLE 4.1. Cases investigated for inlet flow conditions

	Re=50,000	Re=100,000	Re=200,000	Re=300,000
FSTI=0.5%	X	X	X	X
FSTI=2.5%	X	X	X	X
FSTI=10%	X	X	X	

INLET VELOCITY AND TURBULENCE

The free stream uniformity was verified by the measurements of inlet velocity and rms velocity fluctuations about 10.15 cm (89% chord length) upstream of the concave wall leading edge. Figures 4.1 and 4.2 show the cross-stream inlet velocity and rms velocity fluctuation distributions for FSTI=0.5% and Re=50,000 and 300,000 at the mid-span (z=0). The inlet velocity is very uniform and symmetric, as expected. The average velocity variation in the cross-stream direction is less than 0.5%. For the moderate turbulence case of FSTI=2.5%, the velocity and turbulence distributions at various Reynolds numbers (Re=50,000, 100,000, 200,000, and 300,000) are depicted in Figs. 4.3 and 4.4. In Fig. 4.4, all three components of velocity fluctuations, u'_{rms}, v'_{rms} and w'_{rms}, are displayed. The average velocity variation is less than 1% in the core region. Turbulence levels are quite uniform along the cross-span. The average variations of rms velocity fluctuations are generally less than 1%. For the high turbulence case (FSTI=10%), cross stream velocity distributions are pictured in Fig. 4.5, where the average variations are 3 to 4%. Velocity fluctuations along the

cross-stream direction are plotted in Fig. 4.6. The average variations of fluctuations are about 4 to 5%. In the 0.5% and 2.5% FSTI cases, channel boundary layer turbulence is shown on both sides of the core region. Most of the boundary layer flow is withdrawn through the bleed slots and does not enter the test passage. Of the 11.4 cm width of the tunnel, the center 9.1 cm represents flow which enters the test region (essentially the region plotted).

For the 10% FSTI and Re=50,000 case, cross-span profiles were taken with a single hot-wire at several spanwise positions. This low-velocity, high-turbulence case was found to be the toughest one for achieving uniformity, so more attention was given to it. Figure 4.7 shows cross-stream velocity profiles at z=0, -3.4, -5.4, and -17.4 cm. The average variation is about 4% in the core region, while the average variation of rms velocity fluctuations, Fig. 4.8, u'_{rms}, is about 6% of the mean value.

The free stream turbulence and its decay were documented by measuring rms velocity fluctuations at several axial positions. These are presented in Tables 4.2 and 4.3 The -x in the tables is the upstream distance measured from the blade leading edge.

TABLE 4.2. Rms velocity fluctuations at free stream turbulence level of 2.5%

	Re=50,000			Re=100,000			Re=200,000		
-x (cm)	18.3	12.2	5.8	18.3	11.4	5.6	18.3	9.6	5.6
U_8 (m/s)	3.02	3.04	3.03	6.13	6.17	6.17	12.36	12.56	12.51
u_{rms} (m/s)	0.078	0.077	0.076	0.157	0.150	0.15	0.31	0.30	0.30
v_{rms} (m/s)	0.067	0.065	0.062	0.141	0.139	0.13	0.28	0.27	0.26
w_{rms} (m/s)	0.066	0.064	0.062	0.150	0.138	0.14	0.31	0.31	0.29

TABLE 4.3. Rms velocity fluctuations at high free stream turbulence level, 10%

	Re=50,000			Re=100,000			Re=200,000		
-x (cm)	14.7	9.9	6.1	14.7	9.7	5.6	14.7	9.6	5.6
U_8 (m/s)	3.18	3.19	3.19	6.12	6.21	6.22	12.10	12.18	12.18
u_{rms} (m/s)	0.32	0.29	0.29	0.62	0.57	0.55	1.21	1.12	1.06
v_{rms} (m/s)	0.29	0.26	0.25	0.57	0.52	0.49	1.04	0.96	0.89
w_{rms} (m/s)	0.32	0.28	0.28	0.61	0.55	0.53	1.17	1.11	1.03

ONE-DIMENSIONAL POWER SPECTRA

One-dimensional power spectra of u′, v′, and w′ were measured with the triple-wire probe described in Chapter Two. Power spectra measurements were performed at two axial positions, 129% and 49% of the true chord length (14.7 cm and 5.6 cm) upstream of the blade leading edge (concave wall). Only the power spectra at the most upstream location (14.7 cm upstream of the blade leading edge) are presented.

Figure 4.9 shows one-dimensional power spectra of u′, v′ and w′ for the Re=50,000, FSTI=2.5% case. In Fig. 4.9a the same power spectral density functions are multiplied by the frequency and plotted versus the frequency. In the energy coordinates of Fig. 4.9a, the area under the curve in any frequency band is proportional to the energy in that frequency band. At low frequencies, PSD of u′ is much different from PSD of v′ and w′, so are integral length scales. This is expected for such turbulence generation grids. The power spectra of all three components are close to one another at high frequencies, indicating nearly isotropic turbulence in those scales. The energy of u′ is distributed from a low frequency of 5 Hz to a high frequency of 200 Hz with a peak at around 50 Hz.

The energies of v′ and w′ are concentrated in the high frequencies with a peak around 70 Hz. Figures 4.10, 4.10a, 4.11, 4.11a, 4.12 and 4.12a show the power spectra of u′, v′ and w′ in both coordinates for the cases of Re=100,000, 200,000, and 300,000 with 2.5% FSTI. The energy of all three components elevates and the peak of the energy shifts to higher frequencies with the increase of Reynolds number. Also, with increases in Reynolds number, the range of peak frequencies shortens.

For the cases of 10% FSTI, power spectra are plotted in Figs. 4.13 and 4.13a for the Re=50,000 case, 4.14 and 4.14a for the Re=100,000 case, and 4.15 and 4.15a for the case of Re=200,000. As in the 2.5% FSTI cases, PSD's of u′, v′, and w′ are close to one another. Therefore, the turbulence is more nearly isotropic. The energy distributions of all three components are similar except that the u′ high-energy frequency band is wider. The peaks of the energy shift from 20-30 Hz for the Re=50,000 case to around 70 Hz at Re=100,000. At Re=200,000, the peaks of the energy are shifted to around 100-110 Hz. The energy increases with free stream velocity (or Reynolds number). The energy for the 10% FSTI case (Figs. 4.9a, 4.10a, and 4.11a) is higher than that in the 2.5% FSTI case with the same Reynolds number (Figs. 4.13a, 4.14a, and 4.15a).

ENERGY AND INTEGRAL LENGTH SCALES

The integral length scales in the streamwise, Λ_u, normal, Λ_v, and vertical, Λ_w, directions taken 129% chord length (14.7 cm) upstream of the blade leading edge are in Tables 4.4 and 4.5. The integral length scales of Λ_{ux}, Λ_{vx}, and Λ_{wx} were calculated from the auto-correlation of u′, v′ and w′, respectively. The

computed energy scales, L_u, along with turbulence dissipation, ε, and Taylor microscales, λ, are presented in the same tables. The dissipation rate, ε, was computed from the -5/3 slope region (inertial subregion) on the power spectrum of u' using equation (3-33), as discussed in Chapter Three. The energy scale, Lu, was computed with equation (3-34) and the Taylor microscale, λ, was computed with equation (3–35), which are also discussed in Chapter Three.

TABLE 4.4. Integral length scales, energy scales, turbulence dissipation, and Taylor microscales for 2.5 % free stream turbulence cases

	Re=50,000	Re=100,000	Re=200,000	Re=300,000
Λ_{ux} (cm)	4.27	4.85	4.97	5.98
Λ_{vx} (cm)	1.03	1.75	3.19	4.64
Λ_{wx} (cm)	1.03	1.74	3.11	4.44
L_u (cm)	1.37	1.27	1.20	1.14
ε (m^2/sec^3)	0.05	0.40	2.29	12.84
λ (mm)	5.19	3.74	3.12	1.98

TABLE 4.5 Integral length scales, energy scales, turbulence dissipation, and Taylor microscales for 10% free stream turbulence cases

	Re=50,000	Re=100,000	Re=200,000
Λ_{ux} (cm)	2.82	4.2	5.18
Λ_{vx} (cm)	1.37	2.02	3.44
Λ_{wx} (cm)	1.52	1.95	3.00
L_u (cm)	1.36	1.44	1.52
ε (m^2/sec^3)	2.77	18.85	136.49
λ (mm)	2.84	2.18	1.62

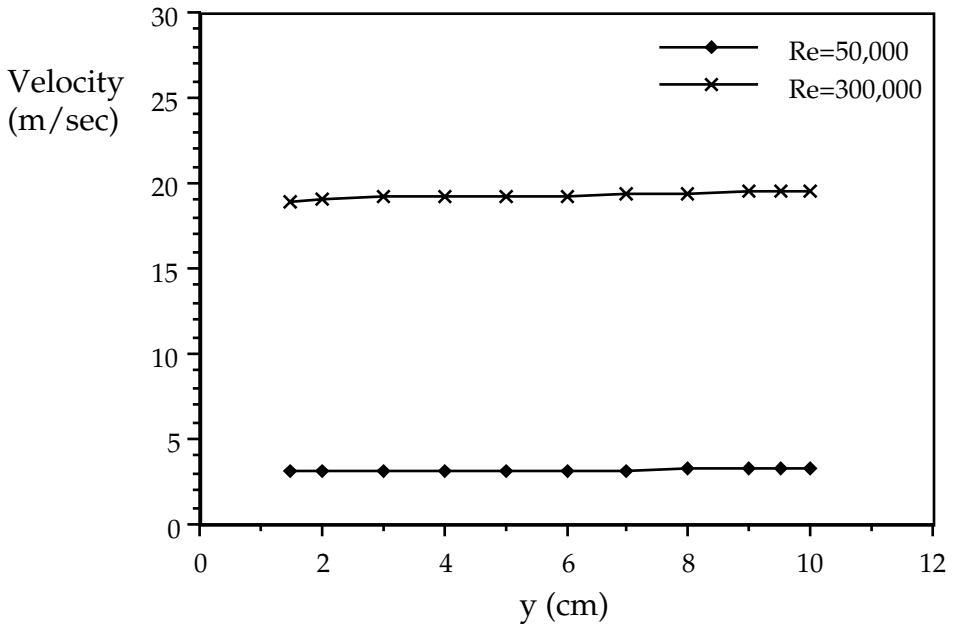

Fig. 4.1 Inlet velocity profiles at mid-span, z=0 cm, FSTI=0.5%

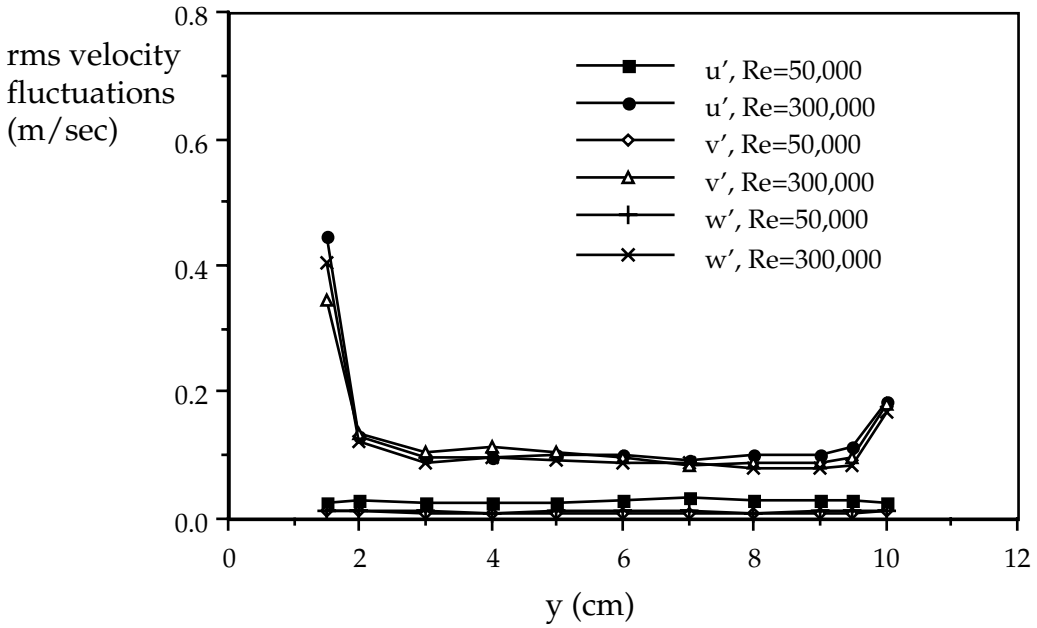

Fig. 4.2 Inlet velocity fluctuations at mid-span, z=0 cm, FSTI=0.5%

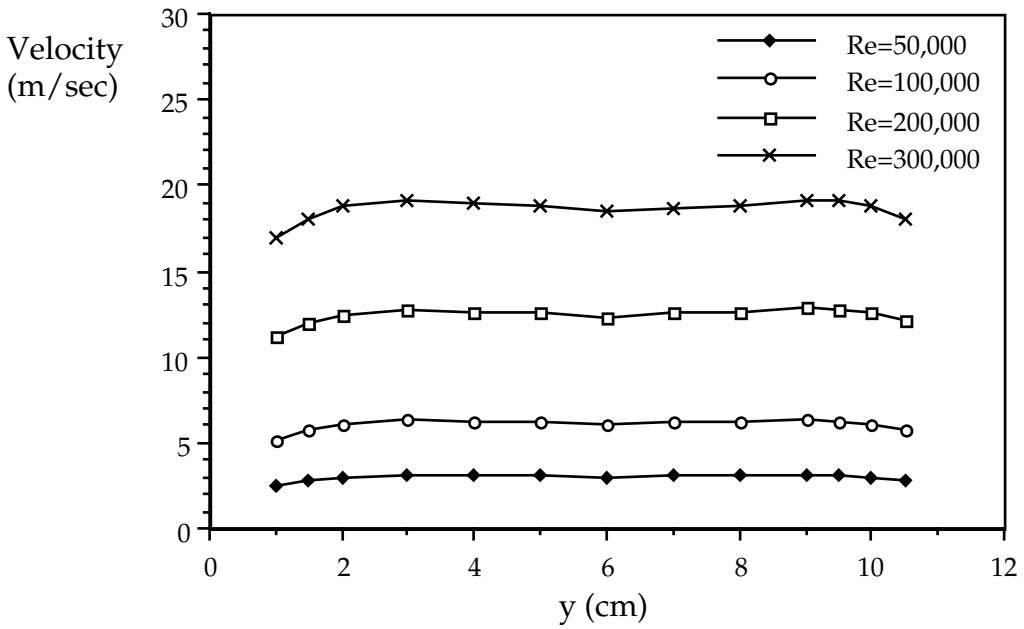

Fig. 4.3 Inlet velocity profiles at mid-span, z=0 cm, FSTI=2.5%

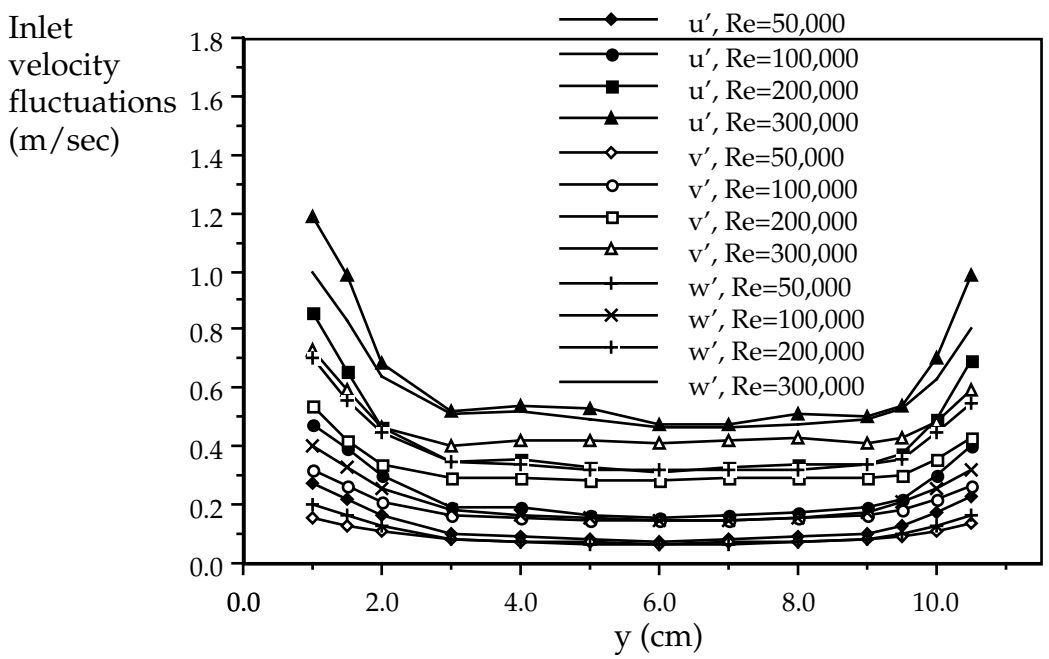

Fig. 4.4 Inlet velocity fluctuations at mid-span, z=0 cm, FSTI=2.5%

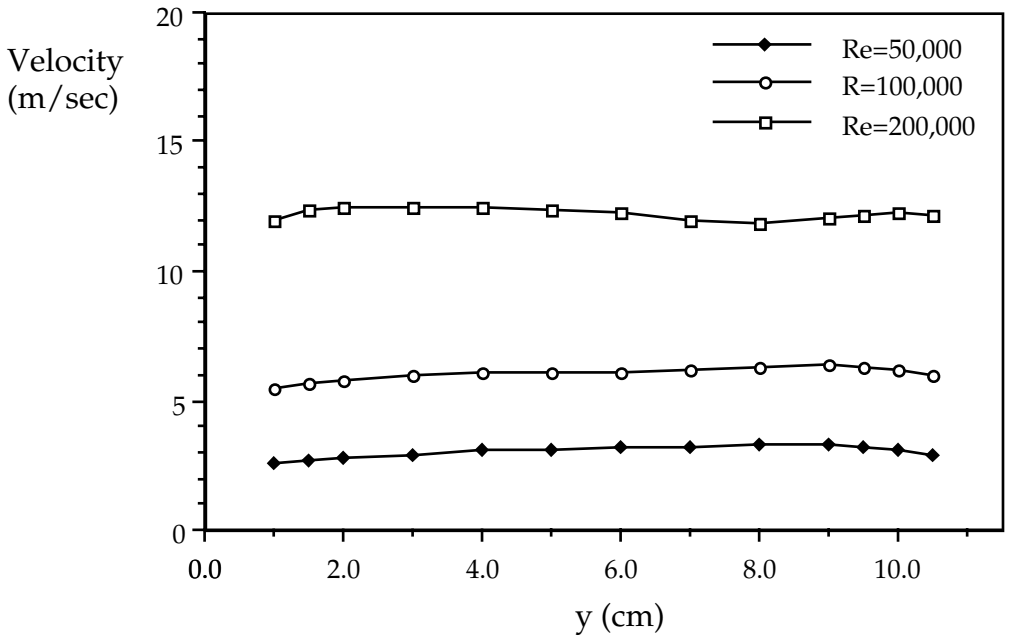

Fig. 4.5 Inlet velocity profiles at mid-span, z=0 cm, FSTI=10%

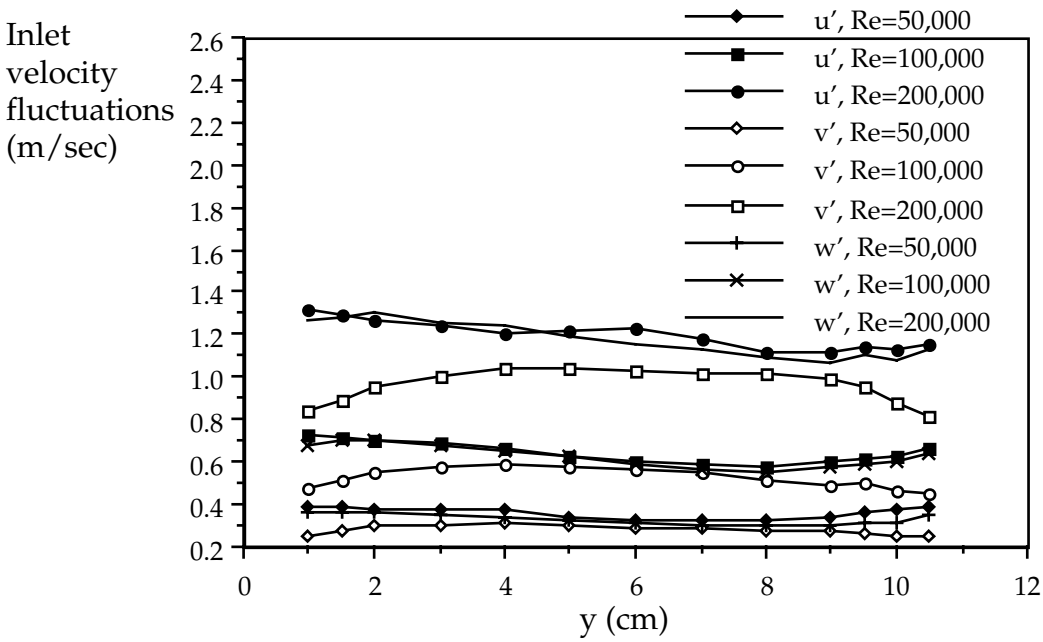

Fig. 4.6 Inlet velocity fluctuations at mid-span, z=0 cm, FSTI=10%

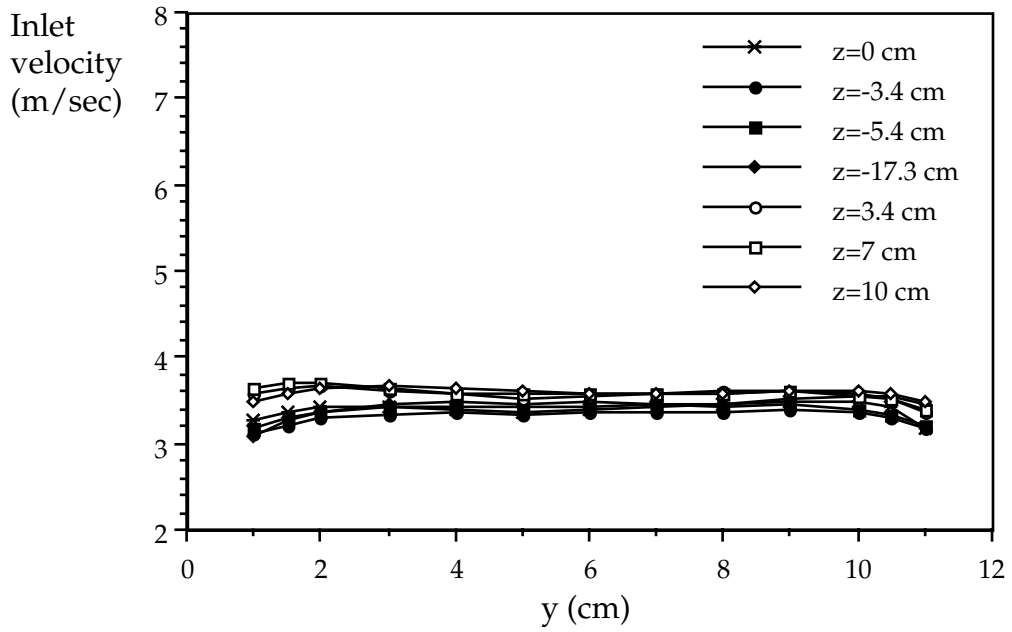

Fig. 4.7 Inlet velocity distributions at various spanwise position, Re=50,000, FSTI=10%

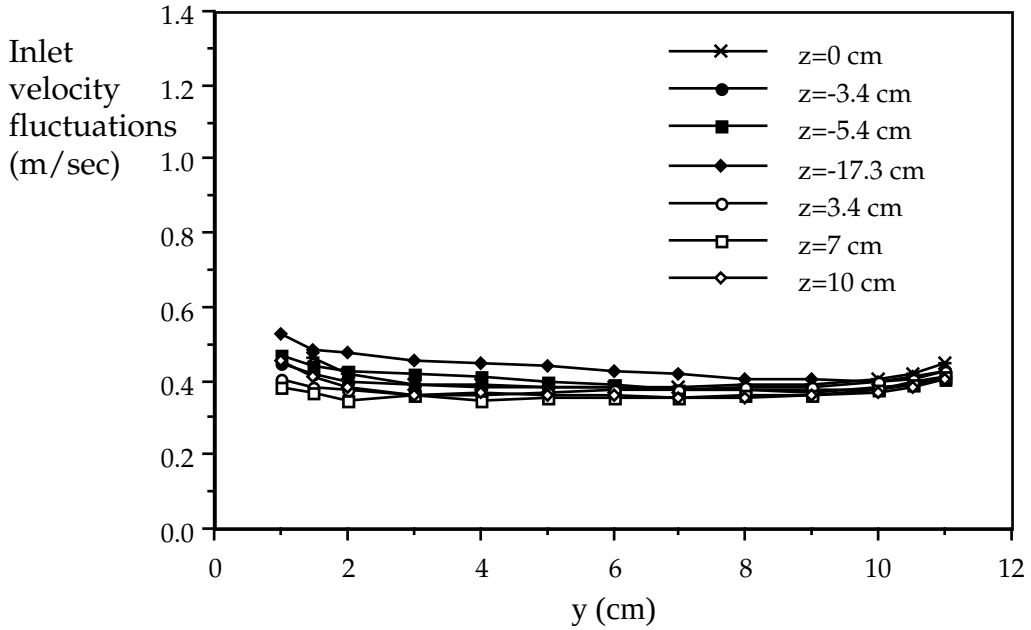

Fig. 4.8 Inlet velocity fluctuation distributions at various spanwise positions, Re=50,000, FSTI=10%

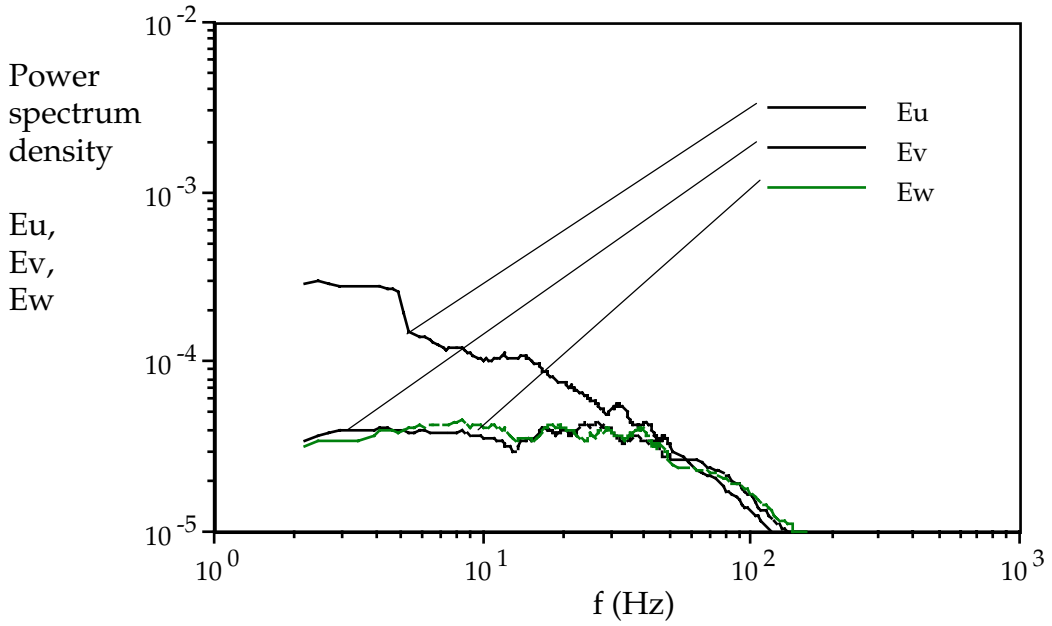

Fig. 4.9 Power spectra of u′, v′ and w′, FSTI=2.5%, Re=50,000
Measurement station is 14.7 cm upstream of the blade leading edge

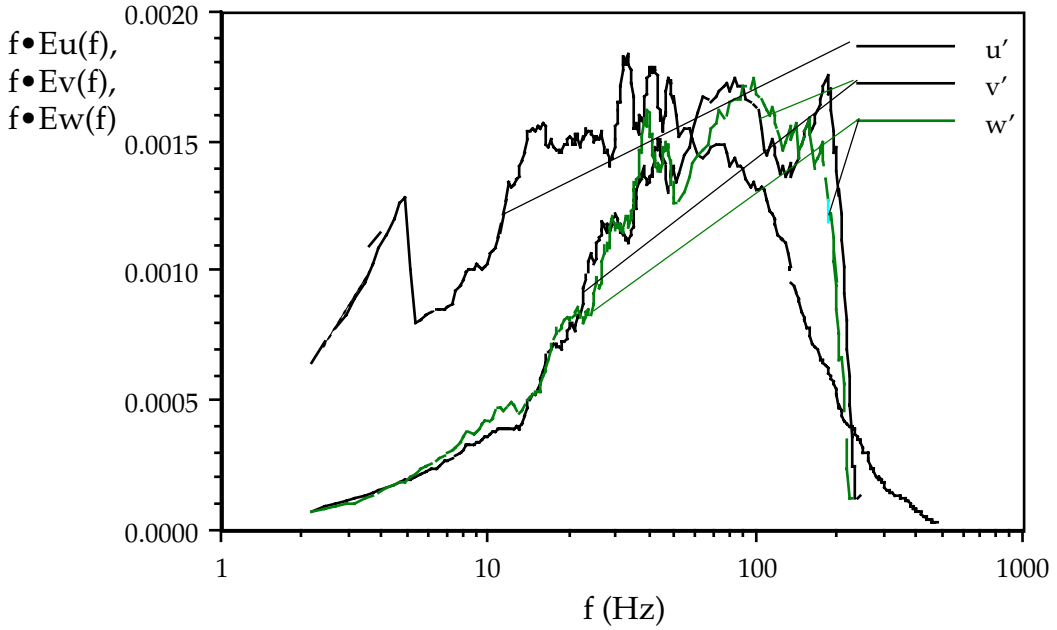

Fig. 4.9a Power spectra of u′, v′ and w′ in energy coordinates, FSTI=2.5%, Re=50,000

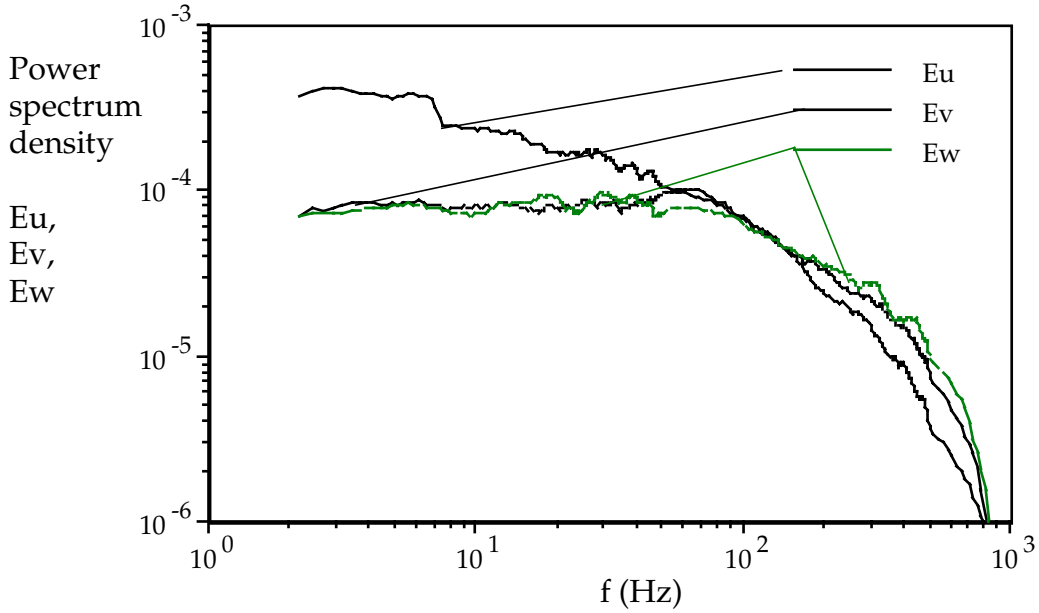

Fig. 4.10 Power spectra of u′, v′ and w′, FSTI=2.5%, Re=100,000

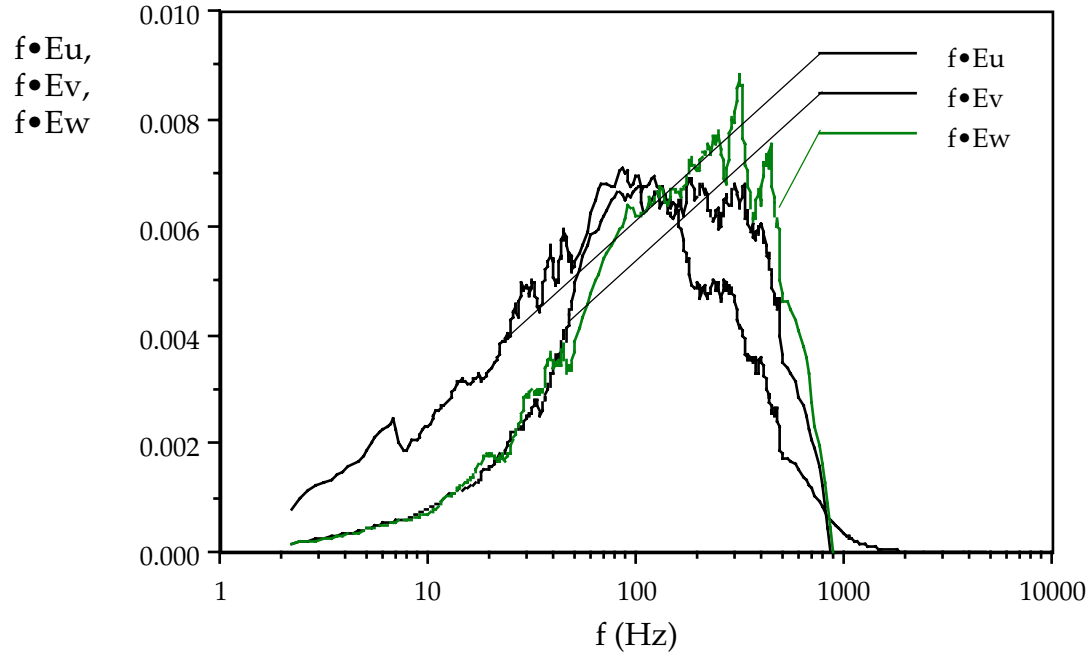

Fig. 4.10a Power spectra of u′, v′ and w′ in energy coordinates, FSTI=2.5%, Re=100,000

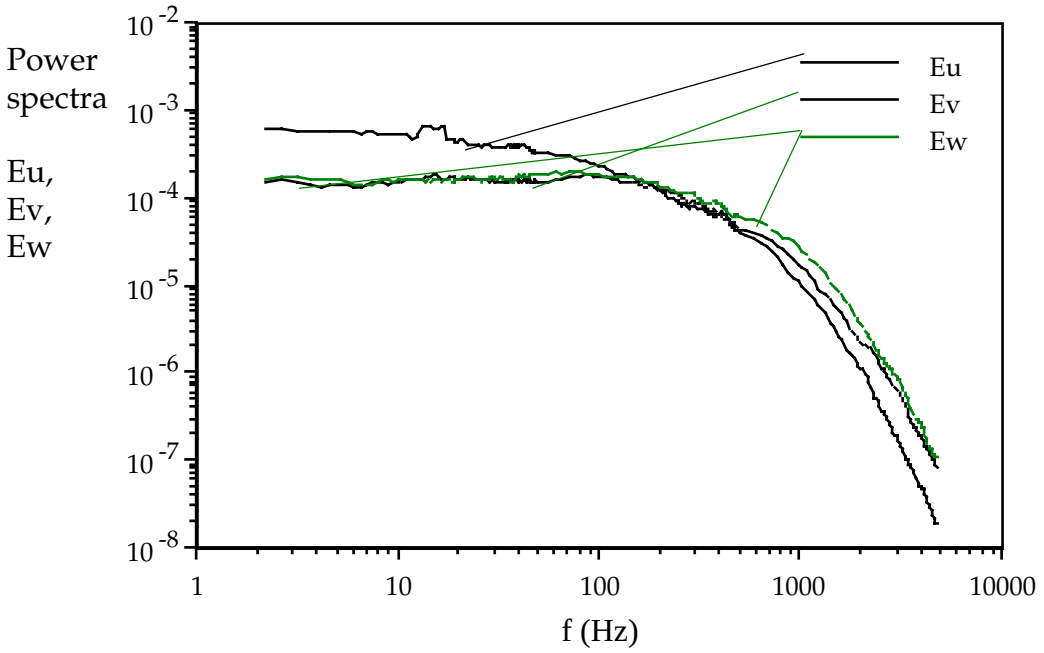

Fig. 4.11 Power spectra of u′, v′ and w′, FSTI=2.5%, Re=200,000

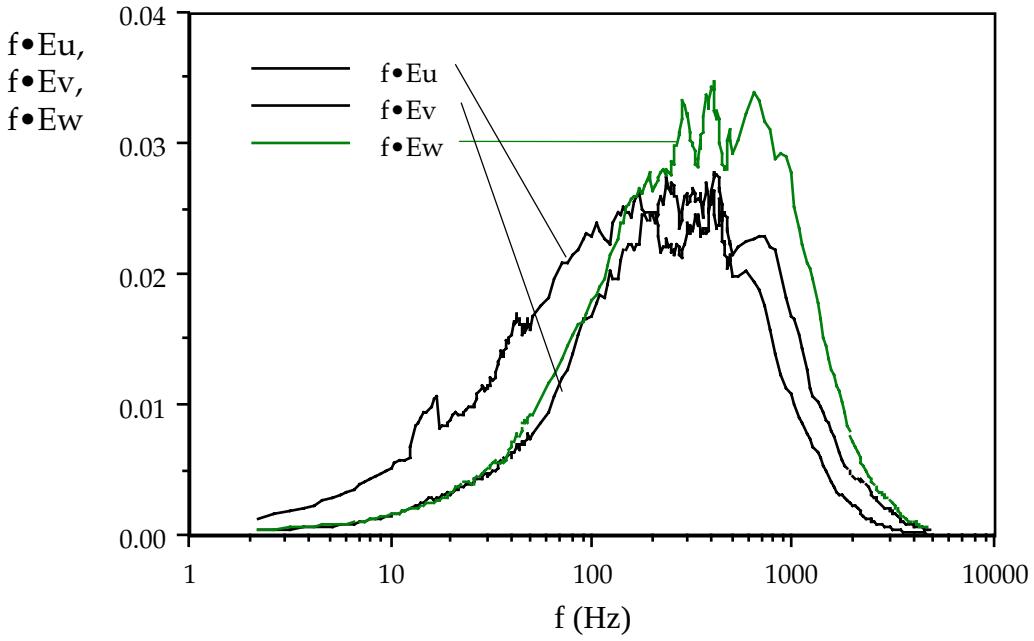

Fig. 4.11a Power spectra of u′, v′ and w′ in energy coordinates, FSTI=2.5%, Re=200,000

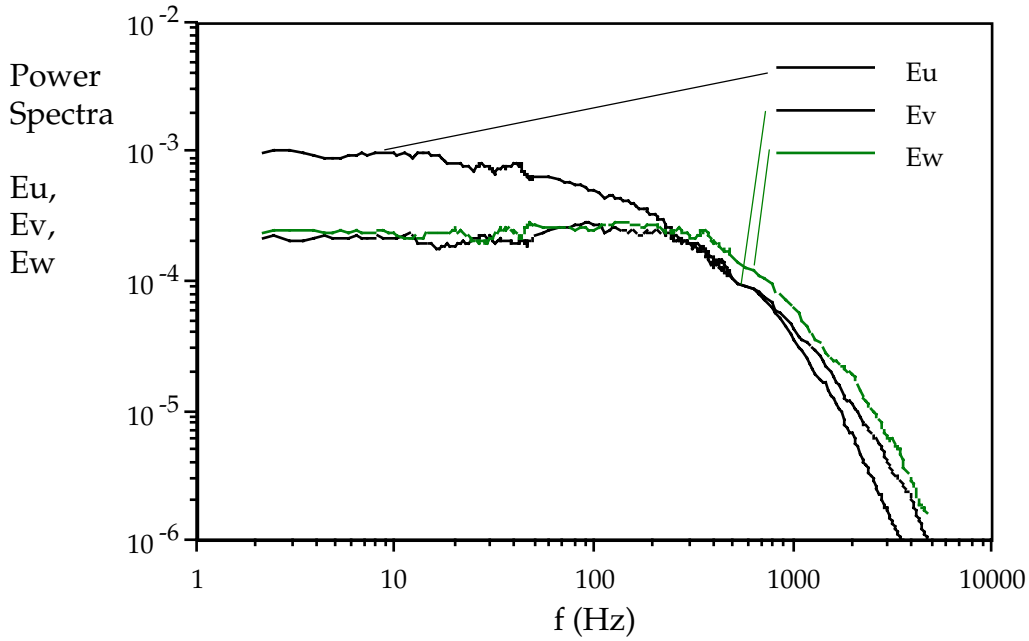

Fig. 4.12 Power spectra of u′, v′ and w′, FSTI=2.5%, Re=300,000

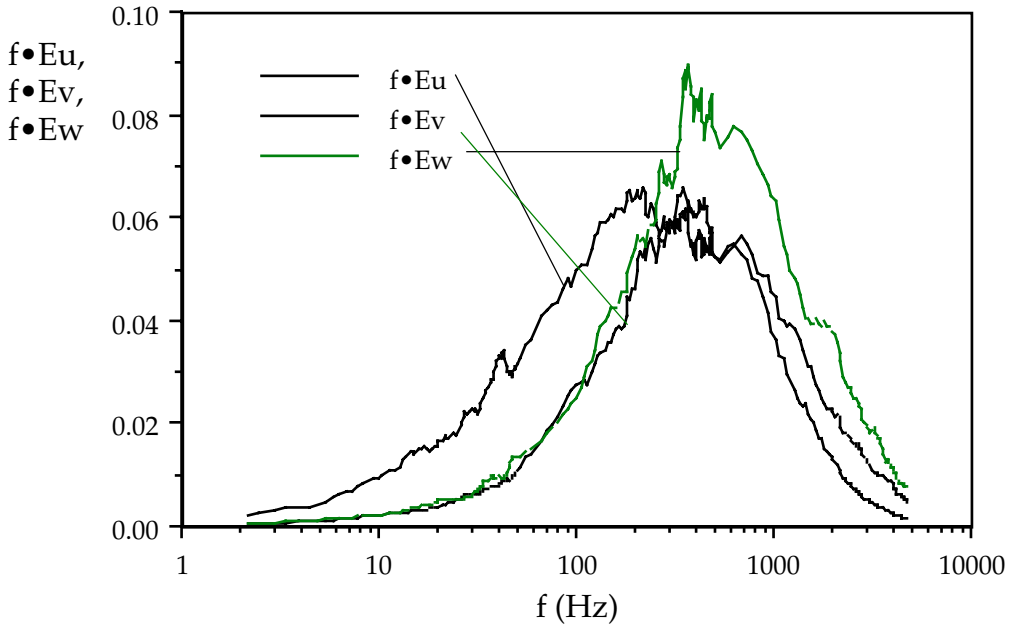

Fig. 4.12a Power spectra of u′, v′ and w′ in energy coordinates, FSTI=2.5%, Re=300,000

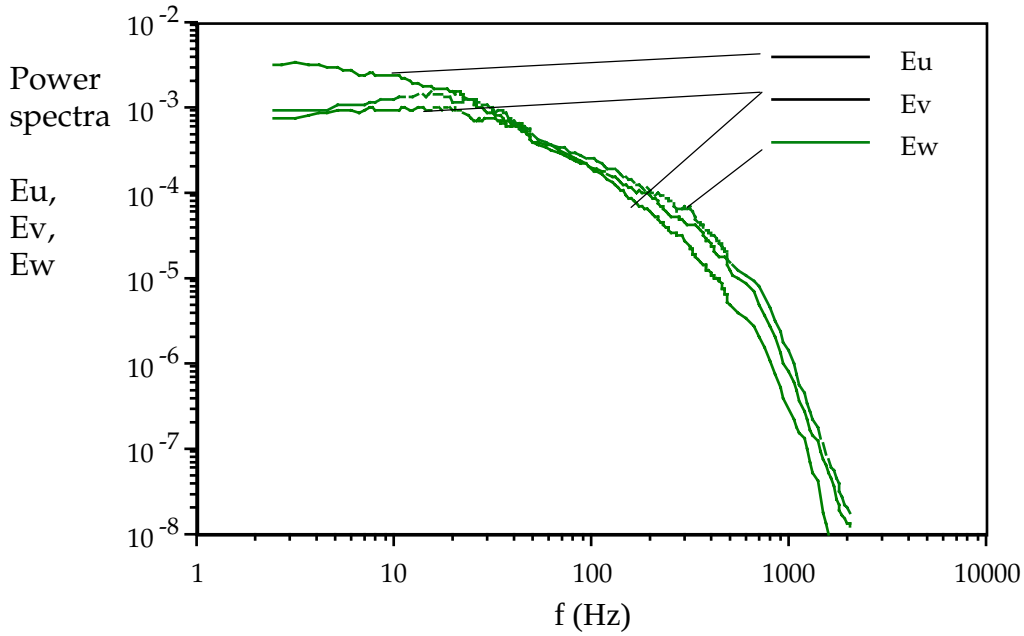

Fig. 4.13 Power spectra of u′, v′ and w′, FSTI=10%, Re=50,000

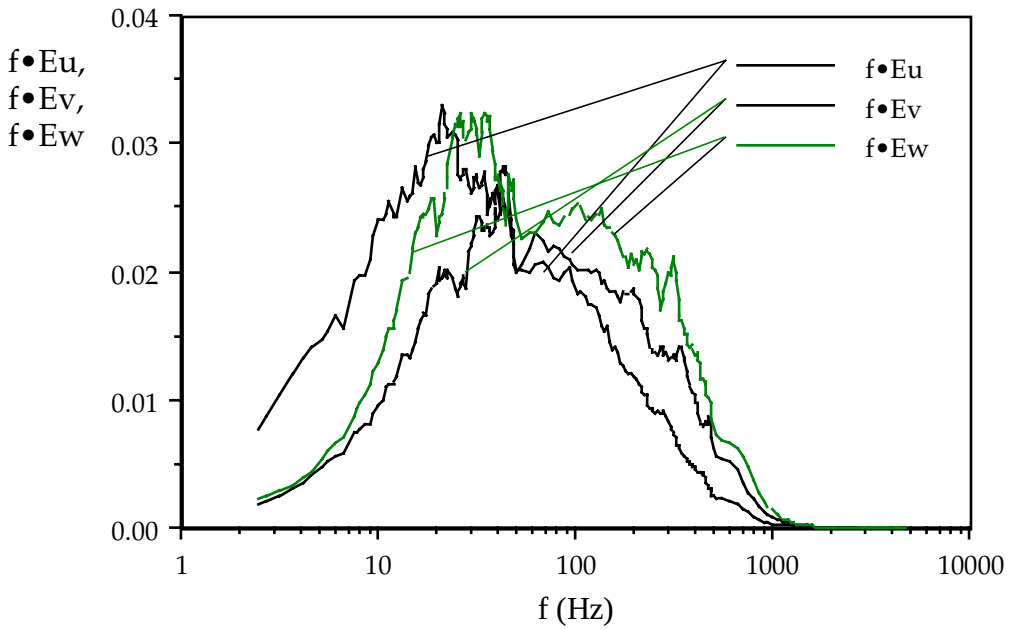

Fig. 4.13a Power spectra of u′, v′ and w′ in energy coordinates, FSTI=10%, Re=50,000

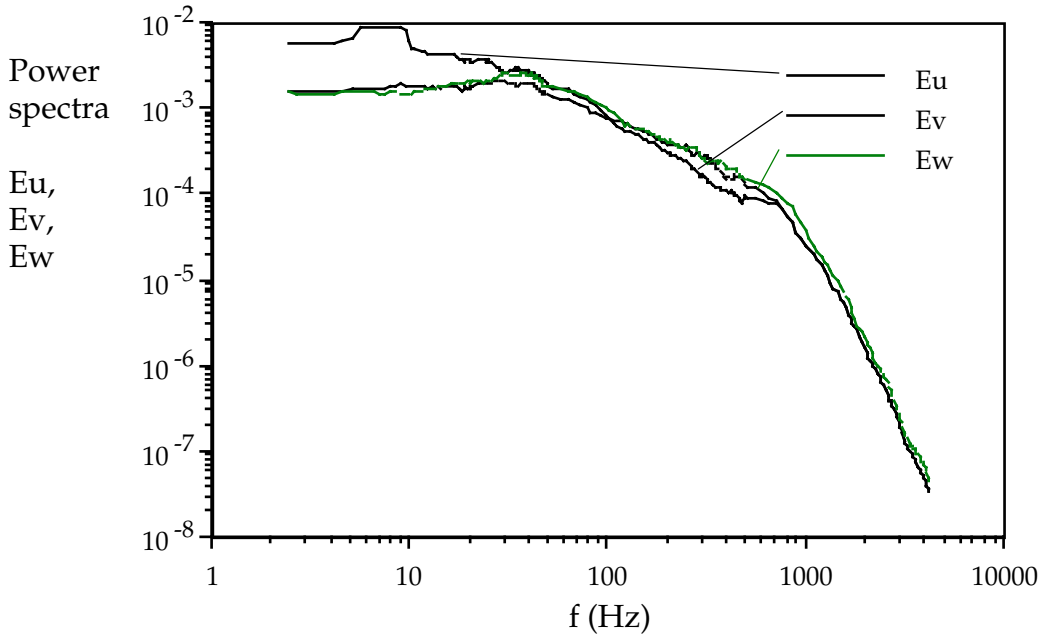

Fig. 4.14 Power spectra of u′, v′ and w′, FSTI=10%, Re=100,000

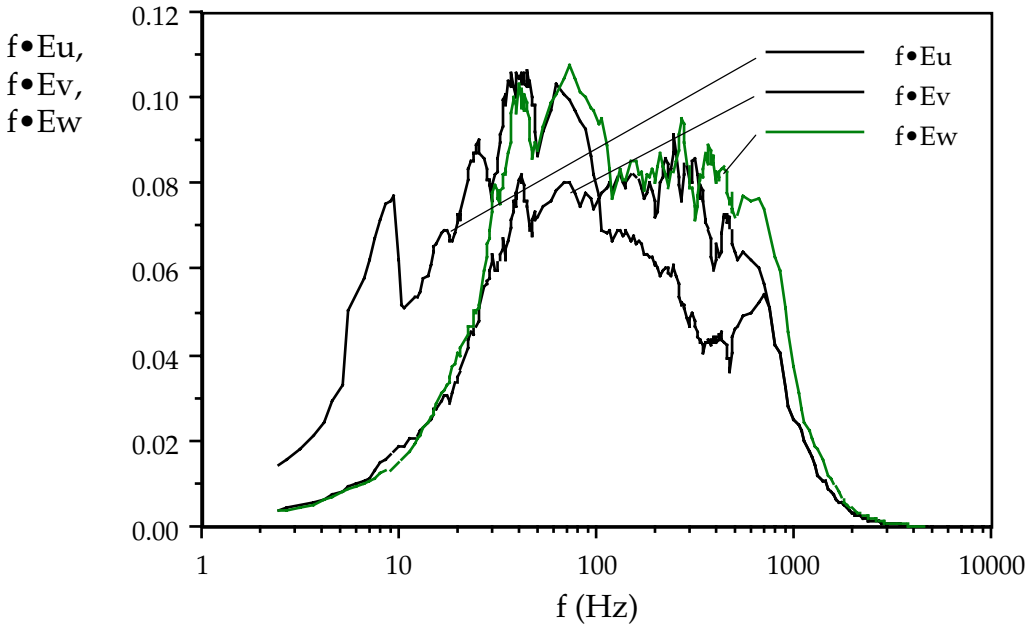

Fig. 4.14a Power spectra of u′, v′ and w′ in energy coordinates, FSTI=10%, Re=100,000

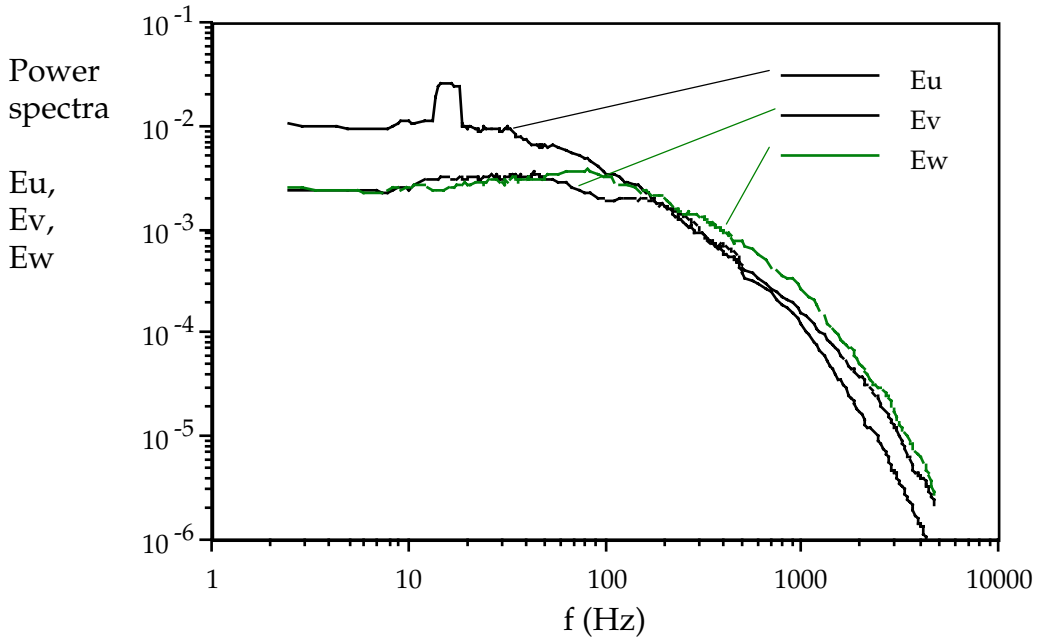

Fig. 4.15 Power spectra of u′, v′ and w′, FSTI=10%, Re=200,000

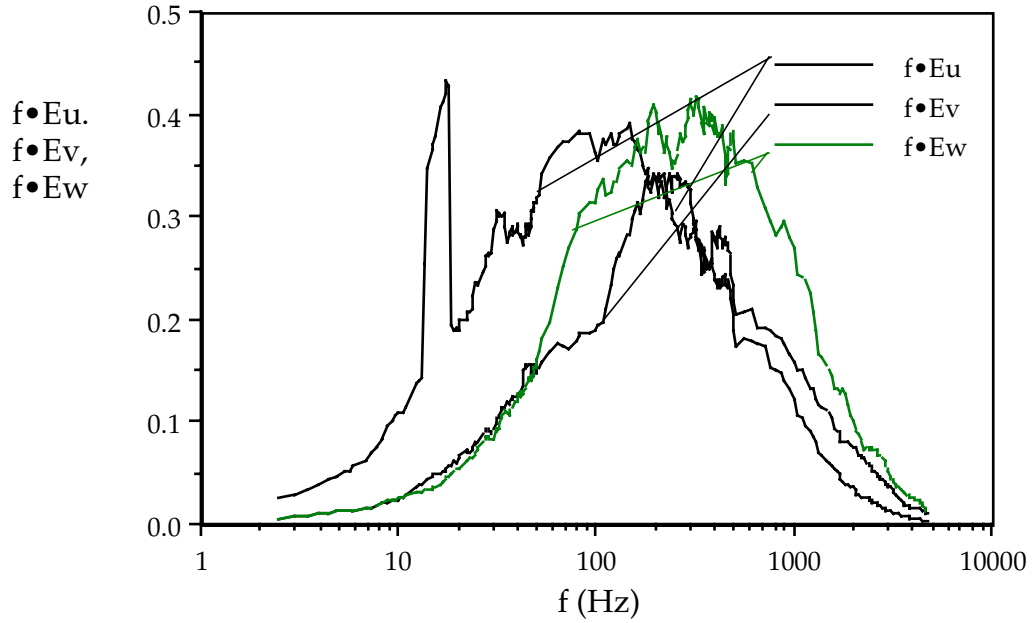

Fig. 4.15a Power spectra of u′, v′ and w′ in energy coordinates, FSTI=10%, Re=200,000

4.2 PRESSURE PROFILES

Static pressure distributions on the suction surface were measured with pressure taps in the surface and a diaphragm-type pressure transducer (see Chapter Two). On the suction surface, there are thirteen pressure taps located according to Table 3.1. The measured local static pressures were normalized to get pressure coefficients, $C_p=(P_t-P_s)/(P_t-P_{s,exit})$, and were compared to the fully-attached, high-Re distribution (shown with the solid line) in Figs. 4.16 to 4.18. Here, P_t is total pressure, P_s is local static pressure, and $P_{s,exit}$, is exit static pressure.

To know the details of the processes which create these variations in pressure distribution, profiles of mean velocity, turbulence intensity, and intermittency (the fraction of the time that the flow is turbulent) were measured. To locate exactly the flow separation and reattachment points, flow visualization of the suction surface flow was conducted with a wall shear stress measurement technique, which will be discussed in the flow visualization section. It was learned that for the low-FSTI cases, the boundary layers on the suction surface followed the same path: a) laminar boundary layer development, b) strong growth rate as a laminar boundary layer when the adverse pressure gradient section is nearly reached, c) laminar separation, d) transition of the shear layer over the separation zone, with turbulent flow observed only in the shear layer, e) turbulent flow throughout the shear layer and near-wall region, f) reattachment, and g) growth as an attached turbulent boundary layer. The speed with which it proceeded through these steps and the degree to which it completed these steps increased as Re increased. These cases are next discussed in more detail.

The stability of the boundary layer and whether the flow separates largely depend on the free stream turbulence level and the airfoil Reynolds number. At low turbulence levels (FSTI=0.5%, Fig. 4.16), two low-Reynolds-number flows (Re=50,000 and 100,000) seem to start separation between station p7 (x/L_x=62.47%) and p8 (x/L_x=68.89%). Separation was indicated as a perceptible drop in pressure coefficient below the "unseparated" values. Detailed profile data introduced in the next section and flow visualization results are used to verify that flow separation point is indeed between p7 and p8. The significant changes of Cp from p6 (x/L_x=55.06%) to p7 (x/L_x=62.47%) are due to a rapid growth of the unstable, laminar boundary layer flow, as will be demonstrated later with the velocity profile data. Two high-Reynolds-number flows (Re=200,000 and 300,000) do not separate until after p8 (x/L_x=68.89%). The two low-Reynolds-number flows remain separated for the remainder of the suction surface length, though. For the Re=100,000 case, the separation bubble begins to shrink and the flow seems to be near reattachment near the trailing edge of the blade. In the Re=50,000 flow, there is no sign of reattachment. At Re=300,000, the flow is reattached to the wall after p10, near station p11 (x/L_x=85.93%) while the Re=200,000 flow remains separated until near station p12 (x/L_x=91.11%). The mechanism for reattachment under such adverse pressure gradient conditions appears to be transition of the shear flow over the separation zone and the enhanced transport of the turbulent flow. This will be demonstrated with in-flow measurements in a later section. After transition, enhanced turbulent mixing of the streamwise momentum from the core region, free shear layer, and the outer boundary layer regions to the near-wall region, overcomes

the adverse pressure gradient effect and brings higher velocity fluid back to the wall. Again, in-flow measurements will show this.

At a free stream turbulence level of FSTI=2.5% (Fig. 4.17), the onset of rapid growth of the boundary layer starts later on the surface than it does for the 0.5% FSTI case, the separation bubbles are smaller and reattachment is earlier. This behavior is due to earlier flow transition, as induced by the higher free stream turbulence. For Re=50,000, the flow is reattached to the wall by station p13 (x/L_x=97.23%). The reattachment point for the flow of the Re=100,000 case is also moved upstream to around p12 (x/L_x=91.11%). For the highest-velocity case, Re=300,000, it is hard to tell from the pressure measurements whether the flow ever separates. Flow visualization will show that Re=300,000 does separate, though the separation region is very small.

Much smaller separation bubbles and much earlier reattachment were found in the flows with 10% turbulence intensity (Fig. 4.18). The reattachment points moved to 12.67 cm (x/Lx=91.60%), between p12 (x/L_x=91.11%) and p13 (x/L_x=97.28%), for the flow of Re=50,000 and to
11.47 cm (x/Lx=86.71%), between p11 (x/L_x=85.93%) and p12 (x/L_x=91.11%), for the Re=100,000 case.

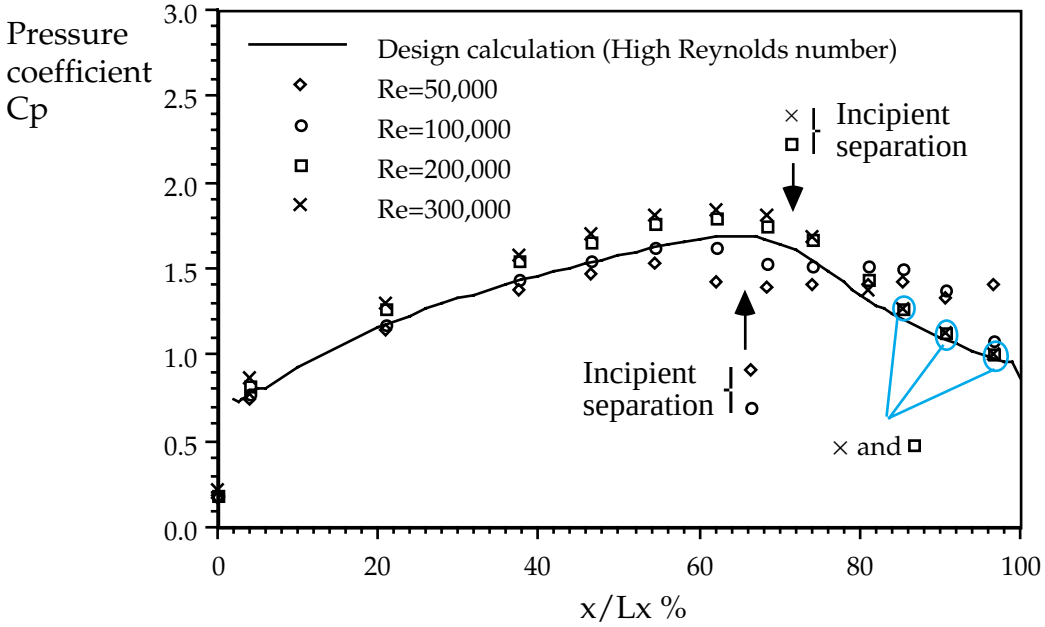

Fig. 4.16 Pressure coefficients on suction surface, FSTI=0.5%

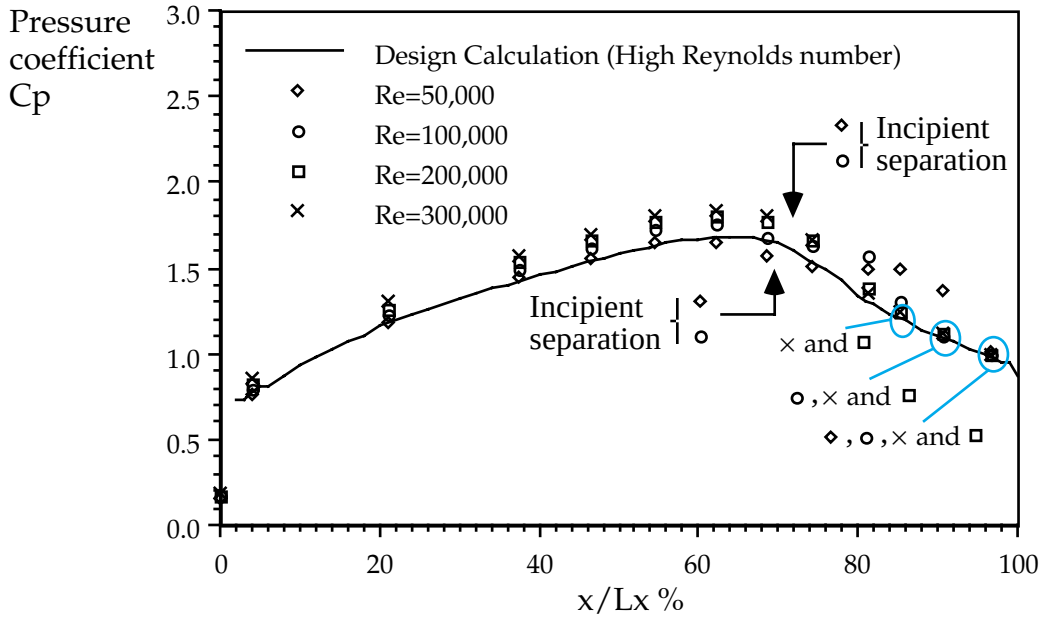

Fig. 4.17 Pressure coefficients on suction surface, FSTI=2.5%

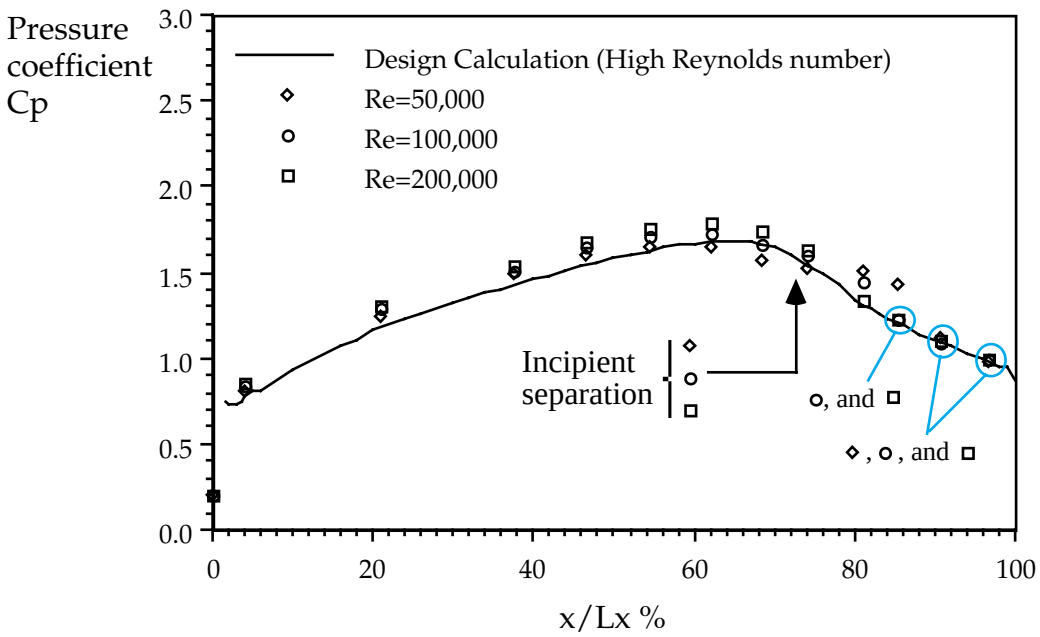

Fig. 4.18 Pressure coefficients on suction surface, FSTI=10%

4.3 FLOW VISUALIZATION

Accurately locating flow separation and reattachment points is important to modeling flow separation and the separation-to-transition length. Surface static pressure measurement is limited by the pressure tap locations on the suction surface. Velocity profile measurements with a hot-wire can be taken at any streamwise location with the present setup, but detailed measurements are time consuming. Generally, velocity measurements were conducted at the static surface pressure measurement stations, i.e., p2 to p13. In the next section, it will be seen that the measured velocity profiles and intermittency distributions provide insight into the flow phenomena of boundary layer development and

flow transition but they are not able to identify clearly the separation and reattachment locations, particularly in the thin separation zones of the high FSTI and high Re cases. Flow visualization with shear stress direction visualization described in Chapter Two was used for determining flow separation and reattachment.

All the cases of Table 4.1 were tested with the shear stress direction technique and the visualization photos are given in Appendix A. A sample visualization is shown in Fig. 4.19. Due to gravity, most of the ink streaks have a downward trend, especially in the near-zero-shear-stress regions. Nevertheless, the separation and reattachment points could be easily identified from the picture. Traces of the shear stress direction, such as shown in Fig.4.19a, were made from these results for better presentation. On all the processed visualization paper, certain measuring stations, such as p6, were located prior to removal from the test wall. The axial positions of separation and reattachment were determined by measuring the distances between labeled stations and the separation and reattachment lines. The following table summarizes these measurements.

TABLE 4.1 Flow separation and reattachment measurements

	FSTI=0.5%		FSTI=2.5%		FSTI=10%	
	S_s (cm)	S_r (cm)	S_s (cm)	S_r (cm)	S_s (cm)	S_r (cm)
Re=50,000	7.57	18.32 (1)	8.07	14.0	8.27	12.67
Re=100,000	7.77	15.72 (1)	8.10	12.14	8.37	11.47
Re=200,000	8.17	12.02	8.32	10.77	8.47	10.42
Re=300,000	8.27	10.97	8.32	10.27		

(1) If more than 15.27 cm, reattachment is on the downstream extension wall shown in Fig. 2.2

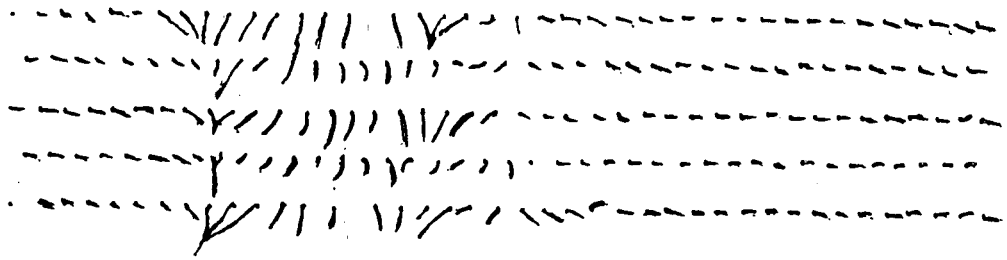

Fig. 4.19 Photo of visualization of suction surface flow for the Re=100,000, FSTI=2.5% case

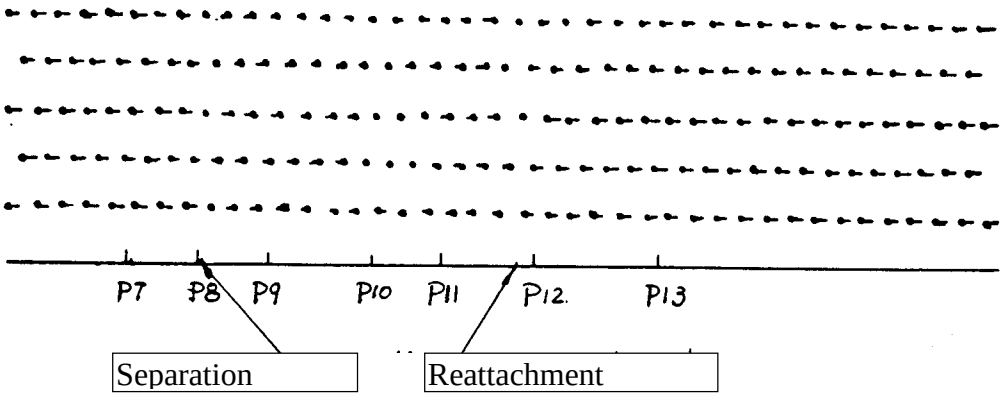

Fig. 4.19a Processed visualization of suction surface flow for the Re=100,000, FSTI=2.5% case

4.4 VELOCITY PROFILES

Much of the above description of the pressure distribution was done with the aid of velocity profile and intermittency measurements in the boundary layers and the shear layers of the separation zones. This section describes these measurements in detail.

Near-wall velocity profiles were measured for cases of three turbulence levels (FSTI=0.5%, 2.5% and 10%) with a single hot-wire, boundary type probe (TSI 1218, T1.5), as described in Chapter Two. The sensor was carefully brought to the wall until it touched, then was slowly stepped away. Upon lift-off, a knee in indicated velocity was observed. The probe was considered to be effectively the radius of the sensor away from the wall at the position of that knee. With this technique, velocity could be measured as close to the wall as $y^+=0.2$. The intermittency was determined with the intermittency circuit described in Chapter Two.

LOW TURBULENCE FLOW, FSTI=0.5%

As stated in the pressure profile discussion, low-turbulence flows in the present setup presented many interesting patterns along the suction surface. The flows always started with laminar boundary layer development through most of the accelerating flow section, p2 to p7. The velocity profiles and velocity fluctuations in the laminar boundary layer on the suction surface are shown in Figs. 4.20 to 4.27. Laminar boundary layer growth is apparent in these figures, note the shape change of the profiles. Measured local turbulence intensities,

u'/u, for all Reynolds numbers are less than 12% throughout the boundary layers at p2 to p7 and the intermittency measurements (not shown) have almost zero (laminar flow) for all four cases. Since turbulence levels are not very high, the velocities measured with a hot-wire are reliable. The Reynolds number effect on the boundary growth is clear on Fig. 4.28, where higher Re cases have smaller boundary layer thicknesses. The turbulence intensities at p7 (Fig. 4.29) are less than 12%.

Velocity profiles at station p8 (x/L_x=68.89%) are displayed in Fig 4.30. Flow visualization showed that two low Re cases, Re=50,000 and Re=100,000, are separated at p8, which can hardly be seen from Fig. 4.30. Local turbulence intensities are less than 10% in all four boundary layers so the mean velocity measurements are accurate throughout. The intermittency values are near zero throughout the flow, meaning that they are either attached or separated laminar boundary layer flows.

At station p9 (x/L_x=74.57%, Fig. 4.31), all four Re cases have separated. The separation of two low-Reynolds-number flows is evidenced by near-zero velocities in the near-wall region. The size of the separation bubble depends upon the suction surface length Reynolds number. The flow of the Re=50,000 case has a larger separation zone, which extends from the wall to around 1 mm while the flow of the Re=100,000 case has separated up to about 0.6 mm. The separation bubble sizes for the cases of Re=200,000 and 300,000 are too small to be identified from velocity profiles, although wall shear stress visualization showed that these two cases are separated at p9 with separation zone thicknesses of about 0.1 mm. Carefully analyzing the near-wall data, or enlarging the near-wall part of the profiles in Fig. 4.31 would support the conclusion drawn from

flow visualization that two high-Re cases are separated at p9. Measured velocities are reasonably accurate for these cases since the local turbulence intensities are not excessive (Fig. 4.32) over most of the flow and uncertainties in flow measurement associated with instantaneous flow in those regions are, therefore, acceptable. The exception is the Re=100,000 case over $0.1 < y < 0.75$ mm where TI > 25%. Error due to excessive TI will lead to artificially high values of the mean velocity. In Fig. 4.31, for the Re=100,000 over $0.1 < y < 0.75$ mm, the mean velocity values are essentially equal to zero. The true readings will be more nearly zero; thus, the measurements can be accepted. Measurements show zero intermittency (not shown) for all four flows at station p9 (x/L=74.57%) over the full boundary layer thickness. This means that no flow transition exists and the flows are laminar, separated flows at this station. The rms velocity fluctuations normalized with inlet velocity, u_{in}, are presented in Fig. 4.33.

All flows are separated at station p10 (x/L_x=81.73%), as shown in Fig. 4.34. The separation zones grow for progressively downstream stations in this decelerated flow. At station p10, the separated flow zone in the lowest-Reynolds-number case (Re=50,000) has grown to 3.3 mm (1 mm at p9) while the separation bubble in the Re=100,000 case has inflated from 0.6 mm (at station p9) to 2.5 mm. The recirculation zone in the Re=300,000 flow is much smaller than those in the low-Reynolds-number flows. Figures 4.35 and 4.36 show regions of high turbulence intensities in most of the separation zones, implying that the measured velocities in these regions are artificially high. With high turbulence intensities, there will be instances of reverse flow over the sensor. Since the anemometer cannot determine direction, it will accept these as a forward velocity of equal magnitude and, hence, the time-averaged velocity will be recorded as

artificially high. These errors begin to become significant as the local turbulence intensity, u'/u, exceeds 25 - 30%. Since the measured velocities in the separated region are near zero, the velocities are still accurate and simply mean that separation regions are essentially dead zones with velocity fluctuations which are large relative to the mean velocity, though both fluctuation and mean values are low. The intermittency measurements (Fig. 4.37) indicate that the Re=300,000 case is turbulent in the recirculation zone and in the shear layer. It is believed that recorded values of intermittency in the highly turbulent zones (u'/u > 25 - 30%) are accurate though the mean velocities are artificially high and the turbulence intensity values are artificially low. Recall that the intermittency is essentially the velocity time-derivative and, as such, would not be subject to rectification error, except at the exact moment of zero-crossing of the true velocity signal. Though this flow is now turbulent, this new turbulence has just developed and there has been insufficient streamwise distance (insufficient residence time) for effecting much turbulent mixing that would lead to reattachment. From Fig. 4.37, it can be noted that for the Re=200,000 case, shear flow transition has just begun at station p10.

At station p11 (x/L_x=85.93%), Fig. 4.38, the Re=300,000 flow has reattached, which is consistent with flow visualization. At station p11, the flow has had enough streamwise distance to bring sufficient energy from the core to the near-wall region by turbulent transport to overcome the adverse pressure gradient. The separated flow zones at the two low Reynolds numbers continue to expand. At station p11, the flow of the Re=200,000 case is turbulent in the separation zone (Fig. 4.39) and the shear layer (throughout the boundary layer), as evidenced by unity intermittency from the wall to the outer edge of the shear

layer (Fig. 4.41). It is clear that transition within the shear layer has affected the flow inside the separation zone and that transition has propagated from the shear layer to the wall region. Due to enhanced turbulent mixing, the recirculation zone for the Re=200,000 has been greatly reduced and the flow is almost reattached to the wall. In Fig. 4.41, the small hump around 3 mm in the intermittency curve for the case of Re=100,000 indicates the initiation of shear flow transition. Figure 4.39 displays the local turbulence intensities at station p11. High turbulence in the separated region causes measured velocities, given in Fig. 4.38, to be artificially high. Figure 4.40 depicts the rms velocity fluctuations normalized by inlet velocity at station p11. The high fluctuations in Re=200,000 and 300,000 cases indicate turbulent boundary layer flows. The high, sharp fluctuation profile for the Re=100,000 is typical for transitional flow.

At station p12 (x/L_x=91.11%), the recirculation zone in the Re=50,000 flow case continues to grow, as shown in Fig. 4.42. Initiation of flow transition was found in the shear layer of the separation zone for this case. At Re=100,000, the separation bubble has begun to shrink. Transition has penetrated far down into the recirculation zone (Figs. 4.44 and 4.45). The flow of the Re=200,000 case has completely reattached. The Re=300,000 case is turbulent, though immature. The relatively low turbulence intensities throughout the boundary layer for the Re=300,000 case, see Fig. 4.43, indicate that the measured velocities are reliable. For cases of other Reynolds number, the high TI values in the recirculation zone and part of the shear region cause artificially high measurements of mean velocities in these regions.

Shear flow transition is relatively slowly progressing. Intermittency is still small at station p13 (x/L_x=97.28%) for the Re=50,000 case (Fig. 4.49). The

recirculation zone of that flow continues growing, but at a much slower pace (Fig. 4.46). The separation bubble in the Re=100,000 case is reduced in size (Fig. 4.46) by turbulent transport. The low turbulence intensities throughout the boundary layer for the Re=200,000 and 300,000 cases (Fig. 4.47) indicate that the measured velocities are reliable. The velocity profile for the case of Re=300,000 can be used to compute the wall shear stress by casting it in terms of wall coordinates (Fig. 4.46a). The flow in the Re=200,000 case can also be converted into u^+, y^+ coordinates, but it is very immature and a skin friction evaluated by this technique would be only approximate. The turbulent boundary layer flows for Re=100,000 and 200,000 cases are evidenced by high rms fluctuations in these cases (see Fig. 4.48).

Figures 4.50 through 4.65 are velocity profiles, velocity fluctuations, turbulence intensities, and intermittency distributions for the four Reynolds-number cases (Re=50,000, 100,000, 200,000, and 300,000) at measurement stations (p8 - p13). They are presented as an summary of flow behavior from p8 to p13. The development of the flow pattern follows the description detailed before. For example, the Re=200,000 case shows the following flow pattern: laminar boundary layer development before p7; strong growth rate as a laminar boundary layer when the adverse pressure gradient section is nearly reached, from p7 to p8; laminar separation before p9; transition of the free shear layer at p10; turbulent flow throughout the shear layer and near-wall region after p11; and turbulent reattachment before p12.

From the above discussion, it is clear that for low free stream turbulence (FSTI=0.5%) cases in the present study, flow transition always starts at the shear layer over the separation zone and transition propagates toward the wall. To

investigate this separated shear layer transition, intermittency was measured at many axial locations in the vicinity of transition and the results are presented in Fig. 4.66 for the Re=100,000 case. The locations of intermittency measurement station for this case are tabulated in Table 4.7. The transition begins at about p10a (x=8.76 cm, x/Lx=85.19%). The intermittency has a peak value of 0.034 at around y=0.36 cm (y/δ_2=10.6), which is in the shear layer of the separation zone. The separation bubble size is 0.33 cm. At p11a (x=8.89 cm, x/Lx=86.42%), the peak intermittency increases to 0.209, centered around y=0.4 cm (y/δ_2=10). When the flow reaches the axial position of p11b (x=9.02 cm, x/Lx=87.65%), intermittency elevates to 0.508 with its peak at y=0.42 cm (y/δ_2=7.9). Downstream, intermittency rises rapidly from 0.692 at p11c (x=9.14 cm, x/Lx=88.89%) to 0.974 at p12a (x=9.40 cm, x/Lx=91.36%) while the peak migrates from y=0.43 cm (y/δ_2=6.7)to 0.5 cm (y/δ_2=5.6). It can be noted that with progressively downstream locations, the transition region spreads and the near-wall region intermittency is beginning to rise at p11c. At the axial location p12b (x=9.65 cm, x/Lx=93.83%), most of the boundary layer flow is turbulent-like ($\gamma > 0.5$) with only the very near-wall (y<0.02 cm, y/δ_2<0.17) part of the boundary layer flow still laminar-like ($\gamma < 0.5$). Further downstream to p12c (x=9.91 cm, x/Lx=96.3%), almost all the boundary layer is filled with turbulent-like flow.

The values of boundary layer thickness, $\delta_{99.5}$, momentum thickness, δ_2, displacement thickness, δ^*, local free stream velocity, u_8, and momentum thickness Reynolds number, $Re_{\delta 2}$, for the four cases of different Reynolds number were computed from the measured velocity profiles presented above and are shown in Tables 4.8 to 4.11. Free-stream velocities were also computed

from surface static pressure with equation, $u_\infty = \sqrt{2(p_t - p)/\rho}$, and compared to measured velocities listed in Tables 4.8 to 4.11. The comparison of these velocities are shown in Fig. 4.67.

TABLE 4.7 Locations of intermittency measurement stations for Re=100,000 and FSTI=0.5% case

Station #	x (cm)	x/Lx (%)	l (cm)	l/L (%)	s (cm)	s/Lss (%)
p10a	8.76	85.2	8.64	75.6	11.11	72.8
p11a	8.89	86.4	8.87	77.6	11.40	74.7
p11b	9.02	87.7	9.10	79.6	11.71	76.7
p11c	9.14	88.9	9.32	81.5	11.99	78.5
p12a	9.40	91.4	9.78	85.6	12.62	82.7
p12b	9.65	93.8	9.87	86.6	13.24	86.7
p12c	9.91	96.3	10.33	90.4	13.89	91.0

TABLE 4.8. Streamwise variation of $\delta_{99.5}$, δ_2, δ^*, u_8, and $Re_{\delta 2}$ for the Re=50,000, FSTI=0.5% case

x	$\delta_{99.5}$ (mm)	δ^* (mm)	δ_2 (mm)	u_8 (m/s)	$Re_{\delta 2}$
p2	0.461	0.176	0.068	3.733	14.930
p3	1.070	0.311	0.138	4.865	40.863
p4	1.189	0.350	0.150	5.484	49.689
p5	1.379	0.405	0.172	5.519	63.029
p6	1.460	0.424	0.182	5.882	64.439
p7	1.610	0.458	0.204	6.095	78.150
p8	2.096	0.656	0.231	5.981	86.447
p9	3.719	1.926	0.334	5.929	123.714
p10	5.822	3.930	0.415	5.899	158.082
p11	7.861	6.001	0.449	5.603	157.171
p12	10.000	7.486	0.531	5.675	188.444
p13	12.055	8.324	0.688	5.511	237.065

TABLE 4.9. Streamwise variation of $\delta_{99.5}$, δ_2, δ^*, u_8, and $Re_{\delta 2}$ for the Re=100,000, FSTI=0.5% case

x	$\delta_{99.5}$ (mm)	δ^* (mm)	δ_2 (mm)	u_8 (m/s)	$Re_{\delta 2}$
p2	0.359	0.125	0.051	7.780	23.964
p3	0.845	0.215	0.097	9.906	65.017
p4	0.904	0.242	0.109	10.973	72.905
p5	1.022	0.335	0.119	11.266	84.003
p6	1.048	0.381	0.130	11.779	93.392
p7	1.172	0.460	0.144	12.200	107.56
p8	1.311	0.501	0.171	12.001	128.548
p9	2.395	1.237	0.237	12.083	179.301
p10	4.642	3.288	0.333	11.444	238.089
p11	5.805	4.137	0.349	11.359	247.875
p12	7.775	5.401	0.864	11.471	616.310
p13	10.055	5.409	1.637	10.772	1102.30

TABLE 4.10. Streamwise variation of $\delta_{99.5}$, δ_2, δ^*, u_8, and $Re_{\delta 2}$ for the Re=200,000, FSTI=0.5% case

x	$\delta_{99.5}$ (mm)	δ^* (mm)	δ_2 (mm)	u_8 (m/s)	$Re_{\delta 2}$
p2	0.283	0.087	0.038	17.041	35.716
p3	0.646	0.184	0.079	21.128	96.976
p4	0.743	0.226	0.087	23.311	120.442
p5	0.754	0.260	0.099	24.263	143.303
p6	0.821	0.291	0.100	25.036	151.728
p7	0.814	0.309	0.109	25.221	162.296
p8	0.989	0.314	0.118	24.939	178.388
p9	1.433	0.647	0.174	24.388	250.527
p10	2.694	1.689	0.222	22.641	306.889
p11	3.970	2.580	0.472	21.238	625.221
p12	5.275	1.481	0.733	20.009	930.529
p13	7.326	1.582	0.961	18.882	1095.65

TABLE 4.11. Streamwise variation of $\delta_{99.5}$, δ_2, δ^*, u_8, and $Re_{\delta 2}$ for the Re=300,000, FSTI=0.5% case

x	$\delta_{99.5}$ (mm)	δ^* (mm)	δ_2 (mm)	u_8 (m/s)	$Re_{\delta 2}$
p2	0.214	0.057	0.026	23.401	37.042
p3	0.513	0.139	0.060	29.624	109.539
p4	0.673	0.191	0.075	33.244	153.561
p5	0.682	0.204	0.083	34.689	181.304
p6	0.723	0.216	0.089	36.060	191.648
p7	0.764	0.246	0.100	36.675	225.329
p8	0.814	0.289	0.106	36.374	246.238
p9	1.275	0.493	0.135	35.030	296.024
p10	2.000	0.655	0.165	32.985	339.347
p11	3.296	0.895	0.374	30.604	715.740
p12	4.719	0.799	0.515	29.249	941.554
p13	6.341	0.964	0.668	27.576	1151.64

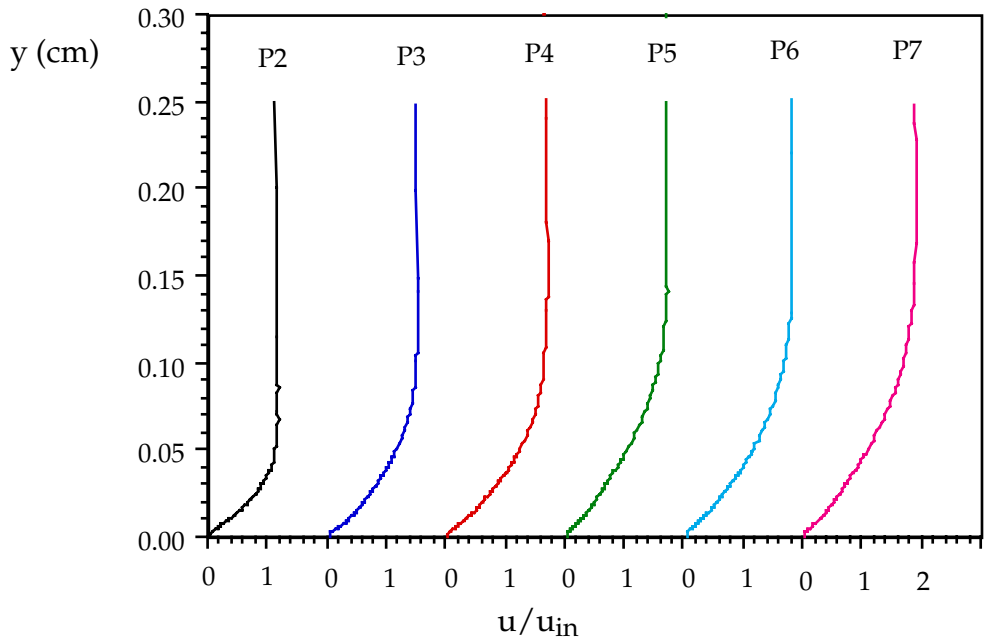

Fig. 4.20 Velocity profiles, p2 to p7, Re=50,000, FSTI=0.5%

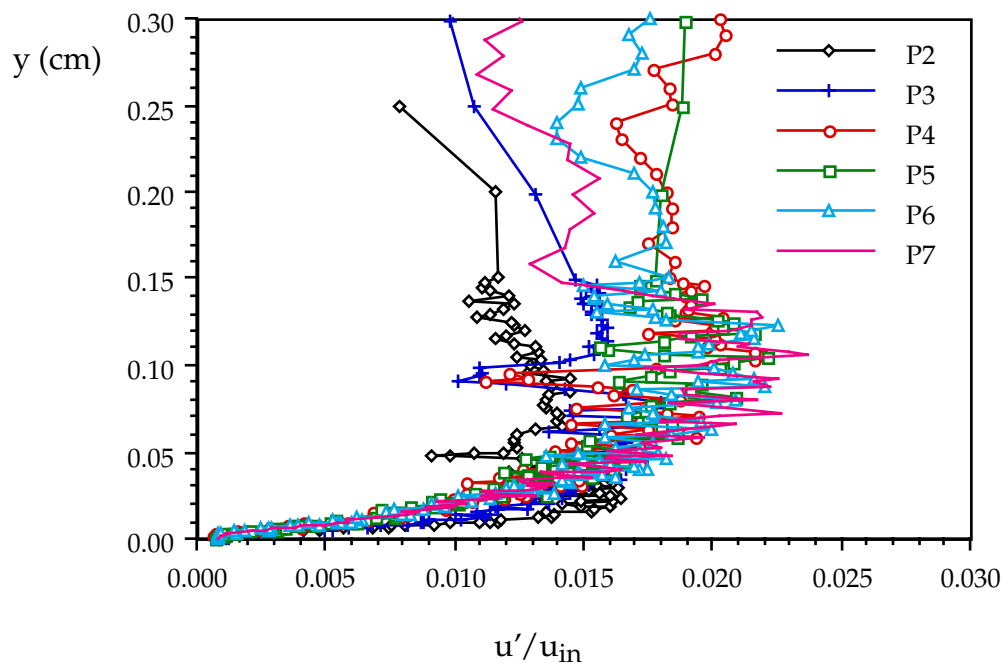

Fig. 4.21 Velocity fluctuations at p2 to p7, Re=50,000, FSTI=0.5%

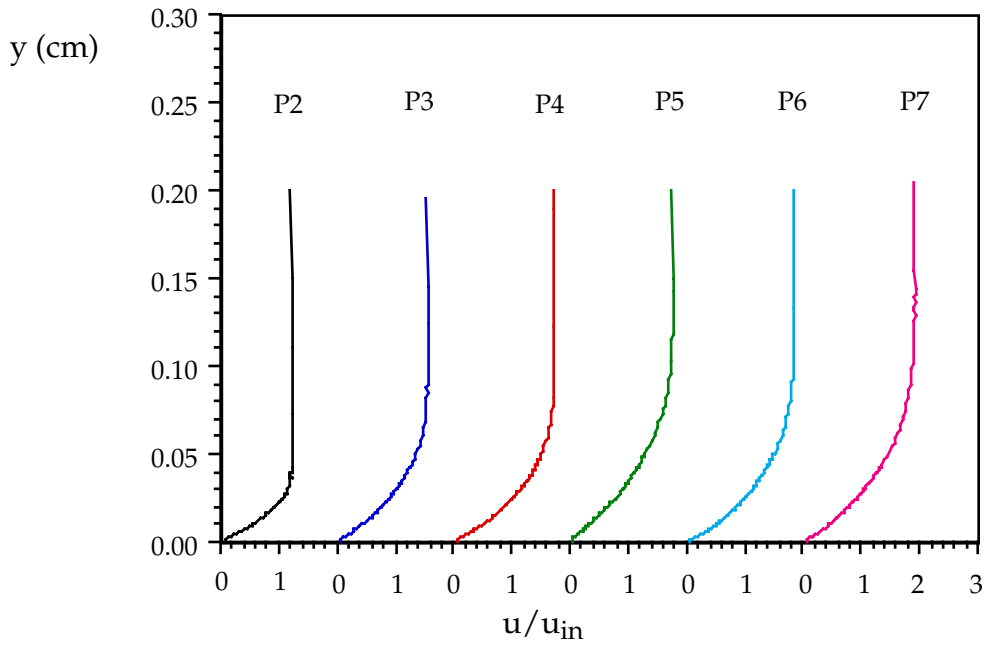

Fig. 4.22 Velocity profiles, p2 to p7, Re=100,000, FSTI=0.5%

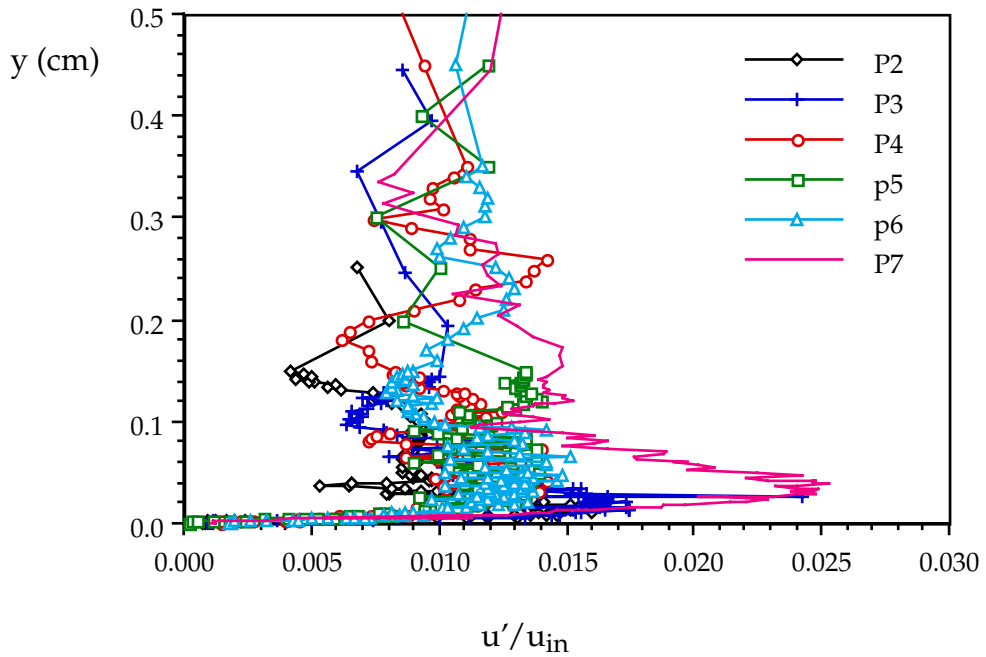

Fig. 4.23 Velocity fluctuations at p4 to p7, Re=100,000, FSTI=0.5%

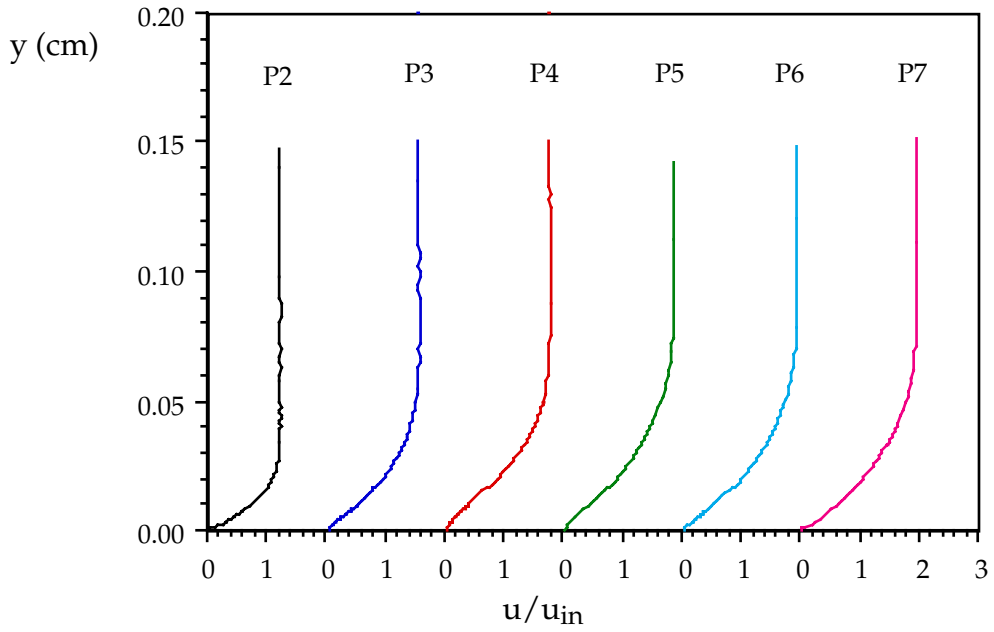

Fig. 4.24 Velocity profiles, p2 to p7, Re=200,000, FSTI=0.5%

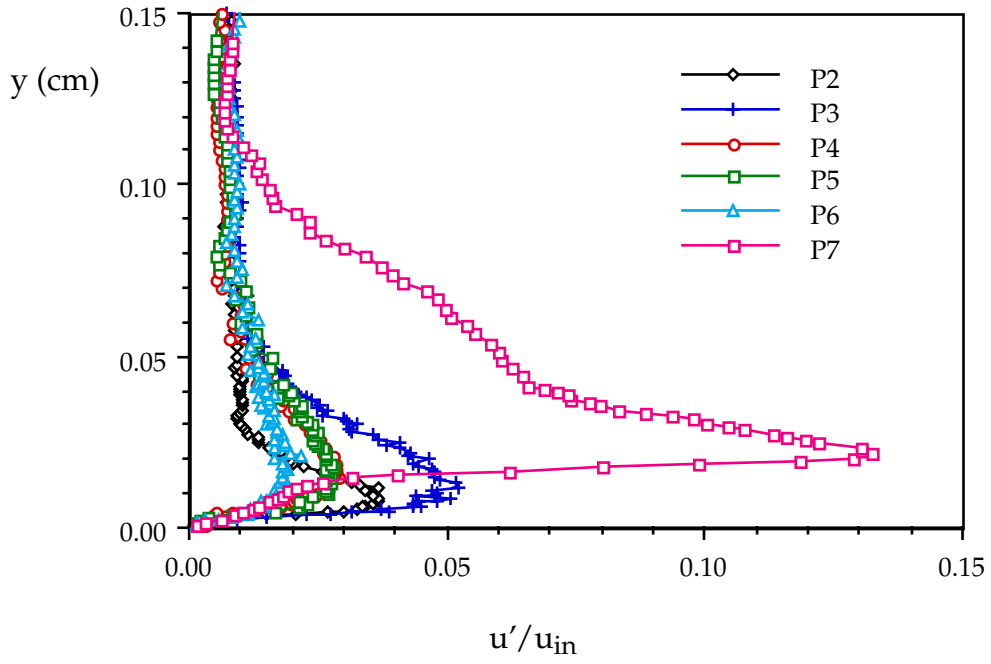

Fig. 4.25 Velocity fluctuations at p2 to p7, Re=200,000, FSTI=0.5%

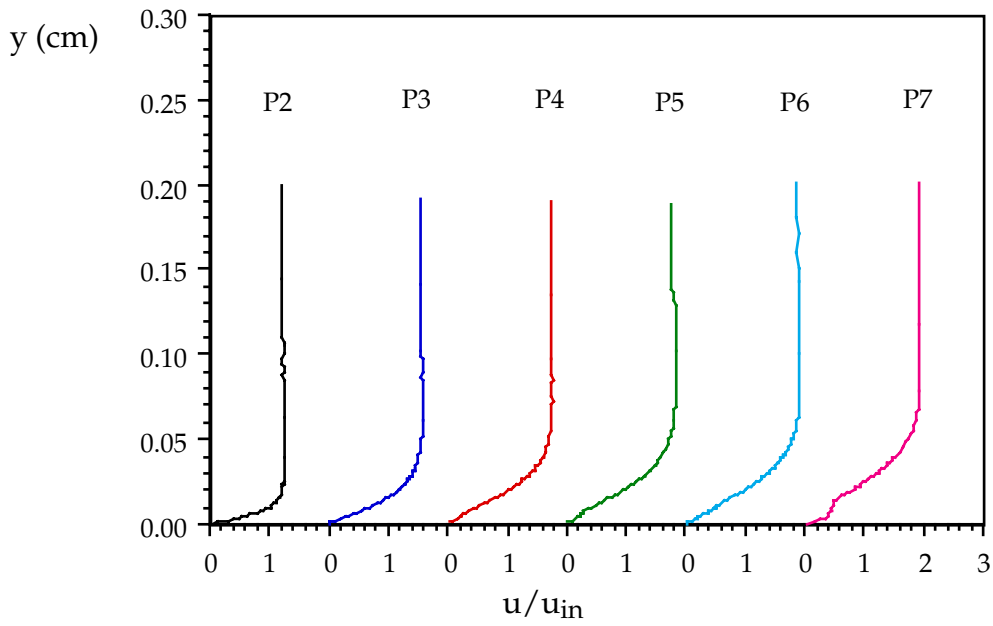

Fig. 4.26 Velocity profiles, p2 to p7, Re=300,000, FSTI=0.5%

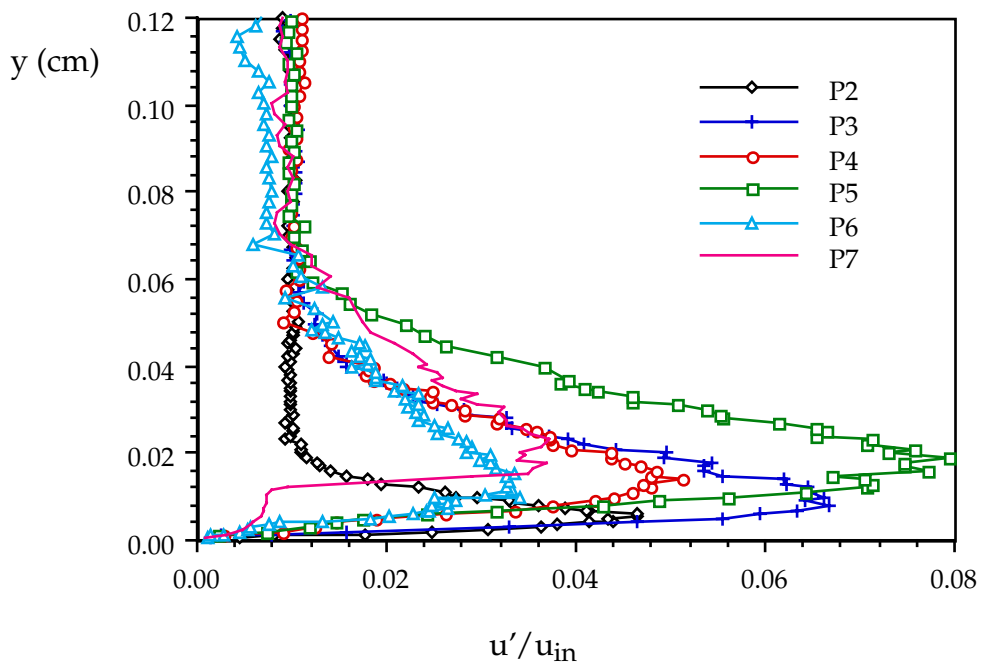

Fig. 4.27 Velocity fluctuations at p2 to p7, Re=300,000, FSTI=0.5%

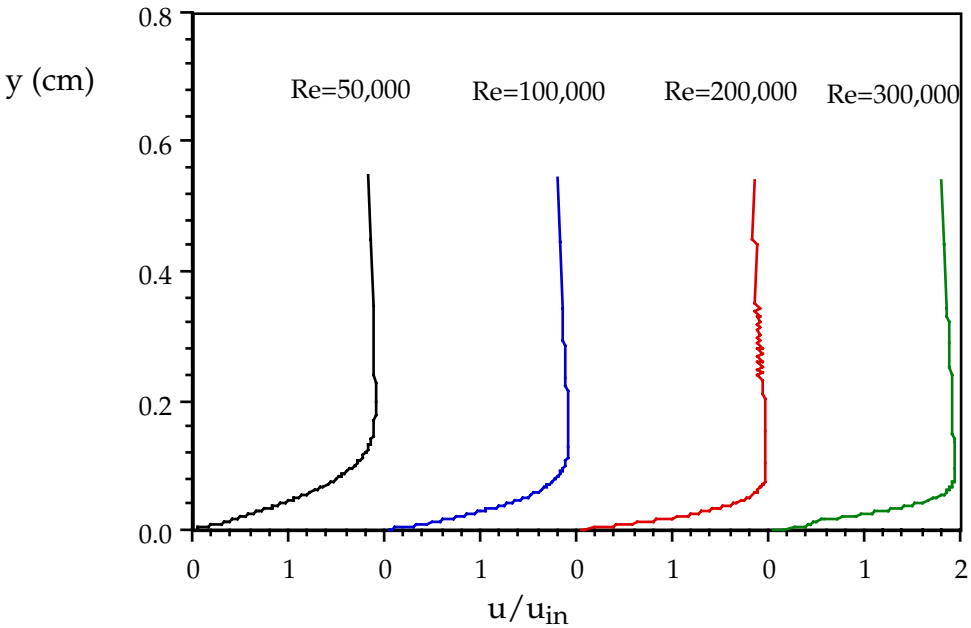

Fig. 4.28 Velocity profiles at p7 (x/Lx=62.47%), FSTI=0.5%

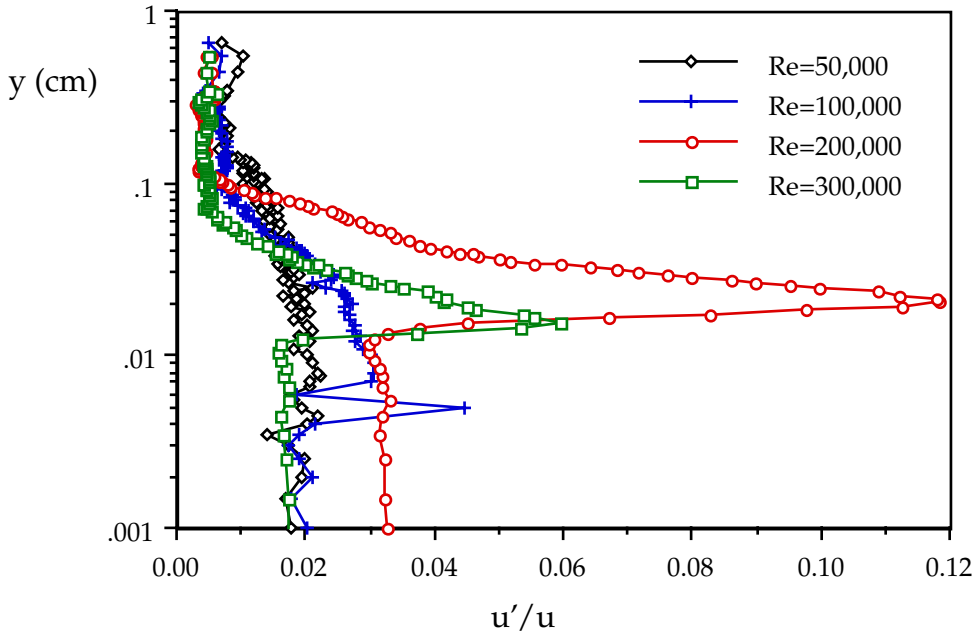

Fig. 4.29 Velocity fluctuations at p7 (x/Lx=62.47%), FSTI=0.5%

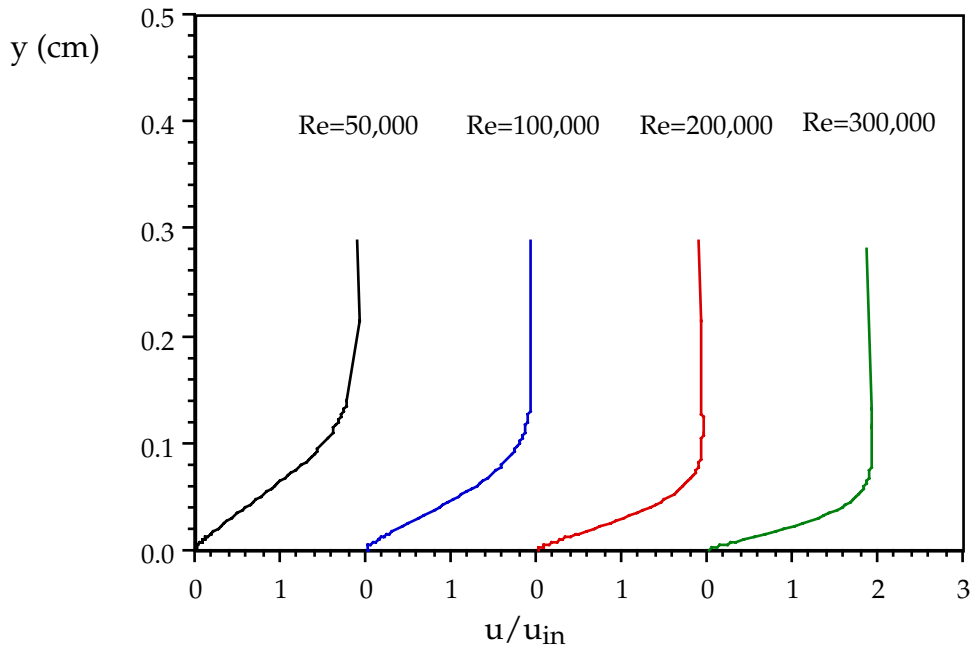

Fig. 4.30 Velocity profiles at station p8 (x/Lx=68.89%), FSTI=0.5%

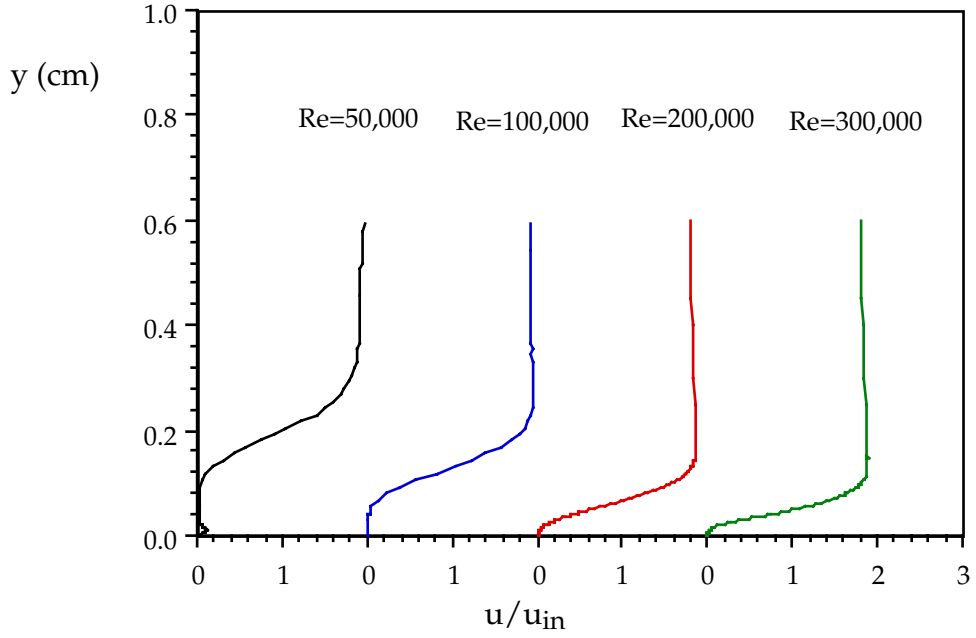

Fig. 4.31 Velocity profiles at station p9 (x/Lx=74.57%), FSTI=0.5%
Caution: measured values are artificially high at y=0.014 - 0.07 cm for Re=100k

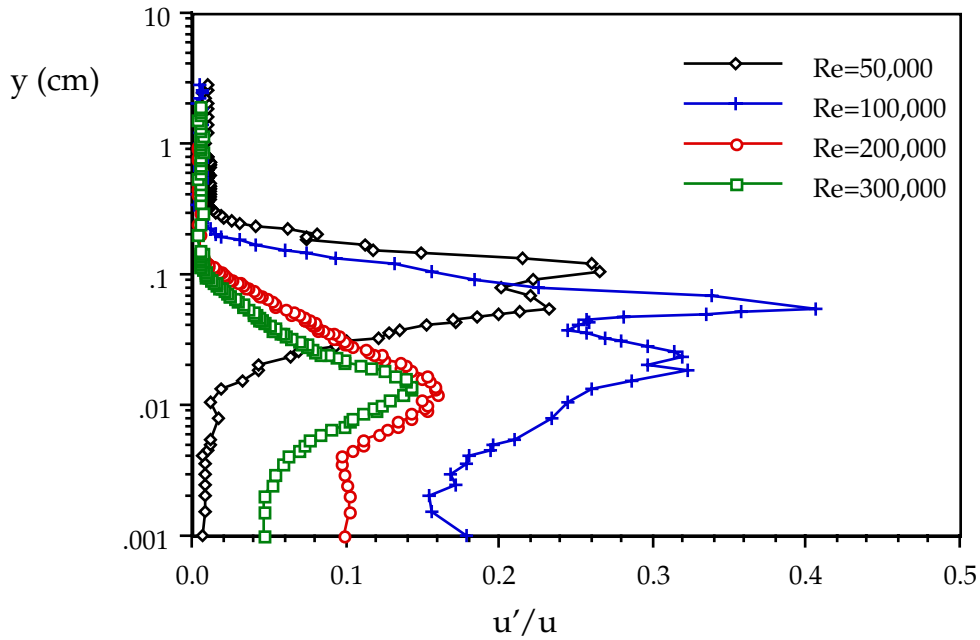

Fig. 4.32 Turbulence intensities at station p9 (x/Lx=74.57%), FSTI=0.5%

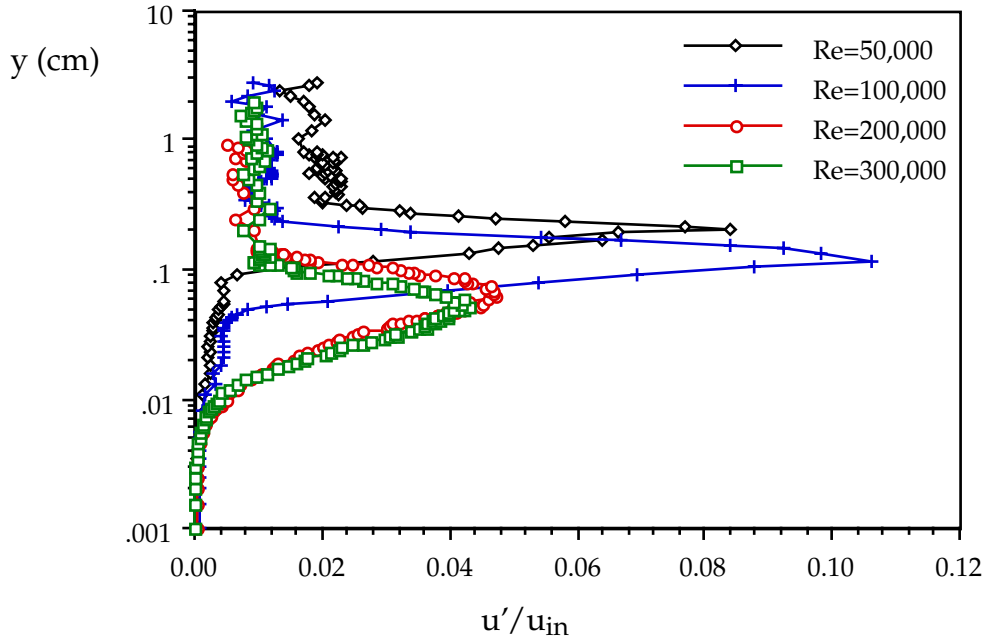

Fig. 4.33 Velocity fluctuations at station p9 (x/Lx=74.57%), FSTI=0.5%

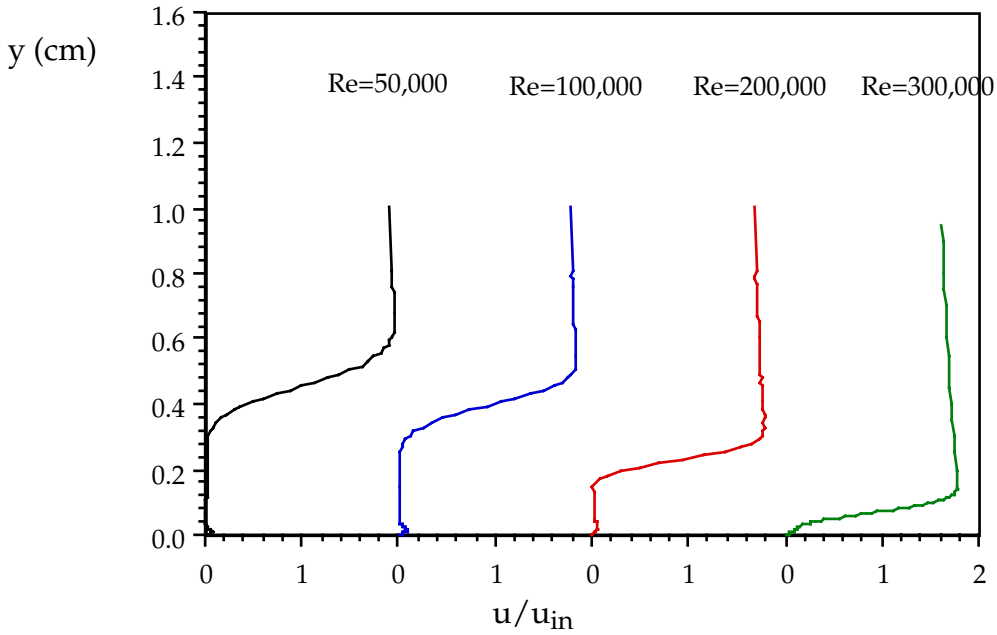

Fig. 4.34 Velocity profiles at station p10 (x/Lx=81.73%), FSTI=0.5%
Caution: measured values are artificially high at y=0.05 - 0.4 cm for Re=50k, y=0.05 - 0.4 cm for Re=100k, y=0.05 - 0.2 cm for Re=200k,
y=0 - 0.03 cm for Re=300k

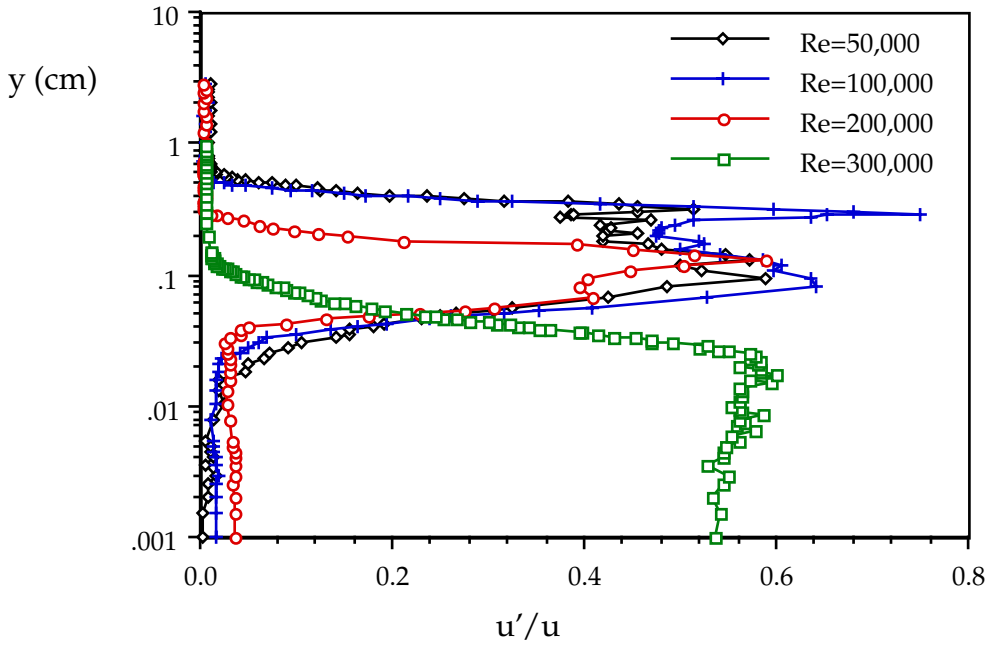

Fig. 4.35 Turbulence intensities at station p10 (x/Lx=81.73%), FSTI=0.5%

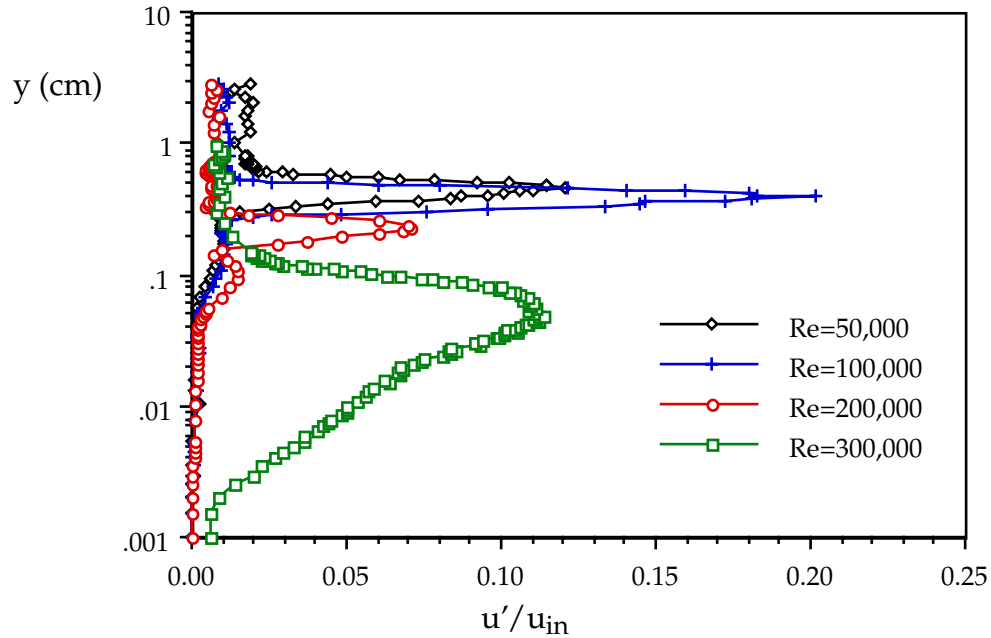

Fig. 4.36 Velocity fluctuations at station p10 (x/Lx=85.93%), FSTI=0.5%

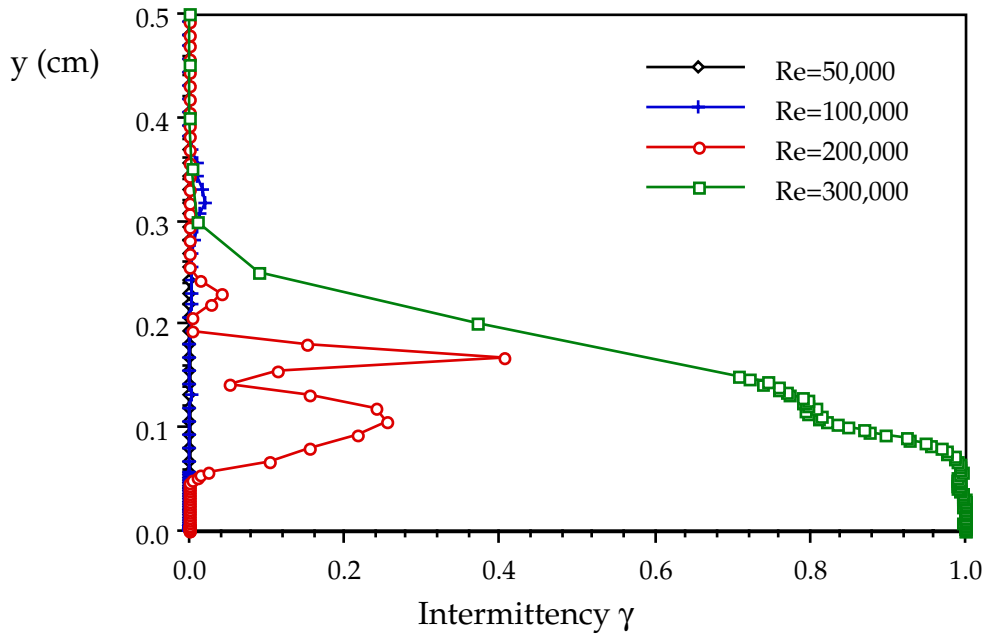

Fig. 4.37 Intermittency distributions at station p10 (x/Lx=85.93%), FSTI=0.5%

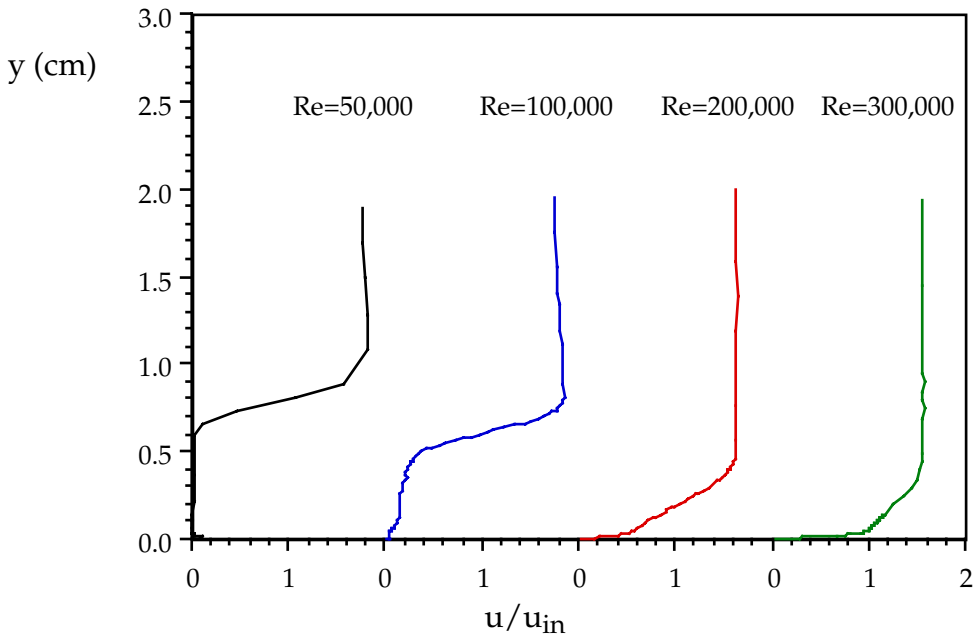

Fig. 4.38 Velocity profiles at station p11 (x/Lx=85.93%), FSTI=0.5%
Caution: measured values are artificially high at y=0.032 - 0.54 cm for Re=50k, y=0 - 0.4 cm for Re=100k, y=0 - 0.2 cm for Re=200k, y=0 - 0.043 cm for Re=300k

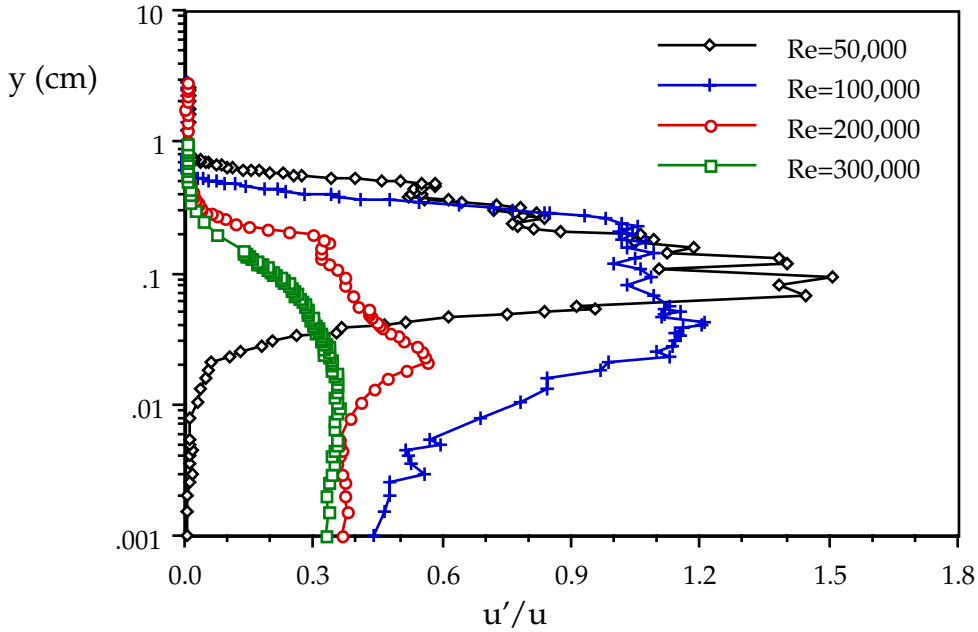

Fig. 4.39 Turbulence intensities at station p11 (x/Lx=85.93%), FSTI=0.5%

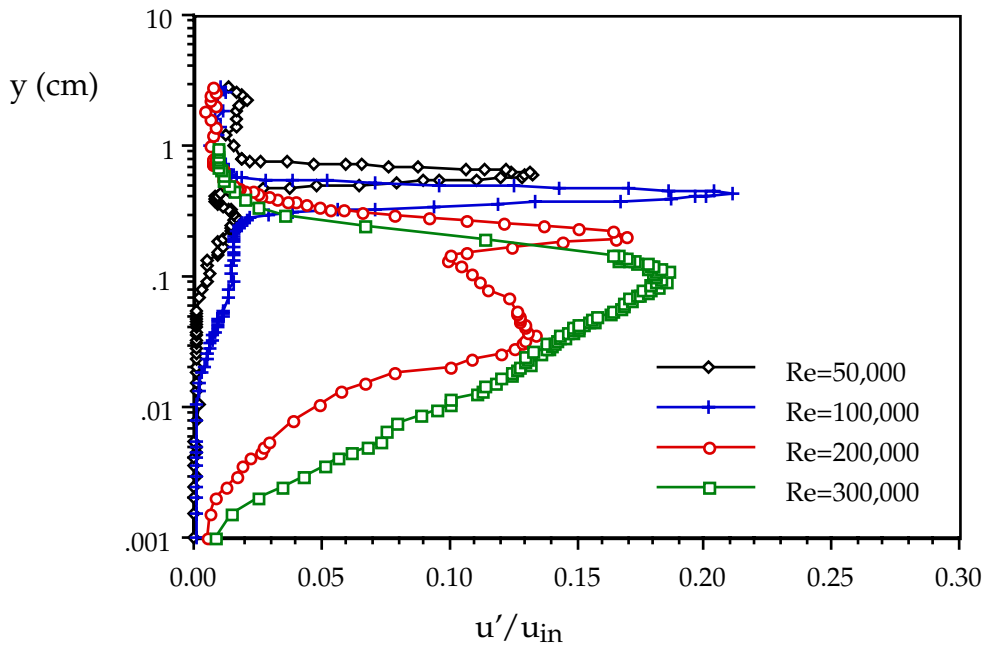

Fig. 4.40 Velocity fluctuations at station p11 (x/Lx=85.93%), FSTI=0.5%

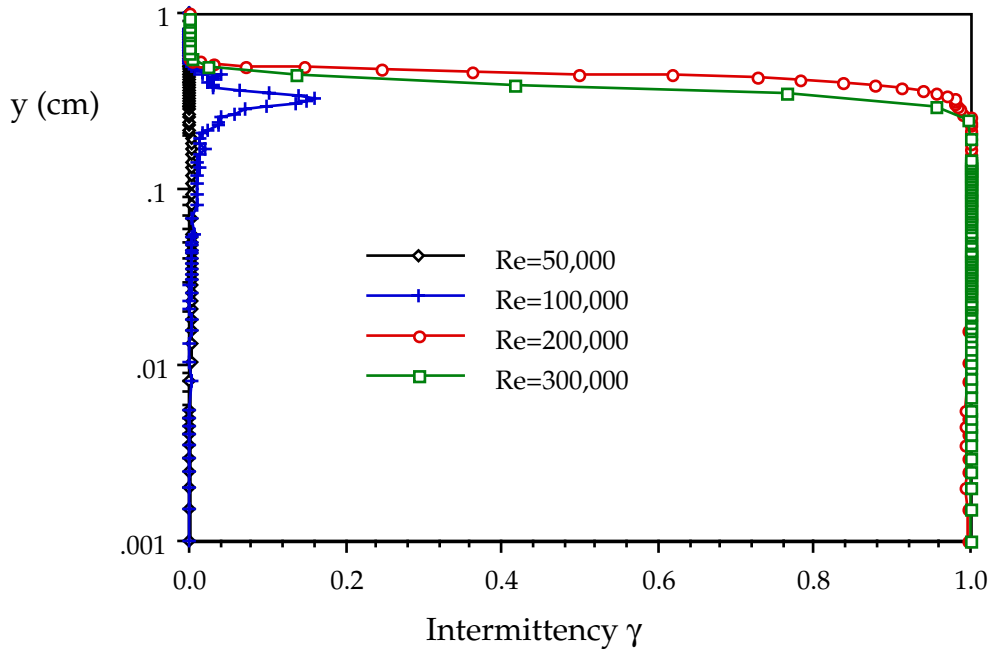

Fig. 4.41 Intermittency distributions at station p11 (x/Lx=85.93%), FSTI=0.5%

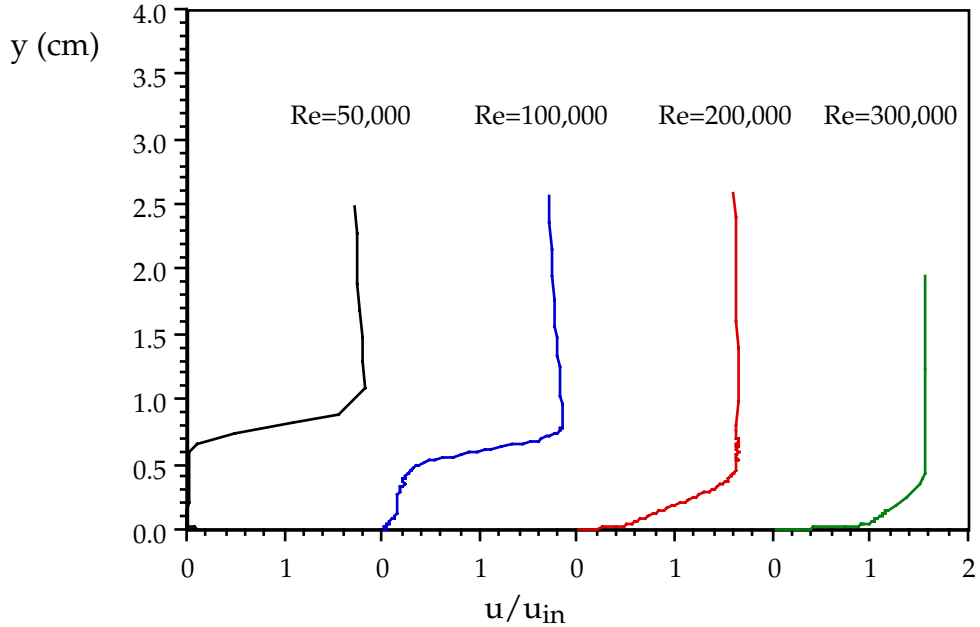

Fig. 4.42 Velocity profiles at station p12 (x/Lx=91.11%), FSTI=0.5%
Caution: measured values are artificially high at y=0.033 - 0.8 cm for Re=50k, y=0.012 - 0.65 cm for Re=100k, y=0 - 0.18 cm for Re=200k

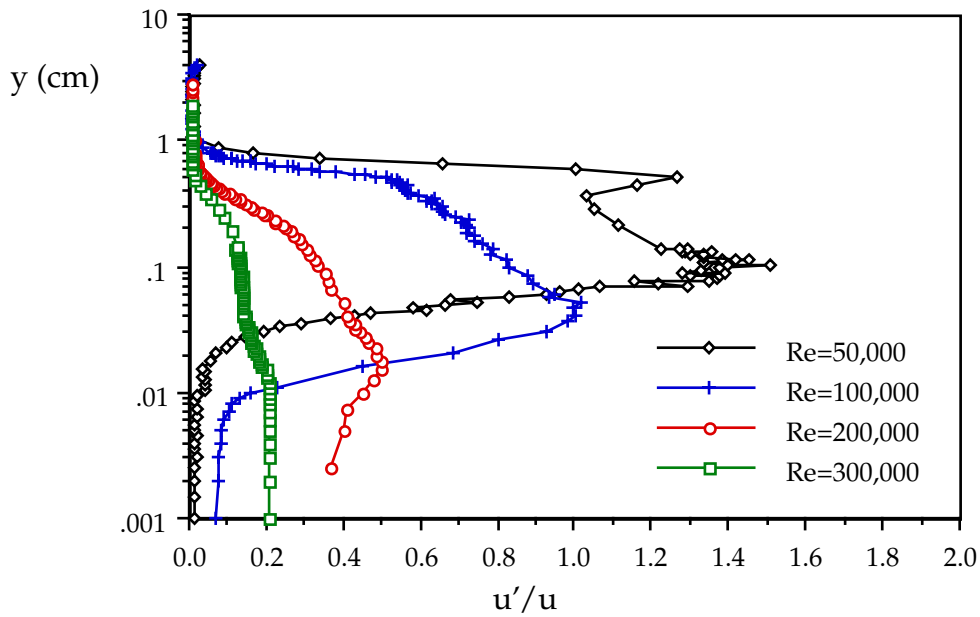

Fig. 4.43 Turbulence intensities at station p12 (x/Lx=91.11%), FSTI=0.5%

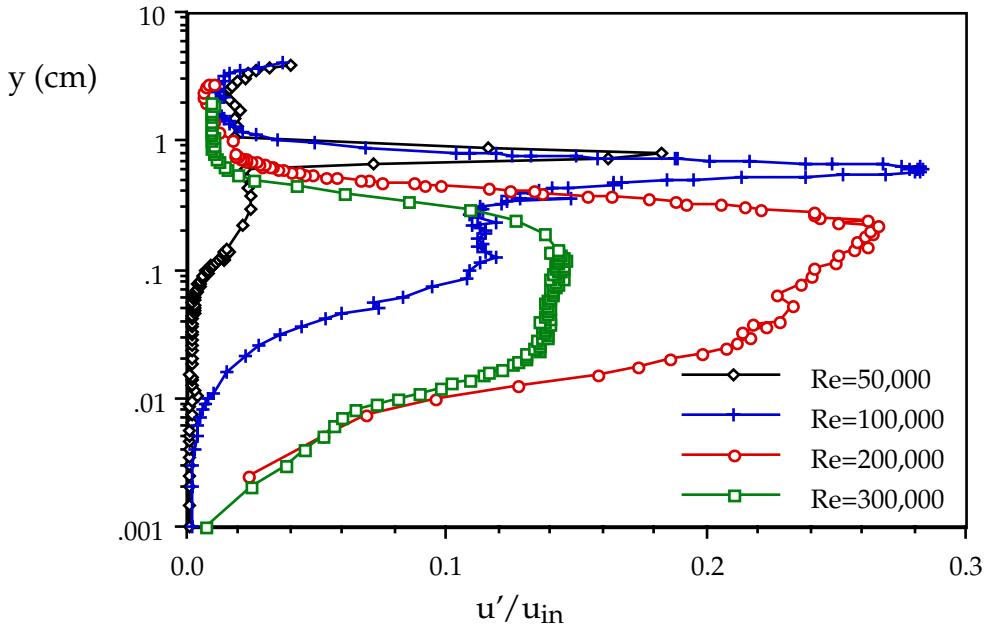

Fig. 4.44 Velocity fluctuations at station p12 (x/Lx=91.11%), FSTI=0.5%

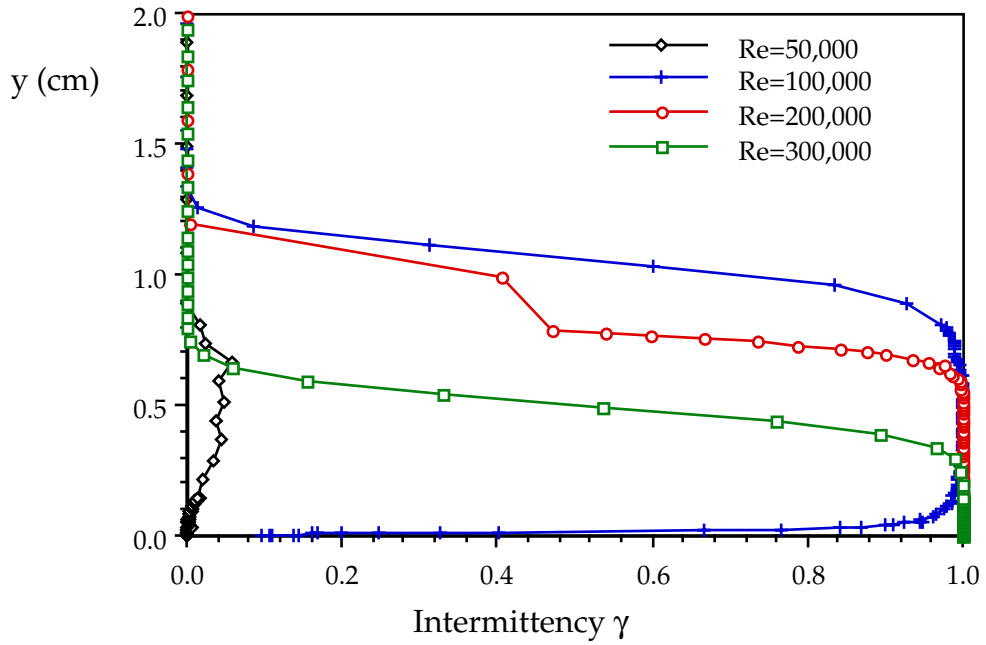

Fig. 4.45 Intermittency distributions at station p12 (x/Lx=91.11%), FSTI=0.5%

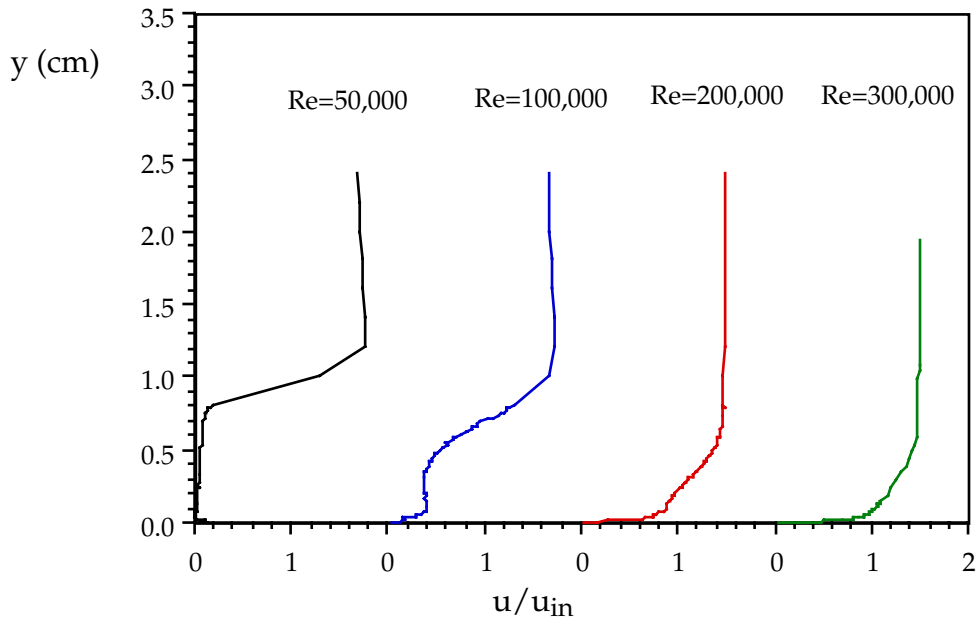

Fig. 4.46 Velocity profiles at station p13 (x/Lx=97.28%), FSTI=0.5%
Caution: measured values are artificially high at y=0.025 - 1 cm for Re=50k, y=0.024 - 0.76 cm for Re=100k, y=0.006 - 0.023 cm for Re=200k

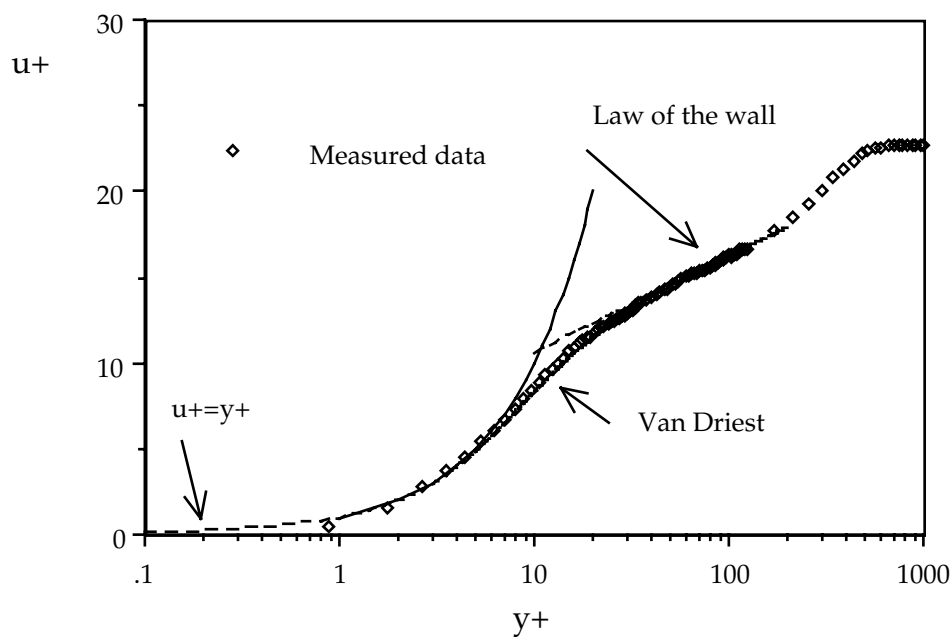

Fig. 4.46a Velocity profile in wall coordinates, P13 (x/Lx=97.28%), Re=300,000, FSTI=0.5%

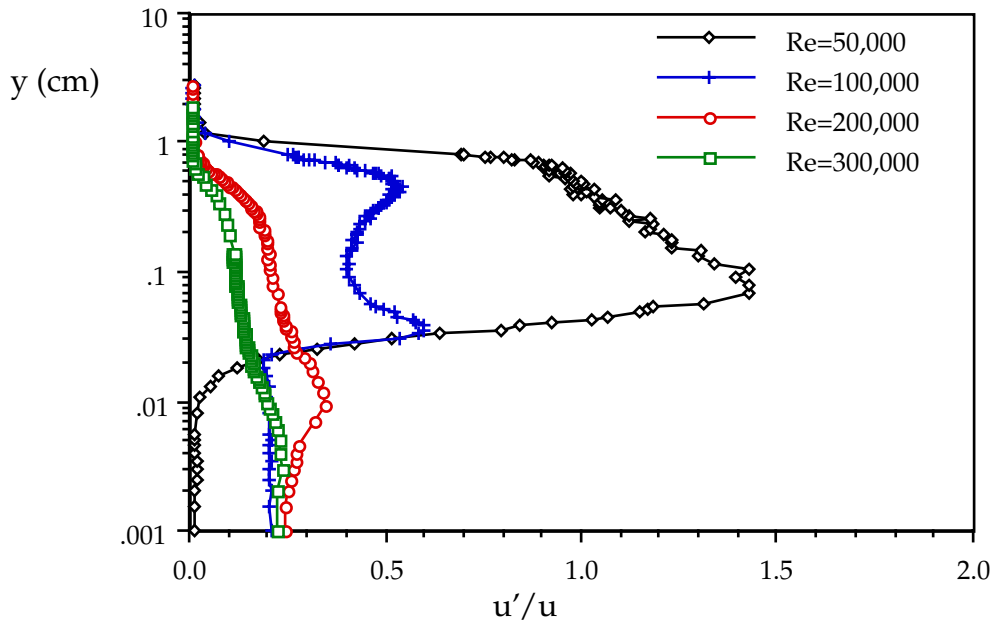

Fig. 4.47 Turbulence intensities at station p13 (x/Lx=97.28%), FSTI=0.5%

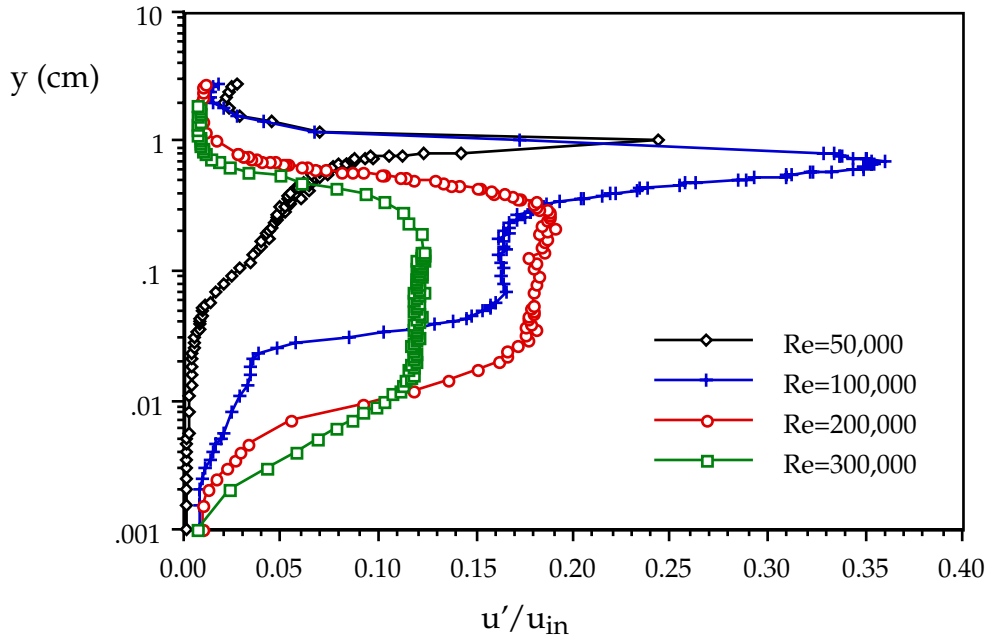

Fig. 4.48 Velocity fluctuations at station p13 (x/Lx=97.28%), FSTI=0.5%

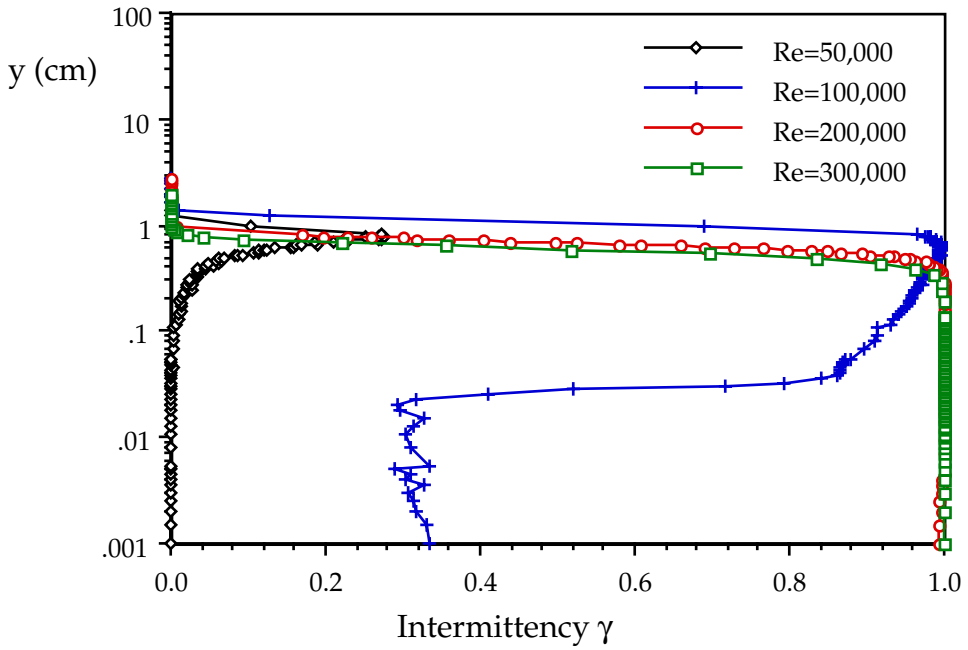

Fig. 4.49 Intermittency distributions at station p13 (x/Lx=97.28%), FSTI=0.5%

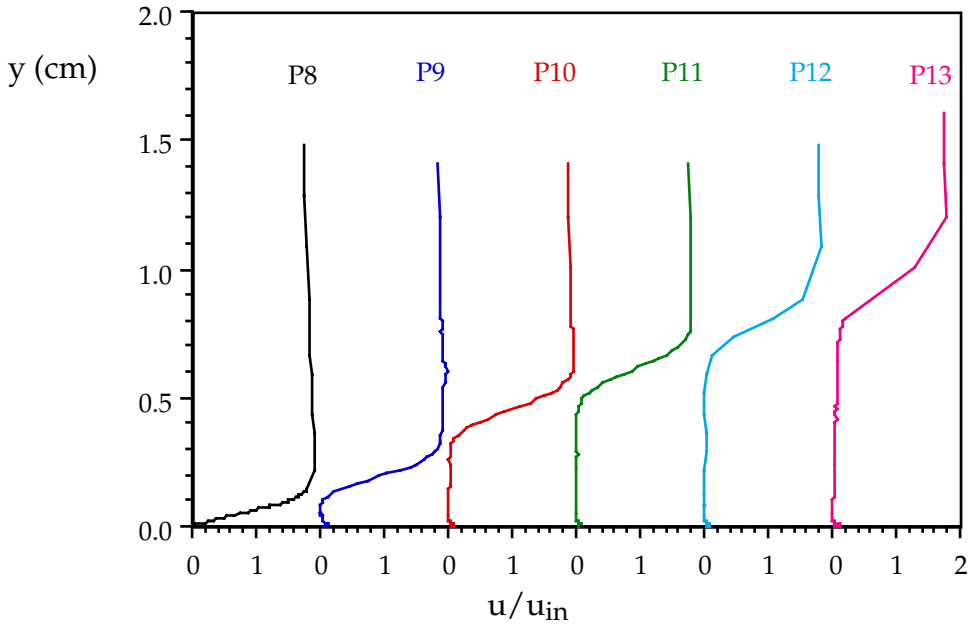

Fig. 4.50 Velocity profiles at p8 - p13, Re=50,000, FSTI=0.5%
Caution: measured values are artificially high at y=0.05 - 0.4 cm for p10, y=0.032 - 0.54 cm for p11, y=0.033 - 0.8 cm for p12, y=0.025 - 1 cm for p13

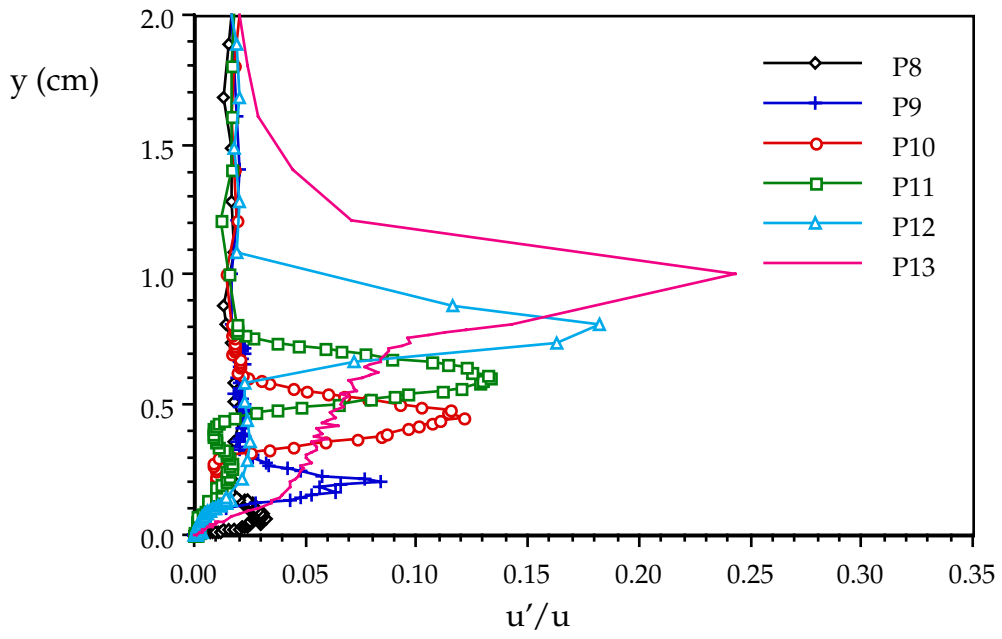

Fig. 4.51 Velocity fluctuations at p8 - p13, Re=50,000, FSTI=0.5%

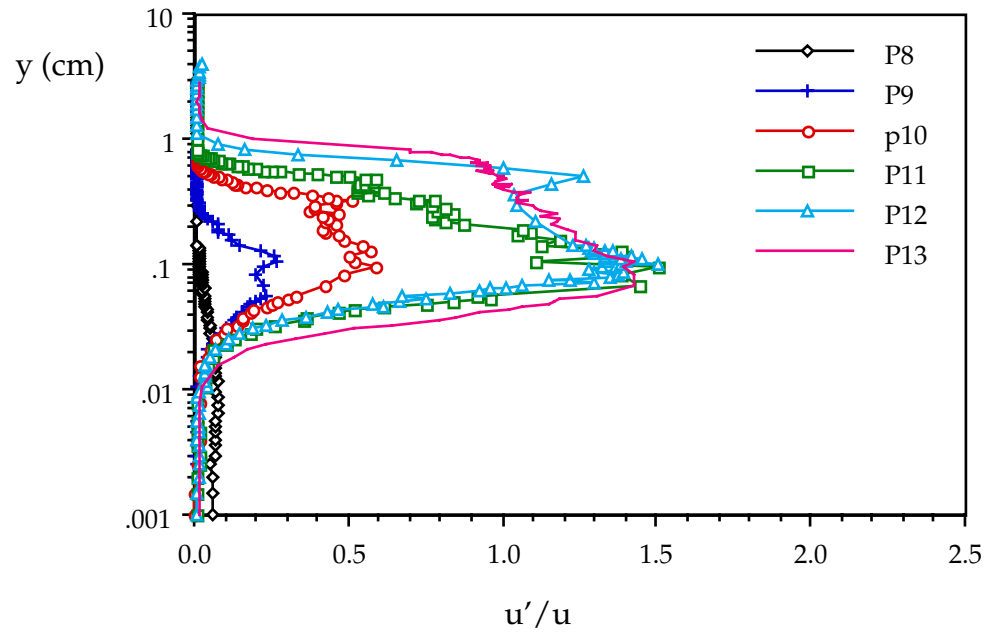

Fig. 4.52 Turbulence intensity at p8 - p13 for Re=50,000, FSTI=0.5%

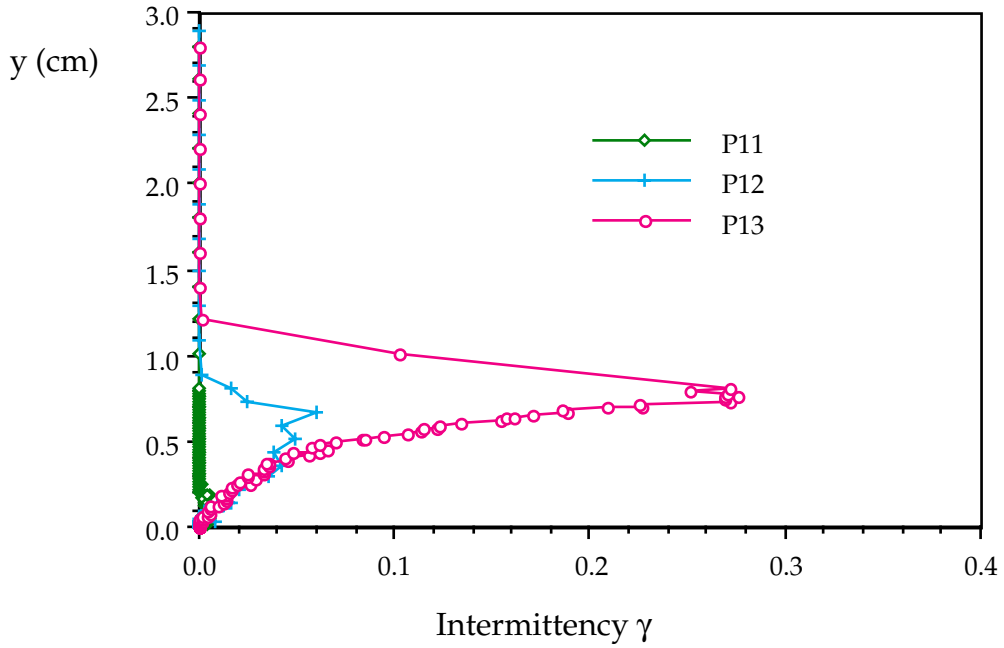

Fig. 4.53 Intermittency distributions at p11 - p13, Re=50,000, FSTI=0.5%

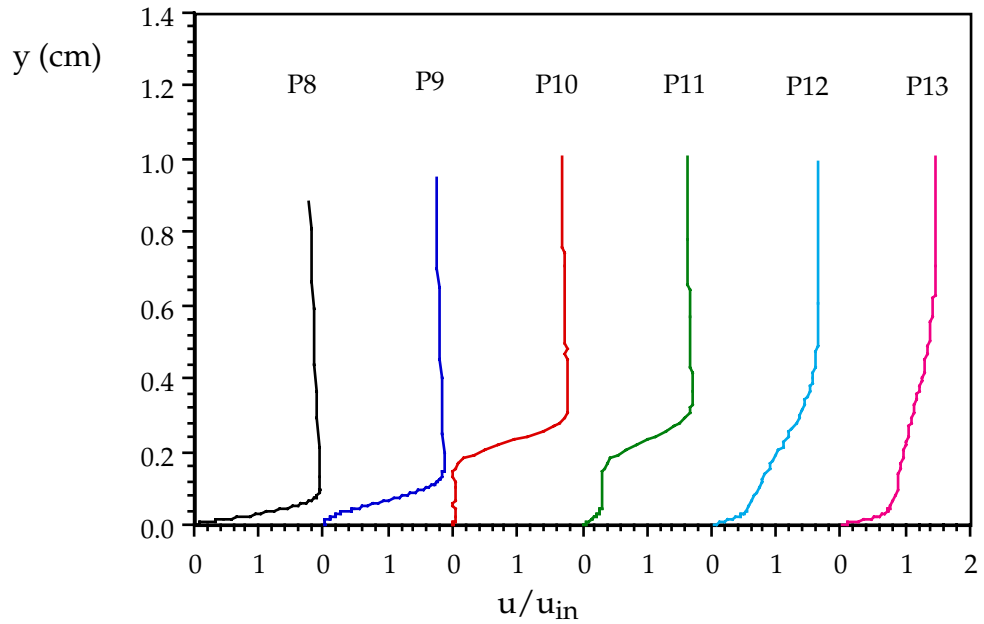

Fig. 4.54 Velocity profiles at p8 - p13, Re=100,000, FSTI=0.5%
Caution: measured values are artificially high at y=0.05 - 0.4 cm for p10, y=0 - 0.4 cm for p11, y=0.012 - 0.65 cm for p12, y=0.024 - 0.76 cm for p13

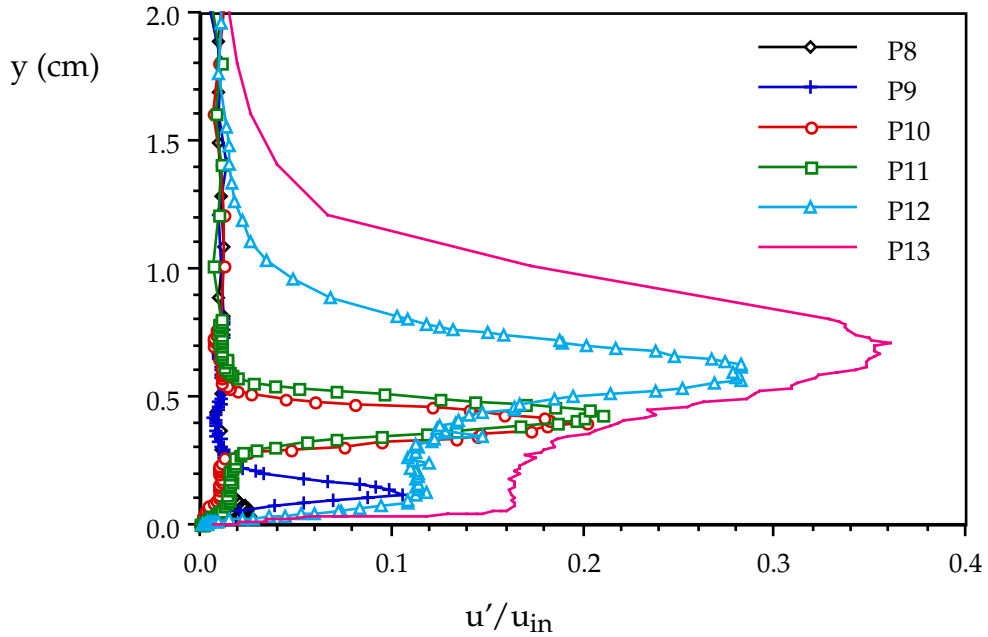

Fig. 4.55 Velocity fluctuations at p8 - p13, Re=100,000, FSTI=0.5%

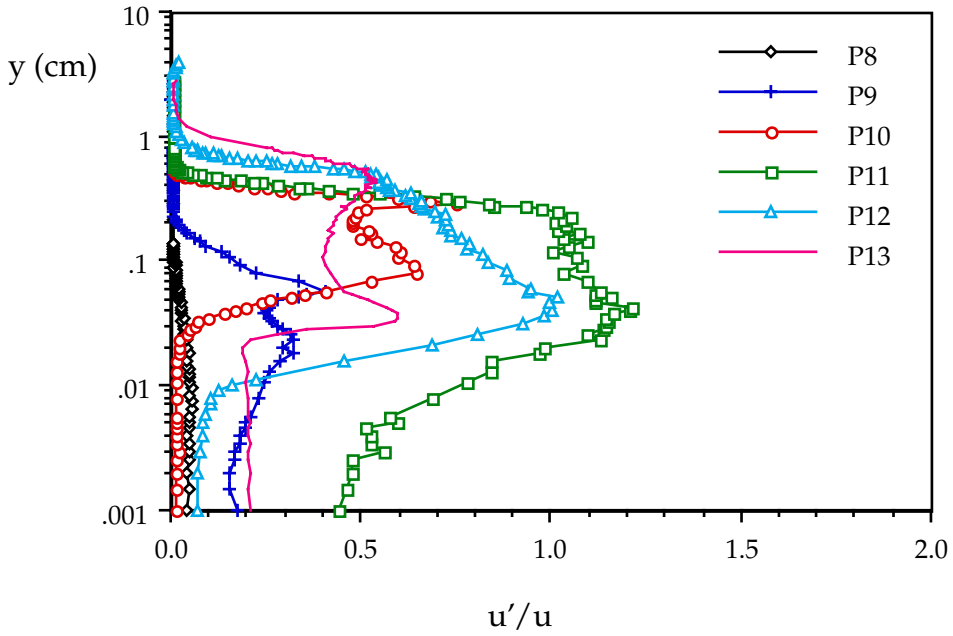

Fig. 4.56 Turbulence intensity at p8 - p13 for Re=100,000, FSTI=0.5%

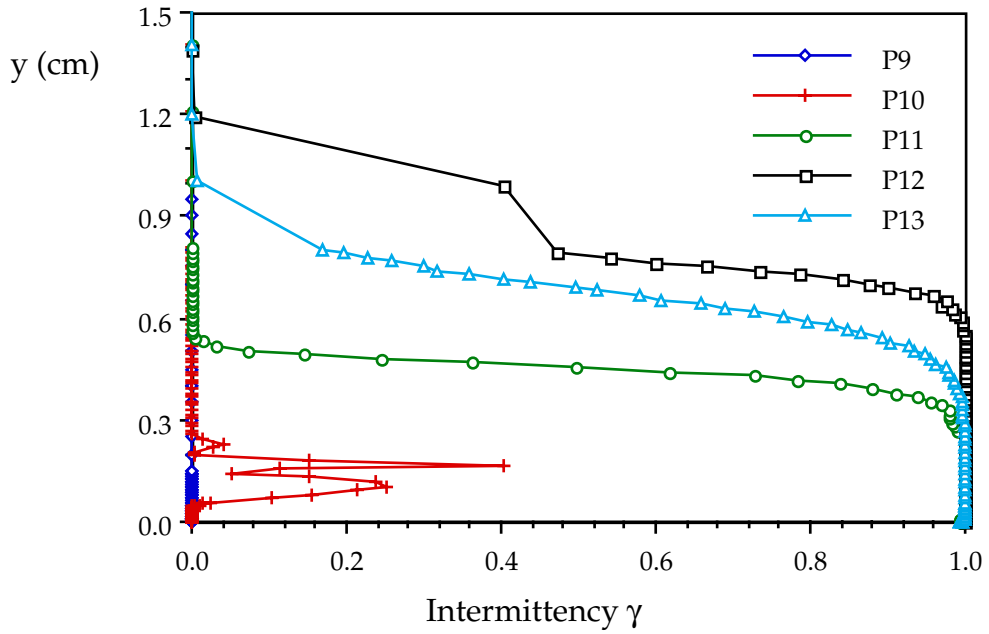

Fig. 4.57 Intermittency distributions at p9 - p13, Re=200,000, FSTI=0.5%

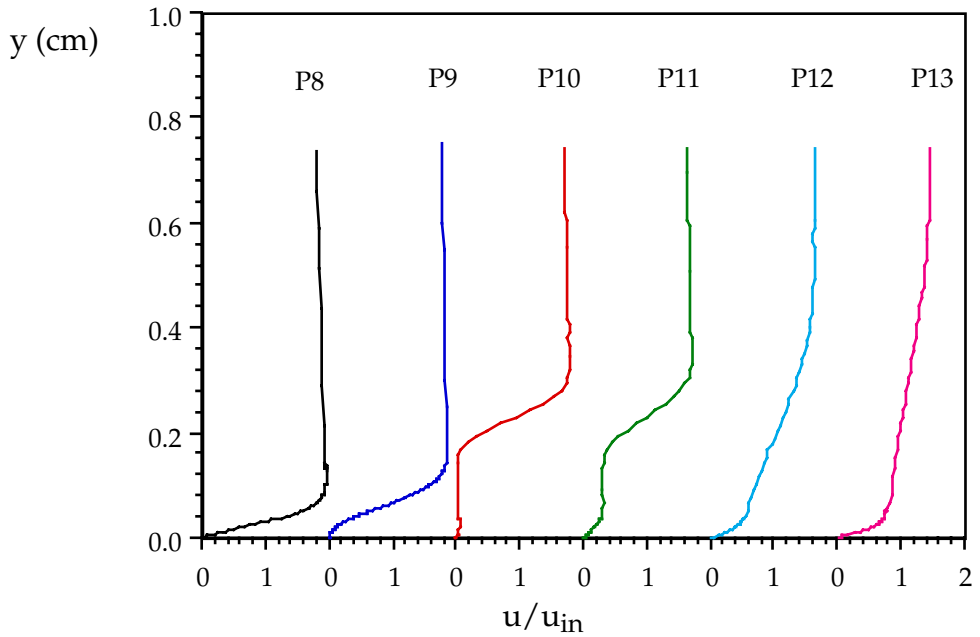

Fig. 4.58 Velocity profiles at p8 - p13, Re=200,000, FSTI=0.5%
Caution: measured values are artificially high at y=0.05 - 0.2 cm for p10, y=0 - 0.2 cm for p11, y=0 - 0.18 for p12, y=0.006 - 0.023 cm for p13

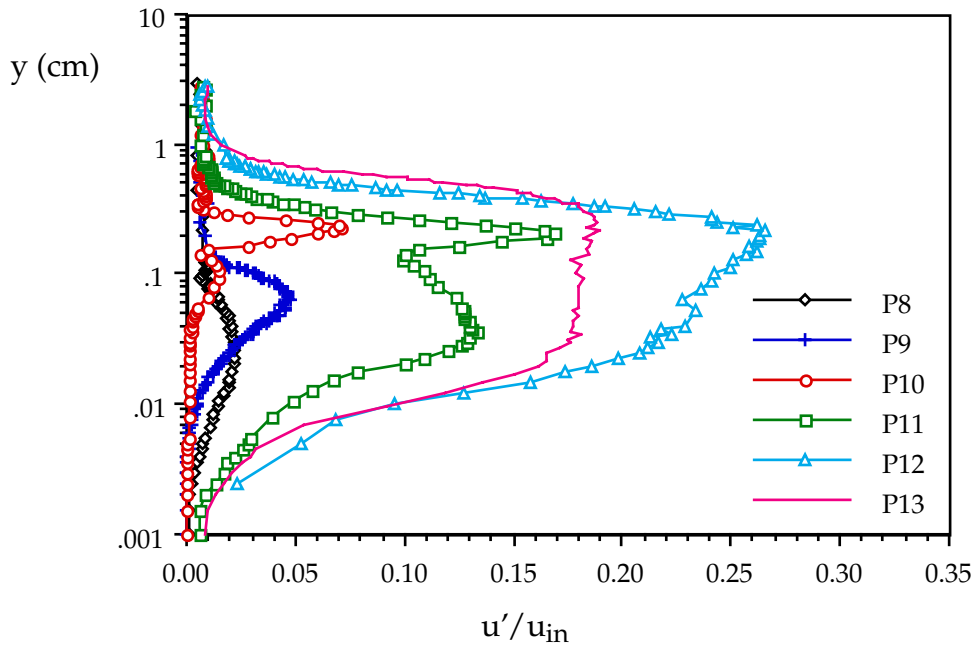

Fig. 4.59 Velocity fluctuations at p8 - p13, Re=200,000, FSTI=0.5%

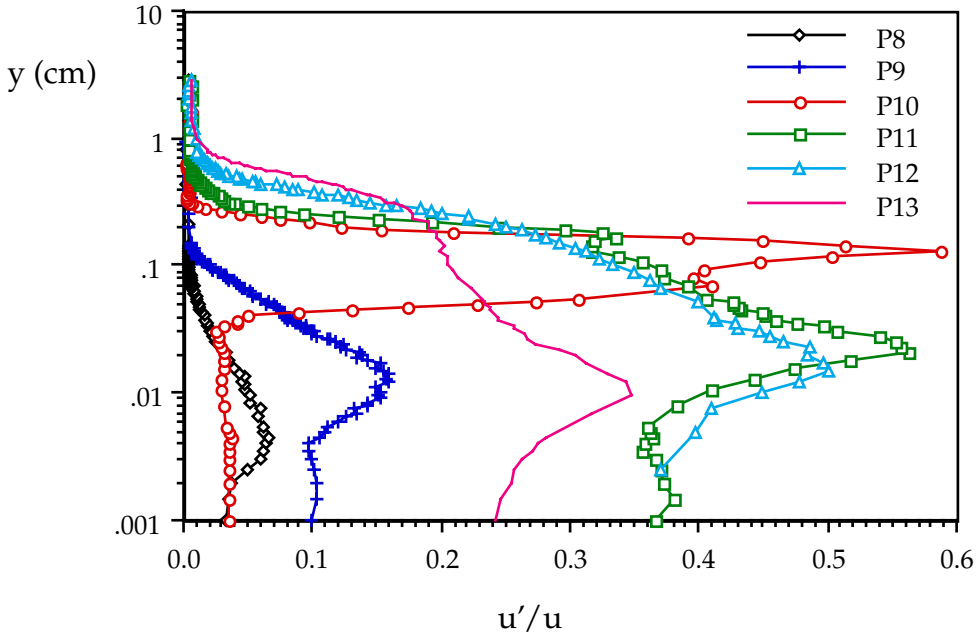

Fig. 4.60 Turbulence intensity at p8 - p13 for Re=200,000, FSTI=0.5%

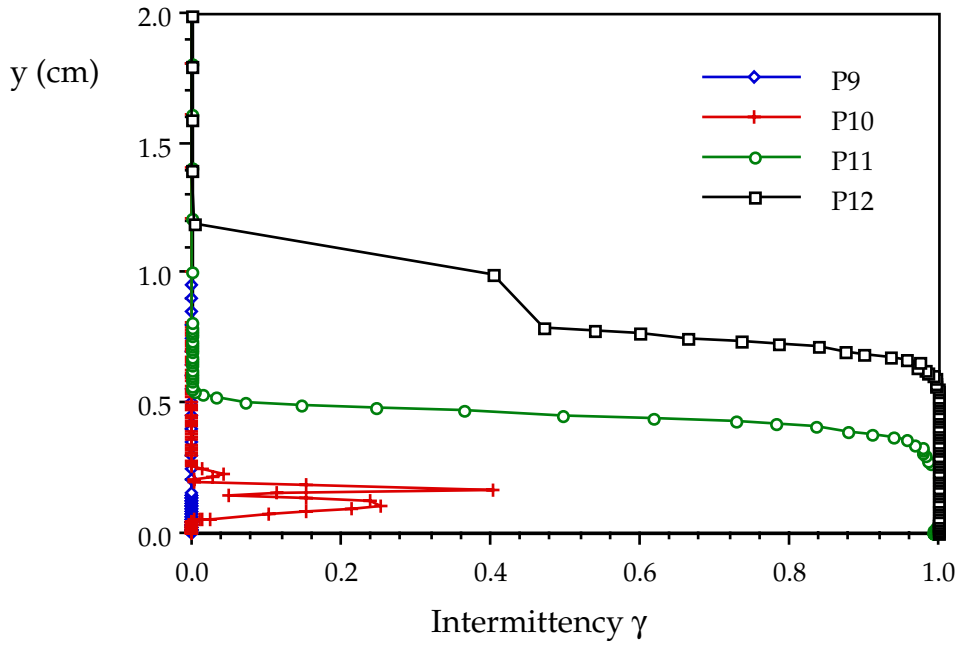

Fig. 4.61 Intermittency distributions at p9 - p12, Re=200,000, FSTI=0.5%

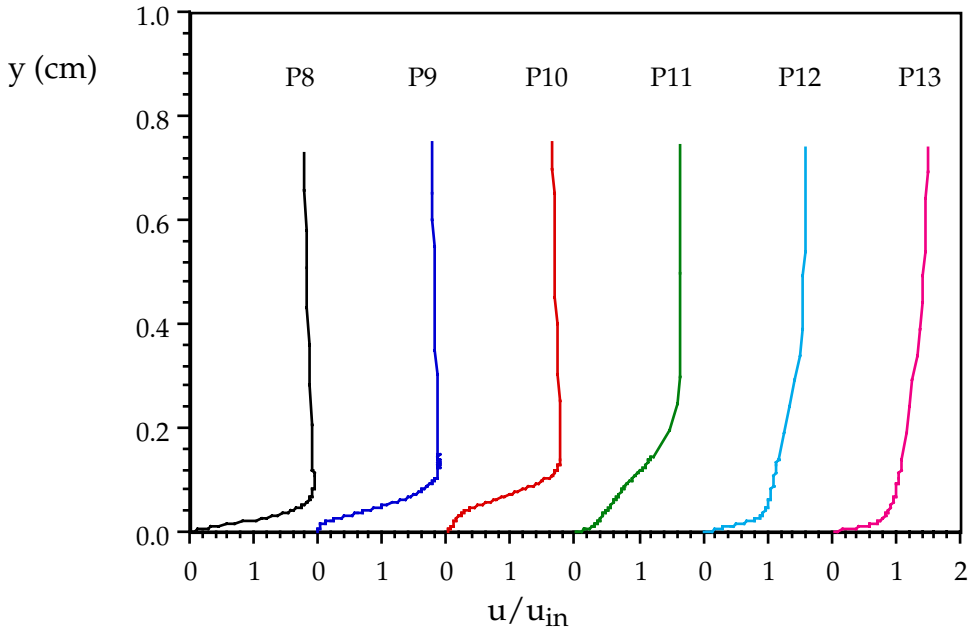

Fig. 4.62 Velocity profiles at p8 - p13, Re=300,000, FSTI=0.5%
Caution: measured values are artificially high at y=0 - 0.03 cm for p10, y=0 - 0.043 for p11

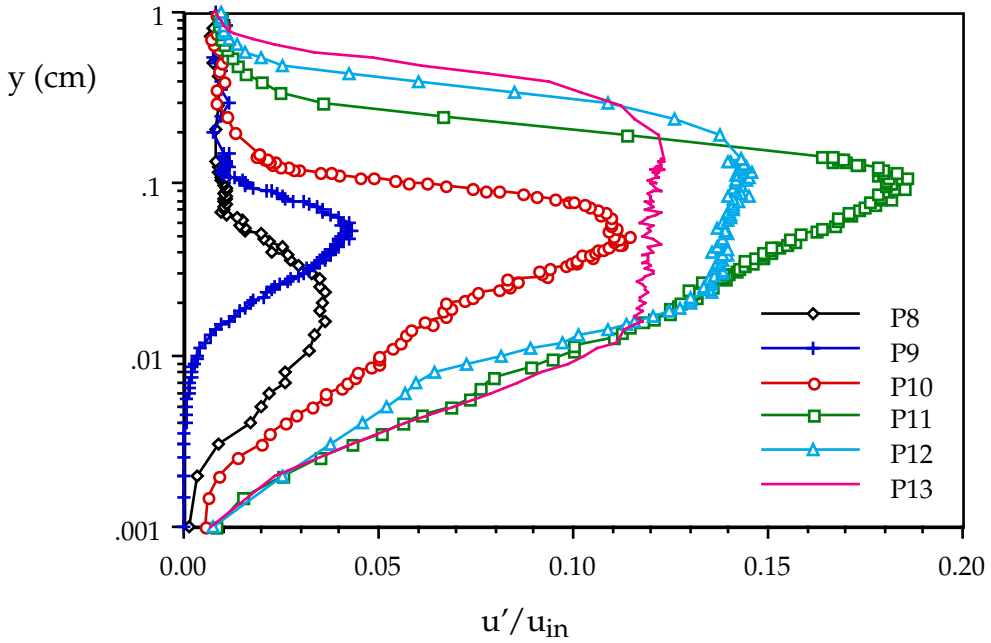

Fig. 4.63 Velocity fluctuations at p8 - p13, Re=300,000, FSTI=0.5%

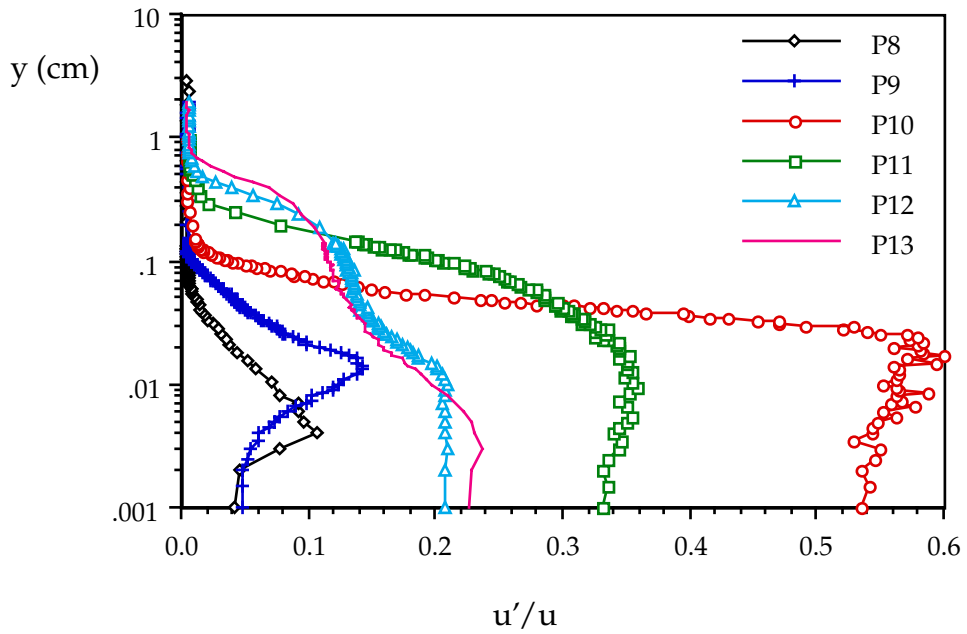

Fig. 4.64 Turbulence intensity at p8 - p13 for Re=300,000, FSTI=0.5%

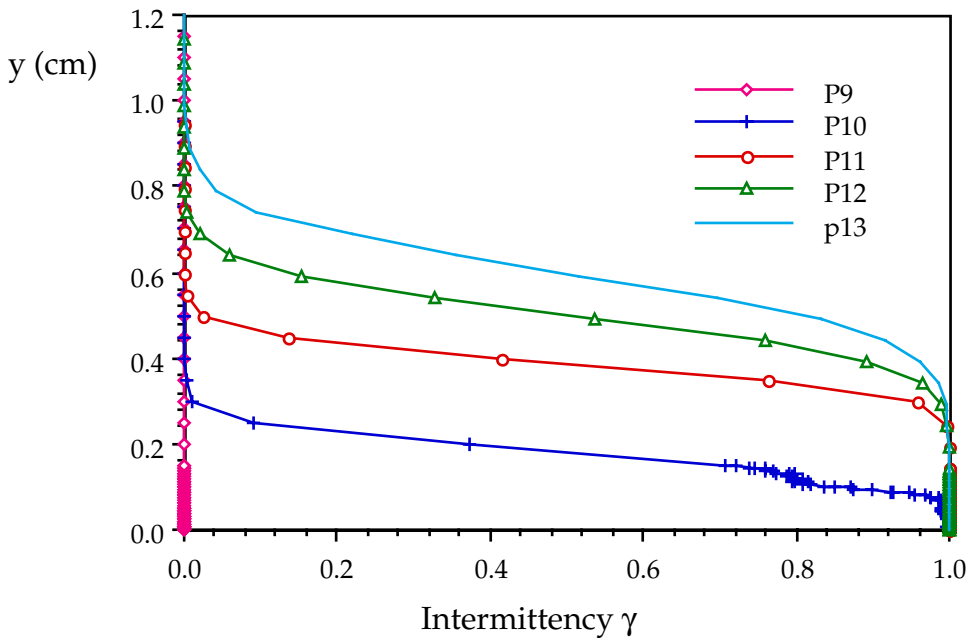

Fig. 4.65 Intermittency distributions at p8 - p13, Re=300,000, FSTI=0.5%

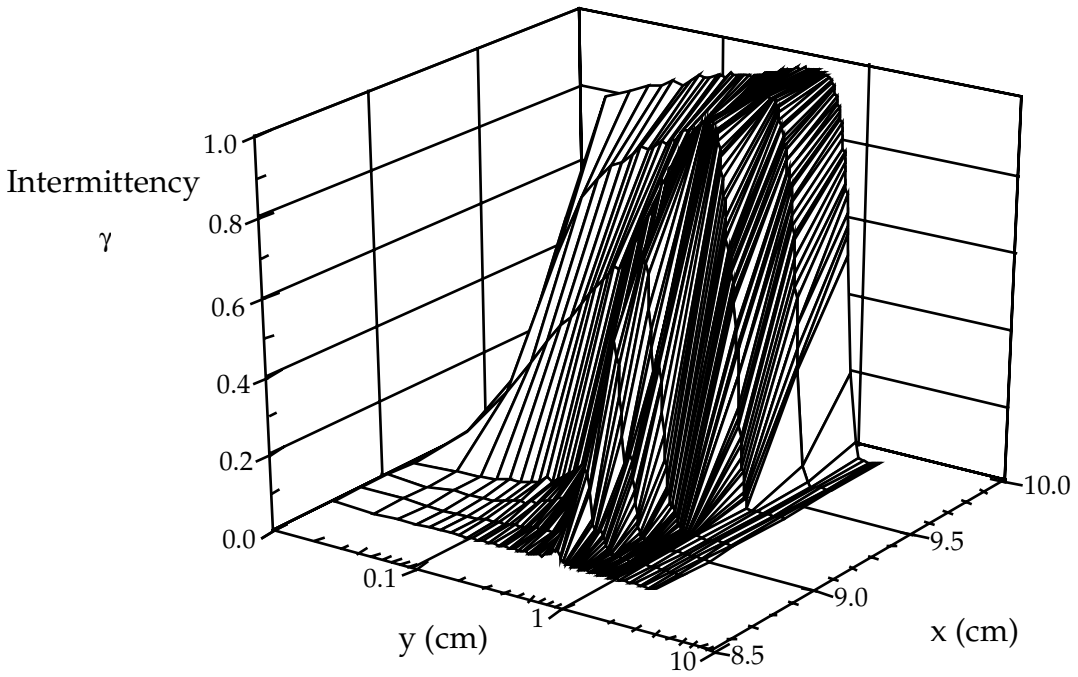

Fig. 4.66 Intermittency distributions for Re=100,000, FSTI=0.5%, constructed from profiles at p10a, p11a, p11b, p11c, p12a, p12b, and p12c

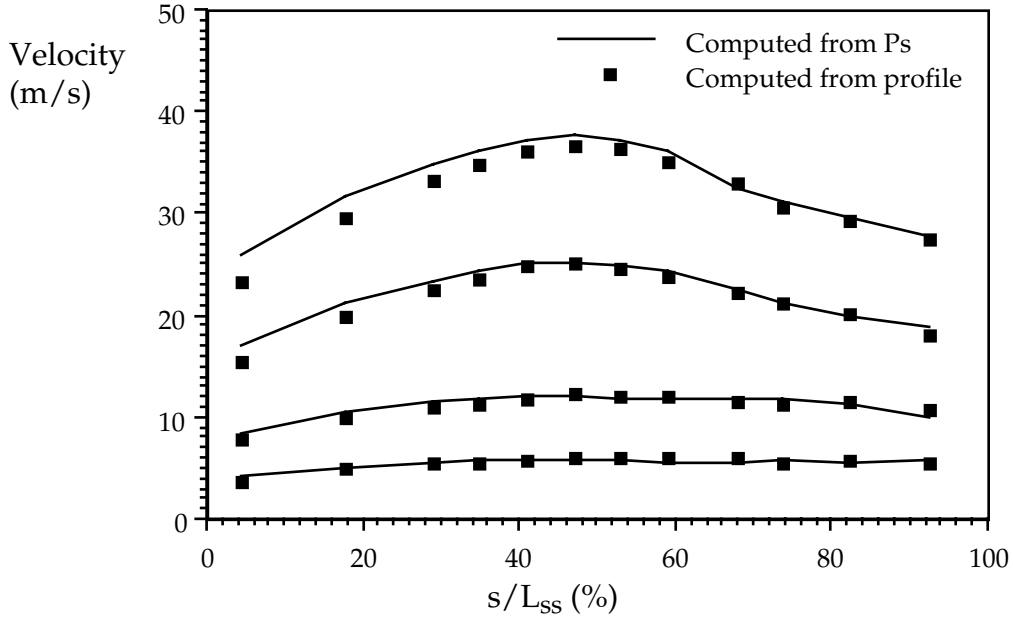

Fig. 4.67 Comparison of measured free-stream velocity to computed velocity from static pressure distributions for FSTI=0.5%; progressively higher velocities are for Reynolds numbers of 50,000, 100,000, 200,000 and 300,000.

MODERATE TURBULENCE FLOW, FSTI=2.5%

Pressure profiles, Fig. 4.17, show that under 2.5% FSTI, the flows start with laminar boundary layer development through most of the accelerating section, as in the 0.5% FSTI cases. Near the throat, low Reynolds number cases continue laminar boundary layer development until they reach a critical point where they start laminar separation, as with the low (0.5%) FSTI cases discussed above. At the highest Reynolds number, flow starts transition before flow separation begins. From stations p2 to p7, Figs 4.68 to 4.75 (velocity profiles and rms fluctuations) show attached, laminar boundary flows. Figures 4.76 and 4.77 show the Reynolds number effects on the boundary layer growth. As in the 0.5% FSTI cases, all turbulence intensities are less than 12% at p7; therefore, measured velocities are reliable from p2 to p7. Figure 4.78 shows velocity profiles measured at station p8 (x/Lx=68.89%) for four Reynolds number cases of Re=50,000, 100,000, 200,000 and 300,000 with 2.5% FSTI. No separation could be identified from these four profiles at this station. Wall shear stress visualization showed that the Re=50,000 case has just started flow separation at P8, but the separation bubble is too small to tell from Fig. 4.78. The 2.5% case starts separation later than did the 0.5% FSTI case. This is expected, for the elevated free-stream turbulence enhances cross stream momentum transport and retards flow separation. Local turbulence intensities for all four cases are shown in Fig. 4.79. Low TI's in the boundary layers ensure the reliability of the measured data. Rms velocity fluctuations are plotted in Fig. 4.80. Intermittency profiles of all four Re cases are plotted in Fig. 4.81. Intermittency profiles for two low-Reynolds-number cases (Re=50,000 and 100,000) are zero throughout the laminar

boundary layers. It can be noted that the highest Re (Re=300,000) flow case starts transition from laminar to turbulent flow just before this station (p8). Apparently, this earlier transition than in the 0.5% FSTI case is induced by the elevated free-stream turbulence. According to Narisimha (1985), attached boundary layer transition with 1% < FSTI < 4% may exhibit some elements of both Tollmien-Schlichting and bypass transition modes.

As in the 0.5% FSTI case, all four Reynolds number (Re=50,000, 100,000, 200,000 and 300,000) flows are separated at station p9 (x/Lx=74.57%) under 2.5% FSTI, see Fig. 4.82 (also supported by the surface shear visualization). The Re=50,000 flow appears to have a separation bubble size of about 0.2 mm and the separation zone of the Re=100,000 flow appears to span about 0.05 mm in the wall-normal direction. The Re=200,000 and 300,000 cases have much smaller separation bubbles at this station. High turbulence intensities, shown in Fig. 4.83 for all four cases, indicate that portions of the boundary layers have artificially high velocities very near the wall. The true separation zones for the 50,000 and 100,000 Reynolds number cases would be thicker for these profiles, had this error not been present. The normalized rms velocity fluctuation profiles are plotted in Fig. 4.84. The peaks in the profiles shift toward the wall from y=1.3 mm (y/δ_2=4.09) at Re=50,000 to y=0.4 mm (y/δ_2=3.45) at Re=300,000 because the boundary layer thicknesses decrease with increases of Reynolds number. The levels of the peaks increase from 10.5% at Re=50,000 to about 15.6% at Re=300,000. The flows of Re=200,000 and 300,000 cases have higher fluctuating levels than do the two low-Re flows. This situation is typical of transitional flows (Fig. 4.84). At station p9 (Fig. 4.85), the flow of the Re=300,000 case is still going

through transition and the flow of the Re=200,000 case has just begun to transition.

At station p10 (x/Lx=81.73%), the separation bubble for the flow of Re=200,000 has grown rapidly to 0.6 mm (Fig. 4.86), though the flow started transition at station p9. This is a result of a strong adverse pressure gradient and insufficient time for turbulent transport of momentum to overcome the separation tendency. The separation zones of the Re=50,000 and 100,000 flows have expanded to 1.4 mm and 1 mm (Fig. 4.86), respectively. These bubble sizes are much smaller than those of the flows with 0.5% FSTI at the p10 station. The growth of a separation bubble is suppressed by the higher FSTI. Due to early transition (immediately before p8), the Re=300,000 case has already reattached at station p10, see Fig. 4.86. The exceptionally high TI values for the Re=50,000 and 100,000 cases (Fig. 4.87) are due to near-zero velocities of the fluid in the separation zone. High TI's for all four flows imply that measured velocities in the marked regions are artificially high and must be used with caution. The errors for these two cases would be artificially high velocities for $y < 2$ mm. The u'/u_{in} profiles are shown in Fig. 4.88. The peaks of the profiles appear at y=3 mm for the case of Re=50,000 and at y=0.6 mm for the Re=300,000 case. The Re=200,000 case has the highest fluctuating levels, since this flow is transitional while the Re=300,000 flow has finished its transition process. The difference between the turbulent boundary layer flows and transitional or laminar boundary layer flows can be noted in Fig. 4.88, where the u'/u_{in} profiles for the transitional flows have sharp peaks away from the wall while the u'/u_{in} profiles of the turbulent flows are more rounded and nearer to the wall. Figure 4.89 shows measured intermittency profiles. At station p10, transition of the

Re=200,000 case is near its end and two the high-Re flows are turbulent throughout the boundary layers. The flow for the case of Re=100,000 starts transition just before station p10, shown in Fig. 4.89.

The velocity profiles measured at station p11 are plotted in Fig. 4.90. Here, the separation zone of the Re=50,000 case continues its growth to 2 mm while the Re=100,000 case flow is almost reattached to the wall. The Re=200,000 case has just reattached to the wall and its velocity profile is immature and different from that of a fully-developed turbulent boundary layer flow. Again, these wall layer sizes are smaller than those of the lower-FSTI cases. The Re=200,000 flow has completely reattached to the wall due to flow transition. The shape of Re=200,000 case is more mature than that of Re=100,000 case. The measured velocity data of the Re=300,000 case are reliable, as the TI for this flow is less than 20% (Fig. 4.91). The high TI yields artificially high velocities for $y < 3.5$ mm for the Re = 50,000 case and for $y < 2.5$ mm for the Re = 100,000 case. The rms velocity fluctuations are plotted versus y in Fig. 4.92. Again, the peaks of the fluctuating profiles shift toward the wall as the Reynolds number increases. The transitional flow of the Re=100,000 case at station p11 has the highest peak of all four profiles. The sharp peak of the u'/u_{in} profile of the Re=200,000 case is now rounded as the flow is finishing transition. The u'/u_{in} profile of the Re=300,000 case has further flattened. The initiation of transition from laminar to turbulent flow at station p11 for the lowest Reynolds number case is evidenced by the small hump in the intermittency profiles in Fig. 4.93. Note a small hump in the Re=50,000 curve.

The separation bubble for the Re=50,000 case starts shrinking at station p12 (x/Lx=91.11%) due to flow transition, see Fig. 4.94. Figure 4.94 shows also

that the Re=100,000 case is completely reattached to the wall at p12. The two low-Re flows of Re=50,000 and 100,000 still have high TI values, as demonstrated in Fig. 4.95, which gives high uncertainties in measured mean velocities. The two high-Re flows have more moderate turbulence intensities. The u'/u_{in} profiles are plotted in Fig. 4.96. Figure 4.97 depicts the intermittency profiles at station p12. The lowest Reynolds number case is in the middle of transition and the other three flows are turbulent, attached boundary layers. At 0.5% FSTI, transition starts in the shear layer and then quickly proceeds while it spreads toward the wall. Under this low FSTI, the shear layer flows are almost fully turbulent while the flows in the near-wall (separated) regions are still laminar. By contrast, for 2.5% FSTI, transition starts in the shear layer but penetrates throughout the entire separation region quickly so that transition appears to proceed at about the same pace throughout the wall layer.

At station p13 (x/Lx=97.28%), the flows for the Re=100,000, and higher, cases are reattached to the wall (Fig. 4.98). Turbulence intensities and fluctuation profiles at station p13 are shown in Figs. 4.99 and 4.100, respectively. Since the Re=50,000 and 100,000 cases are newly reattached, high TI's are expected for these immature flows, as shown in Fig. 4.99. Again, these two cases suffer from error due to rectification near the wall (as noted in the title). The intermittency profiles in Fig. 4.101 show that the Re=50,000 case is a transitional flow. As expected, this flow has the highest peak in u'/u_{in} of the four profiles in Fig. 4.100.

From the above discussion, it can be concluded that at 2.5% FSTI, the case of Re=300,000 starts transition from laminar to turbulent flow immediately before station p8, then separates after p8. The behaviors of the cases with Re=50,000, 100,000 and 200,000 are similar to those in the low-FSTI (0.5%) cases

where the flows start with laminar separation, followed by shear flow transition and reattachment. Velocity, rms velocity fluctuation level, and turbulence intensity profiles, as well as intermittency distributions, are plotted for all four Reynolds number cases at axial locations p8 to p13 (Figs. 4.102 to 4.117). Transition of the Re=100,000 case was studied in more detail, with intermittency measurements shown in Fig. 4.118.

The values of boundary layer thickness, $\delta_{99.5}$, momentum thickness, δ_2, displacement thickness, δ^*, local free stream velocity, u_8, and momentum thickness Reynolds number, $Re_{\delta 2}$, for the four cases of different Reynolds number were computed from the measured velocity profiles presented above and are shown in Tables 4.12 to 4.15. The computed free-stream velocities are compared to the values computed from static pressure measurements and are plotted in Fig. 4.119.

TABLE 4.12. Streamwise variation of $\delta_{99.5}$, δ_2, δ^*, u_8, $Re_{\delta 2}$, and Re_{δ^*} for the Re=50,000, FSTI=2.5% case

x	$\delta_{99.5}$ (mm)	δ^* (mm)	δ_2 (mm)	u_8 (m/s)	$Re_{\delta 2}$
p2	0.637	0.159	0.073	3.960	17.925
p3	1.148	0.323	0.139	5.093	44.347
p4	1.282	0.36	0.161	5.507	53.806
p5	1.289	0.381	0.169	5.592	57.094
p6	1.465	0.403	0.183	5.947	68.918
p7	1.501	0.450	0.190	6.199	71.676
p8	2.055	0.581	0.216	5.782	78.297
p9	3.305	1.153	0.319	5.163	102.948
p10	4.830	2.860	0.443	5.279	146.290
p11	5.805	3.314	0.439	5.665	155.438
p12	7.220	3.295	0.970	5.454	332.582
p13	10.027	8.221	1.378	4.789	430.19

TABLE 4.13. Streamwise variation of $\delta_{99.5}$, δ_2, δ^*, u_8, $Re_{\delta 2}$, and Re_{δ^*} for the Re=100,000, FSTI=2.5% case

x	$\delta_{99.5}$ (mm)	δ^* (mm)	δ_2 (mm)	u_8 (m/s)	$Re_{\delta 2}$
p2	0.526	0.133	0.056	7.823	27.073
p3	0.810	0.228	0.099	10.618	62.972
p4	0.906	0.261	0.111	11.430	77.653
p5	1.132	0.305	0.131	11.657	91.332
p6	1.078	0.313	0.131	11.944	96.452
p7	1.104	0.323	0.132	12.407	100.05
p8	1.237	0.327	0.142	12.400	110.088
p9	2.055	0.630	0.210	11.548	152.000
p10	3.371	1.976	0.315	11.161	219.897
p11	4.180	1.883	0.475	11.685	346.806
p12	5.418	1.570	0.779	10.362	504.400
p13	6.797	1.497	0.935	9.846	569.949

TABLE 4.14. Streamwise variation of $\delta_{99.5}$, δ_2, δ^*, u_8, $Re_{\delta 2}$, and Re_{δ^*} for the Re=200,000, FSTI=2.5% case

x	$\delta_{99.5}$ (mm)	δ^* (mm)	δ_2 (mm)	u_8 (m/s)	$Re_{\delta 2}$
p2	0.357	0.094	0.040	16.224	40.203
p3	0.622	0.180	0.074	20.334	92.356
p4	0.727	0.196	0.082	23.076	116.007
p5	0.765	0.231	0.096	23.684	138.839
p6	0.827	0.262	0.105	24.687	157.517
p7	0.903	0.282	0.108	24.707	163.939
p8	0.968	0.456	0.111	24.574	169.093
p9	1.332	0.532	0.141	23.328	205.890
p10	2.305	0.626	0.270	22.310	376.316
p11	3.116	0.753	0.392	21.399	523.696
p12	4.531	0.784	0.490	20.168	617.647
p13	6.110	0.911	0.635	19.234	763.843

TABLE 4.15. Streamwise variation of $\delta_{99.5}$, δ_2, δ^*, u_8, $Re_{\delta 2}$, and Re_{δ^*} for the Re=300,000, FSTI=2.5% case

x	$\delta_{99.5}$ (mm)	δ^* (mm)	δ_2 (mm)	u_8 (m/s)	$Re_{\delta 2}$
p2	0.305	0.045	0.032	22.949	40.300
p3	0.542	0.150	0.067	29.807	122.410
p4	0.635	0.180	0.073	33.891	153.170
p5	0.707	0.214	0.082	35.059	175.198
p6	0.717	0.231	0.090	36.244	206.014
p7	0.744	0.243	0.099	36.670	204.790
p8	0.785	0.322	0.087	36.536	195.826
p9	1.270	0.470	0.116	35.094	255.474
p10	1.895	0.507	0.237	33.224	492.954
p11	2.784	0.521	0.309	30.473	587.703
p12	3.833	0.532	0.373	29.708	691.834
p13	5.642	0.736	0.469	26.799	906.903

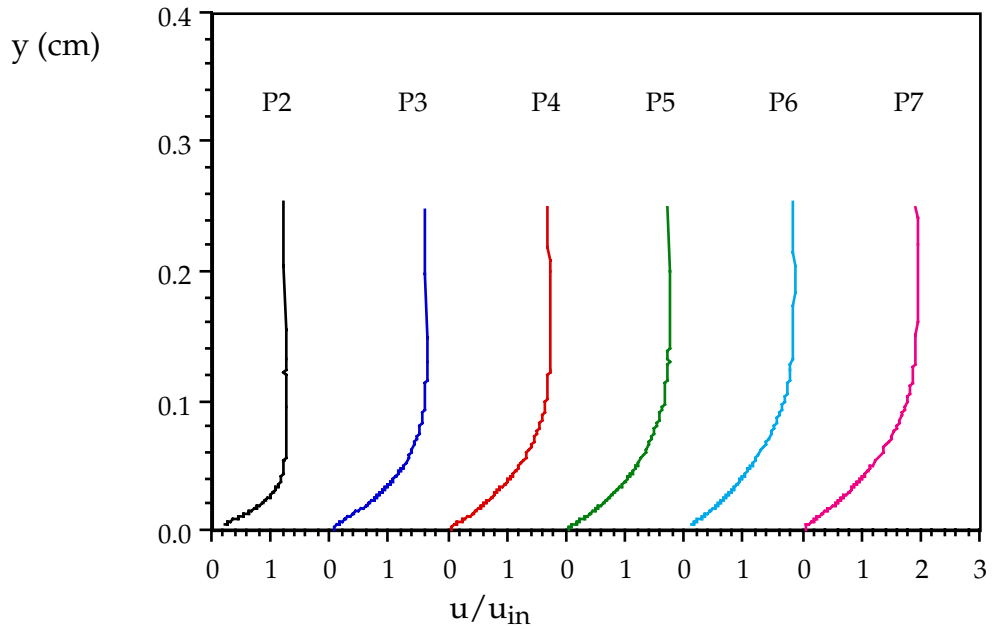

Fig. 4.68 Velocity profiles at p2 - p7, Re=50,000, FSTI=2.5%

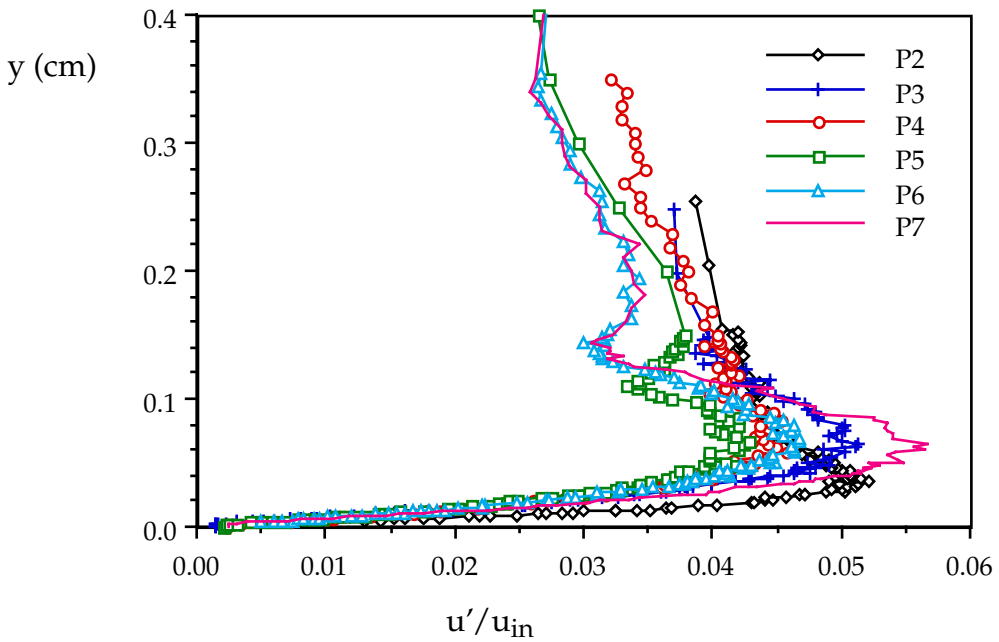

Fig. 4.69 Velocity fluctuations at p2 - p7, Re=50,000, FSTI=2.5%

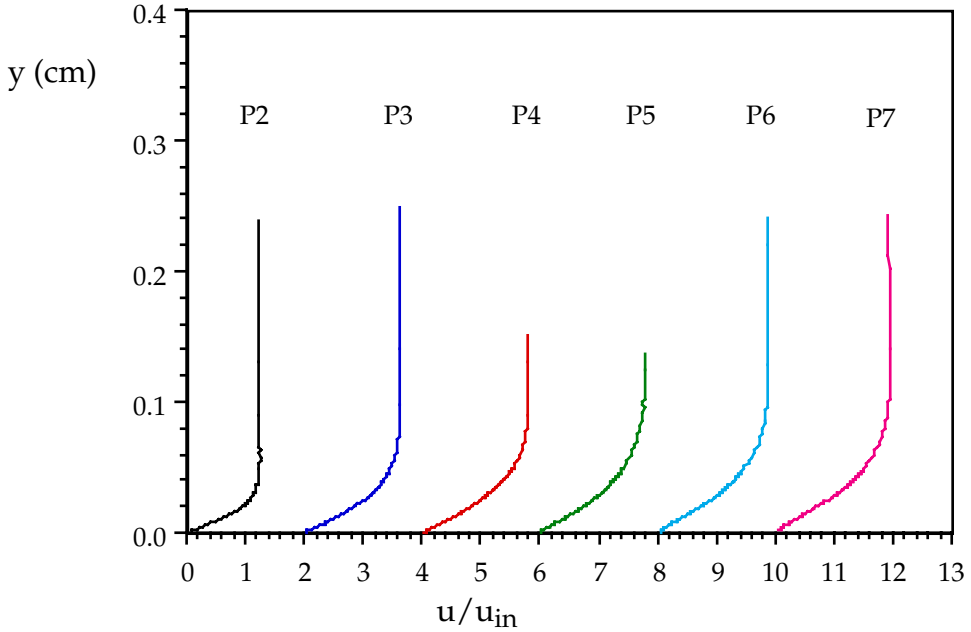

Fig. 4.70 Velocity profiles at p2 - p7, Re=100,000, FSTI=2.5%

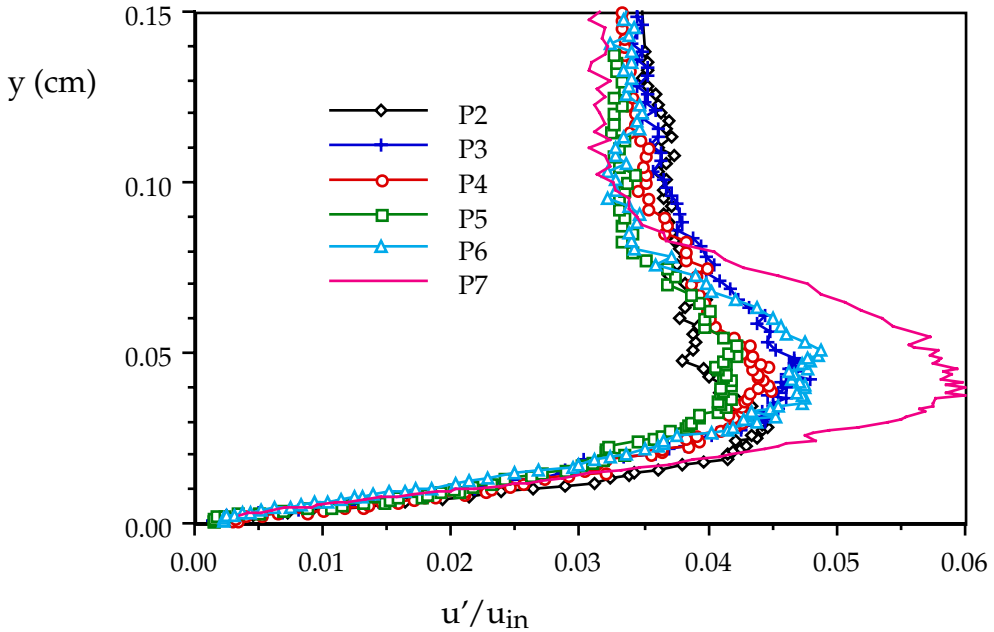

Fig. 4.71 Velocity fluctuations at p2 - p7, Re=100,000, FSTI=2.5%

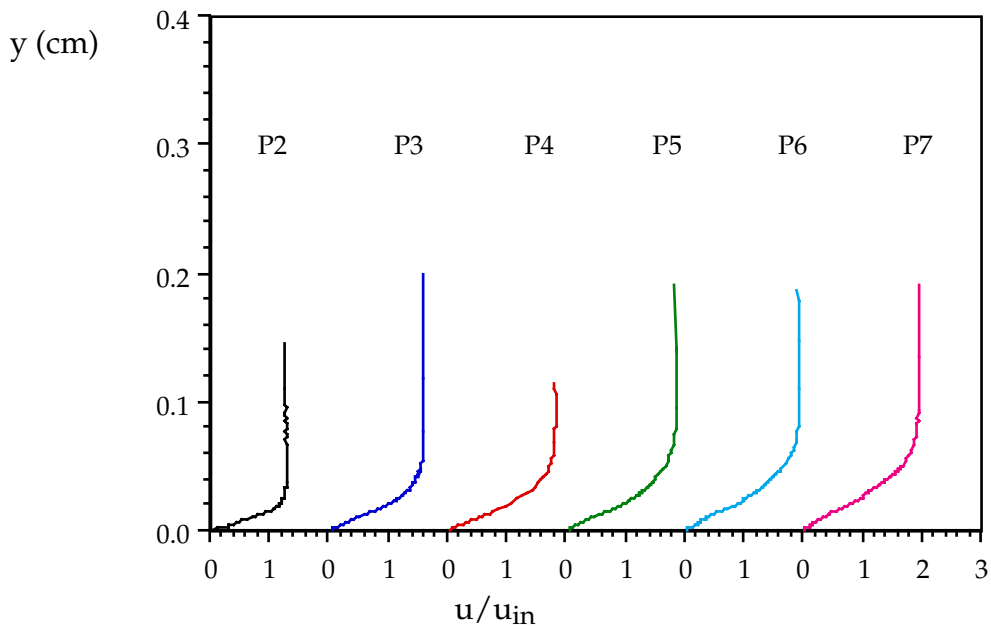

Fig. 4.72 Velocity profiles at p2 - p7, Re=200,000, FSTI=2.5%

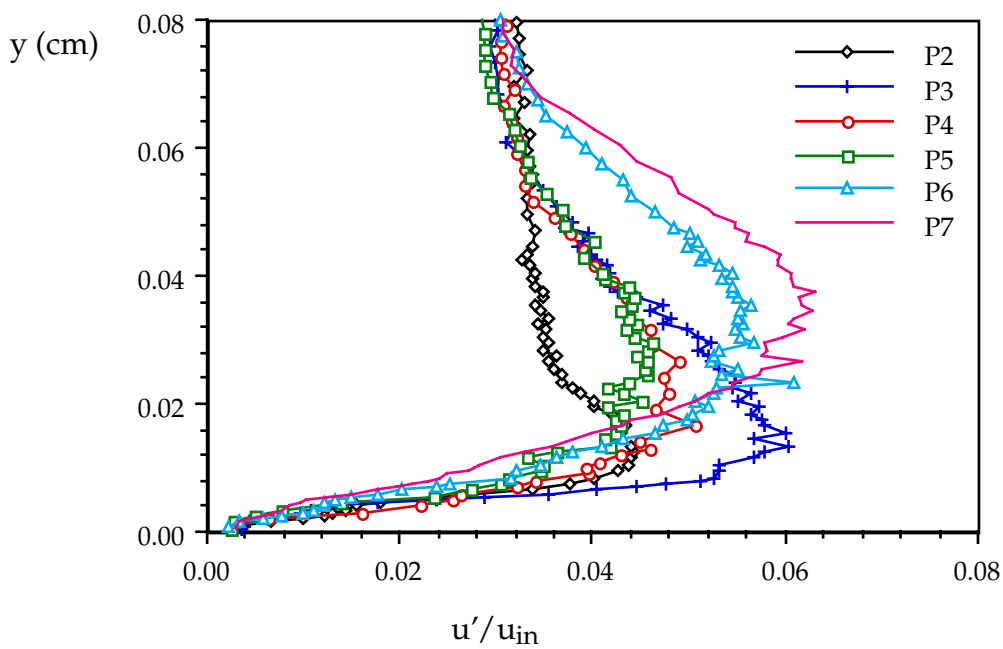

Fig. 4.73 Velocity fluctuations at p2 - p7, Re=200,000, FSTI=2.5%

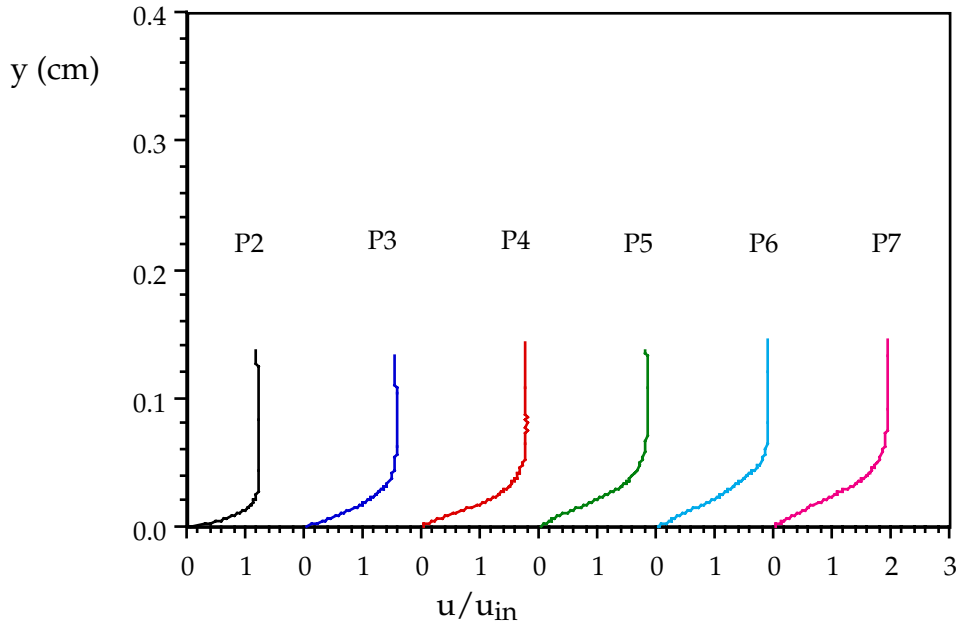

Fig. 4.74 Velocity profiles at p2 - p7, Re=300,000, FSTI=2.5%

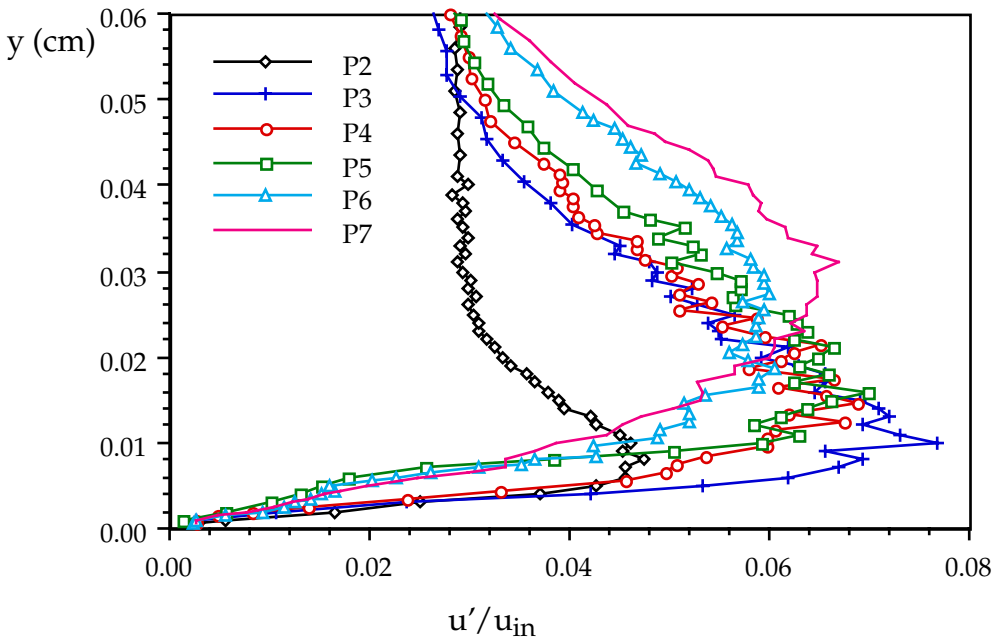

Fig. 4.75 Velocity fluctuations at p2 - p7, Re=300,000, FSTI=2.5%

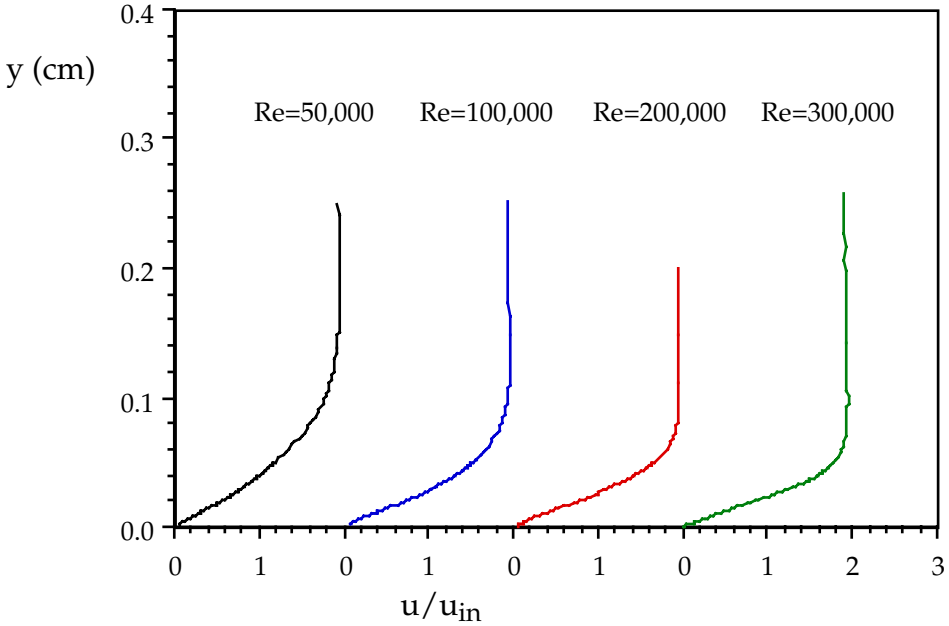

Fig. 4.76 Velocity profiles at p7 (x/Lx=62.47%) for FSTI=2.5%

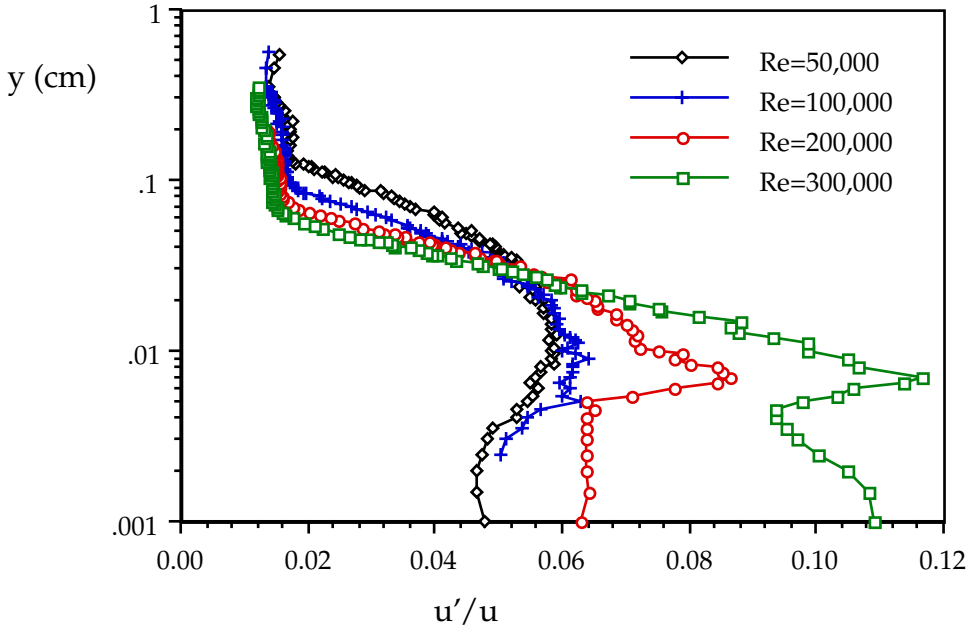

Fig. 4.77 Velocity fluctuations at p7 (x/Lx=62.47%) for FSTI=2.5%

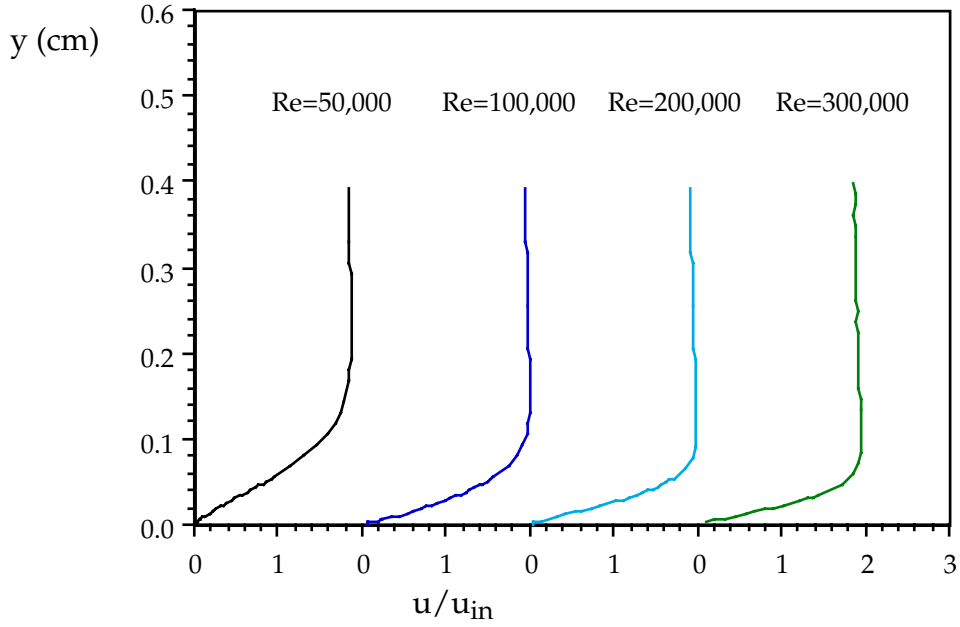

Fig. 4.78 Velocity profiles at station p8 (x/Lx=68.89%), FSTI=2.5%

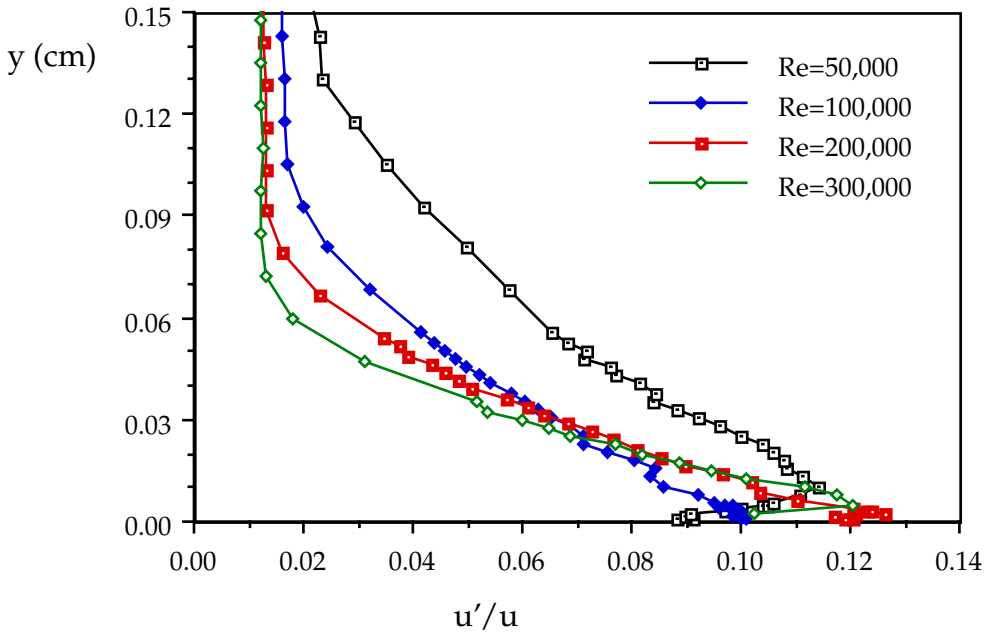

Fig. 4.79 Turbulence intensities at station p8 (x/Lx=68.89%), FSTI=2.5%

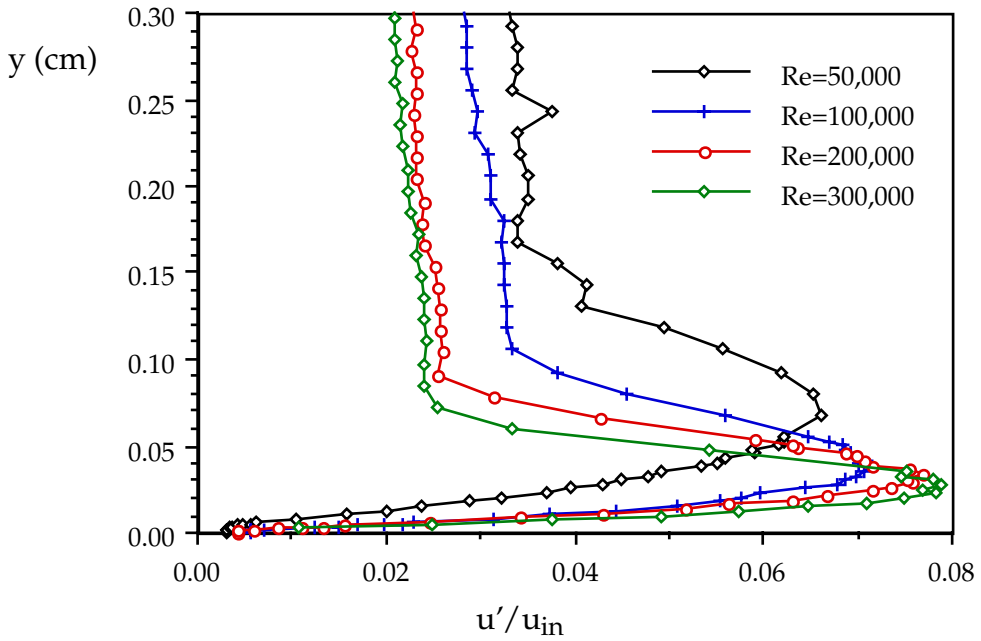

Fig. 4.80 Velocity fluctuations at p8 (x/Lx=68.89%), for FSTI=2.5%

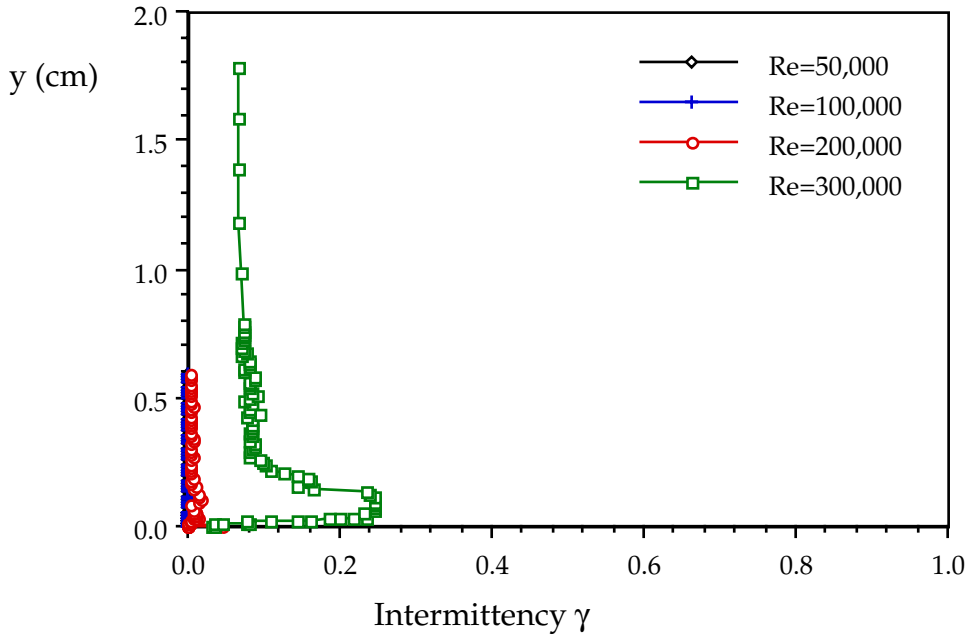

Fig. 4.81 Intermittency distributions at station p8 (x/Lx=68.89%), FSTI=2.5%

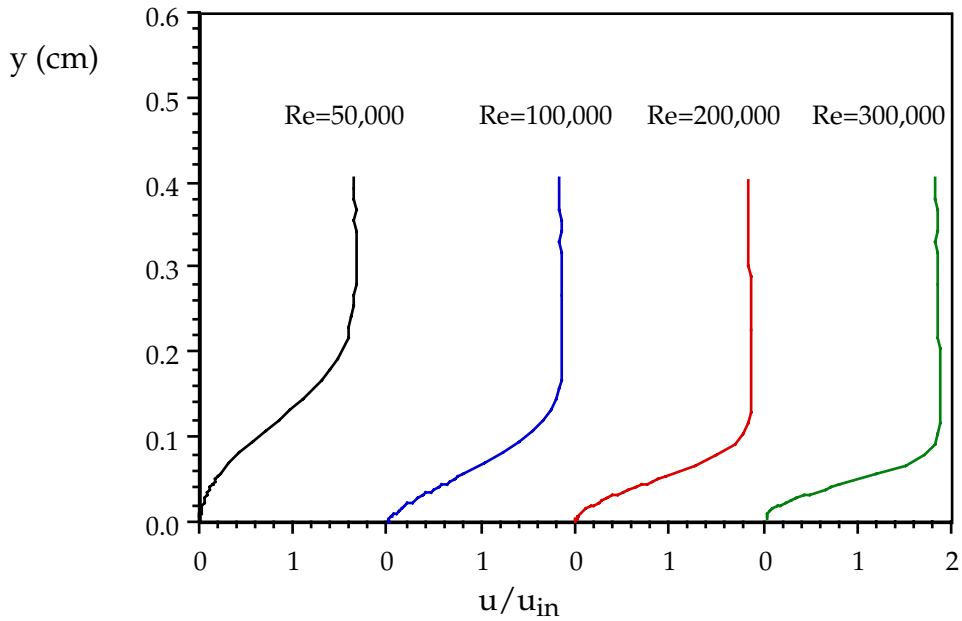

Fig. 4.82 Velocity profiles at station p9 (x/Lx=74.57%), FSTI=2.5% Caution: measured values are artificially high at y=0.03 - 0.05 cm for Re=50k, y=0 - 0.015 cm for Re=100k, y=0.005 - 0.03 cm for Re=200k, y=0.007 - 0.03 cm for Re=300k

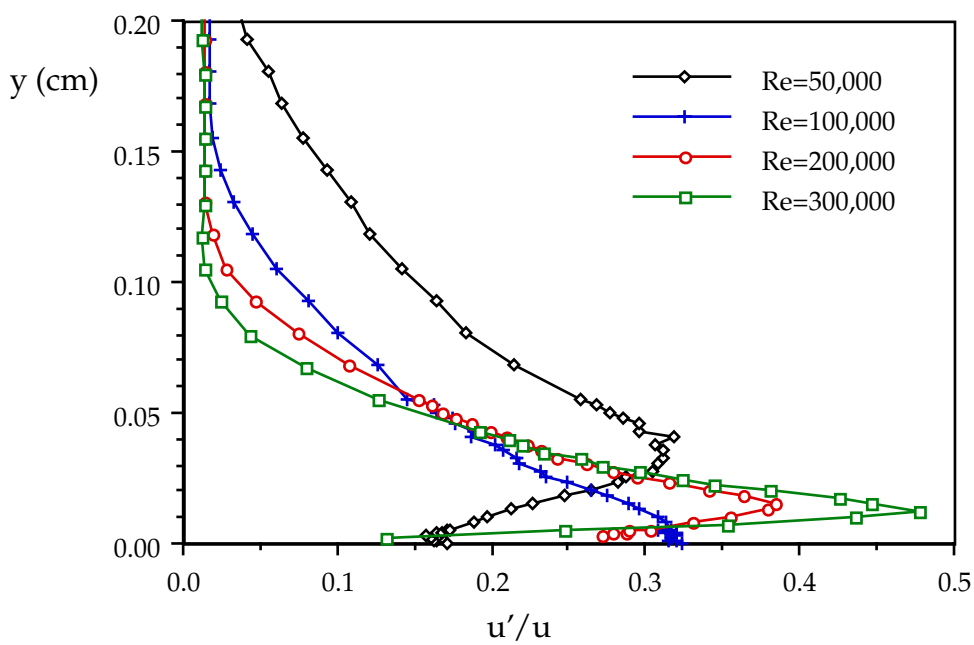

Fig. 4.83 Turbulence intensities at station p9 (x/Lx=74.57%), FSTI=2.5%

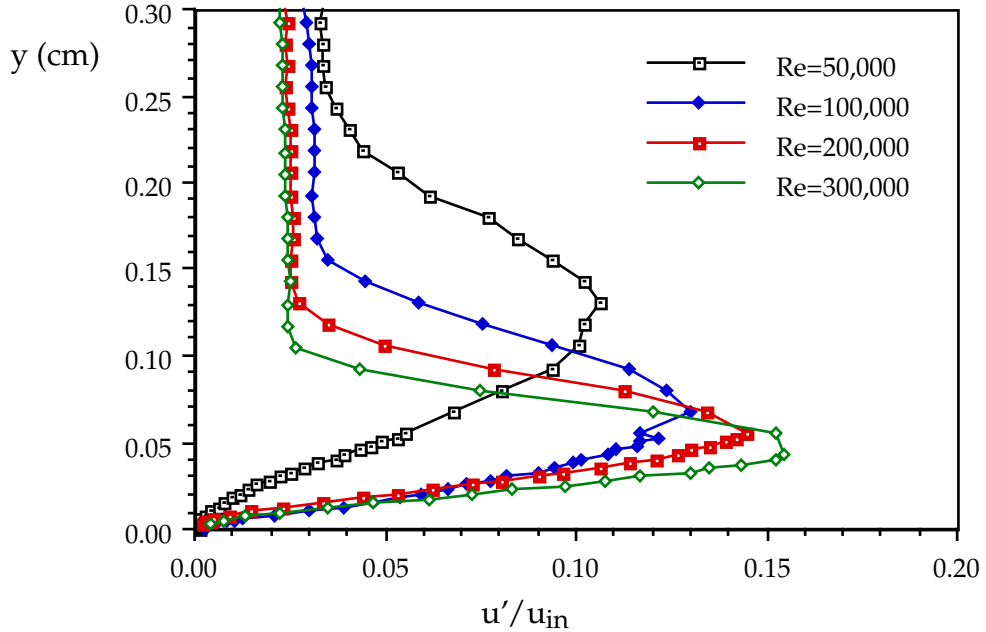

Fig. 4.84 Velocity fluctuations at station p9 (x/Lx=74.57%), FSTI=2.5%

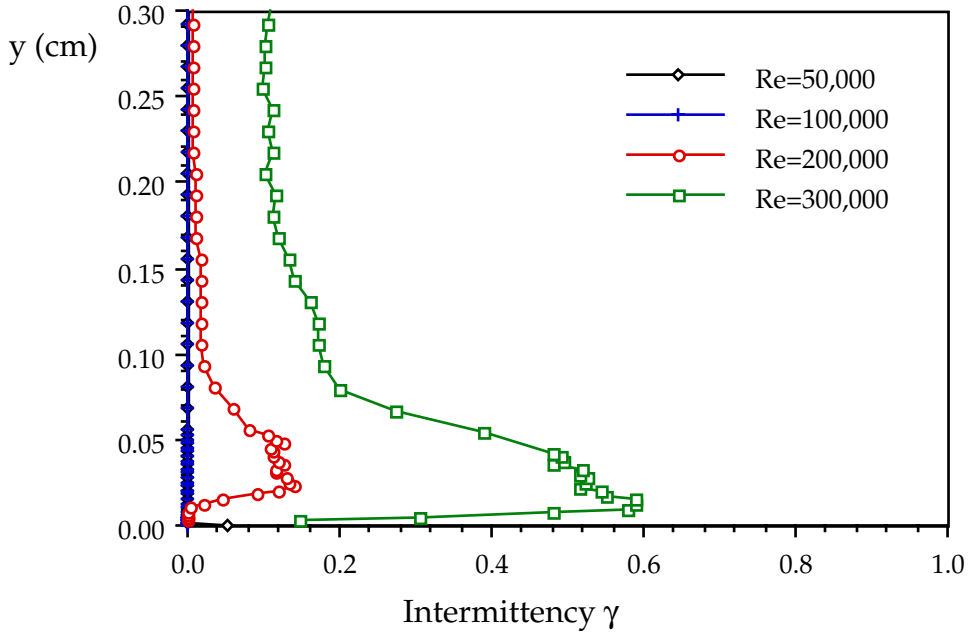

Fig. 4.85 Intermittency distributions at station p9 (x/Lx=74.57%), FSTI=2.5%

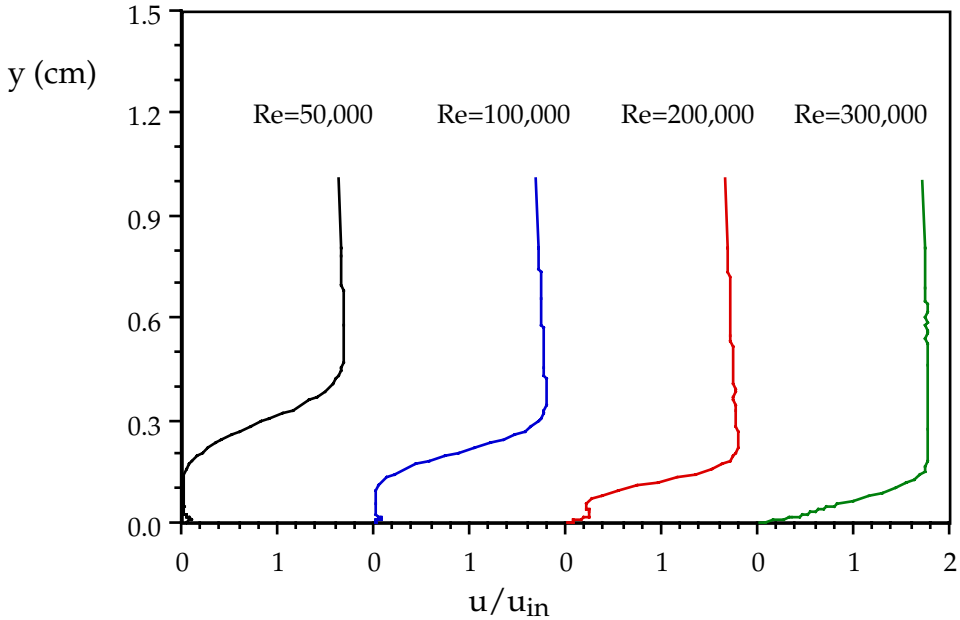

Fig. 4.86 Velocity profiles at station p10 (x/Lx=81.73%), FSTI=2.5% Caution: measured values are artificially high at y=0.06 - 0.26 cm for Re=50k, y=0.023 - 0.2 cm for Re=100k, y=0 - 0.11 for Re=200k, y=0 - 0.044 cm for Re=300k

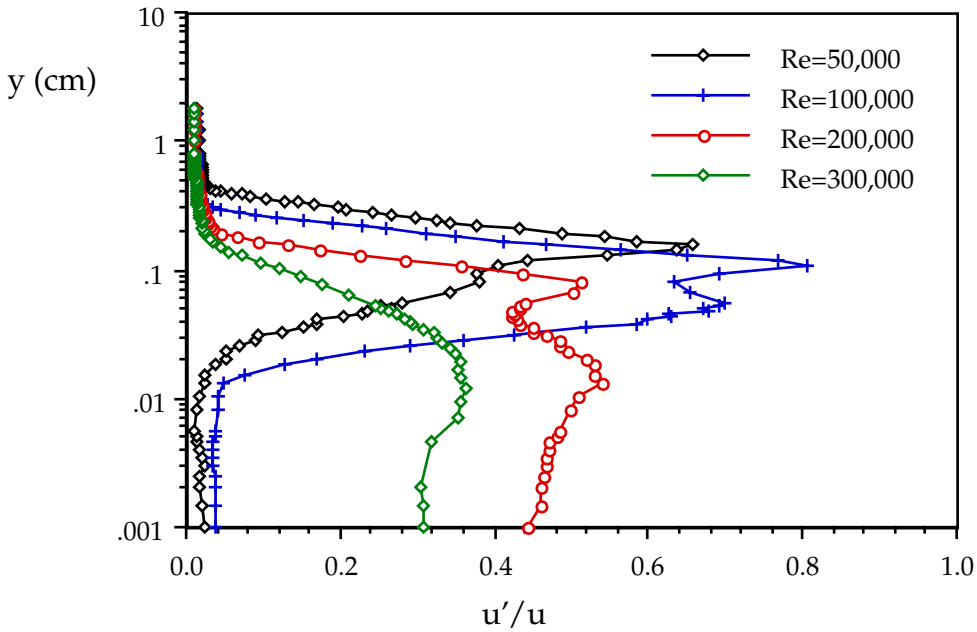

Fig. 4.87 Turbulence intensities at station p10 (x/Lx=81.73%), FSTI=2.5%

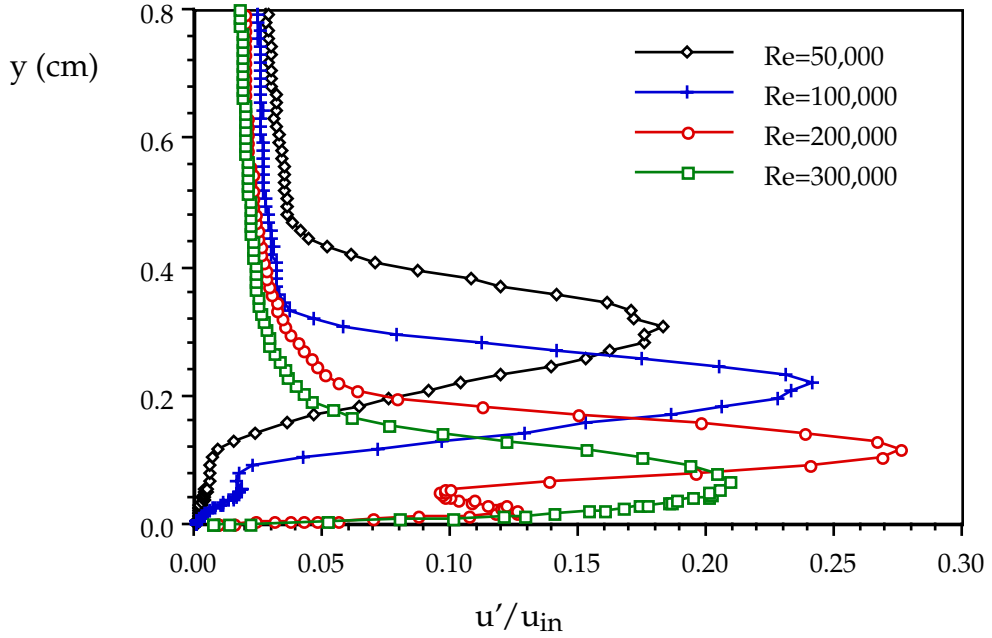

Fig. 4.88 Velocity fluctuations at station p10 (x/Lx=81.73%), FSTI=2.5%

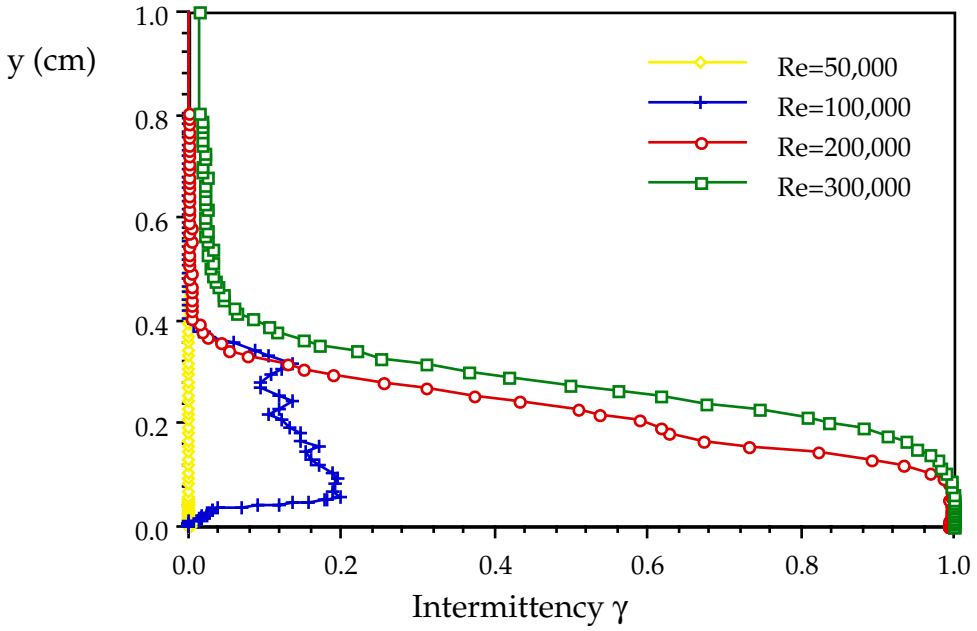

Fig. 4.89 Intermittency distributions at station p10 (x/Lx=81.73%), FSTI=2.5%

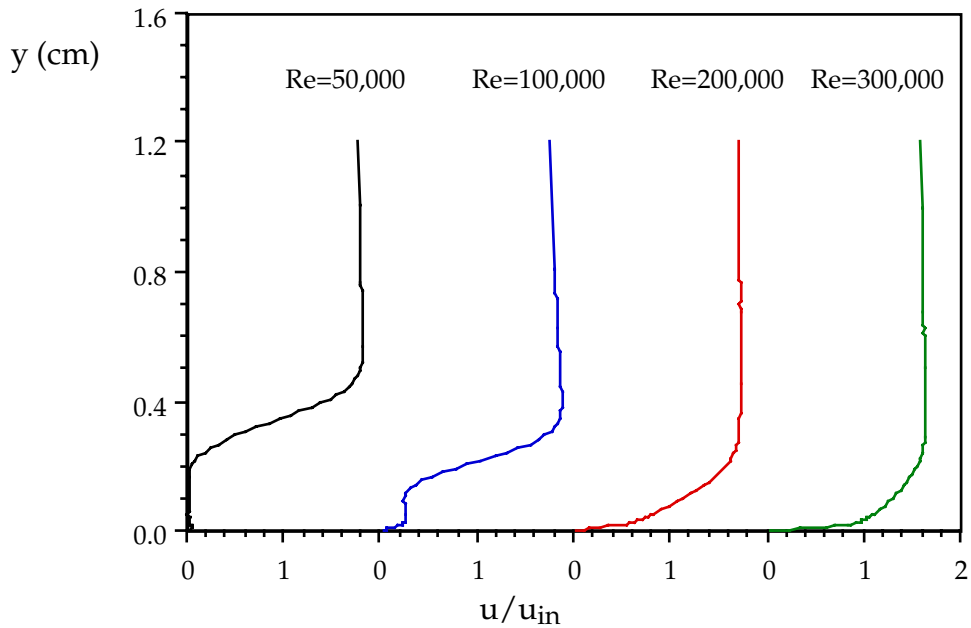

Fig. 4.90 Velocity profiles at station p11 (x/Lx=85.93%), FSTI=2.5%. Caution: measured values are artificially high at y=0 - 0.32 cm for Re=50k, y=0-0.23 cm for Re=100k, y=0 - 0.04 cm for Re=200k

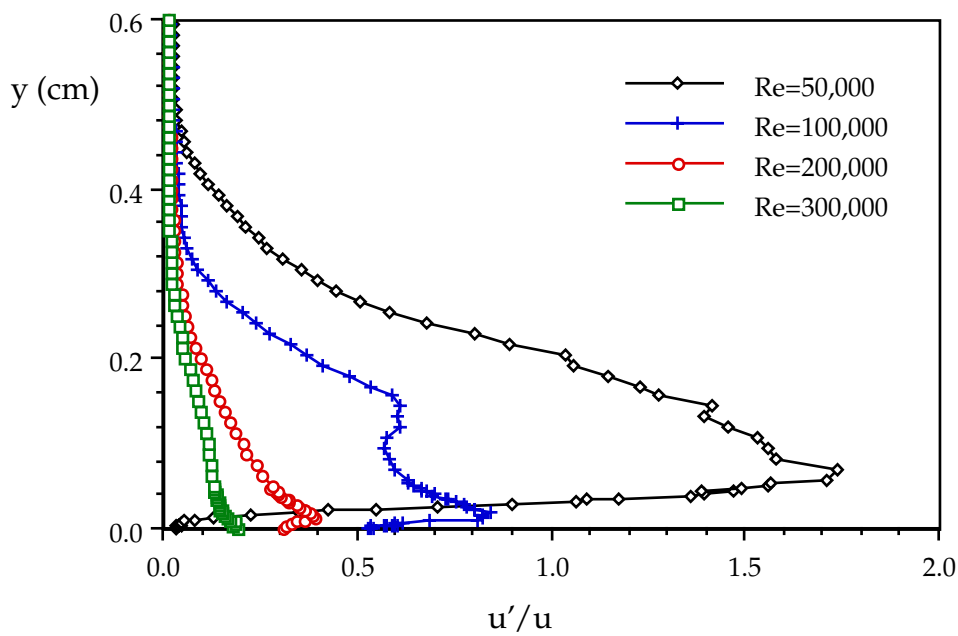

Fig. 4.91 Turbulence intensities at station p11 (x/Lx=85.93%), FSTI=2.5%

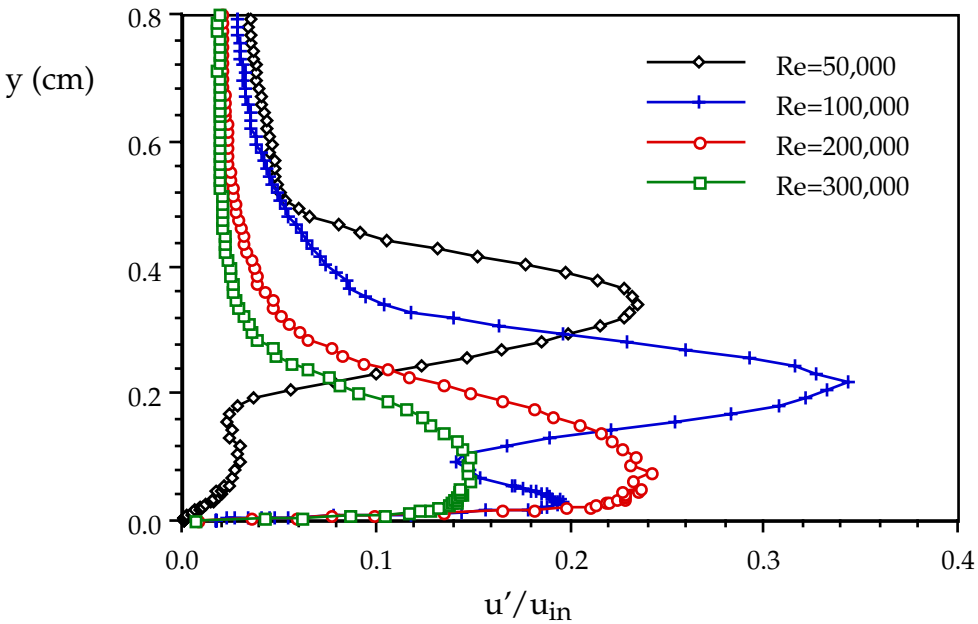

Fig. 4.92 Velocity fluctuations at station p11 (x/Lx=85.93%), FSTI=2.5%

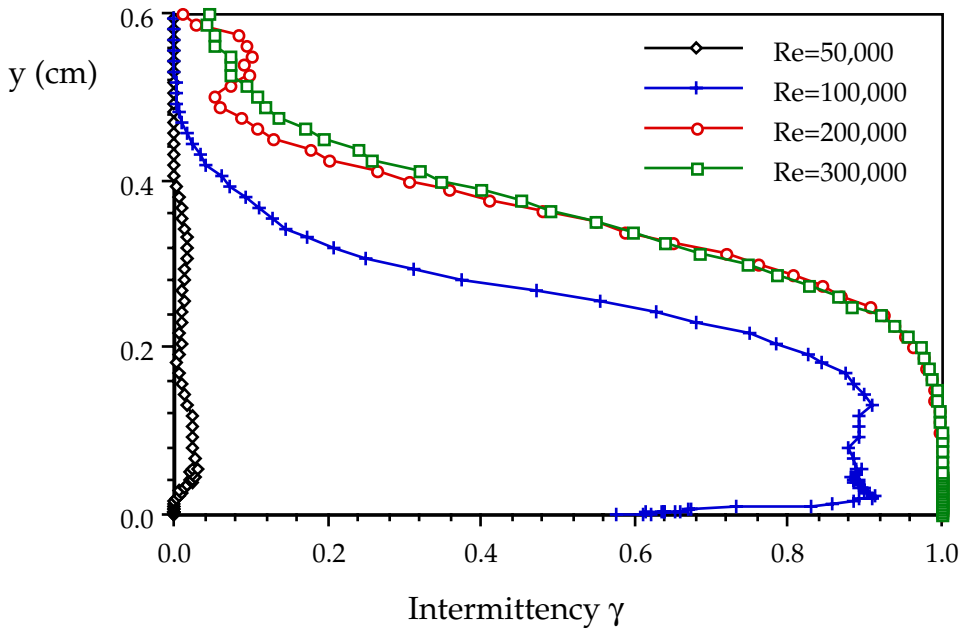

Fig. 4.93 Intermittency distributions at station p11 (x/Lx=85.93%), FSTI=2.5%

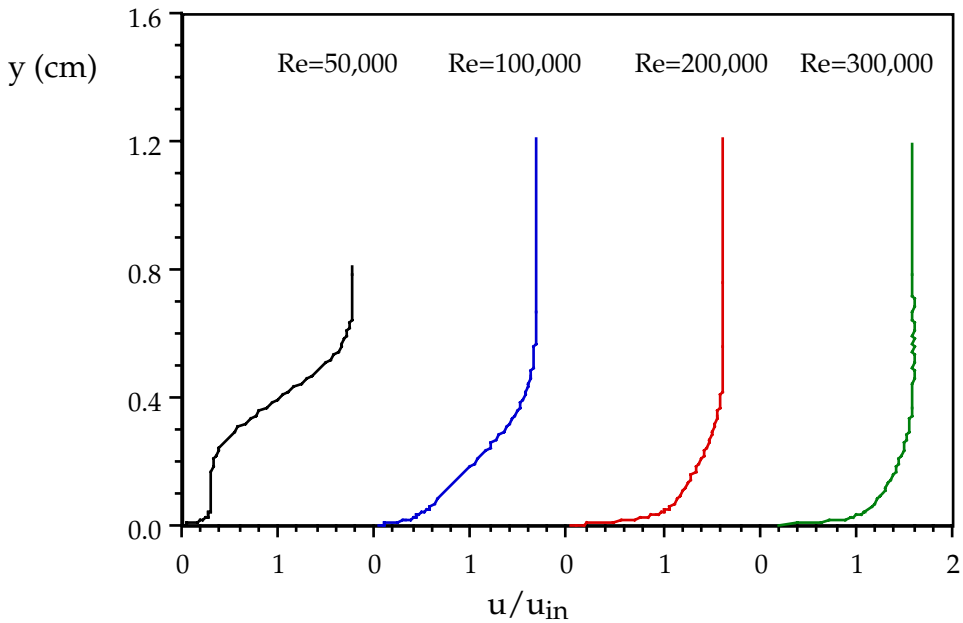

Fig. 4.94 Velocity profiles at station p12 (x/Lx=91.11%), FSTI=2.5%. Caution: measured values are artificially at y=0 - 0.42 cm for Re=50k, y=0 - 0.21 cm for Re=100k

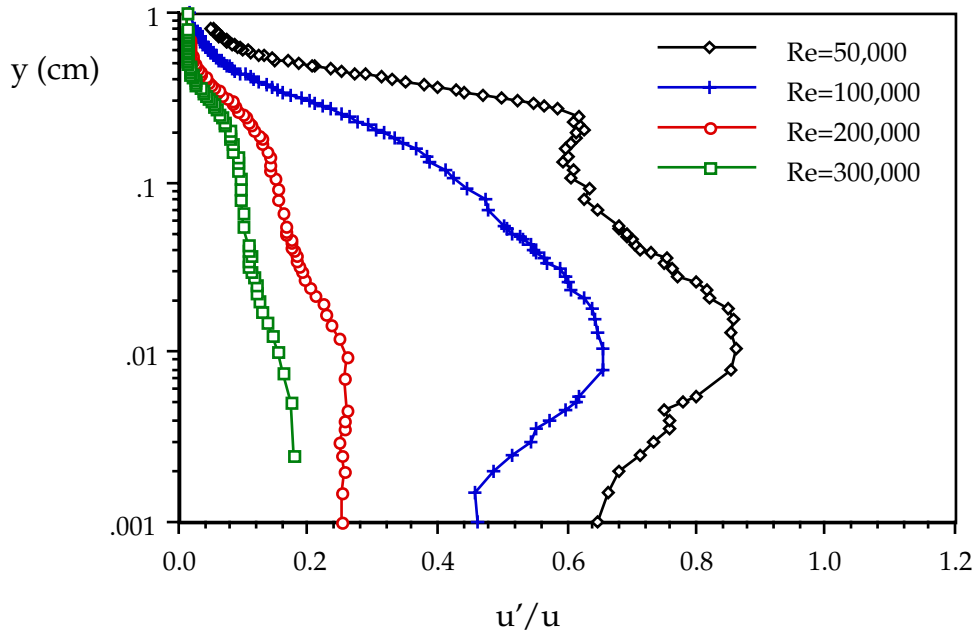

Fig. 4.95 Turbulence intensities at station p12 (x/Lx=91.11%), FSTI=2.5%

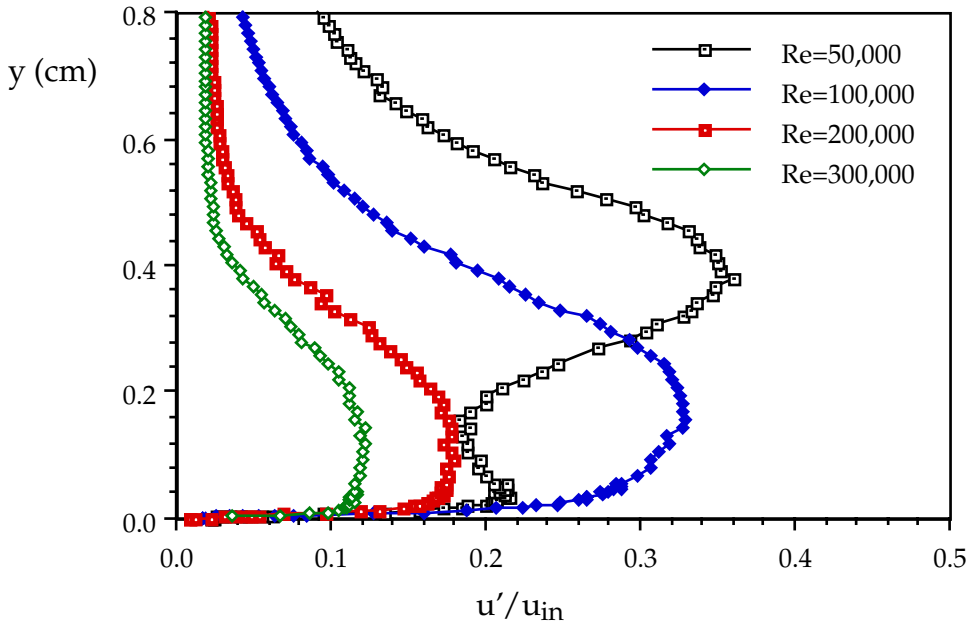

Fig. 4.96 Velocity fluctuations at station p12 (x/Lx=91.11%), FSTI=2.5%

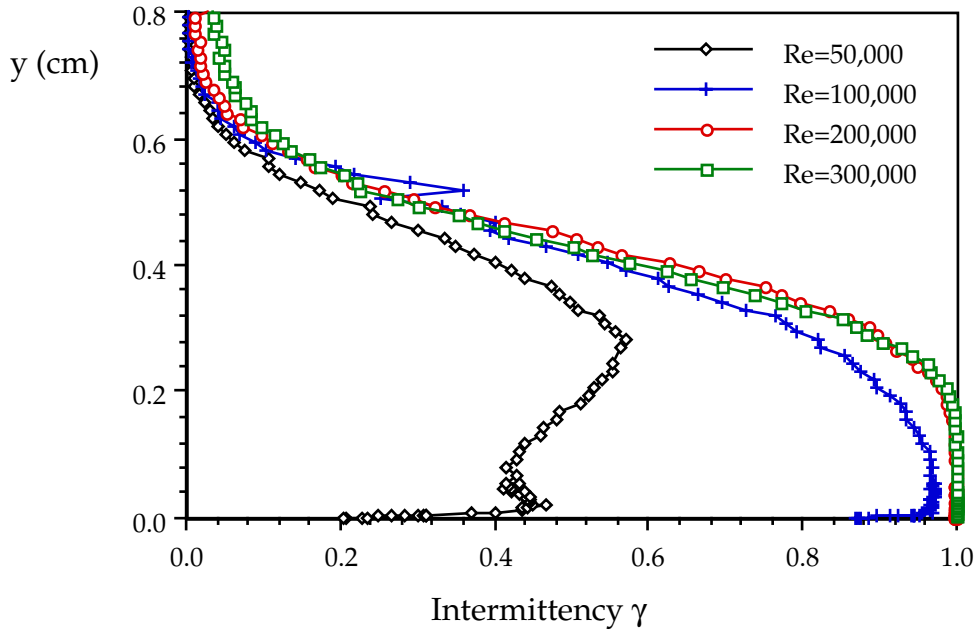

Fig. 4.97 Intermittency distributions at station p12 (x/Lx=91.11%), FSTI=2.5%

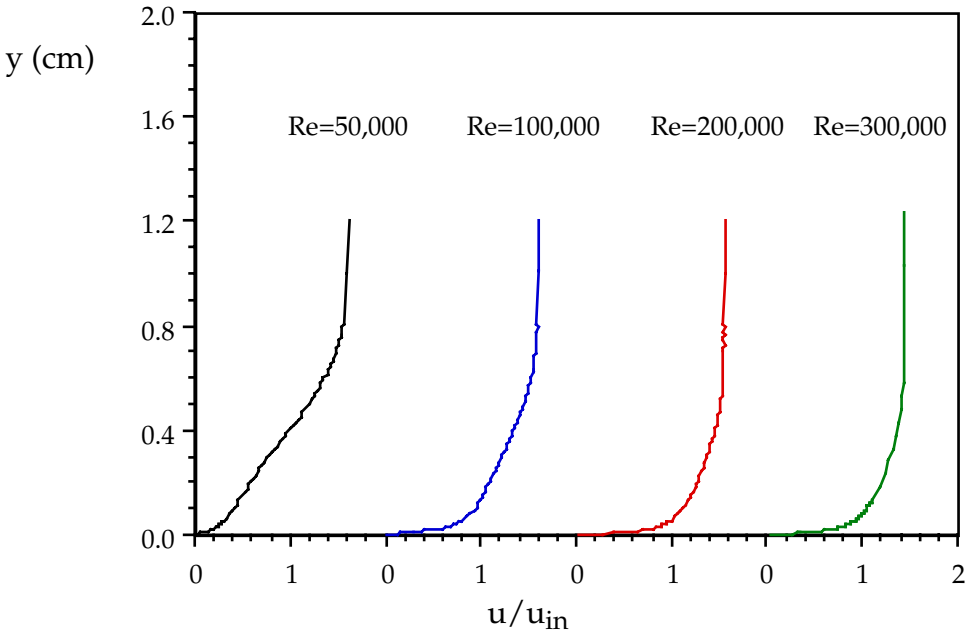

Fig. 4.98 Velocity profiles at station p13 (x/Lx=97.28%), FSTI=2.5%. Caution: measured values are artificially high at y=0 - 0.52 cm for Re=50k, y=0 - 0.1 cm for Re=100k

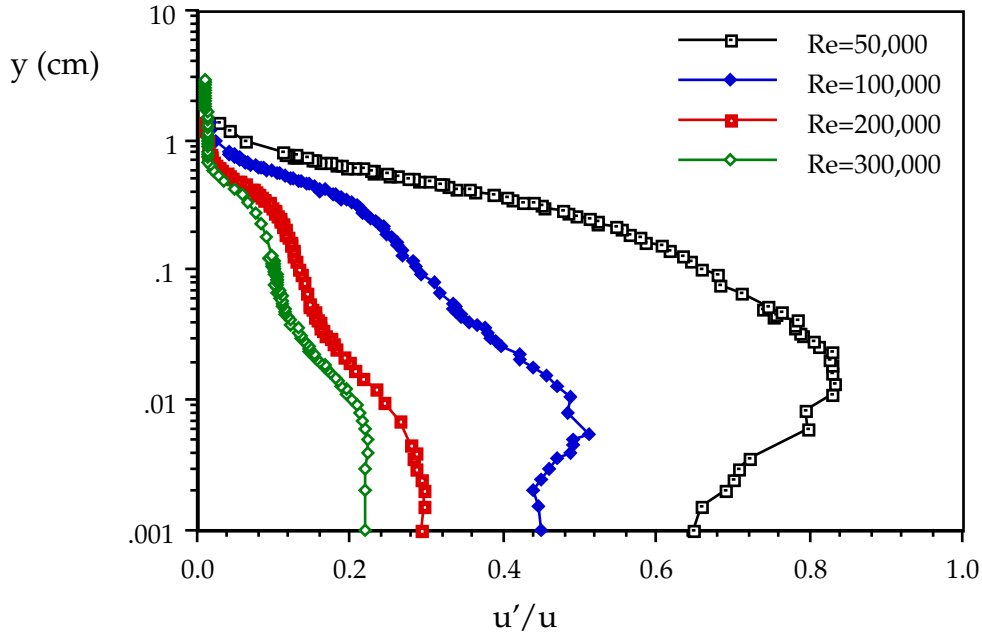

Fig. 4.99 Turbulence intensities at station p13 (x/Lx=97.28%), FSTI=2.5%

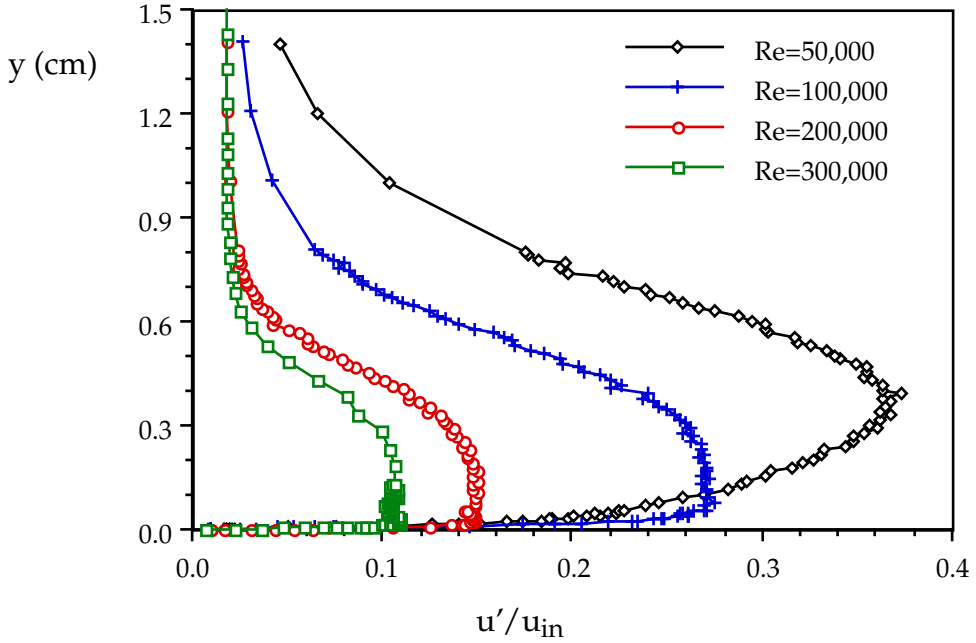

Fig. 4.100 Velocity fluctuations at station p13 (x/Lx=97.28%), FSTI=2.5%

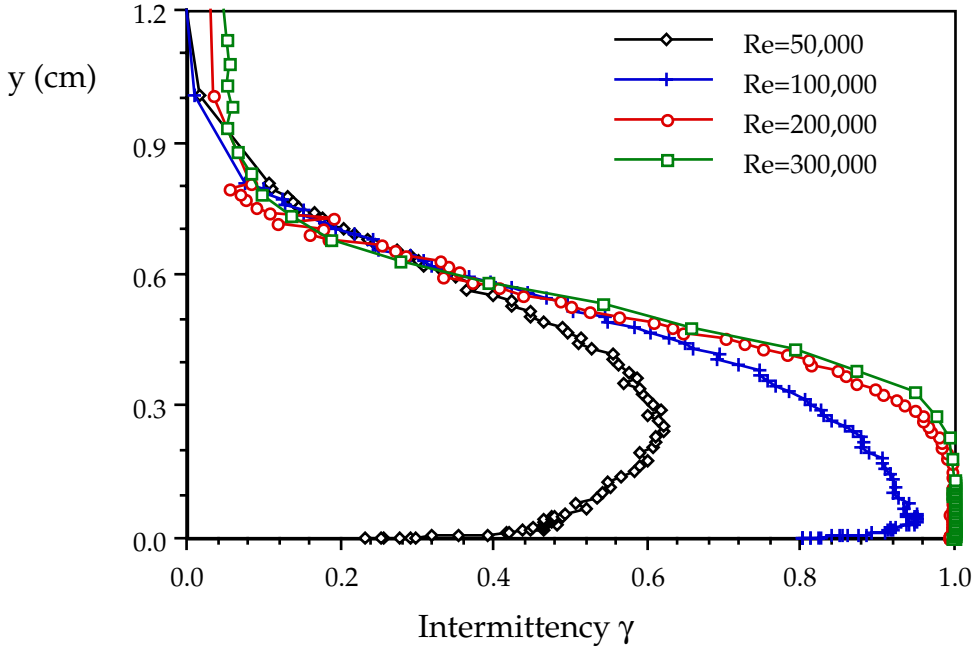

Fig. 4.101 Intermittency distributions at station p13 (x/Lx=97.28%), FSTI=2.5%

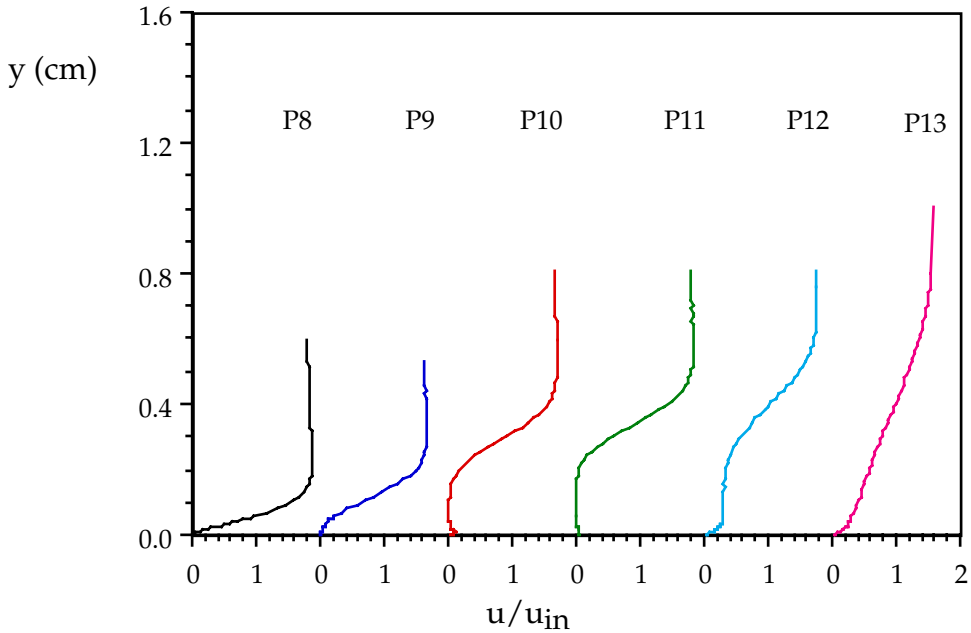

Fig. 4.102 Velocity profiles at p8 - p13 for Re=50,000, FSTI=2.5% Caution: measured values are artificially high at y=0.03 - 0.05 cm for p9, y=0.06 - 0.26 cm for p10, y=0 - 0.32 cm for p11, y=0 - 0.42 cm for p12, y=0 - 0.52 cm for p13

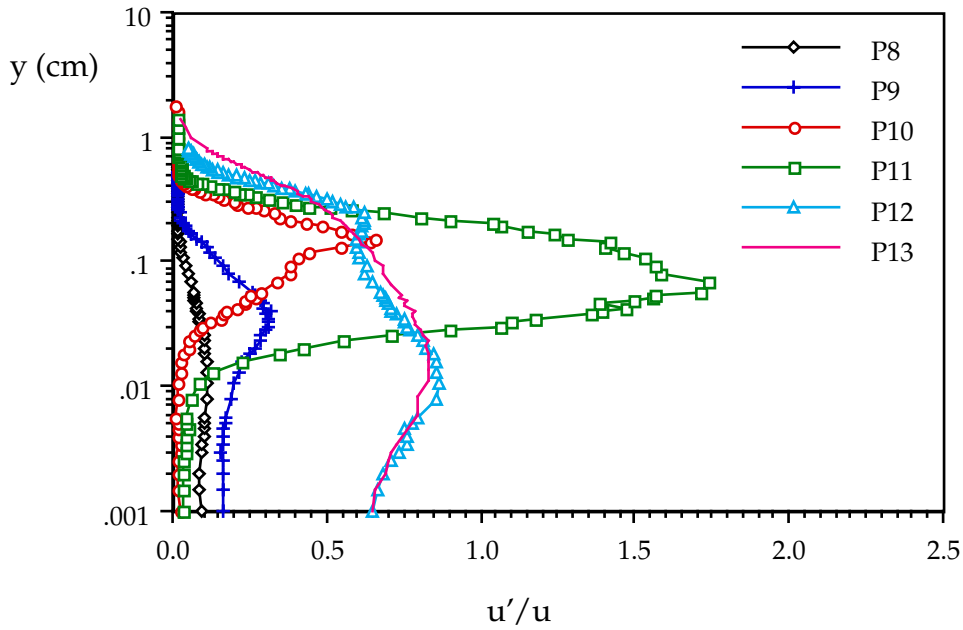

Fig. 4.103 Turbulence intensity at p8 - p13 for Re=50,000, FSTI=2.5%

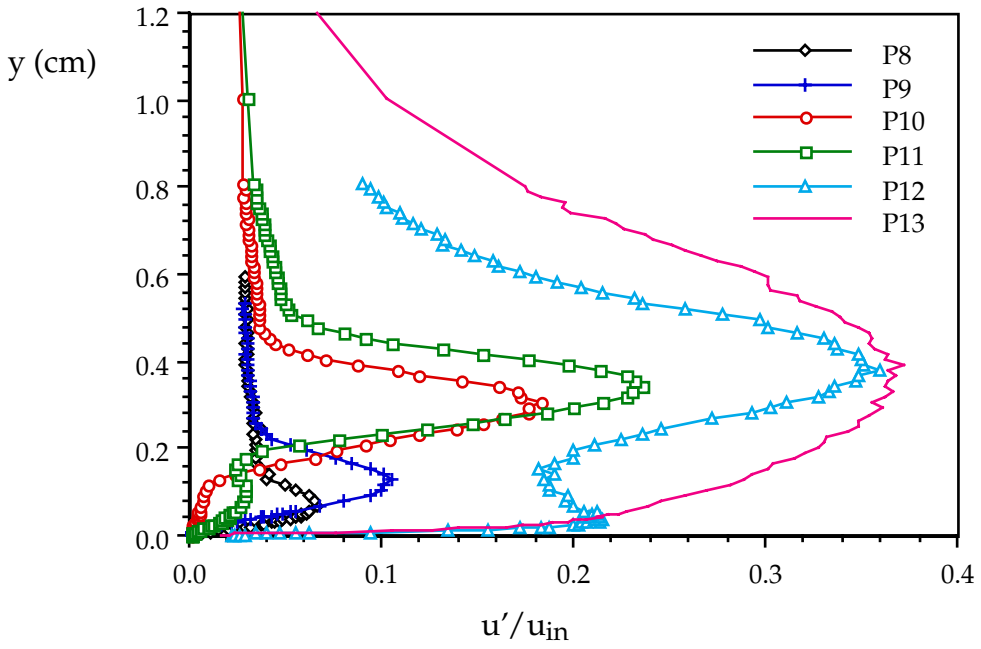

Fig. 4.104 Velocity fluctuations at p8 - p13 for Re=50,000, FSTI=2.5%

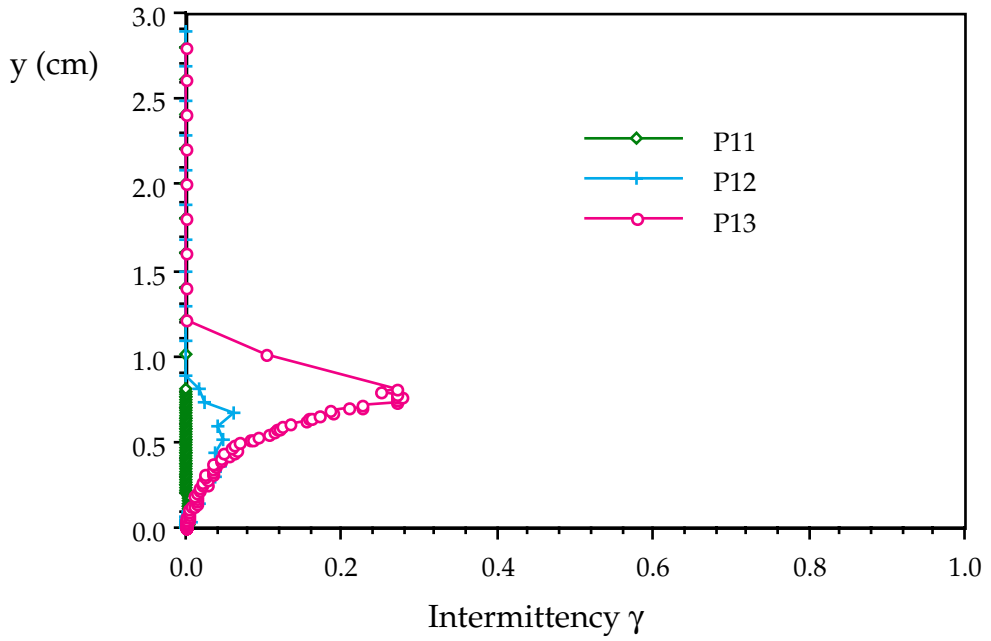

Fig. 4.105 Intermittency distributions for Re=50,000, FSTI=2.5%

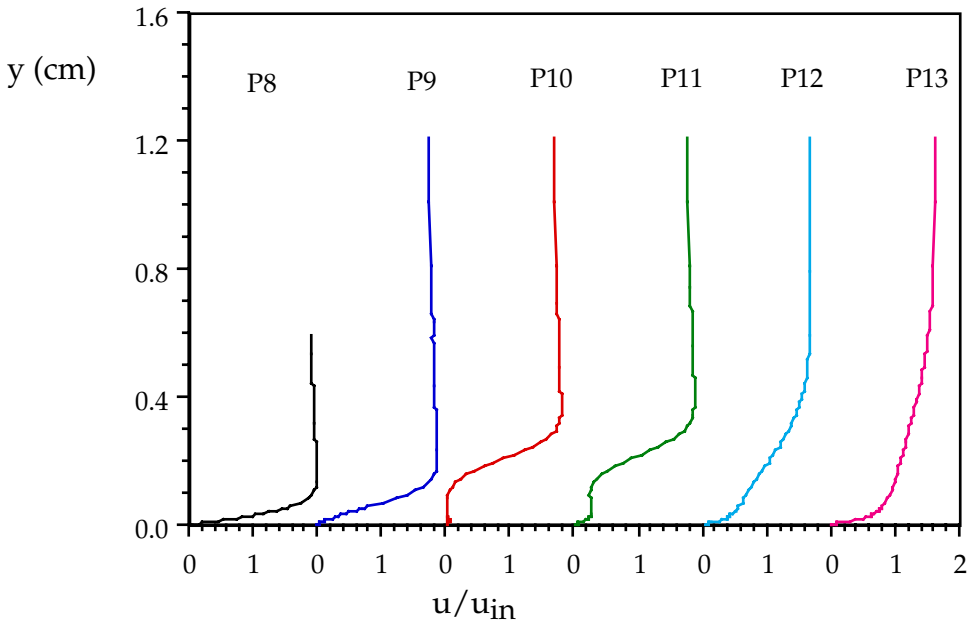

Fig. 4.106 Velocity profiles at p8 - p13 for Re=100,000, FSTI=2.5% Caution: measured values are artificially high at y=0 - 0.015 cm for p9, y=0.023 - 0.2 cm for p10, y=0 - 0.23 cm for p11, y=0 - 0.21 cm for p12, y=0 - 0.1 cm for p13

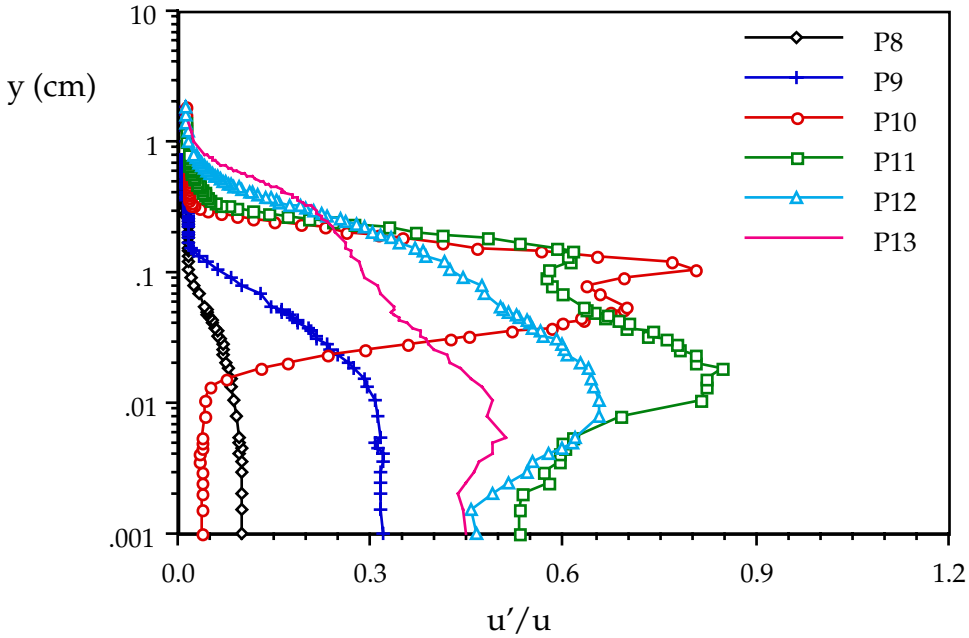

Fig. 4.107 Turbulence intensity at p8 - p13 for Re=100,000, FSTI=2.5%

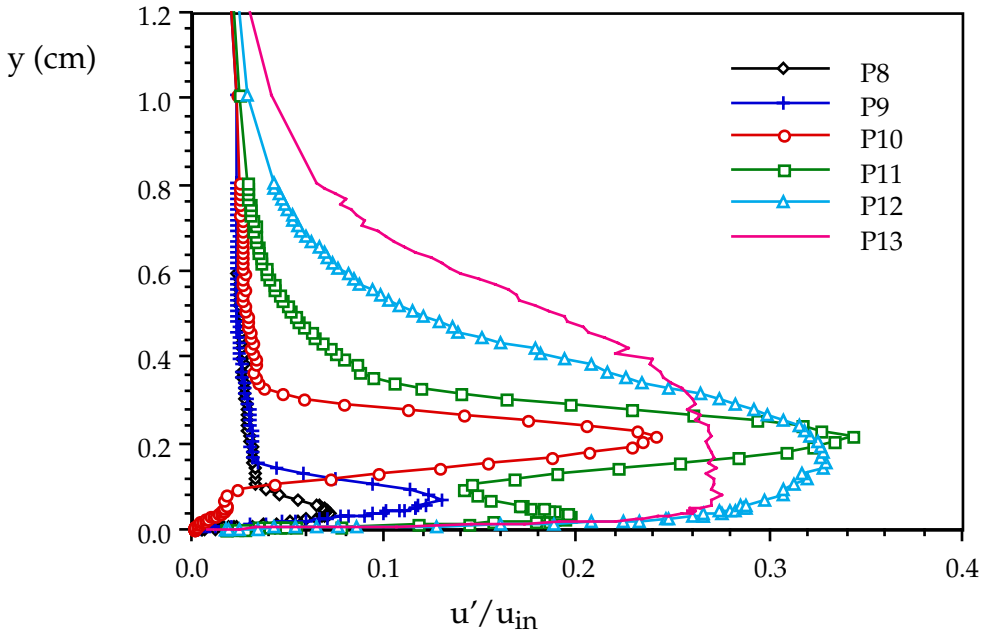

Fig. 4.108 Velocity fluctuations at Re=100,000, FSTI=2.5%

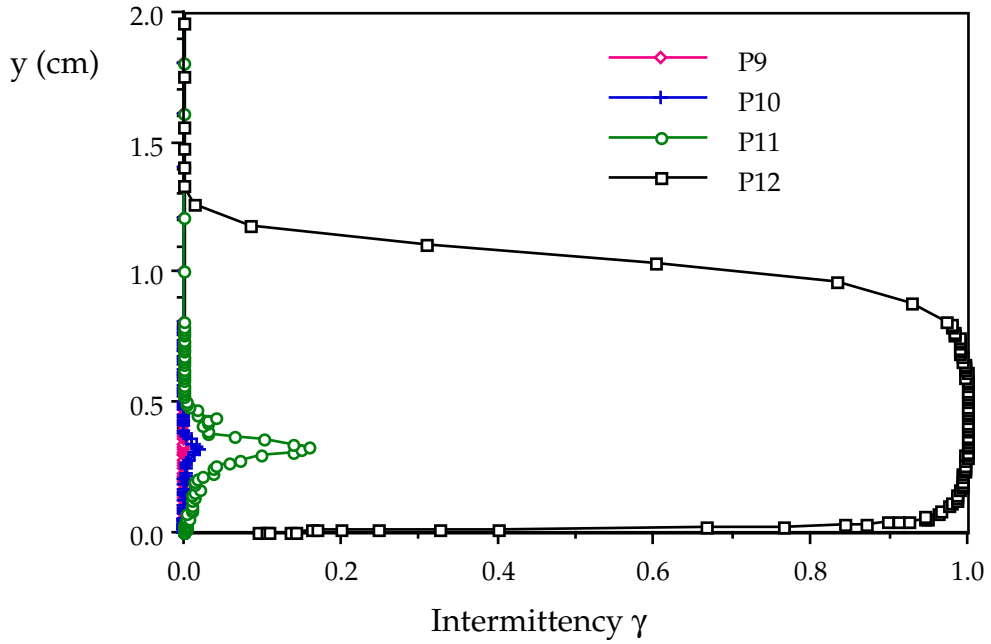

Fig. 4.109 Intermittency distributions for Re=100,000, FSTI=2.5%

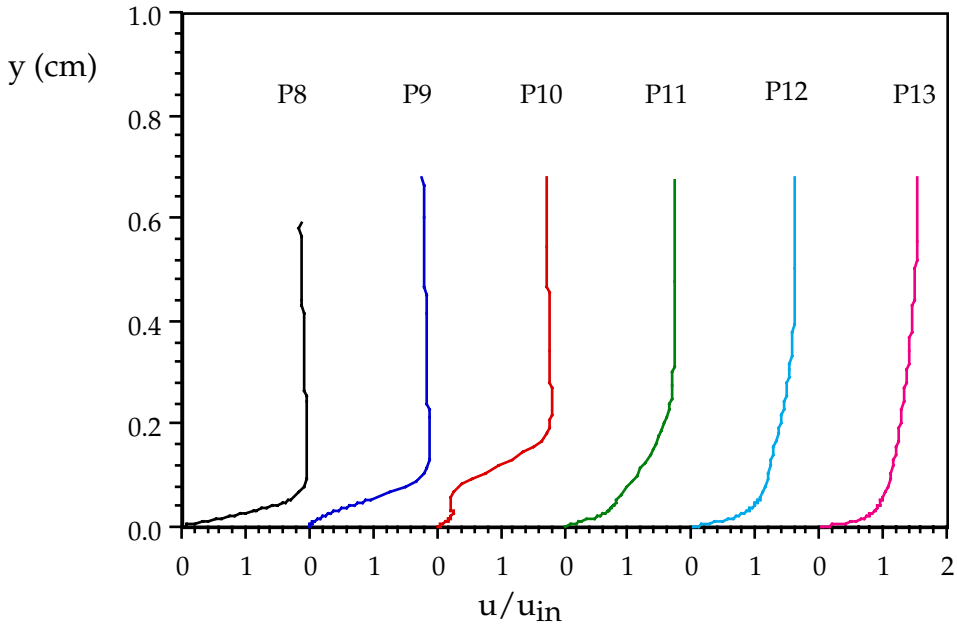

Fig. 4.110 Velocity profiles for Re=200,000, FSTI=2.5%. Caution: measured values are artificially high at p9, y=0 - 0.11 for p10, y=0 - 0.004 cm for p11

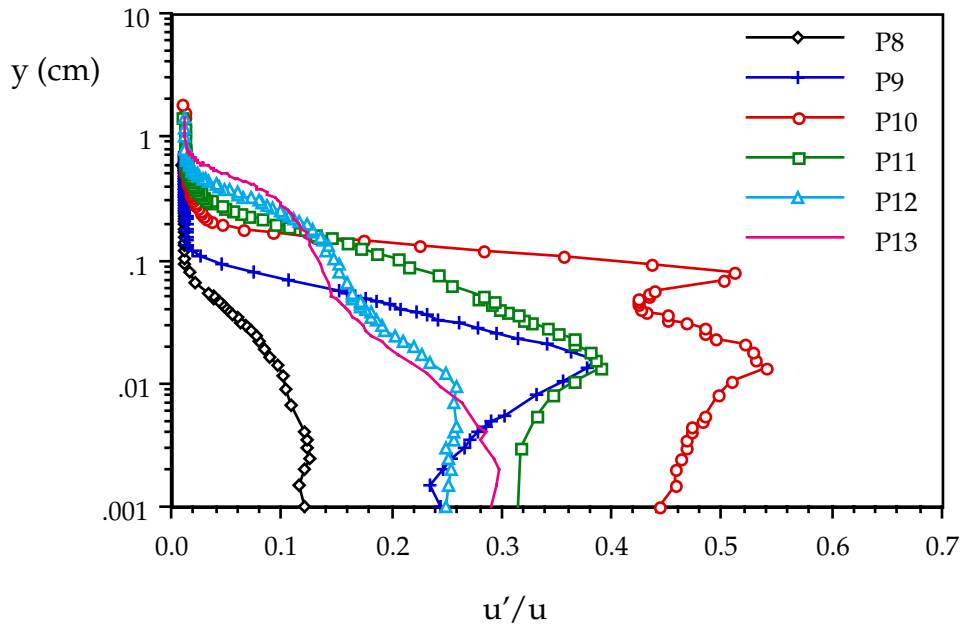

Fig. 4.111 Turbulence intensity at p8 - p13 for Re=200,000, FSTI=2.5%

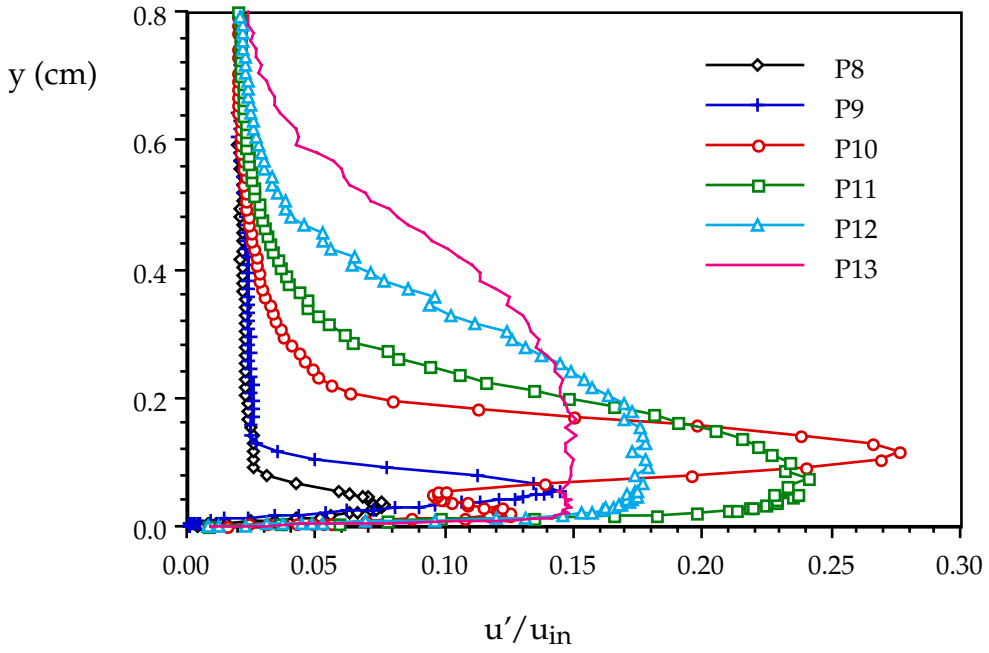

Fig. 4.112 Velocity fluctuations for Re=200,000, FSTI=2.5%

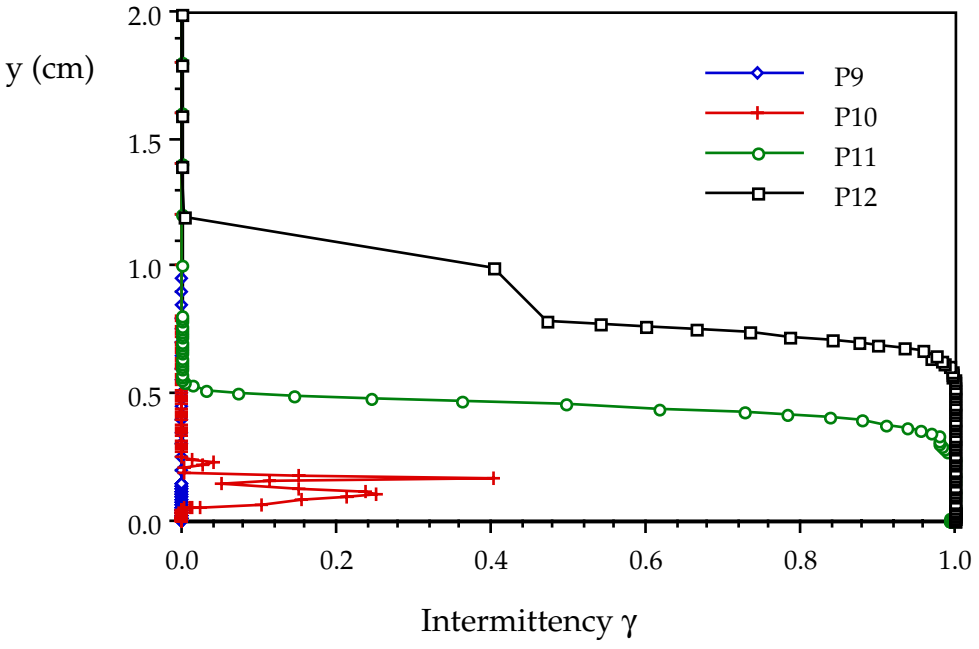

Fig. 4.113 Intermittency distributions for Re=200,000, FSTI=2.5%

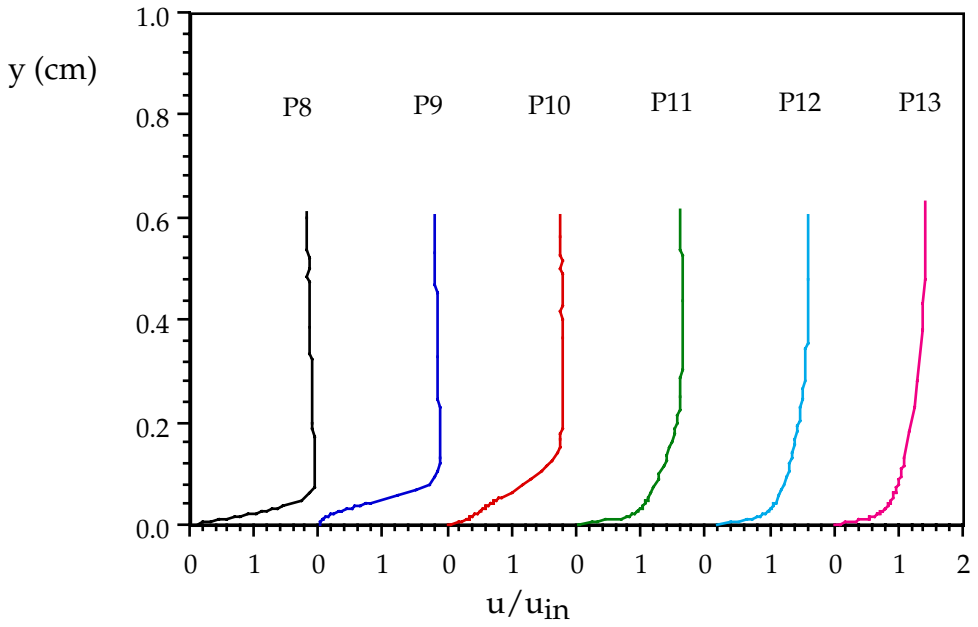

Fig. 4.114 Velocity profiles at p8 - p13 for Re=300,000, FSTI=2.5%. Caution: measured values are artificially high at y=0.007 - 0.03 cm for p9, y==0 - 0.044 cm for p10

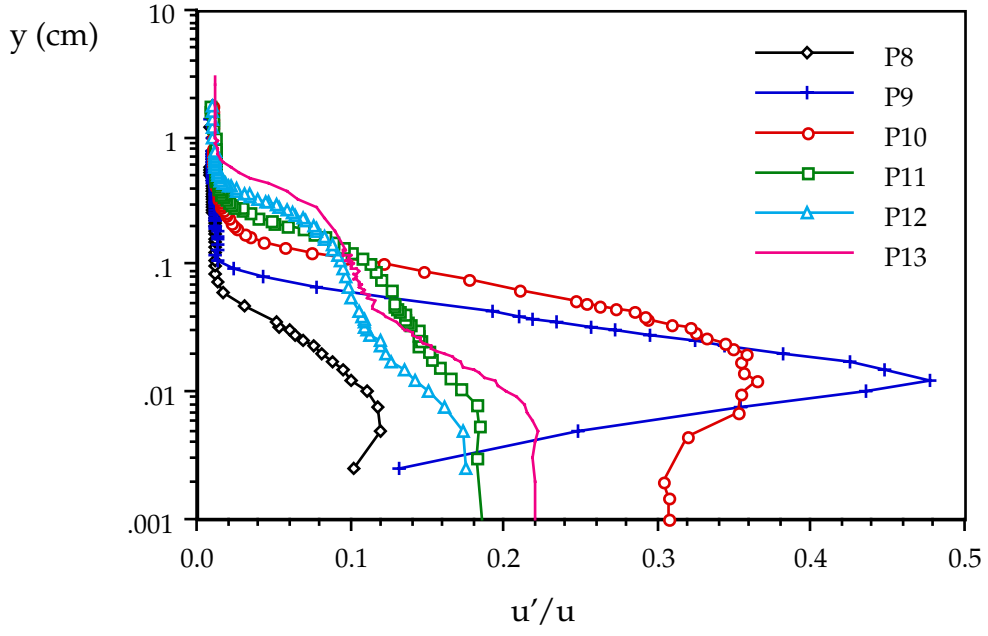

Fig. 4.115 Turbulence intensity at p8 - p13 for Re=300,000, FSTI=2.5%

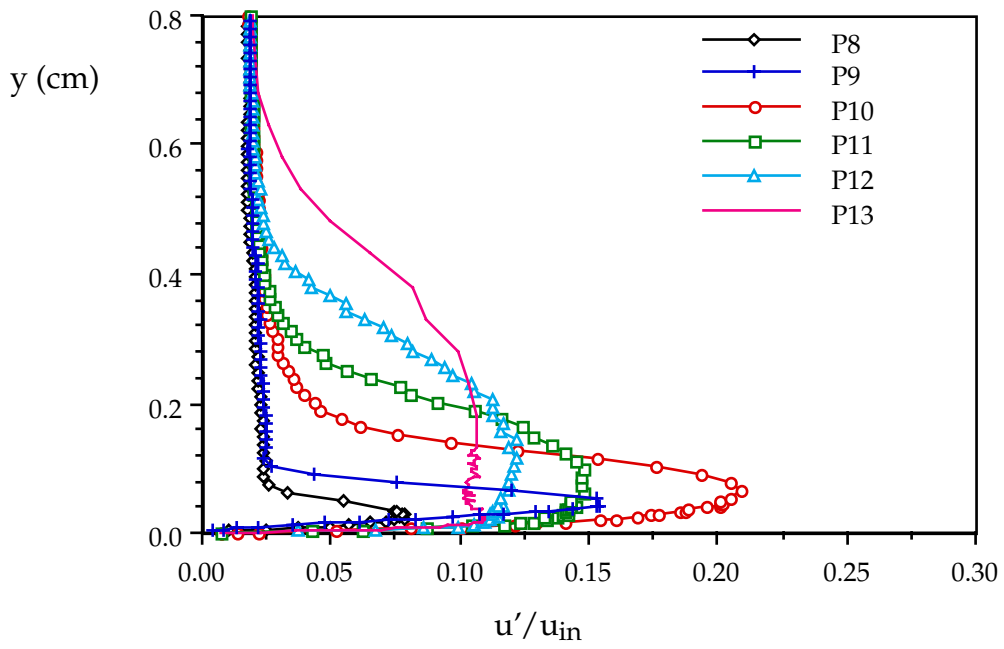

Fig. 4.116 Velocity fluctuations at p8 - p13 for Re=300,000, FSTI=2.5%

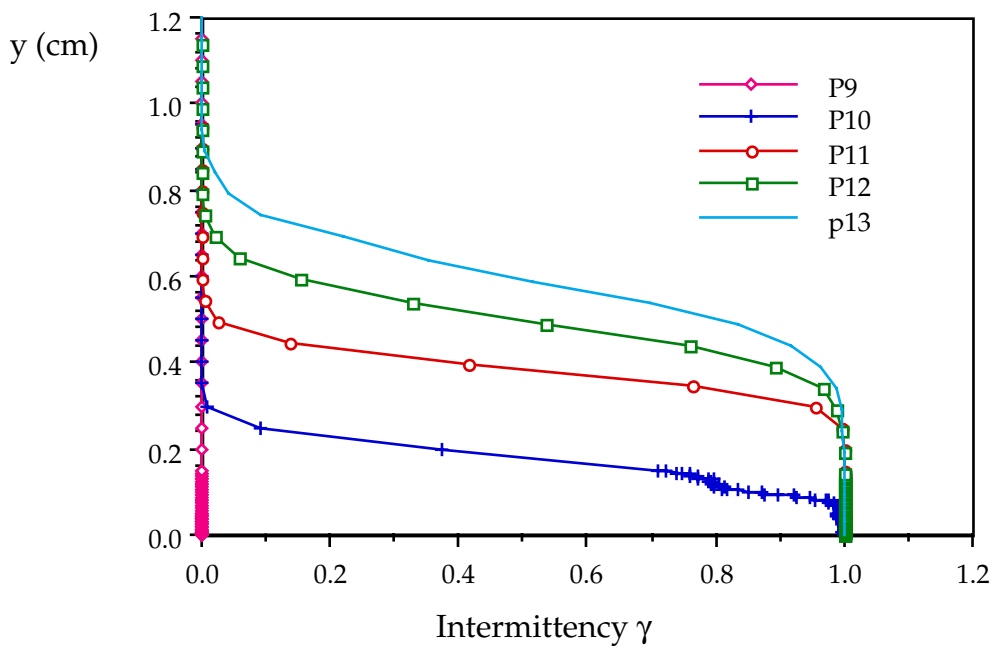

Fig. 4.117 Intermittency distributions at p8 - p13 for Re=300,000, FSTI=2.5%

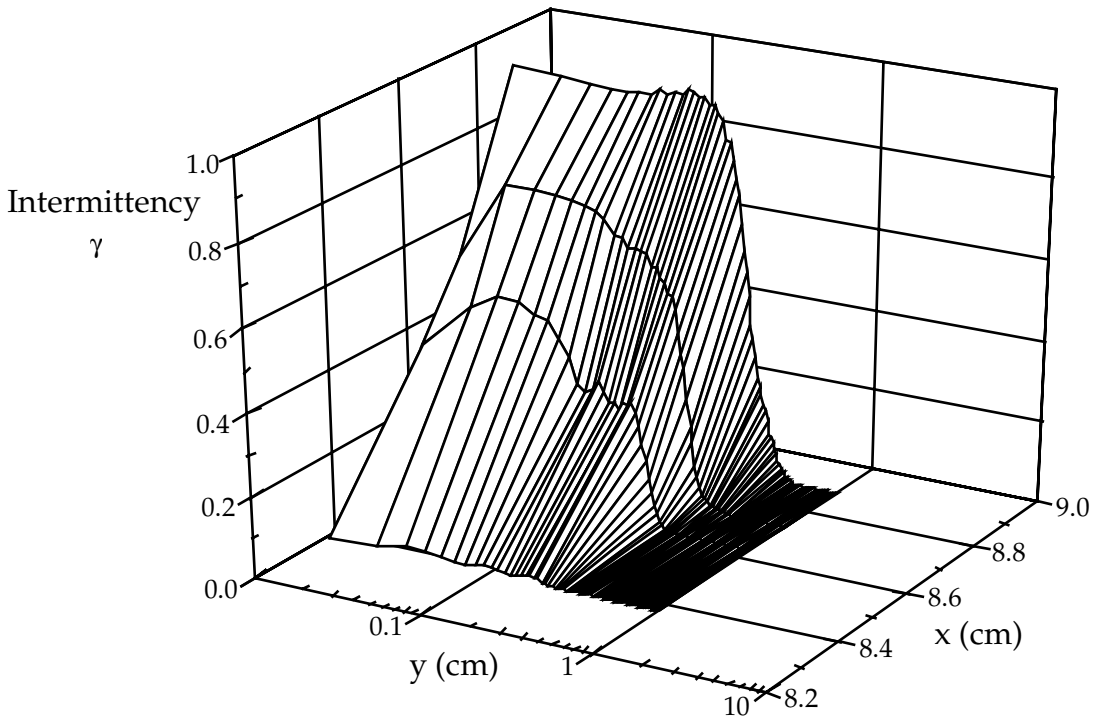

Fig. 4.118 Intermittency distributions for Re=100,000, FSTI=2.5%

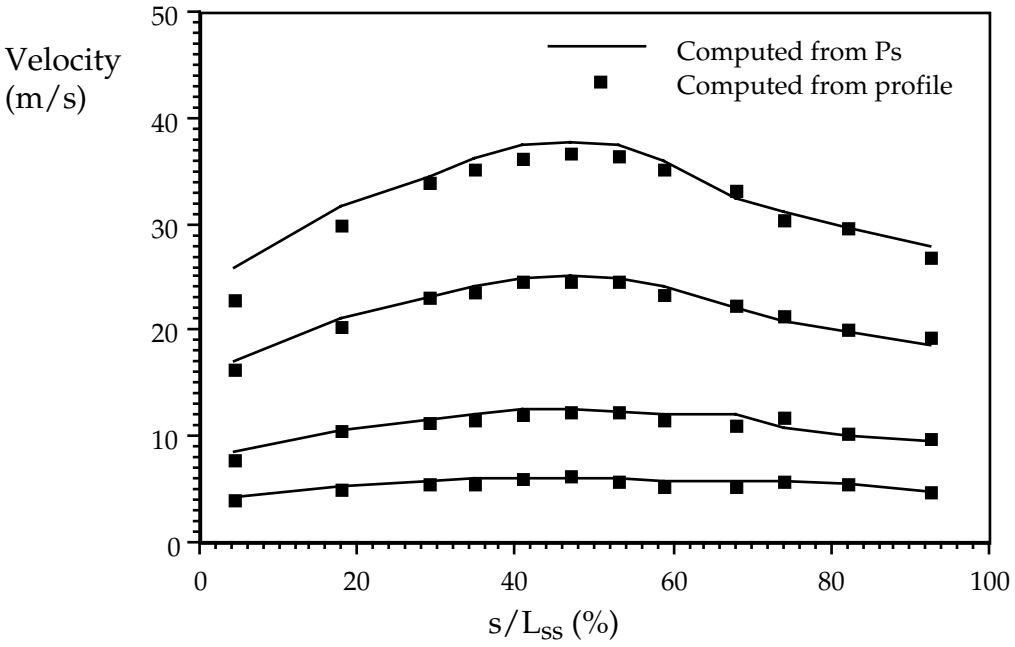

Fig. 4.119 Comparison of measured free-stream velocity to computed velocity from static pressure distributions for FSTI=2.5%; progressively higher velocities are for Reynolds numbers of 50,000, 100,000, 200,000 and 300,000.

HIGH TURBULENCE FLOW, FSTI=10%

Static pressure profiles for the FSTI=10% cases are pictured in Fig. 4.18 and documented in the pressure profile section. Compared with low and moderate FSTI cases, high-FSTI cases have earlier transition due to elevated FSTI. Nevertheless, the three Reynolds number cases are still attached laminar boundary layer flows at p2 to p7, see Figs. 4.120 to 4.125 (also supported by shear stress visualization). Velocity profiles and fluctuations at p7 are displayed in Figs. 4.126 and 4.127 and for p8 in Figs 4.128 through 130. Earlier transition can be seen in Fig. 4.131, where the Re=200,000 case already starts transition at station p8 (x/Lx=68.89%) and the Re=100,000 case is about to start its transition at this station. The intermittency values (non-zero values) in the core region for the Re=200,000 case are due to the high frequency of the flow fluctuations resulting from the high FSTI and high velocity. At the current setting of the intermittency circuit threshold number, the circuit declares 0.3 - 0.5 intermittency values for the flow in this free stream flow. The threshold number can be adjusted to lower the γ in the free stream so that the boundary layer transition can be easily separated from the free-stream turbulence. However, it was decided to not change the threshold value for this case and be consistent with all the other cases. Besides, boundary layer transition can still be identified with the present data. Note the near-wall peak in Fig. 4.131 for the Re=200,000 case. Velocity profiles plotted in Fig. 4.128 show attached boundary layers for all three cases, Re=50,000, 100,000 and 200,000 at station p8, as in the 2.5% FSTI case. The peaks of the u'/u_{in} profiles shift toward the wall as Re increases from 50,000 to 100,000 and 200,000, see Fig. 4.130.

At station p9 (x/Lx=74.57%), Fig. 4.132, the Re=50,000 and 100,000 cases show separated flow, as in the FSTI=0.5% and 2.5% cases. From the shear stress visualization study discussed above, the flow of the Re=200,000 case is also separated, though its separation zone is too small to see from Fig. 4.132. Apparently, the early transition and enhanced mixing promote the cross-stream momentum transport, minimizing the thickness of the flow separation zone. Figure 4.135 shows intermittency values of about 0.6 in the boundary layer for the Re=200,000 case. Transition in this case of separated boundary layer flow with high FSTI (10%) is certainly of the bypass transition mode. The Re=100,000 case has already started its transition at station p9. This separated shear layer transition with high FSTI (10%) is also bypass transition, as in the Re=200,000 case. Turbulence intensity distributions are presented in Fig. 4.133, where the high TI values indicate the high uncertainty of near-wall velocity values. The u'/u_{in} profiles plotted in Fig. 4.134 again show the shift of the peak fluctuations toward the wall as Re increases and the boundary layer thickness decreases.

Velocity profiles at station p10 (x/Lx=81.73%) are presented in Fig. 4.136. The separation bubble has grown to 0.5 mm from 0.3 mm at p9 for the Re=50,000 case while the separation bubble for the Re=100,000 case has stretched from 0.25 mm at p9 to about 0.3 mm at p10. The separation bubble growth is much slower than in the 0.5% and 2.5% FSTI cases. The flow for the Re=200,000 case is almost reattached. The current case (Re=200,000 and FSTI=10%) is similar to the Re=300,000, FSTI=2.5% case. These two cases start attached boundary layer flow transition, then begin to separate before transition is finished. Turbulence intensity distributions are shown in Fig. 4.137 and velocity fluctuations, u'/u_{in}, are plotted in Fig. 4.138. The u'/u_{in} profile is less steep than in upstream

locations for the Re=200,000 case because the flow has become a fully turbulent boundary layer, note the unity intermittency for this case in Fig. 4.139. At station p10, the shear flow is almost turbulent (γ is around 0.64) for the Re=100,000 case and the Re=50,000 case is just starting transition, Fig. 4.139.

At the next station, p11 (x/Lx=85.93%), the flow of the Re=100,000 case is almost reattached to the wall, as shown in Fig. 4.140. The separation bubble in the Re=50,000 case has started shrinking. Figure 4.141 shows that the local turbulence intensity values for the Re=200,000 case are not extremely high, so that the near-wall velocity values are reliable. The TI's in the other two flows are still high in the boundary layer; therefore, the errors due to rectification in the near-wall velocity values are high (within y = 4 mm for Re = 50,000 and y = 2.5 mm for Re = 100,000). Intermittency distributions plotted in Fig. 4.143 show that the Re=100,000 case is almost a fully turbulent flow throughout the boundary layer. The flattened u'/u_{in} profile for the Re=100,000 case in Fig. 4.142 also indicates the near-completion of transition for this case. Transition for the Re=50,000 case has proceeded to about a 0.3 intermittency. Though the shear layer is not turbulent at p11 for this case, enhanced mixing certainly has influenced the separated boundary layer flow, thus changing the velocity profile.

Velocity profiles at station p12 (x/Lx=91.11%) are plotted in Fig. 4.144. The figure shows that in the Re=100,000 case, the flow is completely reattached to the wall and the separation bubble for the Re=50,000 case has shrunk to 0.4 mm at p12. Local TI distributions are shown in Fig. 4.145 and the u'/u_{in} distributions are given in Fig. 4.146. The shape change around the peak of the u'/u_{in} profile for the Re=50,000 case indicates that the shear flow is almost

turbulent. That is also evidenced by the intermittency distribution for the case, see Fig. 4.147.

At the last station, p13 (x/Lx=97.28%), flows for all three Re cases are attached boundary layers, as shown by the velocity profiles in Fig. 4.148. The TI and u'/u_{in} profiles are given in Figs. 4.149 and 4.150, respectively. Clearly, the mean velocities for the Re = 50,000 case for y < 4.5 mm and for the Re = 100,000 case for y < 0.6 mm are in error due to rectification by the hot-wire. The intermittency distributions are plotted in Fig. 4.151. Though the Re=50,000 case has not finished its transition, transition started at the separated shear layer, has spread to the wall, and the flow is nearly turbulent throughout the boundary layer.

The FSTI=10% cases generally exhibit two different patterns, one is an attached boundary layer transition followed by separation; the other is a separated shear layer transition. Shear layer transition follows the same path discussed for the other two FSTI cases. As a summary of the 10% FSTI case, velocity profiles, turbulence intensities, rms velocity fluctuations, and intermittency distributions at various axial locations, p8 - p13, are plotted in Figs. 4.152 to 4.163, respectively.

The values of boundary layer thickness, $\delta_{99.5}$, momentum thickness, δ_2, displacement thickness, δ^*, local free stream velocity, u_8, and momentum thickness Reynolds number, $Re_{\delta 2}$, for the four cases of different Reynolds number were computed from the measured velocity profiles presented above and are shown in Tables 4.16 to 4.18. The comparison of computed free-stream velocities from measured velocity profiles to calculated velocities from static pressure distributions is shown in Fig. 4.164.

TABLE 4.16. Streamwise variation of $\delta_{99.5}$, δ_2, δ^*, u_8, and $Re_{\delta 2}$ for the Re=50,000, FSTI=10% case

x	$\delta_{99.5}$ (mm)	δ^* (mm)	δ_2 (mm)	u_8 (m/s)	$Re_{\delta 2}$
p2	0.457	0.151	0.064	3.710	14.844
p3	1.011	0.302	0.135	4.923	40.075
p4	1.287	0.412	0.172	5.389	55.280
p5	1.329	0.421	0.182	5.570	60.068
p6	1.377	0.447	0.189	6.038	63.368
p7	1.450	0.496	0.214	6.100	79.446
p8	2.080	0.607	0.242	5.903	86.667
p9	3.002	1.328	0.328	5.674	115.043
p10	4.284	2.064	0.489	5.590	170.871
p11	5.001	2.443	0.676	5.321	224.699
p12	6.564	2.670	1.030	4.594	289.926
p13	7.685	2.809	1.212	4.259	322.561

TABLE 4.17. Streamwise variation of $\delta_{99.5}$, δ_2, δ^*, u_8, $Re_{\delta 2}$, and Re_{δ^*} for the Re=100,000, FSTI=10% case

x	$\delta_{99.5}$ (mm)	δ^* (mm)	δ_2 (mm)	u_8 (m/s)	$Re_{\delta 2}$
p2	0.424	0.143	0.056	7.904	26.970
p3	0.858	0.232	0.103	10.006	62.853
p4	1.043	0.292	0.130	10.832	85.197
p5	1.097	0.308	0.137	11.319	91.235
p6	1.124	0.365	0.144	11.716	100.532
p7	1.224	0.386	0.161	11.745	113.285
p8	1.369	0.422	0.171	11.420	128.616
p9	2.138	0.921	0.234	10.997	159.845
p10	3.150	1.567	0.400	10.984	274.557
p11	3.976	1.690	0.553	10.562	335.584
p12	5.254	1.749	0.722	9.274	411.519
p13	6.246	1.762	0.967	9.029	530.556

TABLE 4.18. Streamwise variation of $\delta_{99.5}$, δ_2, δ^*, u_8, $Re_{\delta 2}$, and Re_{δ^*} for the Re=200,000, FSTI=10% case

x	$\delta_{99.5}$ (mm)	δ^* (mm)	δ_2 (mm)	u_8 (m/s)	$Re_{\delta 2}$
p2	0.335	0.089	0.039	15.289	37.195
p3	0.665	0.186	0.078	20.100	95.680
p4	0.733	0.219	0.098	22.464	133.878
p5	0.800	0.240	0.102	23.784	142.858
p6	0.870	0.249	0.112	24.554	167.291
p7	1.012	0.272	0.115	24.621	172.560
p8	1.126	0.353	0.123	23.966	185.711
p9	1.358	0.501	0.155	23.036	221.110
p10	2.136	0.726	0.295	21.086	380.243
p11	2.967	0.647	0.377	20.708	477.495
p12	4.048	0.731	0.459	19.730	558.308
p13	5.450	0.963	0.626	18.543	721.304

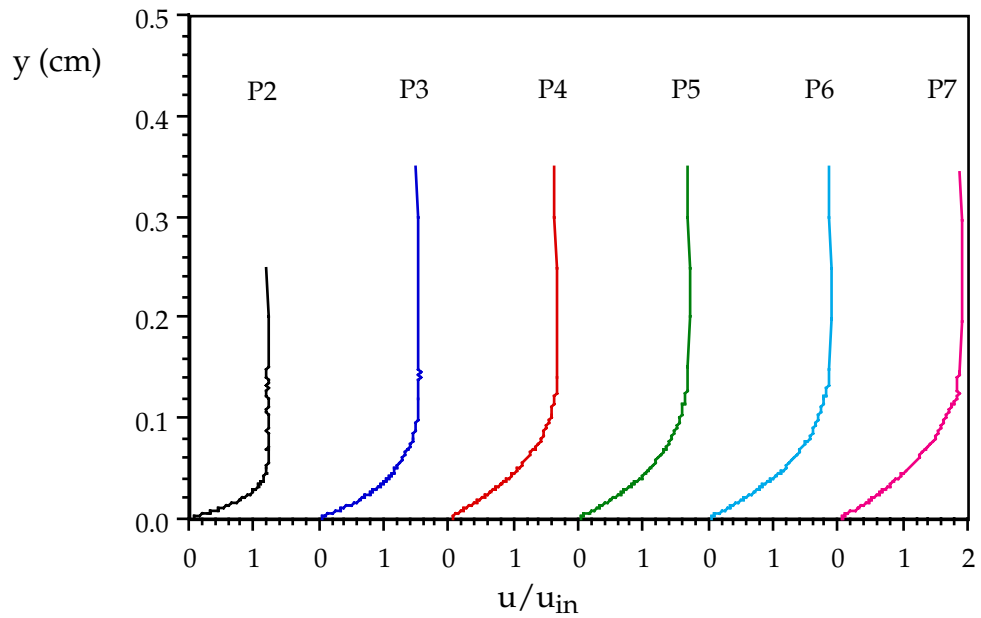

Fig. 4.120 Velocity profiles at p2 - p7 for Re=50,000, FSTI=10%

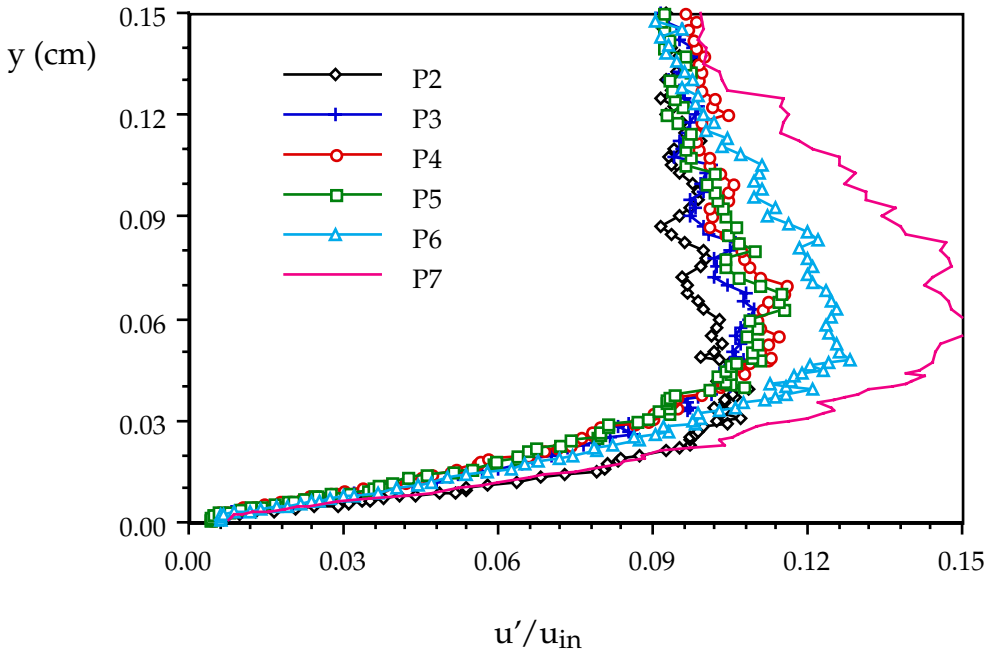

Fig. 4.121 Velocity fluctuations at p2 - p7 for Re=50,000, FSTI=10%

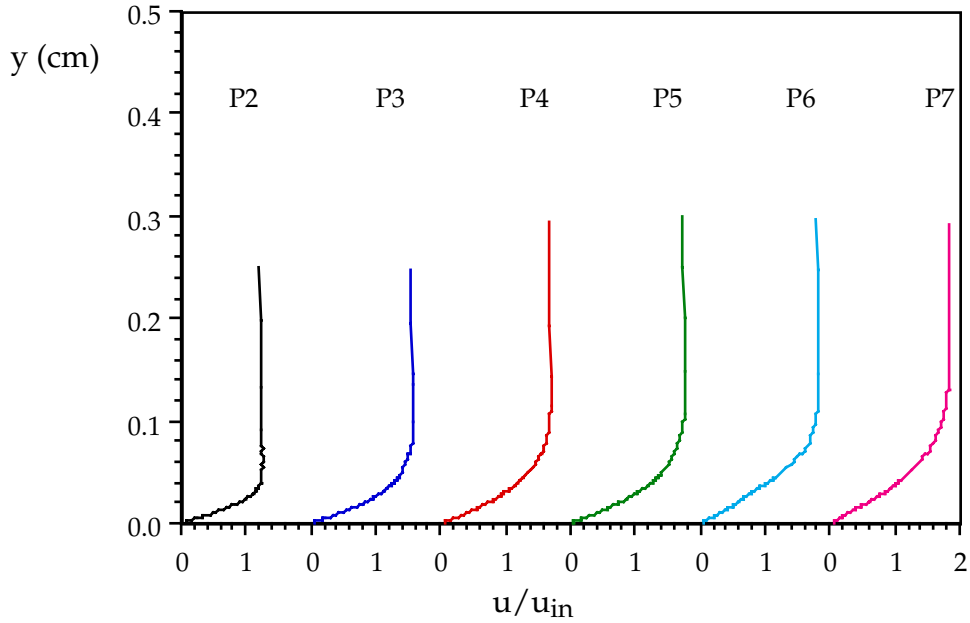

Fig. 4.122 Velocity profiles at p2 - p7 for Re=100,000, FSTI=10%

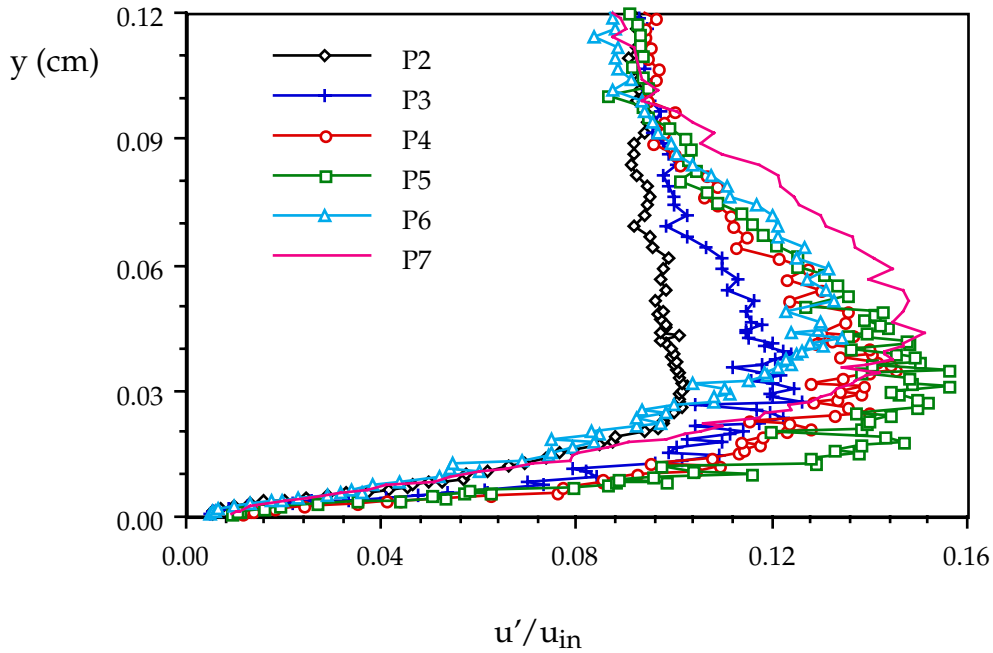

Fig. 4.123 Velocity fluctuations at p2 - p7 for Re=100,000, FSTI=10%

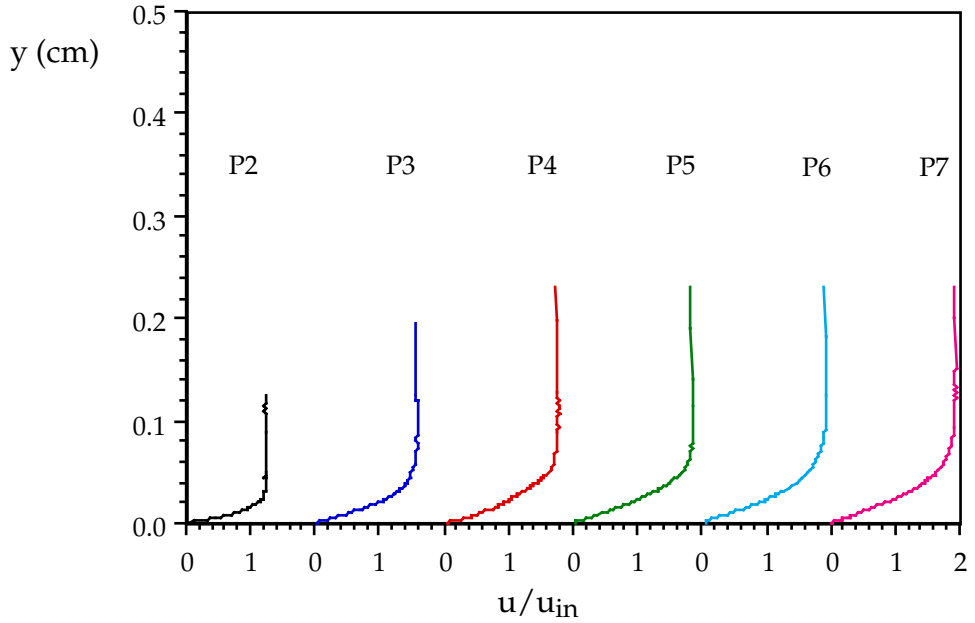

Fig. 4.124 Velocity profiles at p2 - p7 for Re=200,000, FSTI=10%

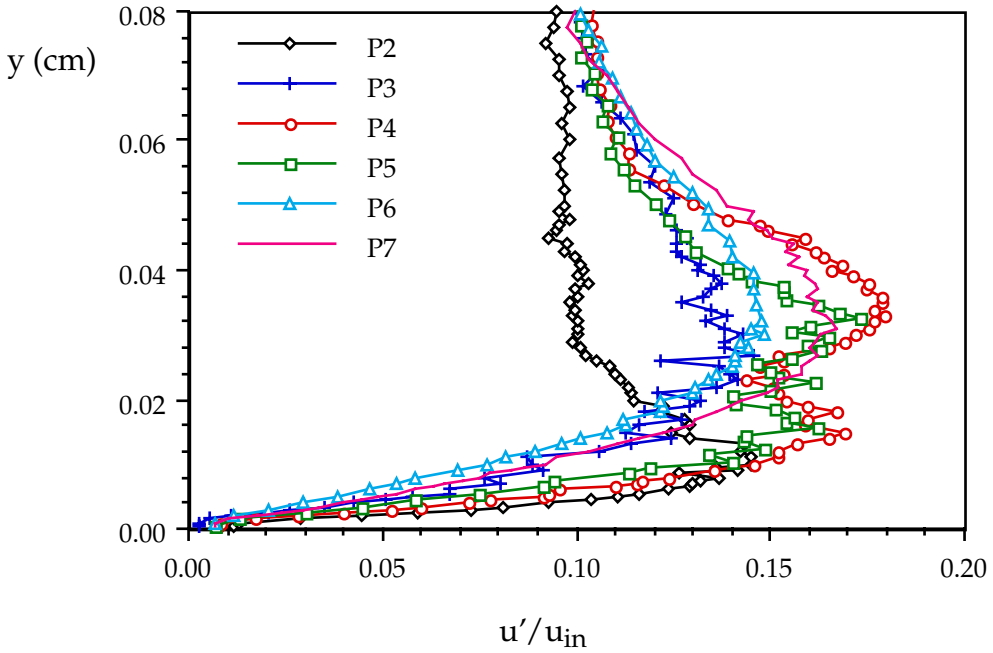

Fig. 4.125 Velocity fluctuations at p2 - p7 for Re=200,000, FSTI=10%

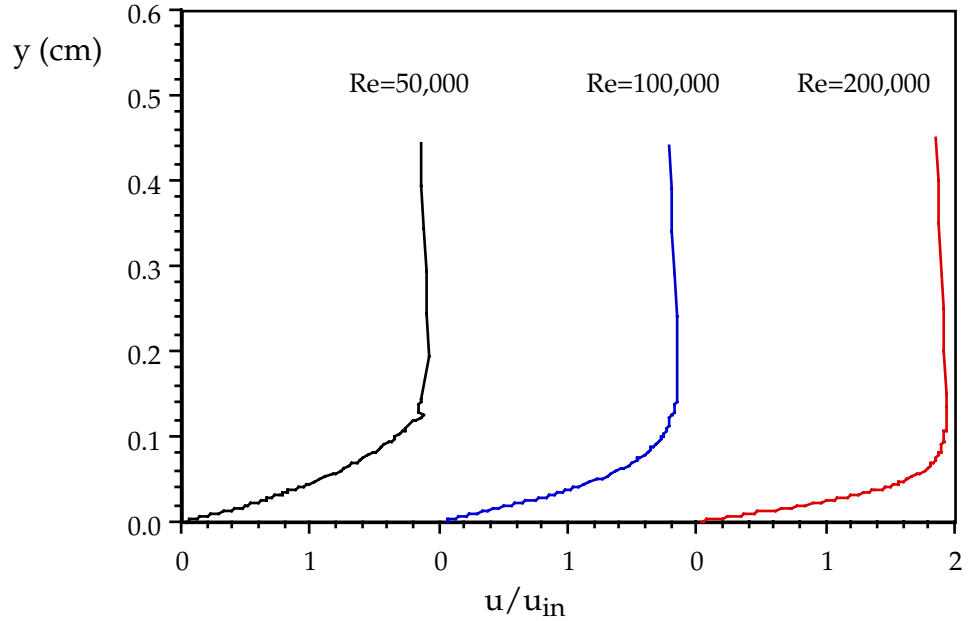

Fig. 4.126 Velocity profiles at station p7 (x/Lx=62.47%), FSTI=10%

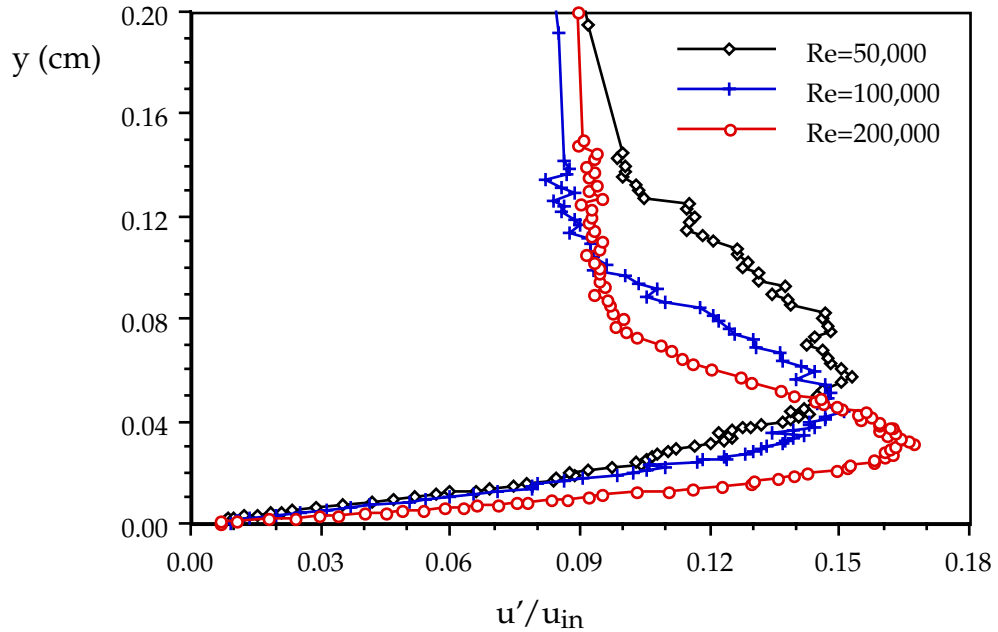

Fig. 4.127 Velocity fluctuations at station p7 (x/Lx=62.47%), FSTI=10%

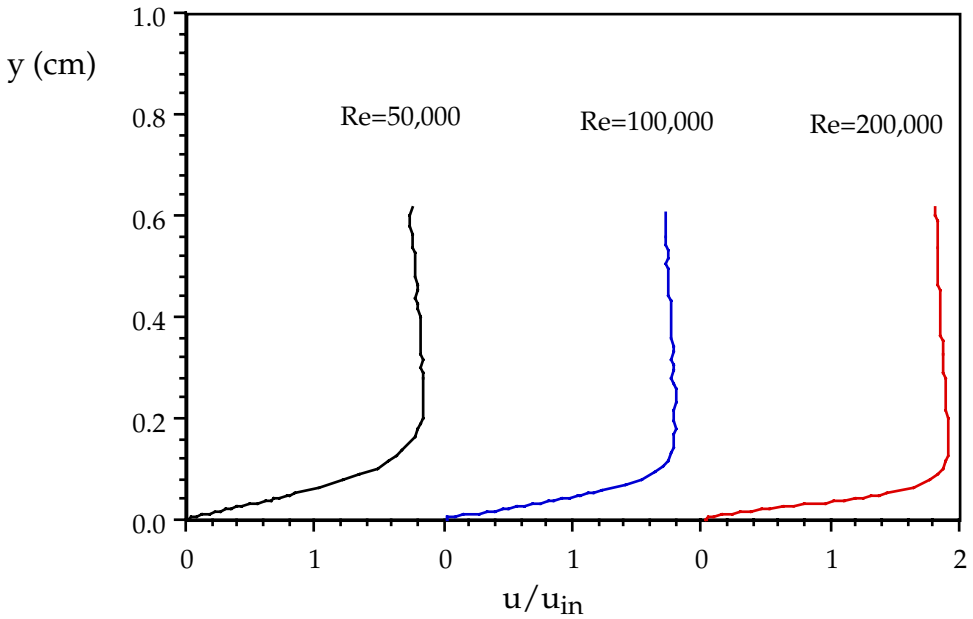

Fig. 4.128 Velocity profiles at station p8 (x/Lx=68.89%), FSTI=10%

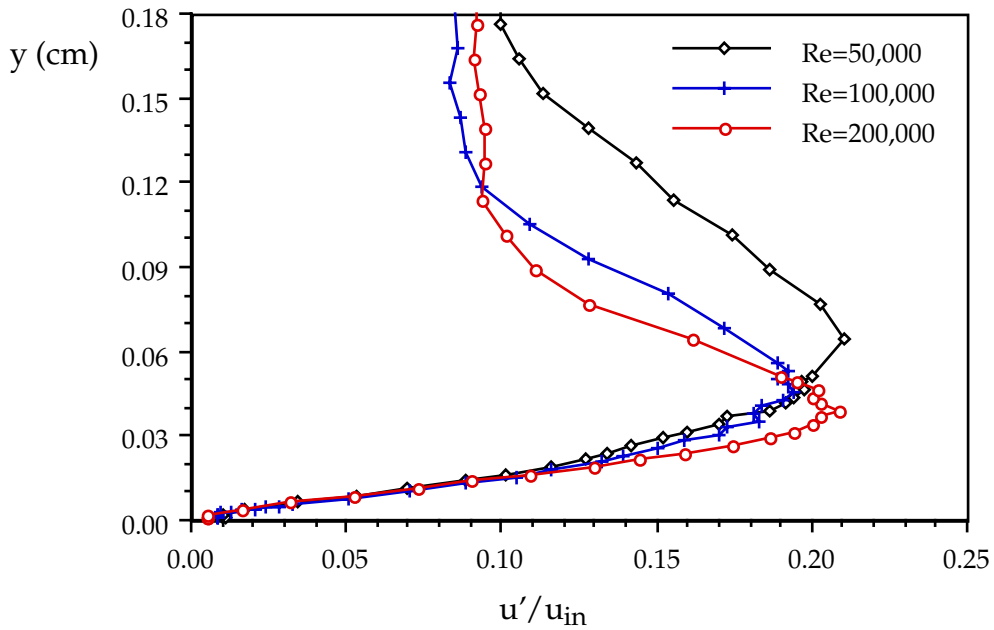

Fig. 4.129 Turbulence intensities at station p8 (x/Lx=68.89%), FSTI=10%

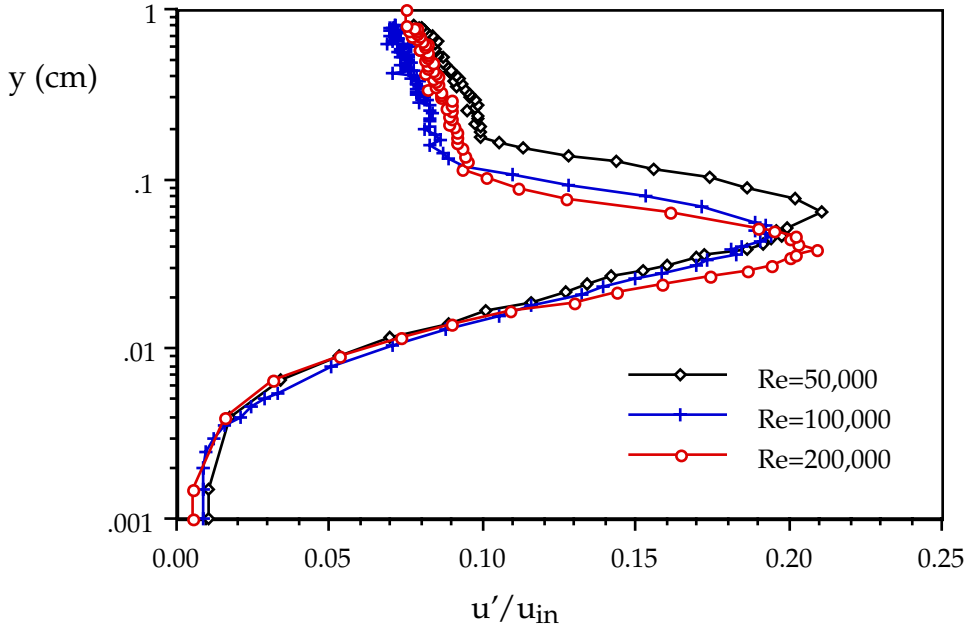

Fig. 4.130 Velocity fluctuations at station p8 (x/Lx=68.89%), FSTI=10%

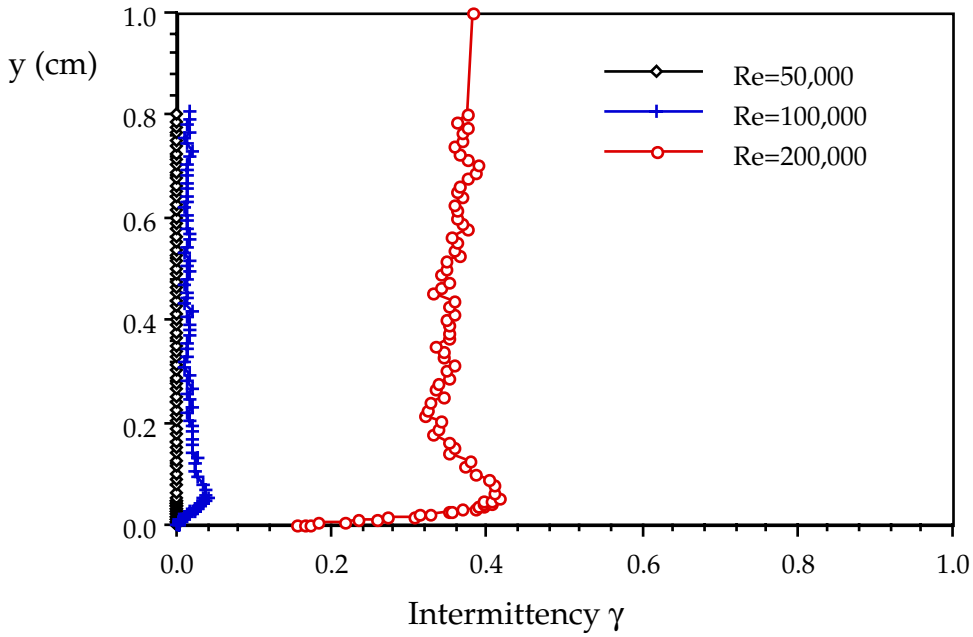

Fig. 4.131 Intermittency distributions at station p8 (x/Lx=68.89%), FSTI=10%

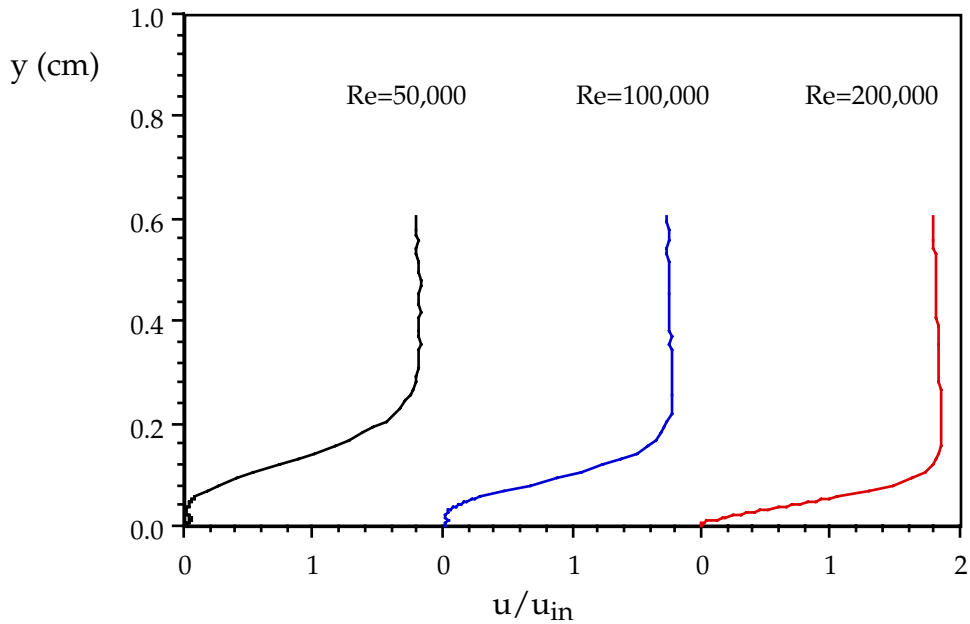

Fig. 4.132 Velocity profiles at station p9 (x/Lx=74.57%), FSTI=10%. Caution: measured values are artificially high at y=0.022 - 0.152 cm for Re=50k, y=0.013 - 0.105 cm for Re=100k, y=0 - 0.06 for Re=200k

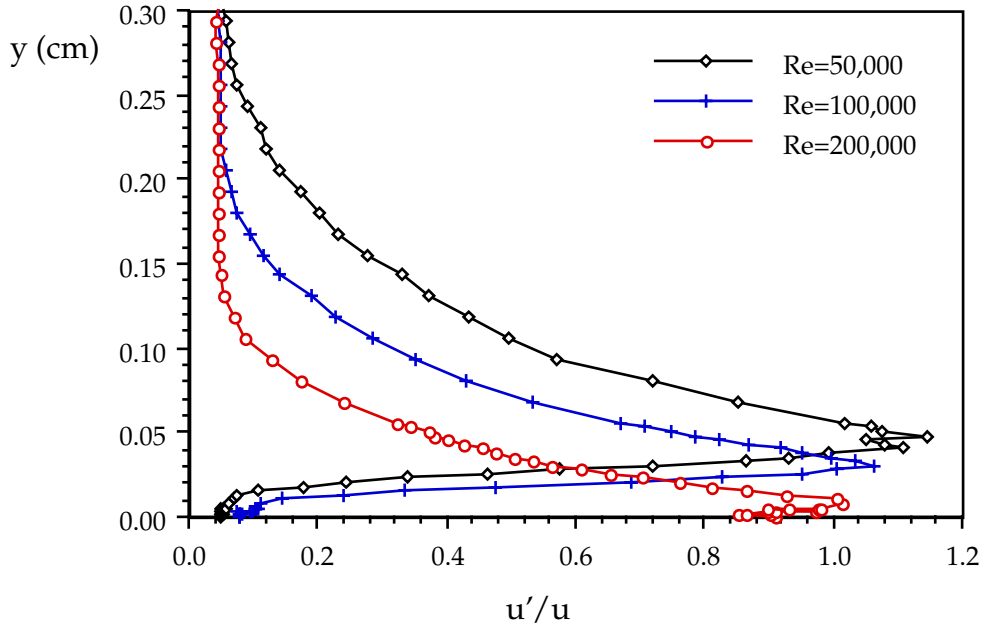

Fig. 4.133 Turbulence intensities at station p9 (x/Lx=74.57%), FSTI=10%

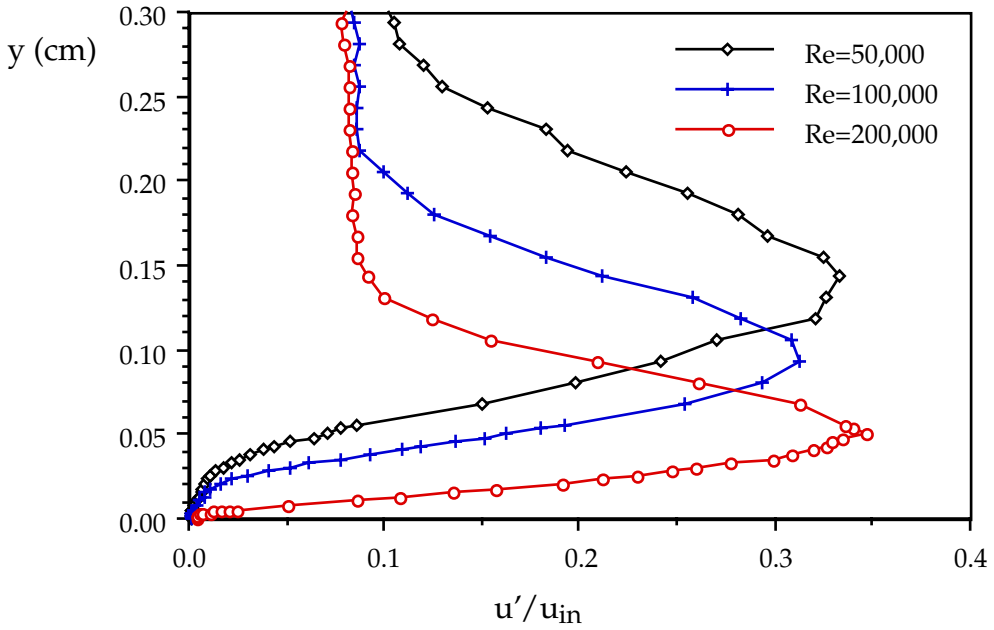

Fig. 4.134 Velocity fluctuations at station p9 (x/Lx=74.57%), FSTI=10%

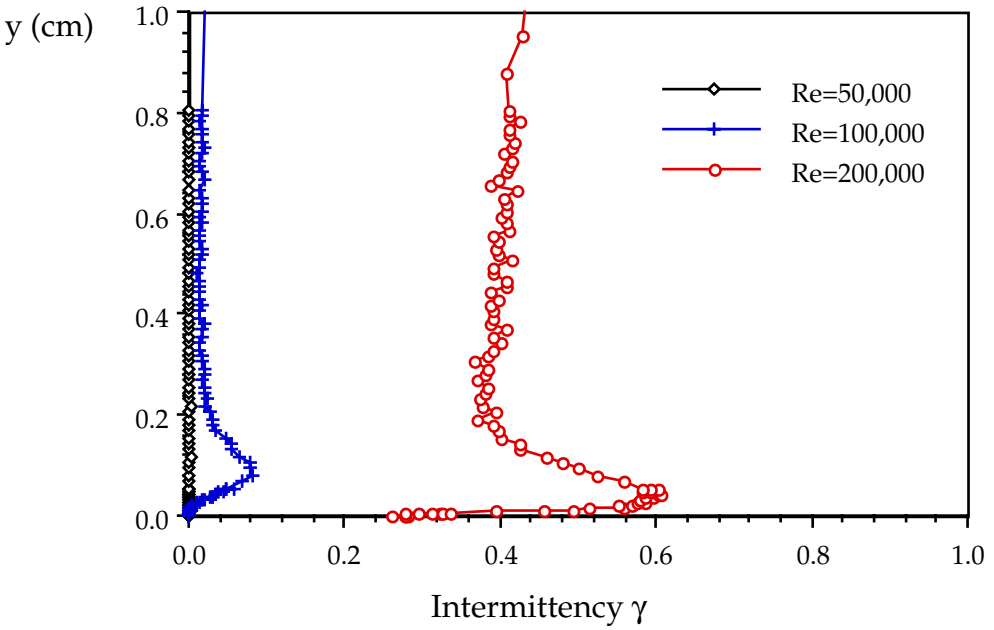

Fig. 4.135 Intermittency distributions at station p9 (x/Lx=74.57%), FSTI=10%

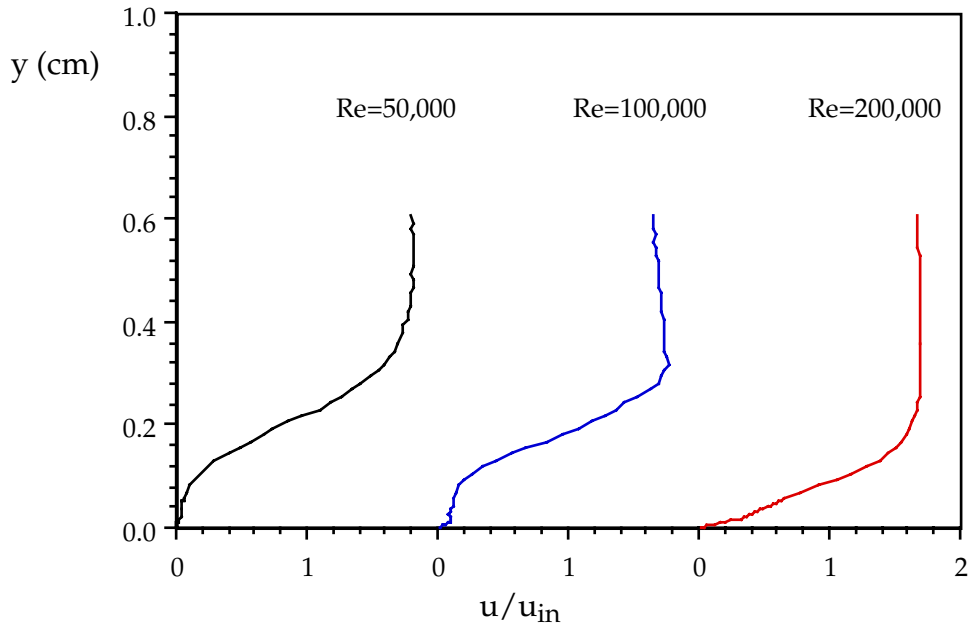

Fig. 4.136 Velocity profiles at station p10 (x/Lx=81.73%), FSTI=10%. Caution: measured values are artificially high at y=0-0.288 cm for Re=50k, y=0 - 0.22 cm for Re=100k, y=0 - 0.11 cm for Re=200k

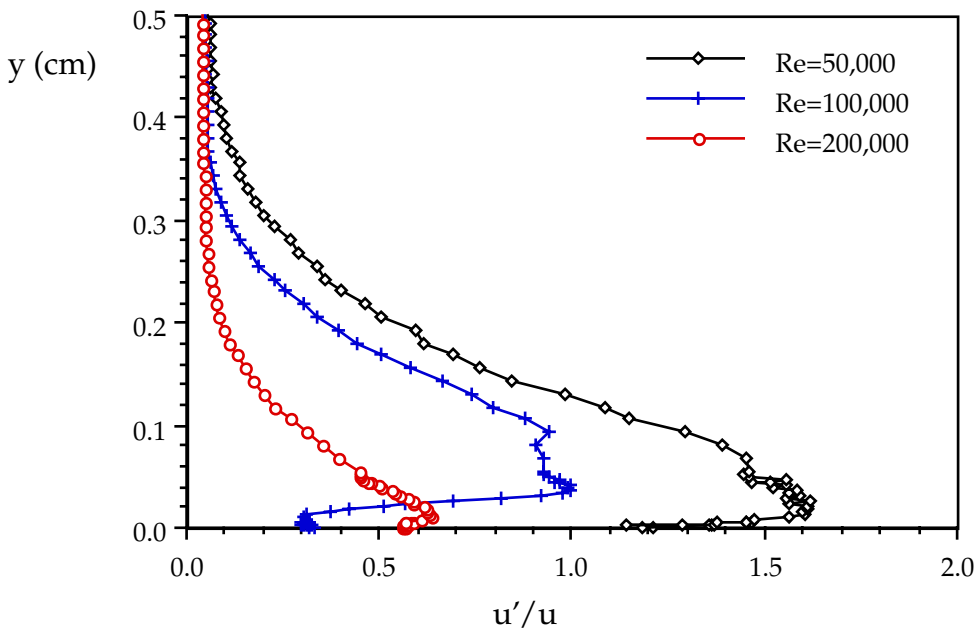

Fig. 4.137 Turbulence intensities at station p10 (x/Lx=81.73%), FSTI=10%

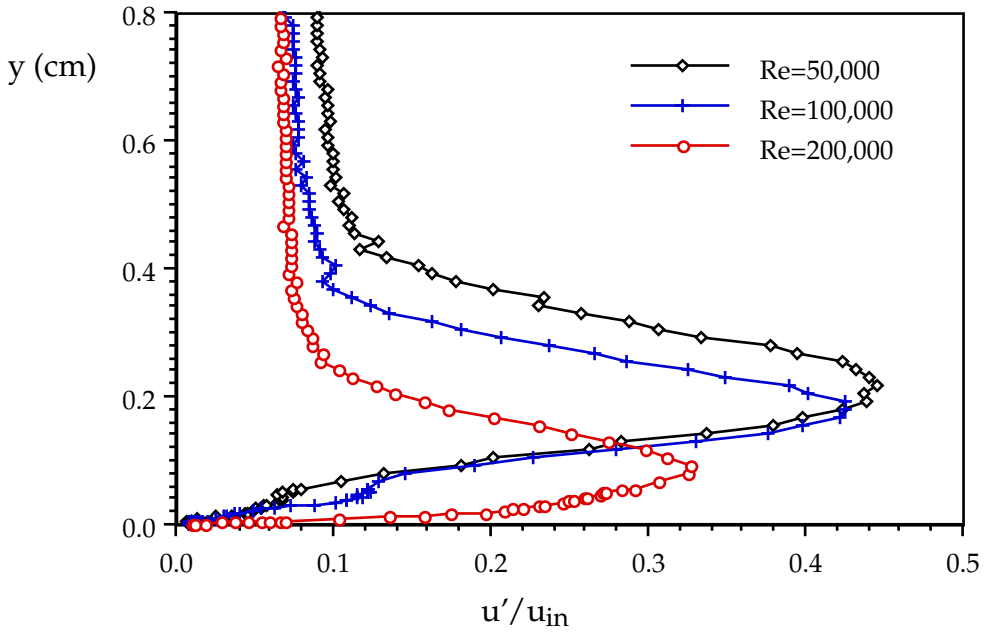

Fig. 4.138 Velocity fluctuations at station p10 (x/Lx=81.73%), FSTI=10%

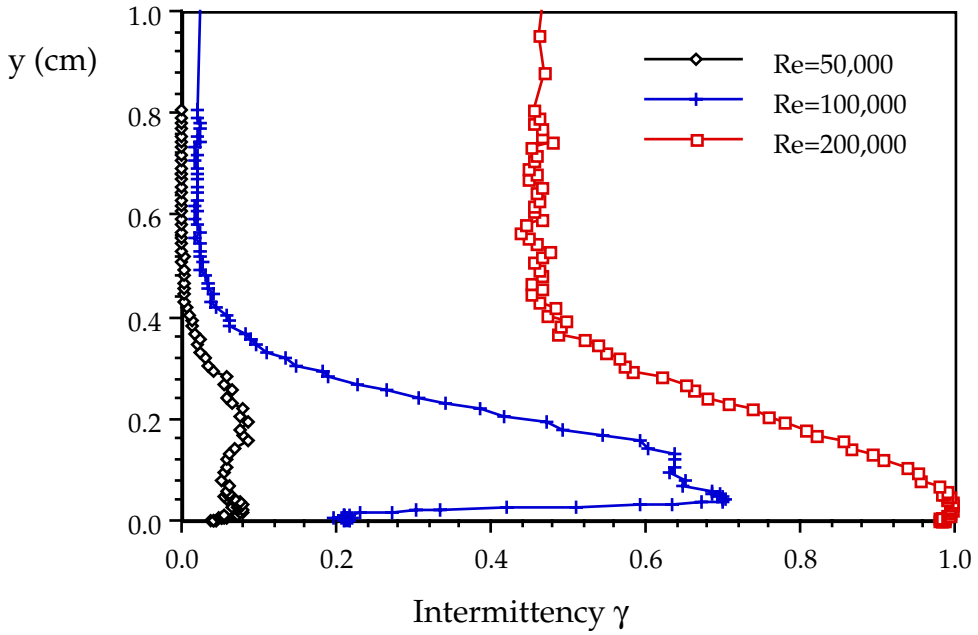

Fig. 4.139 Intermittency distributions at station p10 (x/Lx=81.73%), FSTI=10%

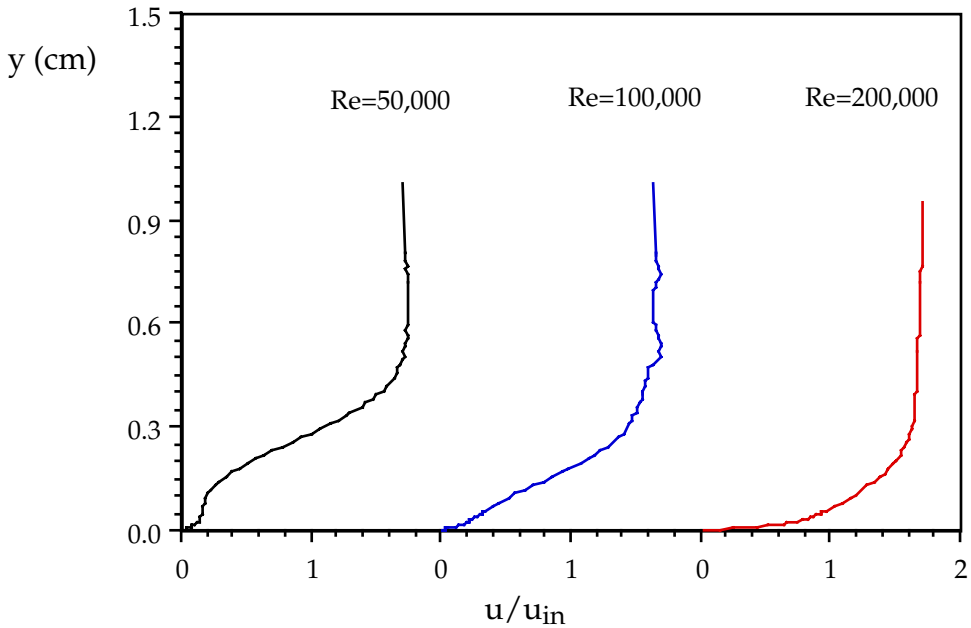

Fig. 4.140 Velocity profiles at station p11 (x/Lx=85.93%), FSTI=10%. Caution: measured values are artificially high at y=0 - 0.356 cm for Re=50k, y=0 - 0.22 cm for Re=100k, y=0 - 0.02 cm for Re=200k

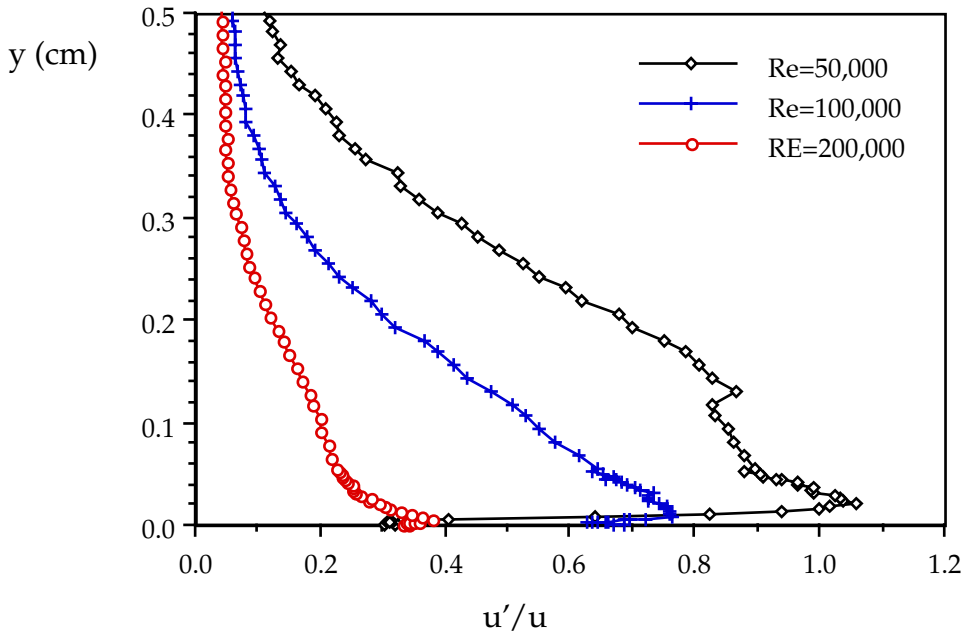

Fig. 4.141 Turbulence intensities at station p11 (x/Lx=85.93%), FSTI=10%

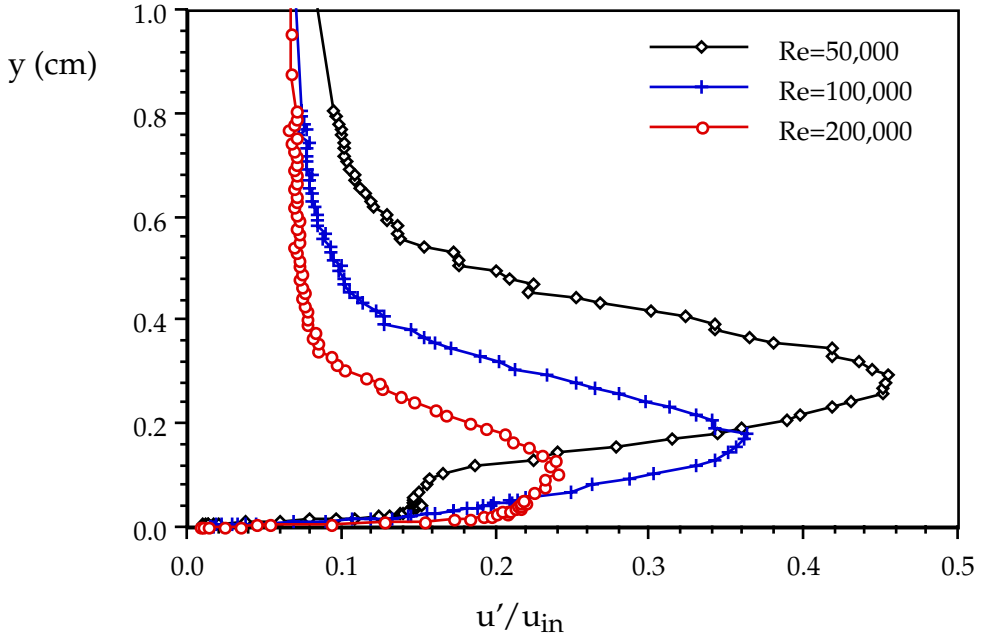

Fig. 4.142 Velocity fluctuations at station p11 (x/Lx=85.93%), FSTI=10%

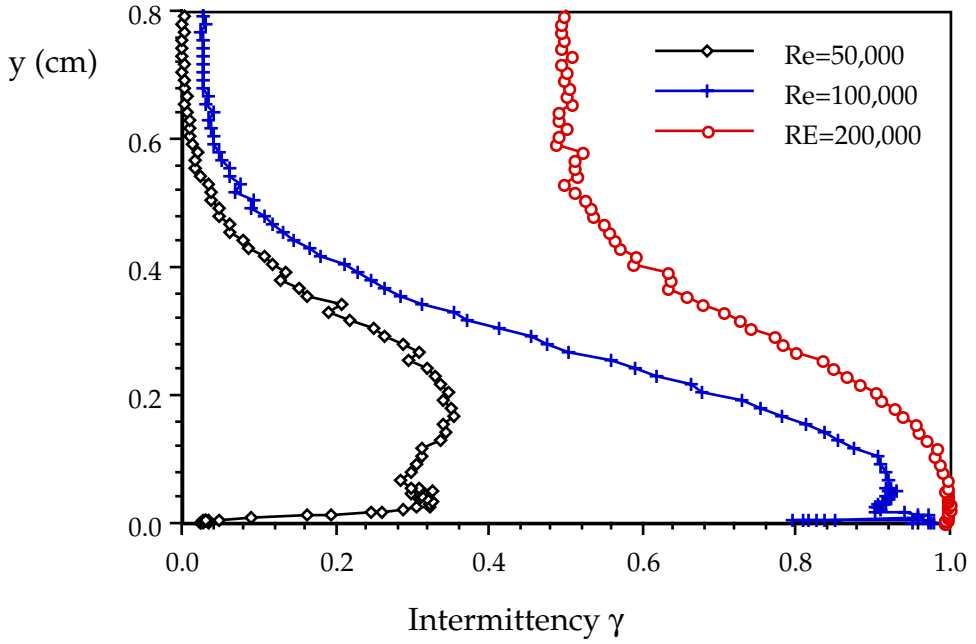

Fig. 4.143 Intermittency distributions at station p11 (x/Lx=85.93%), FSTI=10%

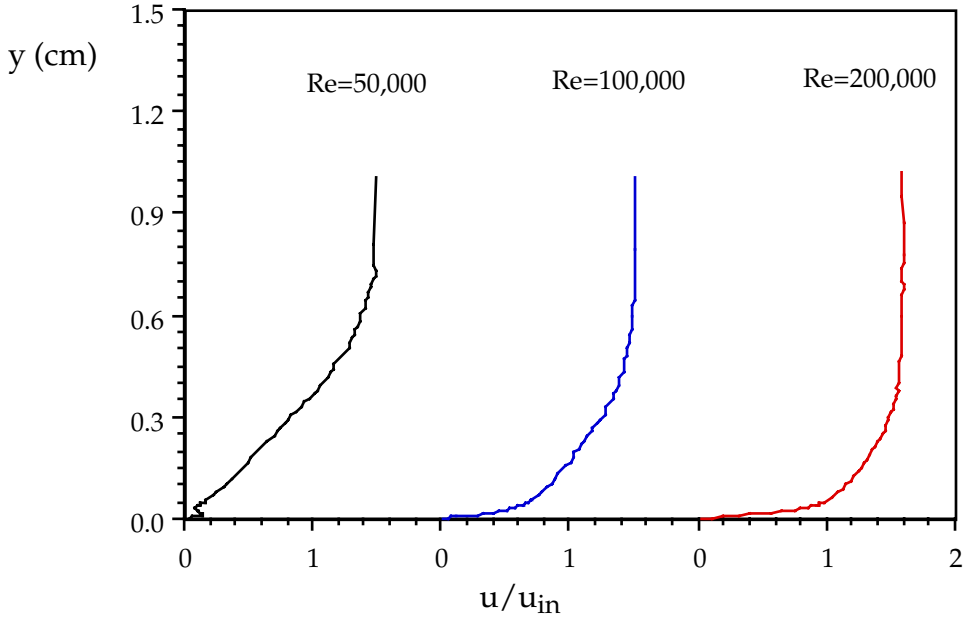

Fig. 4.144 Velocity profiles at station p12 (x/Lx=91.11%), FSTI=10%. Caution: measured values are artificially high at y=0 - 0.46 cm for Re=50k, y=0 - 0.16 cm for Re=100k

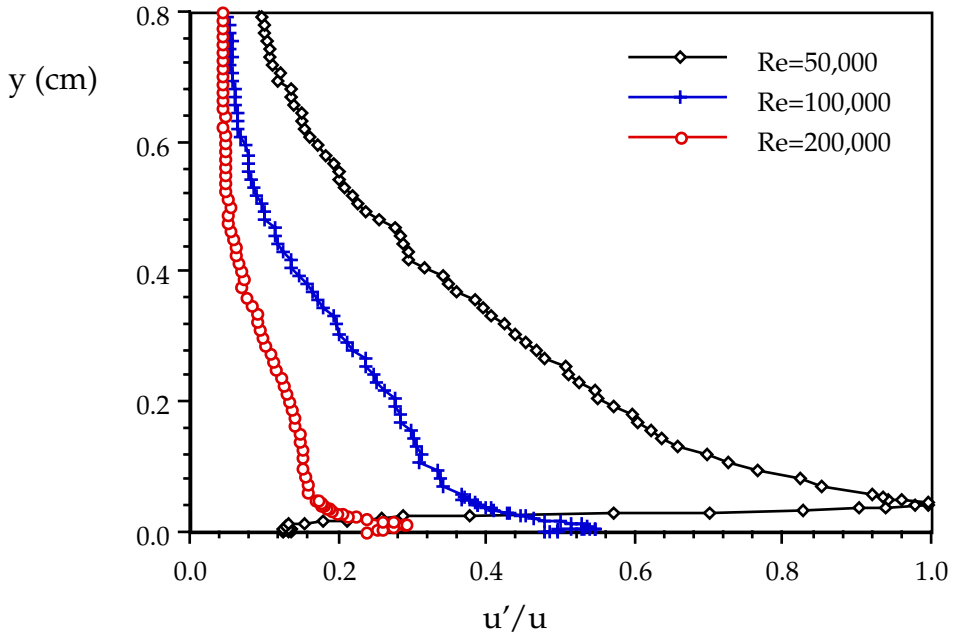

Fig. 4.145 Turbulence intensities at station p12 (x/Lx=91.11%), FSTI=10%

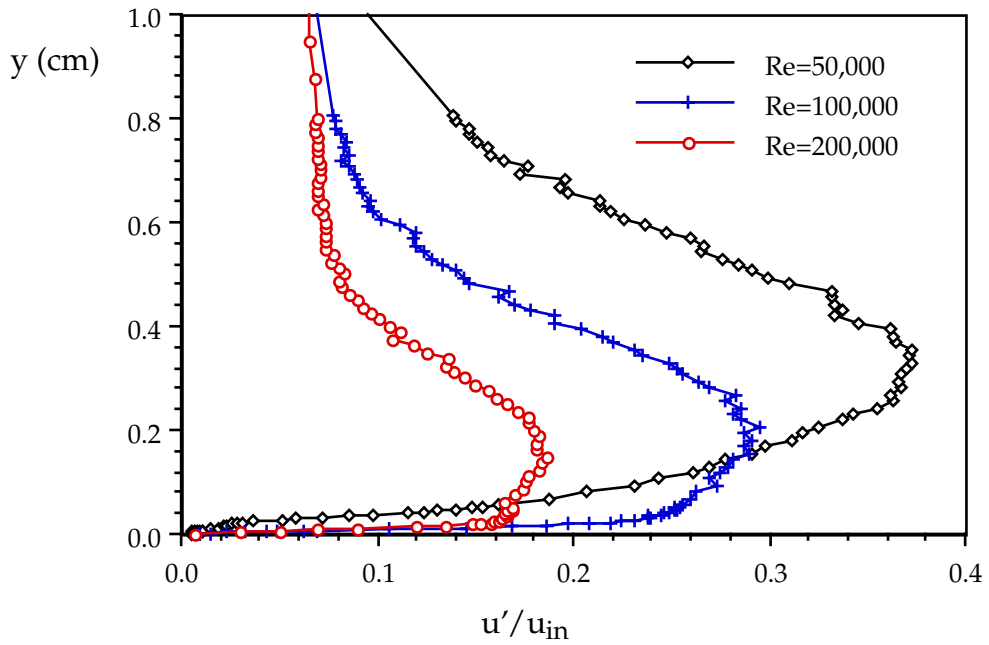

Fig. 4.146 Velocity fluctuations at station p12 (x/Lx=91.11%), FSTI=10%

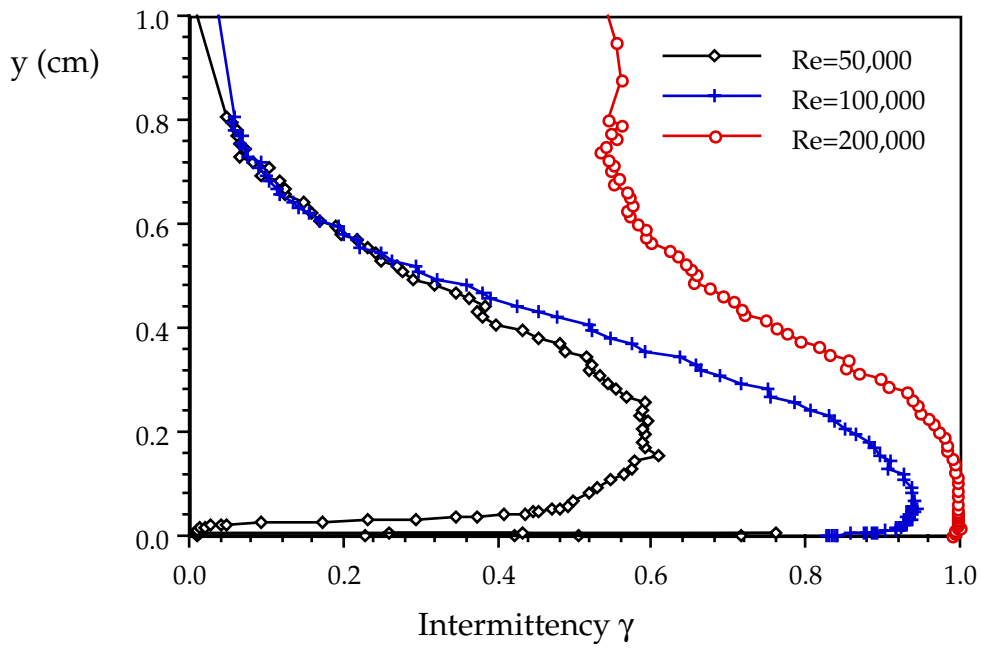

Fig. 4.147 Intermittency distributions at station p12 (x/Lx=91.11%), FSTI=10%

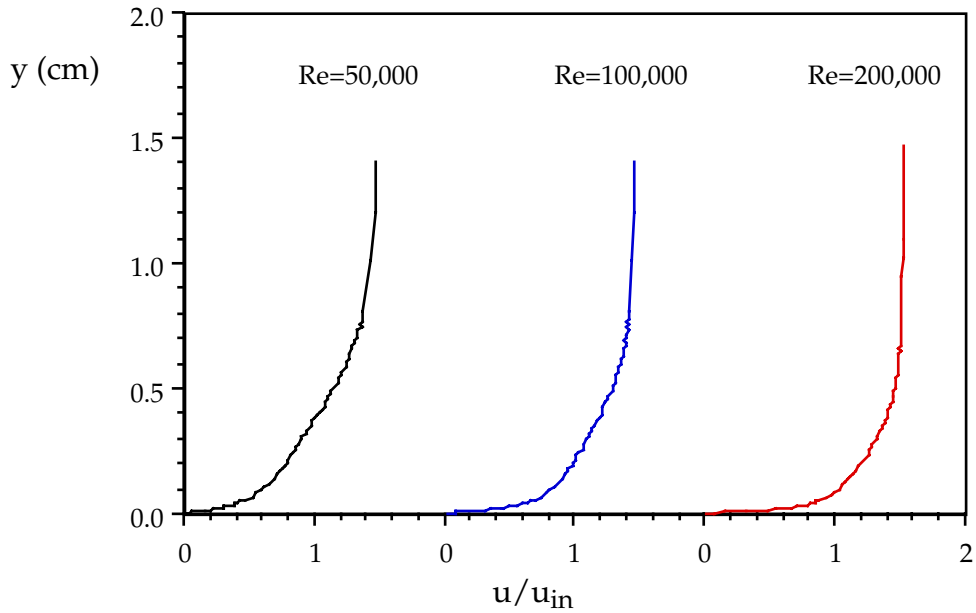

Fig. 4.148 Velocity profiles at station p13 (x/Lx=97.28%), FSTI=10%. Caution: measured values are artificially high at y=0 - 0.45 cm for Re=50k, y=0 - 0.06 cm for Re=100k

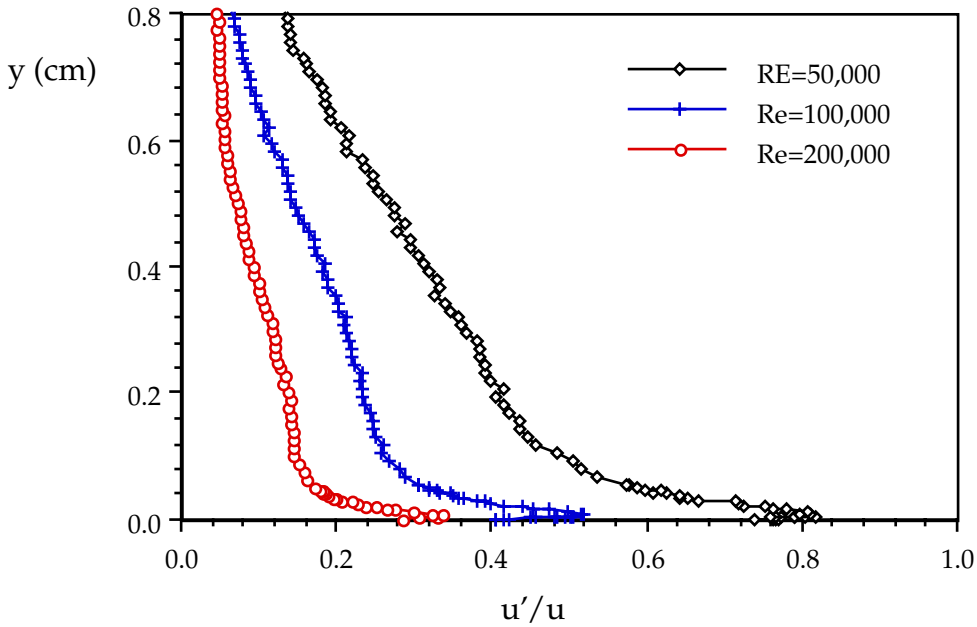

Fig. 4.149 Turbulence intensities at station p13 (x/Lx=97.28%), FSTI=10%

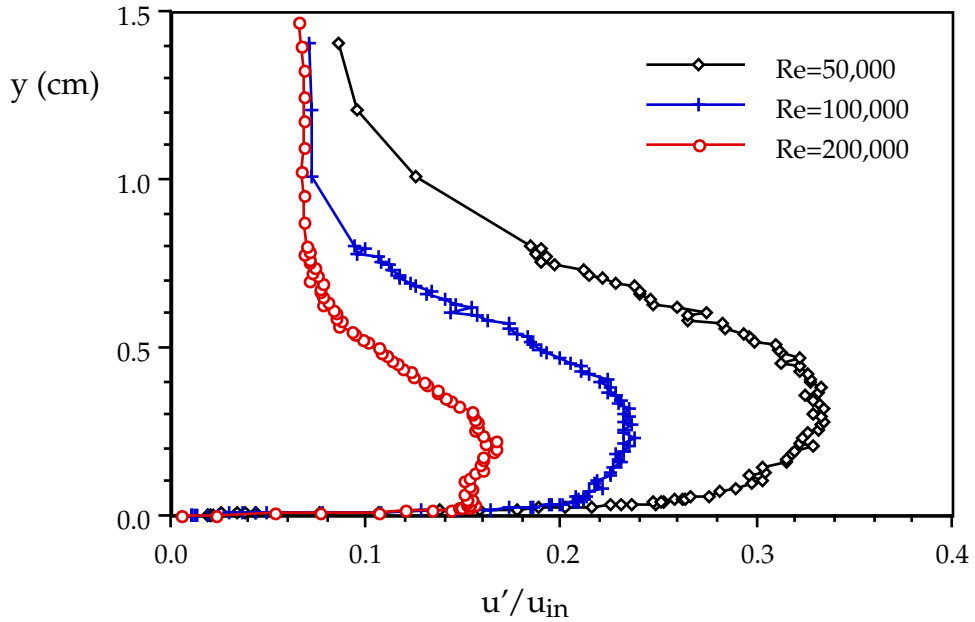

Fig. 4.150 Velocity fluctuations at station p13 (x/Lx=97.28%), FSTI=10%

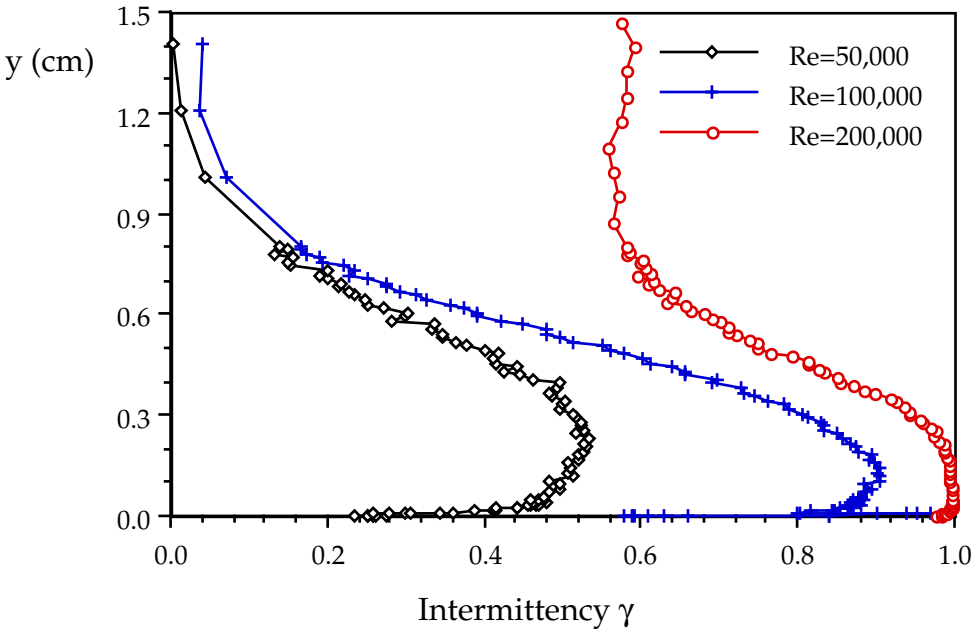

Fig. 4.151 Intermittency distributions at station p13 (x/Lx=97.28%), FSTI=10%

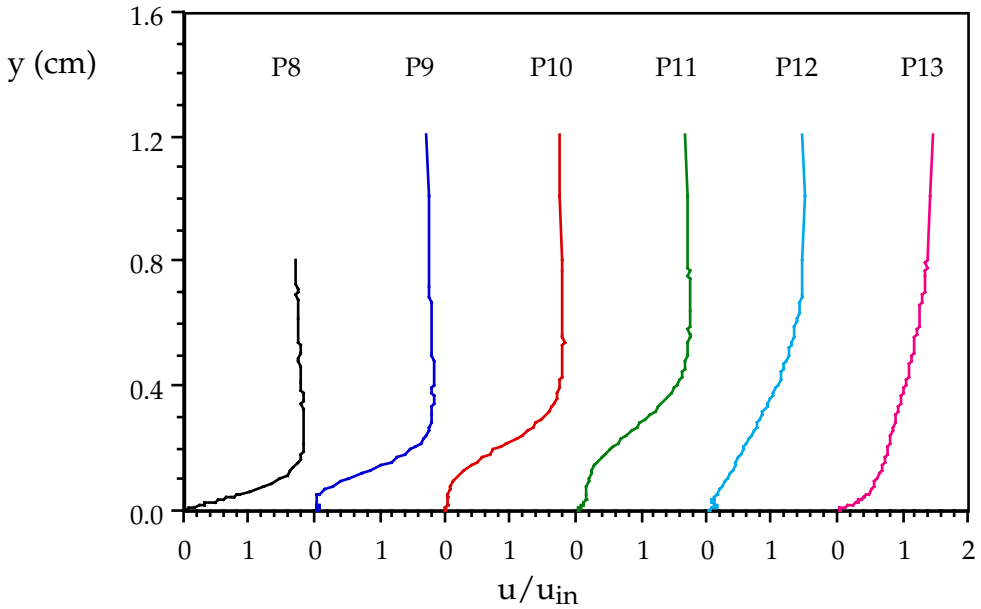

Fig. 4.152 Velocity profiles at p8 - p13 for Re=50,000, FSTI=10%. Caution: measured values are artificially high at y=0.022 - 0.152 cm for p9 y=0 - 0.22 cm for p10, y=0 - 0.356 cm for p11, y=0 - 0.46 cm for p12, y=0 - 0.45 cm for p13

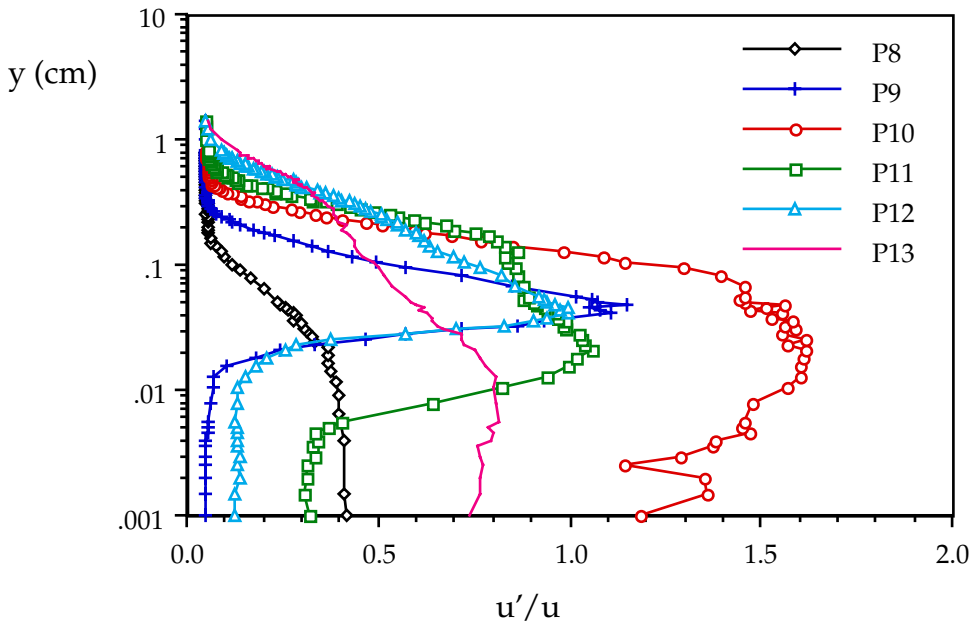

Fig. 4.153 Turbulence intensity at p8 - p13 for Re=50,000, FSTI=10%

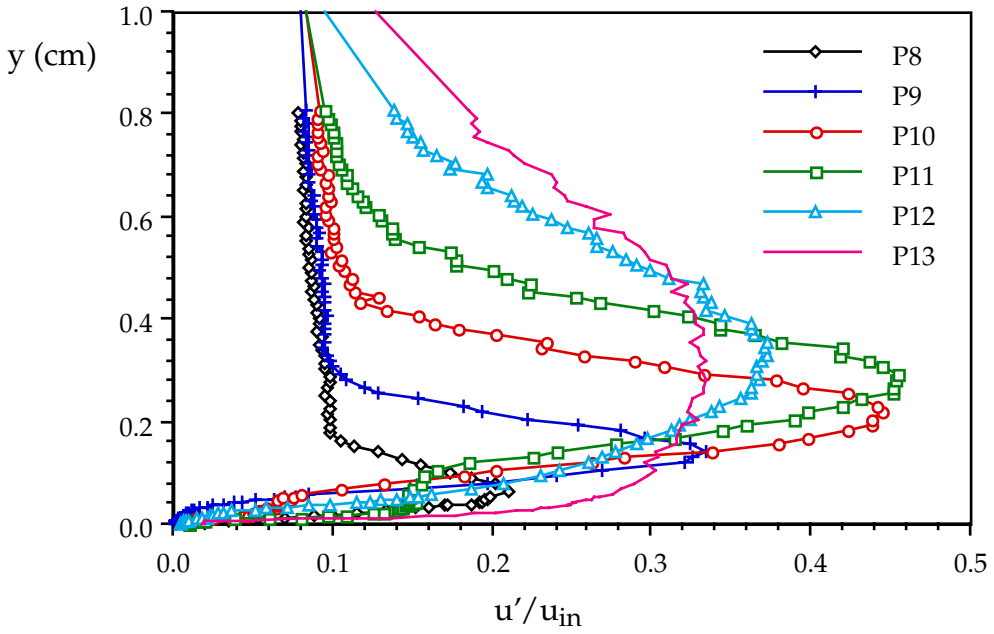

Fig. 4.154 Velocity fluctuations at p8 - p13, Re=50,000, FSTI=10%

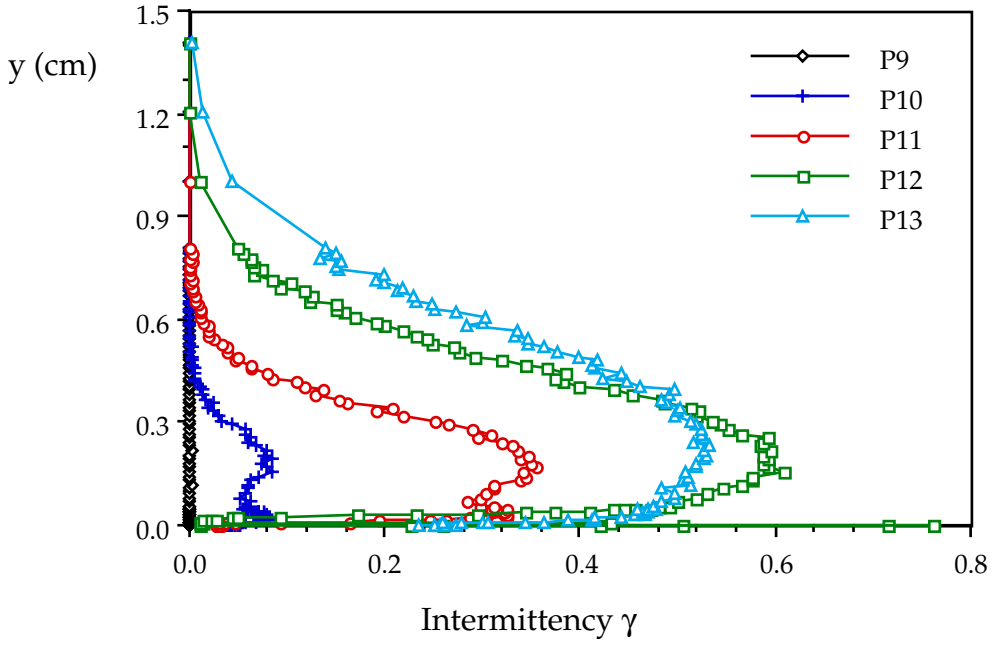

Fig. 4.155 Intermittency distributions for Re=50,000, FSTI=10%

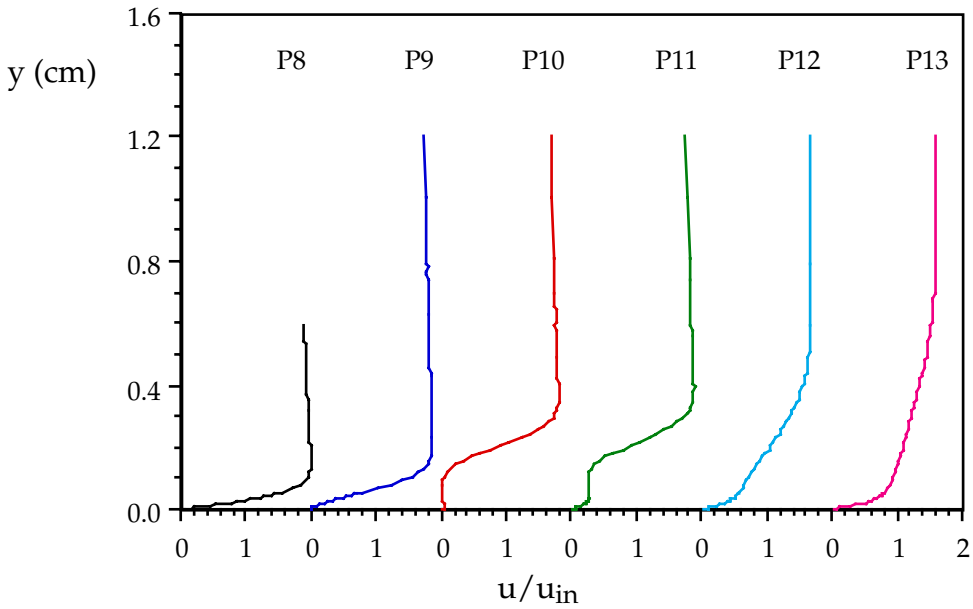

Fig. 4.156 Velocity profiles at p8 - p13 for Re=100,000, FSTI=10%. Caution: measured values are artificially high at y=0.013 - 0.105 cm for p9, y=0 - 0.11 cm for p10, y=0 - 0.02 cm for p11, y=0 - 0.16 cm for p12,y=0 - 0.06 cm for p13

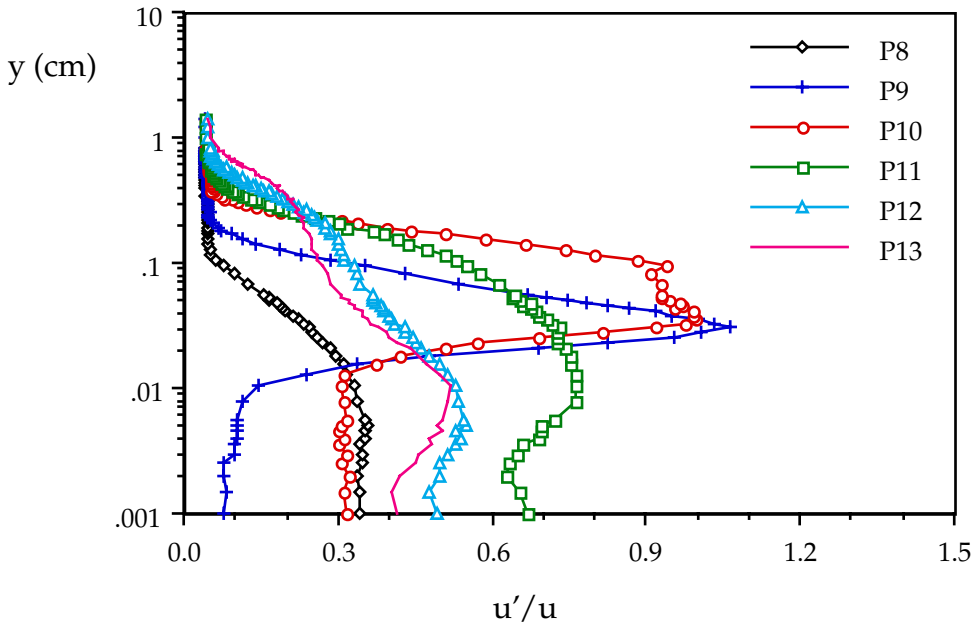

Fig. 4.157 Turbulence intensity at p8 - p13 for Re=100,000, FSTI=10%

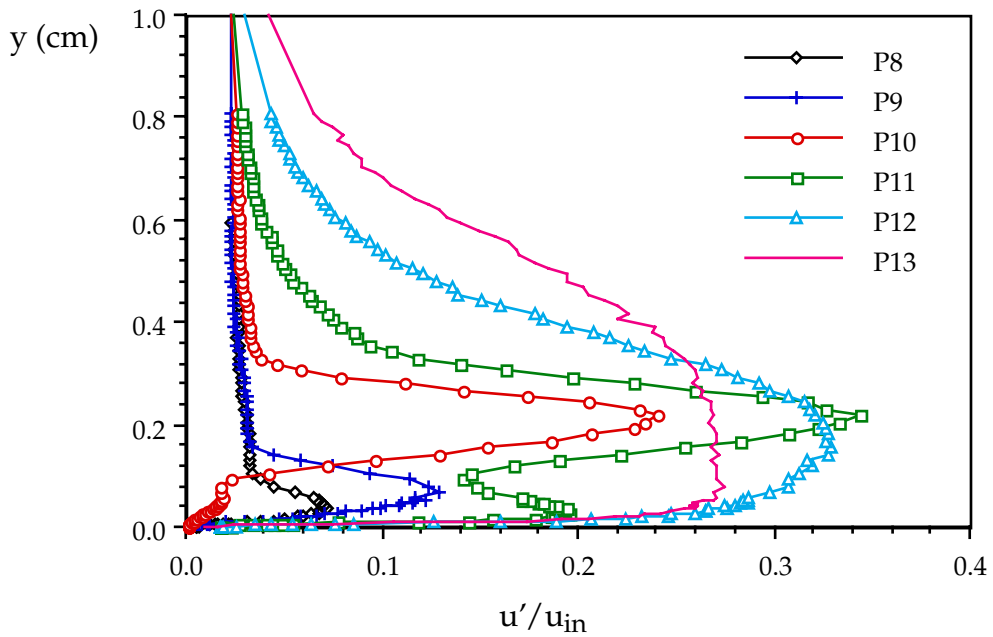

Fig. 4.158 Velocity fluctuations at p8 - p13, Re=100,000, FSTI=10%

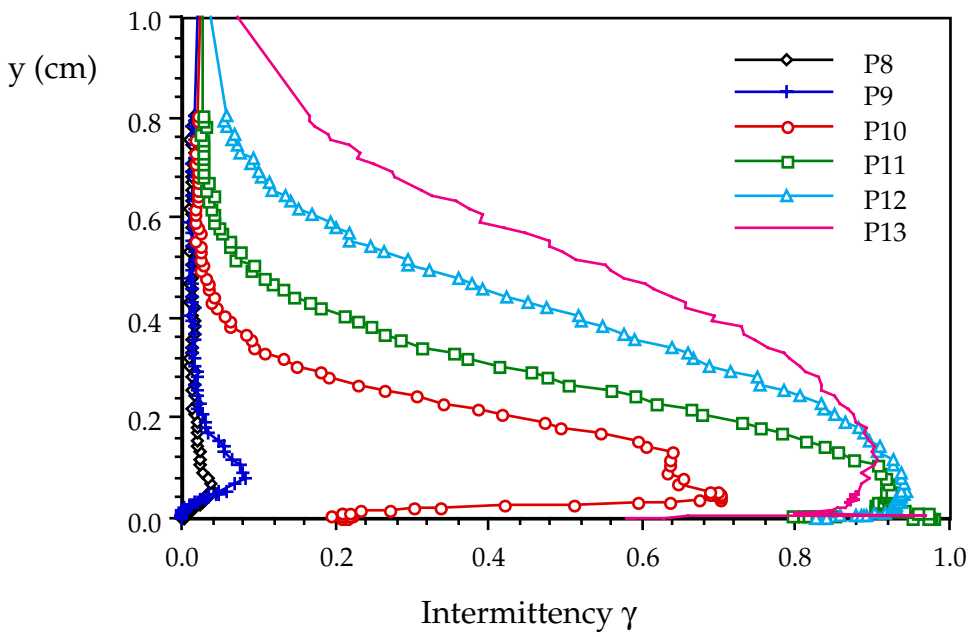

Fig. 4.159 Intermittency distributions for Re=100,000, FSTI=10%

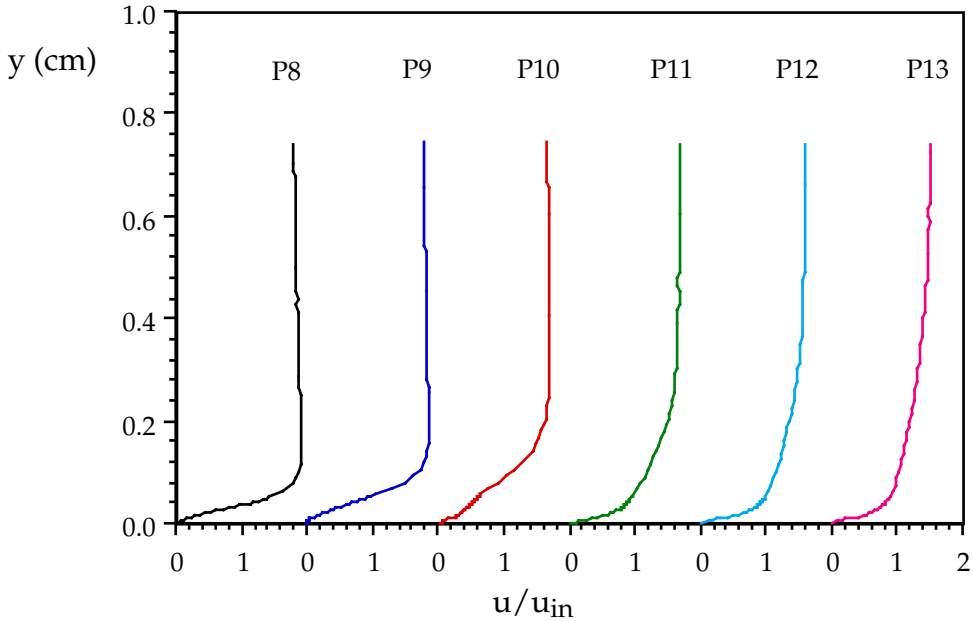

Fig. 4.160 Velocity profiles at p8 - p13 for Re=200,000, FSTI=10%. Caution: measured values are artificially high at y=0 - 0.06 cm for p9, y=0 - 0.11 cm for p10, y=0 - 0.02 cm for p11.

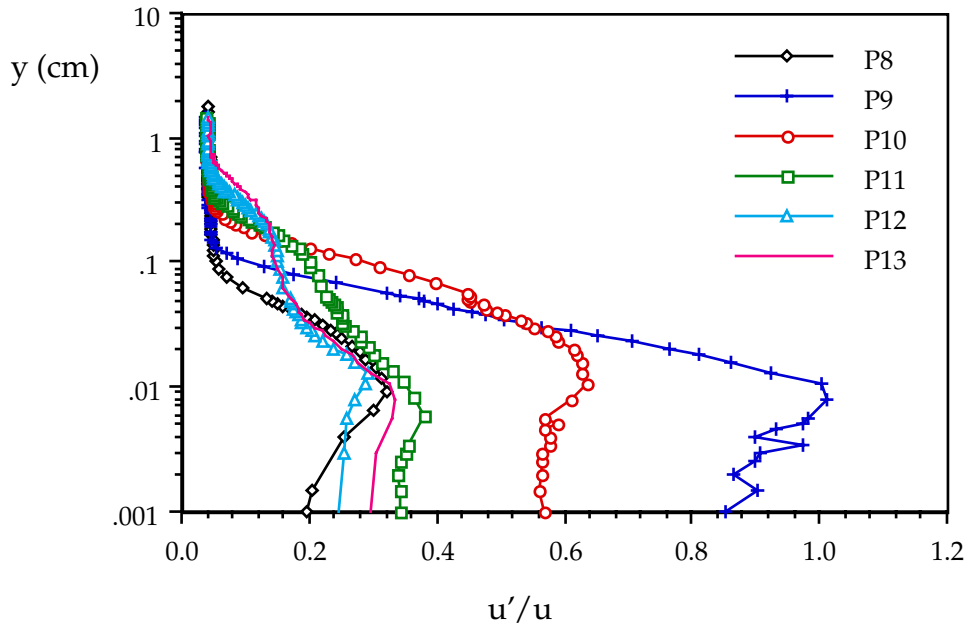

Fig. 4.161 Turbulence intensity at p8 - p13 for Re=200,000, FSTI=10%

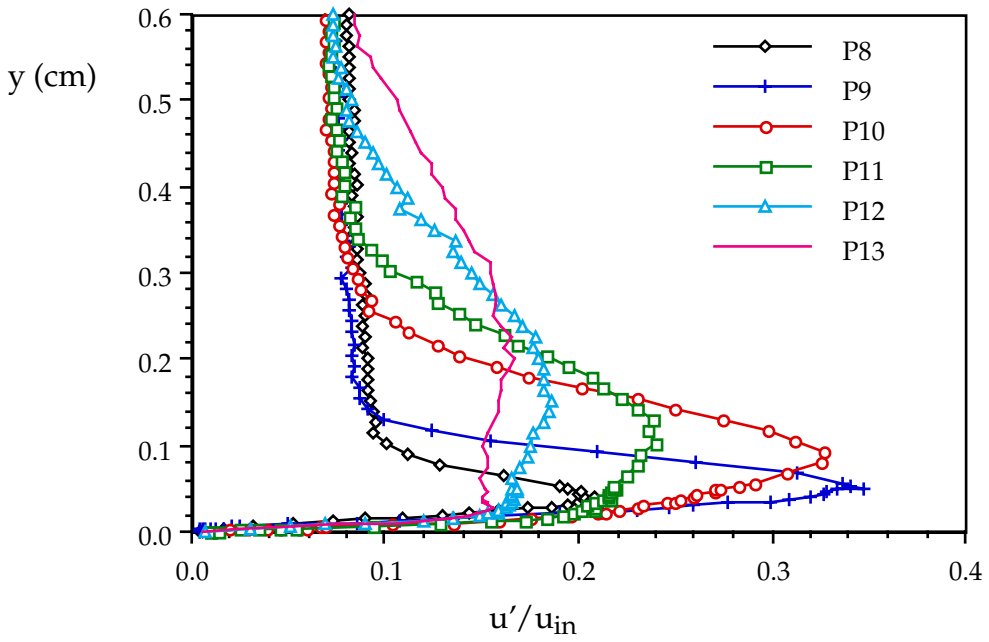

Fig. 4.162 Velocity fluctuations at p8 - p13, Re=200,000, FSTI=10%

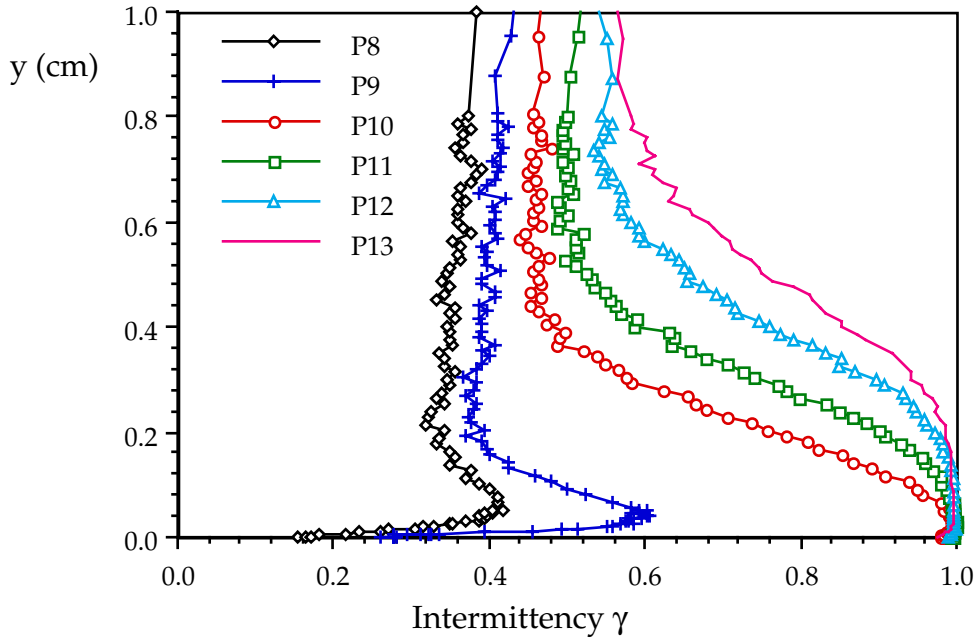

Fig. 4.163 Intermittency distributions for Re=200,000, FSTI=10%

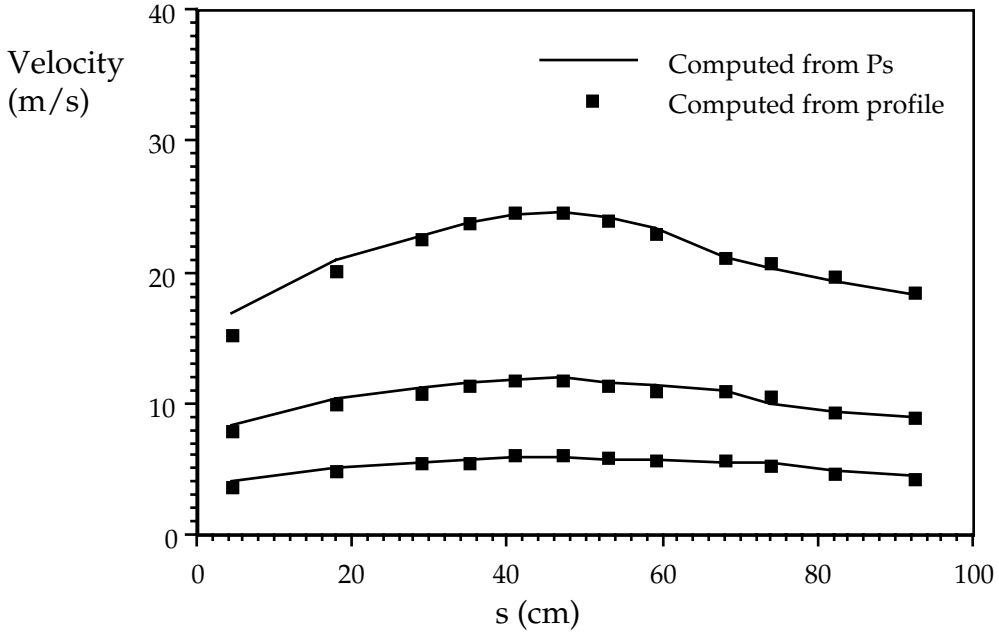

Fig. 4.164 Comparison of measured free-stream velocity to computed velocity from static pressure distributions for FSTI=10%; progressively higher velocities are for Reynolds numbers of 50,000, 100,000, and 200,000.

4.5 SEPARATED FLOW TRANSITION MODELS

A model for intermittency during transition, computed from transition start and end locations, was developed by Narasimha (1985) from turbulent spot theory first suggested by Emmons (1951). A modified version of Narasimha's theory (Volino and Simon, 1995c) was applied to the present study. All the peak (with y-direction) values of γ within the intermittency profiles were selected and used to calculate the function, $f(\gamma) = \sqrt{-\ln(1-\gamma)}$, which was then plotted versus streamwise location, Fig. 4.172. Volino and Simon (1995c) found that in most flows along flat-walls, the data lie along a straight line in these coordinates, although some exceptions may be seen at low γ values (a phenomenon which Narasimha calls "pretransition"). A least-square fit to these data points can be extrapolated to $f(\gamma)=0$ and $f(\gamma)=2.146$, which correspond to $\gamma=0$ and $\gamma=0.99$, respectively, as shown in Fig. 4.172. The corresponding axial positions, s, are taken as the locations of start and end of transition, s_{ts} and s_{te}. The transition start and end positions apparently depend on Reynolds numbers and FSTI, as discussed above. The transition start and end positions and their corresponding Reynolds numbers are presented in Table 4.19. The intermittency within the transition region is plotted against the dimensionless streamwise coordinate $(s - s_{ts}) / (s_{te} - s_{ts})$ in Fig. 4.173. Along with the measured data in Fig. 4.173 is the modified version (Volino and Simon, 1995c) of the Dhawan and Narasimha intermittency distribution model (1958). In the original Dhawan and Narasimha model, s_{ts} was taken at $\gamma=0.25$ and s_{te} was taken at $\gamma=0.75$. Here, s_{ts} is at $\gamma=0$ and s_{te} is taken at $\gamma=0.99$, following the recommendation of Volino and Simon (1995c). Agreement between the data and the model is good; especially

considering that the model was developed for attached boundary layer flow transition whereas the data are for separated flow transition.

Mayle (1991) suggested the following correlations for the length from separation to transition and the length of transition in terms of momentum thickness Reynolds number at separation,

$$Re_{s_{st}} = 300\, Re_{\delta 2_s}{}^{0.7} \qquad \text{(short bubble)} \qquad (4\text{-}1)$$

$$Re_{s_{st}} = 1000\, Re_{\delta 2_s}{}^{0.7} \qquad \text{(long bubble)} \qquad (4\text{-}2)$$

and

$$Re_{LT} = 400\, Re_{\delta 2_s}{}^{0.7} \qquad (4\text{-}3)$$

where $Re_{s_{st}}$ is the Reynolds number based on distance from separation to transition, Re_{LT} is the Reynolds number based on transition length, and $Re_{\delta 2_s}$ is the Reynolds number based on momentum thickness at separation. Roberts (1973, 1980) developed a correlation for the length from separation to transition in terms of both the turbulence level and turbulence length scale. Davis et al. (1985) modified it yielding the correlation :

$$Re_{s_{st}} = 25{,}000 \log_{10}\left(\mathrm{Coth}\left(17.32\ TI_e\right)\right) \qquad (4\text{-}4)$$

where TI_e is the local turbulence intensity, given as $TI_e = FSTI \dfrac{U_{in}}{U_\infty}$.

The Reynolds numbers, $Re_{s_{st}}$, were computed from the measured data and are plotted in Fig. 4.174 as functions of $Re_{\delta 2_s}$. Mayle's (1991) separated-flow models discussed above, Eqns. (4-1) and (4-2), are also shown in Fig. 4.174. Low and moderate free-stream disturbance (FSTI=0.5% and 2.5%) flows agree with Mayle's model. High free stream disturbance flow for Re=100,000 is far too low, compared to the model, as the distance between transition and separation is much smaller than predicted. In Fig. 4.175, transition length Reynolds numbers, Re_{LT}, are compared to Mayle's model, Eqn. (4-3). The model by Davis et al.

(1985), Eqn. (4-4), is compared to the data in Fig. 4.176. This correlation seems to capture a turbulence intensity effect. But the Re=100,000, FSTI=10% case distance to transition is much smaller than given by the model. Since the separation bubble length for this case is small, the error is also small.

Table 4.19 Start and end transition points, separation and reattachment points, free-stream velocity at separation, momentum thickness Reynolds number at separation, and local free-stream turbulence.

	FSTI=0.5%			FSTI=2.5%			FSTI=10%	
Re X1000	50	100	200	50	100	200	50	100
s_s (cm)	7.57	7.77	8.17	8.07	8.10	8.32	8.27	8.37
s_r (cm)	>15.27	>15.27	12.02	13.8-14	12.24	10.77	12.67	11.47
s_{ts} (cm)	12	10.94	10.45	10-11	10.23	8.73	9.28	8.5
s_{te} (cm)	(1)	13.05	11.07	15.81	11.83	10.23	16.33	12.18
u_s (m/s)	5.95	12.07	24.14	5.78	12.4	24.32	5.7	11.1
s_{ts}-s_s (cm)	4.43	3.17	2.28	2.02	2.13	0.41	1.01	0.13
Re_{sst} X1000	16.939	2.461	35.395	7.526	17.017	6.349	3.709	0.928
$\delta 2_s$ (mm)	0.206	0.214	0.120	0.213	0.142	0.117	0.263	0.177
$Re_{\delta 2s}$	78.77	166.11	186.32	79.20	113.23	182.96	96.57	126.35
s_{te}-s_{ts} (cm)	(1)	2.11	0.63	5.71	1.60	1.50	7.05	3.68
Re_{LT} X1000	(1)	16.362	9.71	21.247	12.727	23.473	25.888	26.269
TIe (%)	1.25	0.75	0.51	1.88	1.65	2.26	5.3	4.87

(1) Transition was not complete.

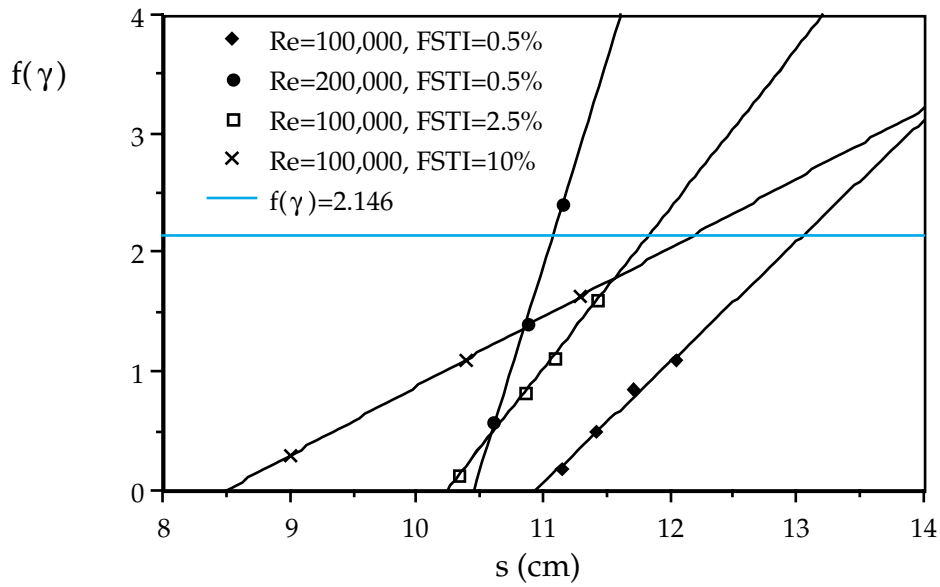

Fig. 4.172 Intermittency in $f(\gamma)=\sqrt{-\ln(1-\gamma)}$ and s coordinates

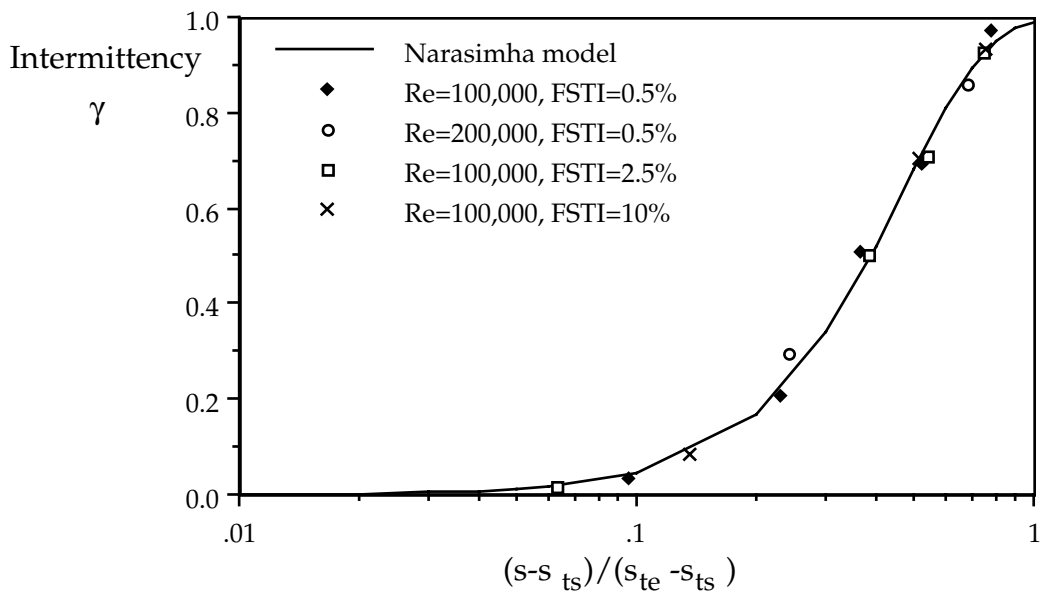

Fig. 4.173 Intermittency distributions through transition

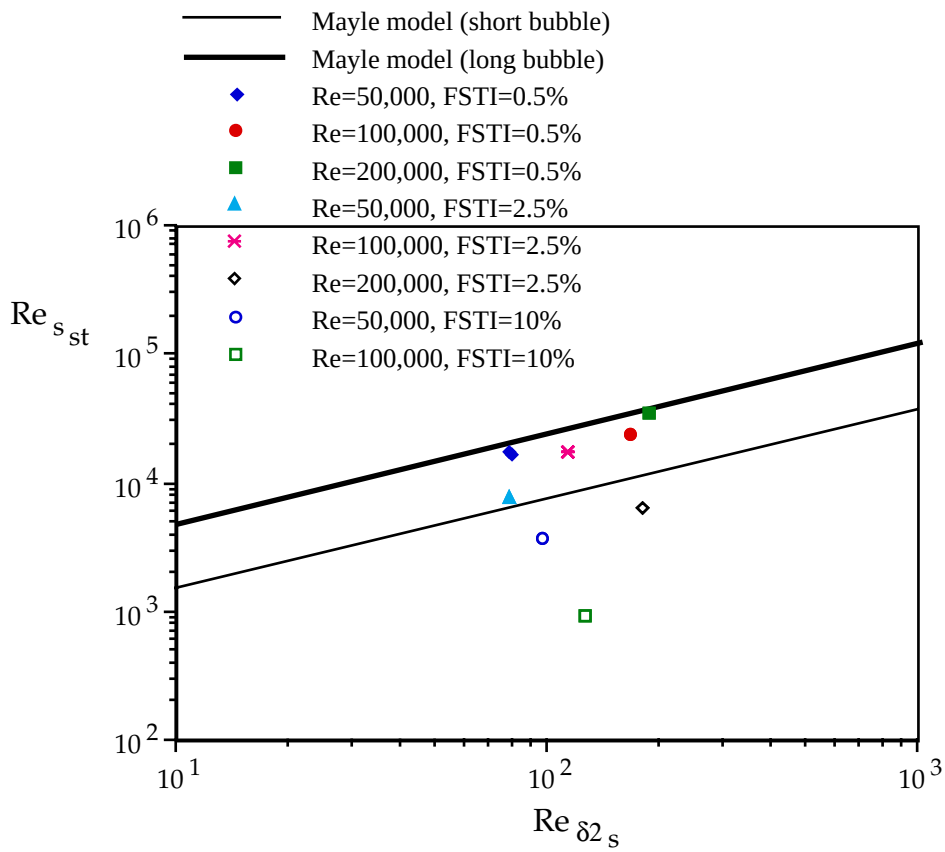

Fig. 4.174 Reynolds number based on distance between separation and transition vs. separation Reynolds number

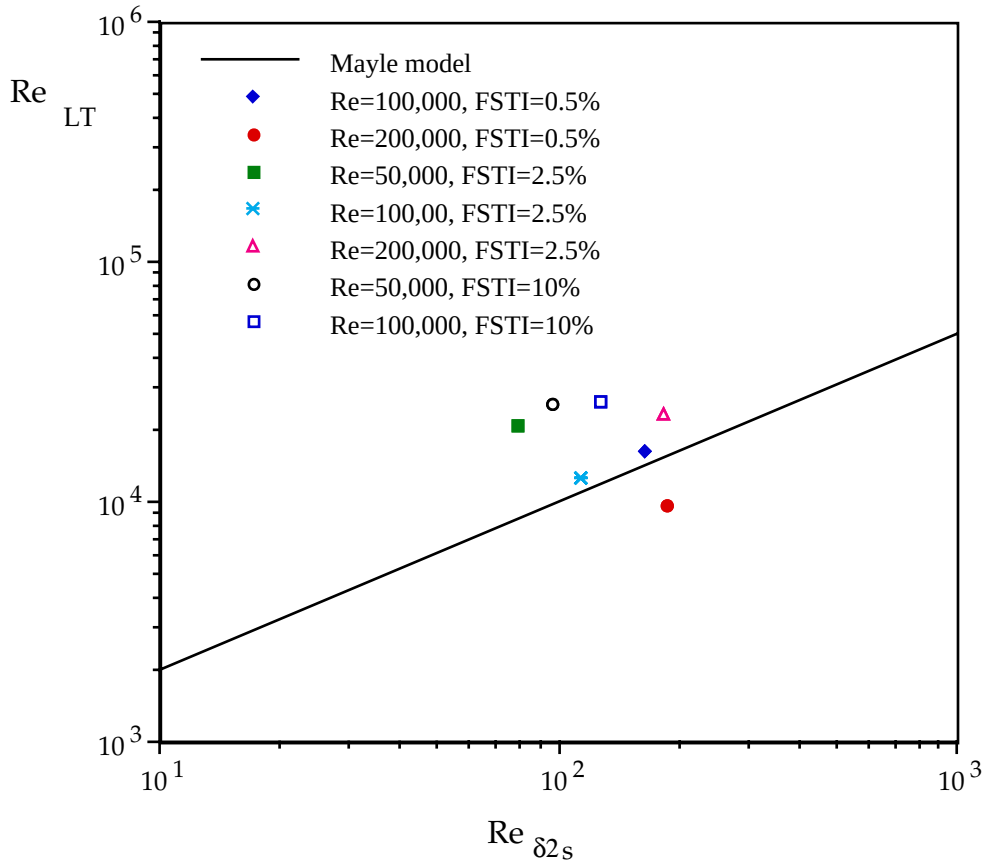

Fig. 4.175 Transition length Reynolds number in separation bubbles vs. separation Reynolds number

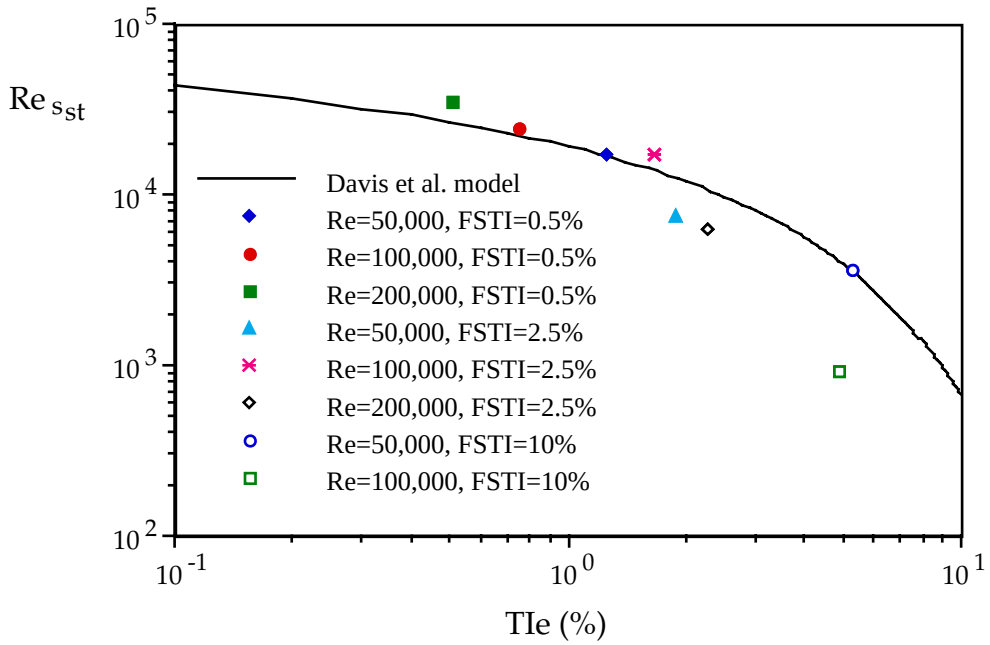

Fig. 4.176 Comparison of $Re_{s_{st}}$ to Davis et al. model (1985)

CHAPTER FIVE
CONCLUSIONS

Velocity, pressure and intermittency profiles were measured in boundary layers on the suction surface of a low-pressure gas turbine airfoil. Flow separation and transition in the separation region were observed for the cases of Re=50,000 and 100,000 with all free-stream turbulence levels. The cases with Re=200,000 showed laminar flow separation and shear flow transition when FSTI=0.5% and 2.5% but for the case of Re=200,000 and FSTI=10% the transition started, then the flow separated, followed by completion of transition. The same was observed for the Re=300,000, FSTI=2.5% case.

For the Re=50,000, FSTI=0.5% case, there was not enough room for shear layer transition to become complete. Transition in the shear layer over the separation bubble was found in all other separated flows. Transition in these separated boundary layers on the suction surface followed the same path:
1) laminar boundary layer development, 2) strong growth rate as a laminar boundary layer when the adverse pressure gradient section is nearly reached, 3) laminar separation, 4) transition of the shear layer, 5) turbulent flow throughout the shear layer and near-wall region, 6) reattachment, and 7) growth as an attached turbulent boundary layer. The speed with which it proceeds through these steps and the degree to which it completes these steps increase as Re or FSTI increases.

Table 5.1 summarizes all the cases investigated. In the table, S indicates separation and T denotes complete transition.

TABLE 5.1 Conclusions of the cases investigated:

	Re=50,000	Re=100,000	Re=200,000	Re=300,000
FSTI=0.5%	S	S, T	S, T	S, T
FSTI=2.5%	S, T	S, T	S, T	T, S
FSTI=10%	S, T	S, T	T, S	

Sketches of the airfoils with lines indicating the edges of the wall layer (boundary layer and shear layer), drawn to scale, for the cases investigated are given in Figs. 5.1 to 5.11. Boundary layer types (laminar or turbulent, attached or separated), onset of transition locations, and separation points are marked also on these sketches.

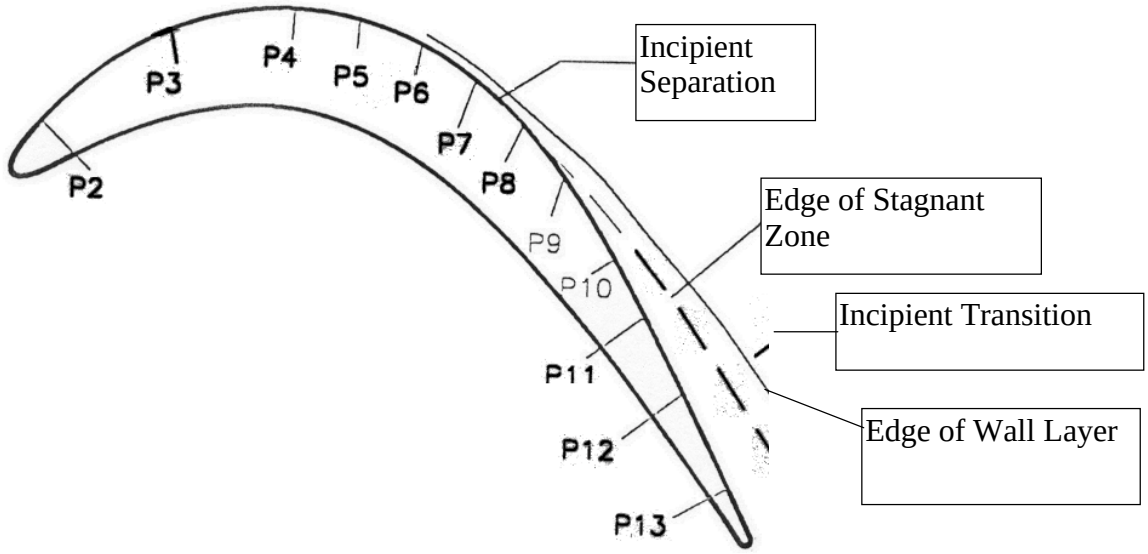

Fig. 5.1 Sketch of the airfoil with lines indicating the edges of the separation zone and wall layer for Re=50,000, FSTI=0.5%

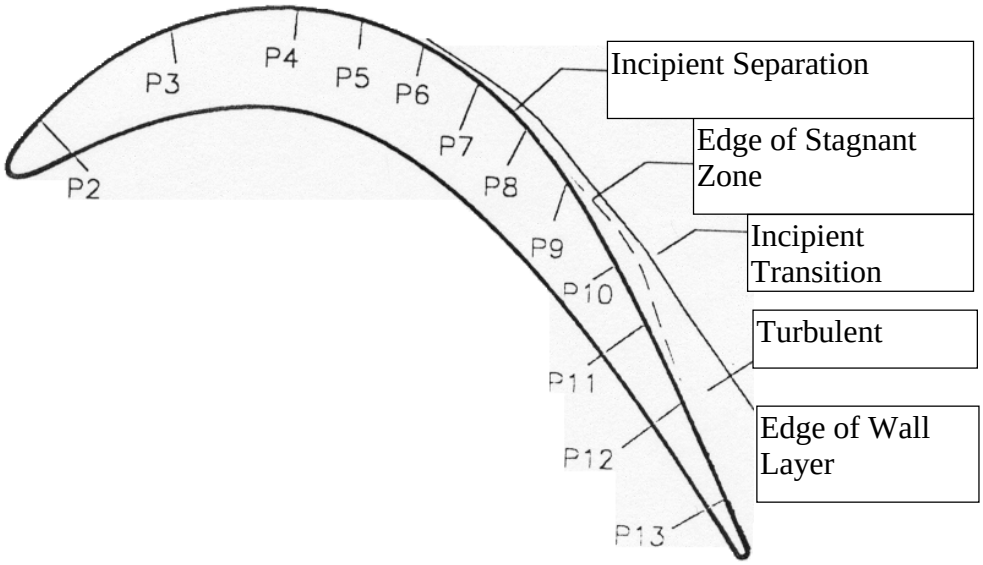

Fig. 5.2 Sketch of the airfoil with lines indicating the edges of the separation zone and wall layer for Re=100,000, FSTI=0.5%

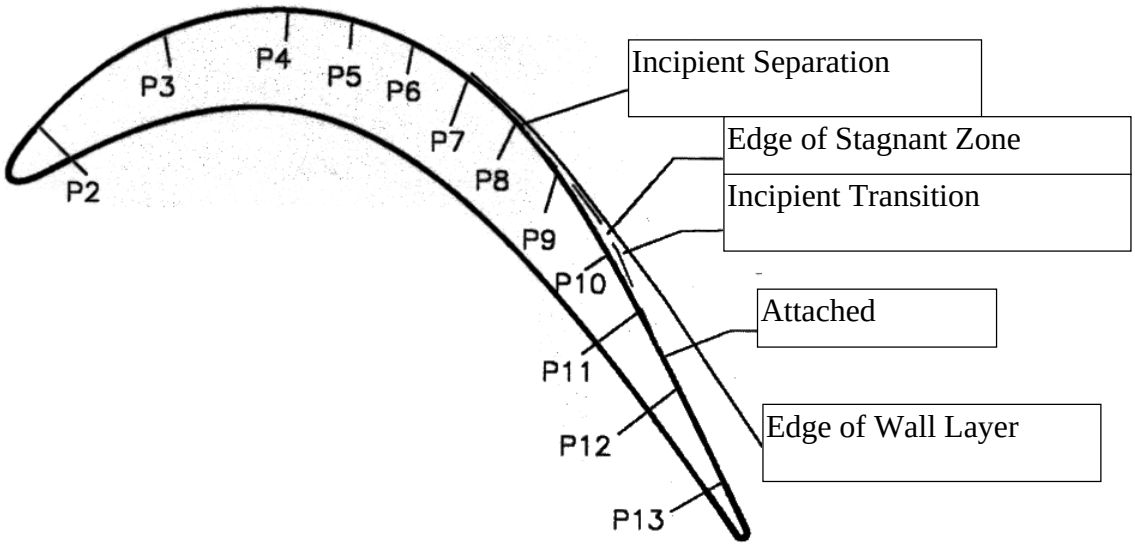

Fig. 5.3 Sketch of the airfoil with lines indicating the edges of the separation zone and wall layer for Re=200,000, FSTI=0.5%

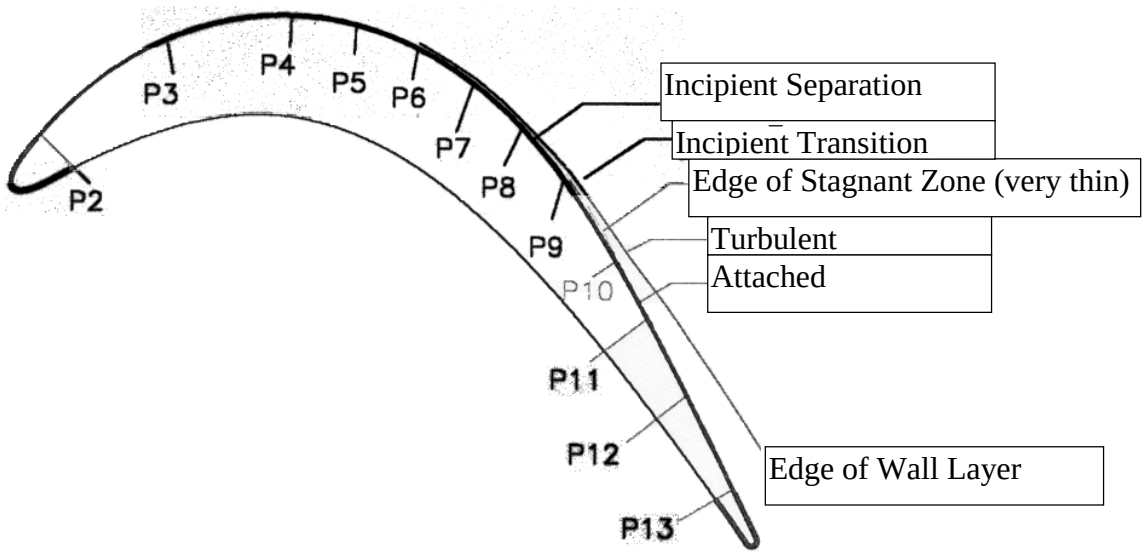

Fig. 5.4 Sketch of the airfoil with lines indicating the edges of the separation zone and wall layer for Re=300,000, FSTI=0.5%

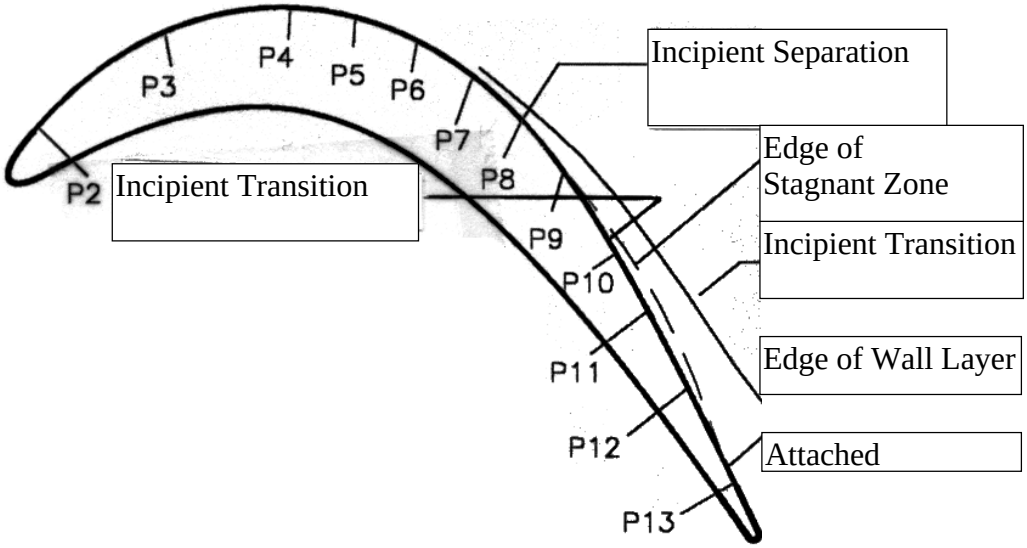

Fig. 5.5 Sketch of the airfoil with lines indicating the edges of the separation zone and wall layer for Re=50,000, FSTI=2.5%

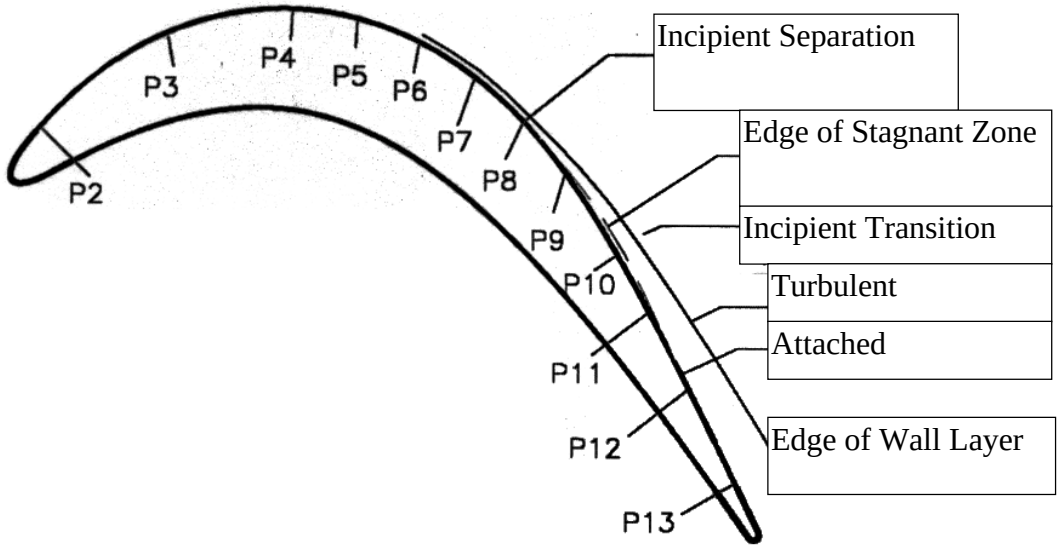

Fig. 5.6 Sketch of the airfoil with lines indicating the edges of the separation zone and wall layer for Re=100,000, FSTI=2.5%

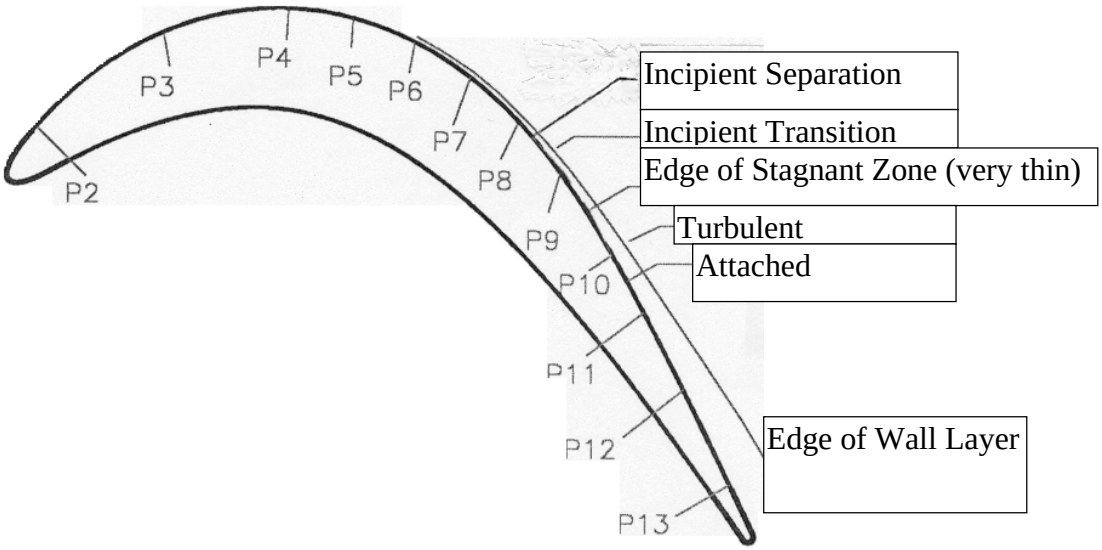

Fig. 5.7 Sketch of the airfoil with lines indicating the edges of the separation zone and wall layer for Re=200,000, FSTI=2.5%

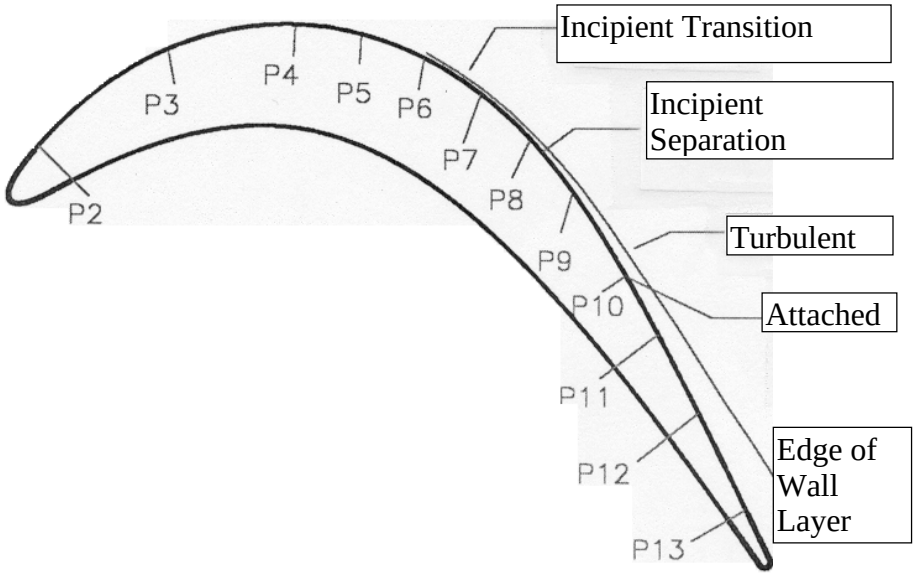

Fig. 5.8 Sketch of the airfoil with lines indicating the edges of the separation zone and wall layer for Re=300,000, FSTI=2.5%

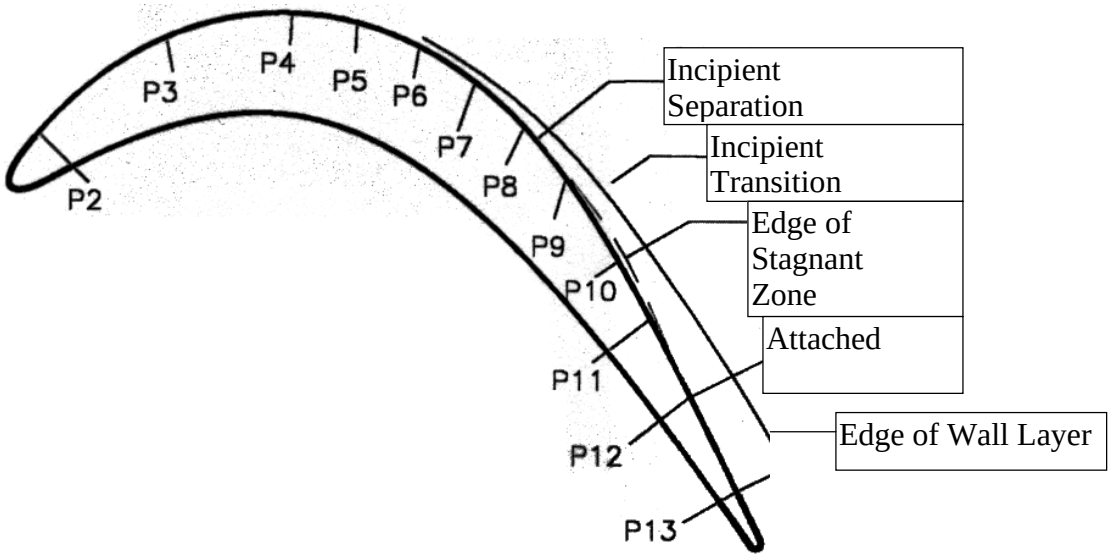

Fig. 5.9 Sketch of the airfoil with lines indicating the edges of the separation zone and wall layer for Re=50,000, FSTI=10%

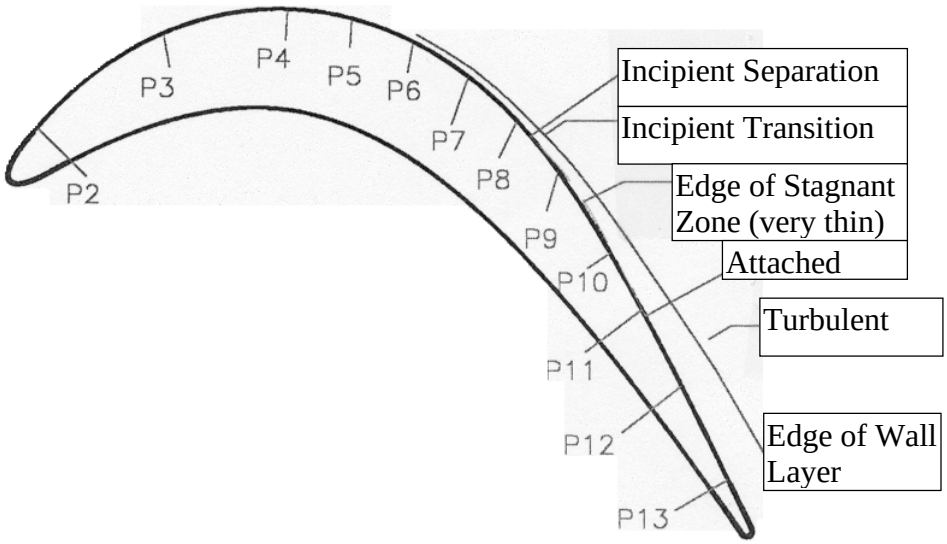

Fig. 5.10 Sketch of the airfoil with lines indicating the edges of the separation zone and wall layer for Re=100,000, FSTI=10%

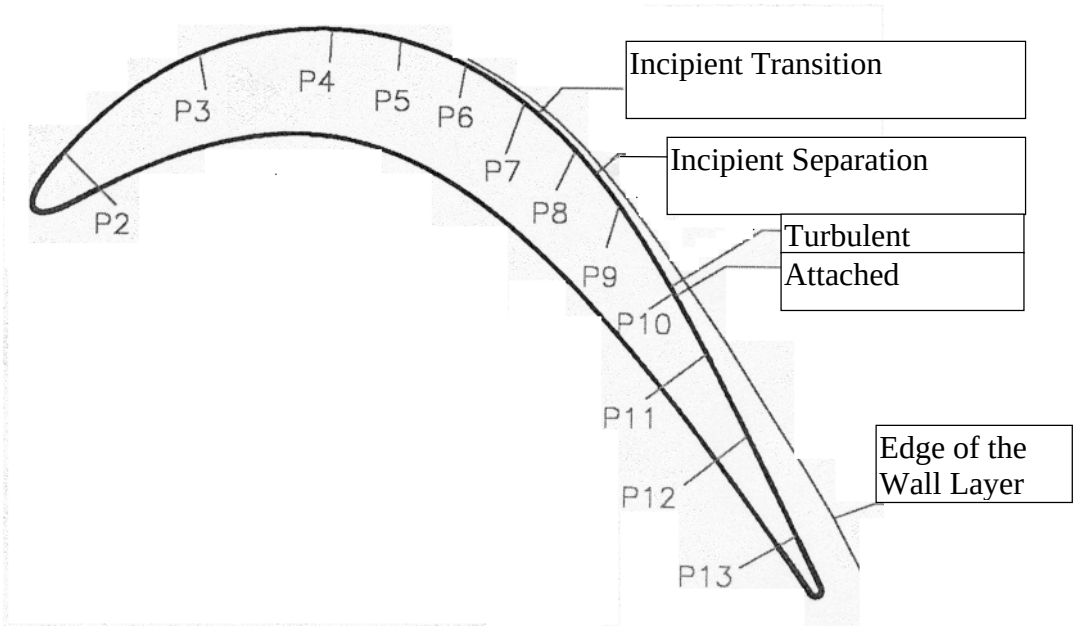

Fig. 5.11 Sketch of the airfoil with lines indicating the edges of the separation zone and wall layer for Re=200,000, FSTI=10%

REFERENCES

Ames, F. E. (1994), "Experimental Study of Vane Heat Transfer and Aerodynamics at Elevated Levels of Turbulence," NASA CR 4633.

Blair, M. F. (1990), "Boundary Layer Transition in Accelerating Flows with Intense Freestream Turbulence," *J. Heat Transfer*, Vol. 105, pp. 33-40.

Blair, M. F. (1992a), "Boundary-Layer Transition in Accelerating Flows with Intense Freestream Turbulence: Part 1 - Disturbances Upstream of Transition Onset," *J. Fluids Eng.*, Vol. 114, pp. 313-321.

Blair, M. F. (1992b), "Boundary-Layer Transition in Accelerating Flows with Intense Freestream Turbulence: Part 2- The Zone of Intermittent Turbulence," *J. Fluids Eng.*, Vol. 114, pp. 322-332.

Champagne, F. H., Sleicher, C. A. and Wehrmann, O. H. (1967a), "Turbulence Measurements with Inclined Hot-Wires, Part 1. Heat Transfer Experiments with Inclined Hot-Wire," *J. Fluid Mech.*, Vol. 28, pp. 153-175.

Champagne, F. H. and Sleicher, C. A. (1967b), "Turbulence Measurements with Inclined Hot-Wires, Part 2. Hot-Wire Response Equations," *J. Fluid Mech.*, Vol. 28, pp. 177-182.

Chew, Y. T., Shi, S. X. and Khoo, B. C. (1995), "On the Numerical Near-Wall Corrections of Single -Wire Measurements," *Int. J. of Heat and Fluid Flow*, Vol. 16, pp. 471-476.

Davis, R. L., Carter, J. E. and Reshotko, E. (1985), "Analysis of Transitional Separation Bubbles on Infinite Swept Wings," AIAA Paper # AIAA-85-1685.

Dhawan, S. and Narasimha, R. (1958), "Some Properties of Boundary Layer Flow During the Transition from Laminar to Turbulent Motion," J. Fluid Mech. Vol. 3, pp 418-436.

Emmons, H. W. (1951), "The Laminar-Turbulent Transition in a Boundary Layer - Part I," *J. Aeronautical Science*, Vol. 18, pp. 490-498.

Halstead, D. E., Wisler, D. C., Okiishi, T. H., Walker, G. J., Hodson, H. P. and Shin, H. (1995a), "Boundary Layer Development in Axial Compressors and Turbines Part 1 of 4: Composite Picture," ASME paper 95-GT-461.

Halstead, D. E., Wisler, D. C., Okiishi, T. H., Walker, G. J., Hodson, H. P. and Shin, H. (1995b), "Boundary Layer Development in Axial Compressors and Turbines Part 2 of 4: Compressors," ASME paper 95-GT-462.

Halstead, D. E., Wisler, D. C., Okiishi, T. H., Walker, G. J., Hodson, H. P. and Shin, H. (1995c), "Boundary Layer Development in Axial Compressors and Turbines Part 3 of 4: LP Turbines," ASME paper 95-GT-463.

Halstead, D. E., Wisler, D. C., Okiishi, T. H., Walker, G. J., Hodson, H. P. and Shin, H. (1995d), "Boundary Layer Development in Axial Compressors and Turbines Part 4 of 4: Computations & Analyses," ASME paper 95-GT-464.

Hinze, J. O. (1975), Turbulence, McGraw Hill, New York, 2nd Ed.

Henk, R. W. (1990), "An Experimental Study of the Fluid Mechanics of an Unsteady, Three-Dimensional Separation," Ph.D. Thesis, Stanford University, Stanford, CA.

Kim, J., Kline, S. J. and Johnston, J. P. (1978), "Investigation of Separation and Reattachment of a Turbulent Shear Layer: Flow Over a Backward-Facing Step," Report MD-37, Thermosciences Division, Department of Mechanical Engineering, Stanford University, Stanford, CA

Kim, J. (1990), "Freestream Turbulence and Concave Curvature Effects on Heated, Transitional Boundary Layers," Ph.D. Thesis, Department of Mechanical Engineering, University of Minnesota, Minneapolis, MN.

Kim, J. and Simon, T. W. (1991). "Free-stream Turbulence and Concave Curvature Effects on Heated Transitional Boundary Layers, Vol. I - Final Report," NASA CR 187150, Vol. II - Programs and Tabulated Data," NASA CR 187151.

Kim, J., Simon, T. W. and Russ, S. G. (1992). “Free-Stream Turbulence and Concave Curvature Effects on Heated, Transitional Boundary Layers,” *J. Heat Transfer* , Vol. 114, pp. 338-347.

Kim, J., Simon, T. W. and Kestoras, M. (1994). "Fluid Mechanics and Heat Transfer Measurements in Transitional Boundary Layers Conditionally Sampled on Intermittency," *J. Turbomachinery*, Vol. 116, pp. 405-416.

Lekakis, J. C., Adrian, R. J. and Jones, B. G. (1989), "Measurement of Velocity Vectors with Orthogonal and Non Orthogonal Triple-Sensor Probe, " *Experiment in Fluid*, Vol. 7, pp. 288-240.

Mayle, R. E. (1991), "The Role of Laminar-Turbulent Transition in Gas Turbine Engines," ASME Paper 91-GT-261.

Malkiel, E. and Mayle, R. J. (1995), "Transition in a Separation Bubble," ASME Paper 95-GT-32.

Morin, B. L. and Patrick, W. P. (1991), "Detailed Studies of a Large-Scale Laminar Separation Bubble on a Flat-Plate," Vol. 1, United Technologies Research Center, Report No. R91-956786-1.

Morkovin, M. V. (1969), "On the many Faces of Transition," Viscous Drag Reduction, ed. C. S. Wells, Plenum Press, New York, pp. 1-31.

Narasimha, R. (1985), "The Laminar-Turbulent Transition Zone in the Boundary Layer ," Progress in Aerospace Science, Vol. 22, No.1, pp. 29-80.

Pauley, L. L., Moin, P. and Reynolds, W. C. (1990), "The Structure of Two-Dimensional Separation," *J. Fluid Mech.*, Vol. 220, pp. 397-41.

Rai, M. M. and Moin, P. (1991), "Direct Numerical Simulation of Transition and turbulence in a Spatially Evolving Boundary Layer," AIAA paper 91-1607.

Roberts, W. B. (1973), "A Study of the Effect of Reynolds Number and Laminar Separation Bubbles on the Flow through Compressor Cascade," D. Sc. Thesis, U. Libre de Bruxelles and VKI.

Roberts, W. B. (1980), "Calculation of Laminar Separation Bubbles and Their Effect on Airfoil Performance," AIAA J., Vol. 18, No. 1, pp. 25-30.

Russ, S. G. and Simon, T. W. (1990). "Signal Processing using the Orthogonal Triple-wire Equations," *Flow Lines*, TSI Inc., Winter 1990.

Sahm, M. K. and Moffat, R. J. (1992), "Turbulent Boundary Layers with High Turbulence: Experimental Heat Transfer and Structure on Flat and Concave Walls," HMT-45, Department of Mechanical Engineering, Stanford University.

Schlichting, H. (1979) Boundary Layer Theory, McGraw-Hill, New York, 7th Edition

Volino, R. J. and Simon, T. W. (1991), "Bypass Transition in Boundary Layers Including Curvature and favorable Pressure Gradient Effects," NASA CR-187187

Volino, R. J. and Simon, T. W. (1994a) "Velocity and Temperature Profiles in Turbulent Boundary Layer Flows Experiencing Streamwise Pressure Gradients," *Fundamentals of Heat Transfer in Forced Convection* -1994, ASME HTD-Vol. 285, ed. F W. Schmidt and R. J. Moffat, pp. 17-24.

Volino, R. J. and Simon, T. W. (1994b) "Transfer Functions for Turbulence Spectra," *Unsteady Flows in Aeropropulsion*-1994, ASME AD-Vol. 40, ed. W. Ng, D. Fant and L. Povinelli, pp. 147-155.

Volino, R. J. and Simon, T. W. (1994c), "An Application of Octant Analysis to Turbulent and Transitional Flow Data," *J. Turbomachinery*, Vol. 116, pp. 752-758

Volino, R. J. and Simon, T. W.(1995a), "Bypass Transition in Boundary Layers Including Curvature and Favorable Pressure Gradient Effects," *J. of Turbomachinery*. Vol. 117, pp. 166-174.

Volino, R. J. and Simon, T. W. (1995b), "Boundary Layer Transition Under High Free-Stream Turbulence And Strong Acceleration Conditions: Mean Flow Results," Proc. of the 4th ASME/JSME Thermal Engineering Joint Conference, Vol. 1, ed. L. S. Fletcher and T. Aihara, pp. 335-342.

Volino, R. J. and Simon, T. W. (1995c), "Measurements in Transitional Boundary Layers Under High Free-Stream Turbulence and Strong Acceleration Conditions," NASA CR-198413.

Wang, T. (1984), "An Experimental Investigation of Curvature and Freestream Turbulence Effects on Heat Transfer and Fluid Mechanics in Transitional Boundary Layer Flows," Ph.D. Thesis, Department of Mechanical Engineering, University of Minnesota.

Wills, J. A. B. (1962), "The Correction of Hot-Wire Readings for Proximity to a Solid Boundary," *J. of Fluid Mechanics*, Vol. 12, pp. 388-396

APPENDIX A

SHEAR STRESS DIRECTION VISUALIZATION

Visualization photos of shear stress direction for all cases are shown in Fig. A.1 to Fig. A.11, where P7 is a measuring station and S_s and S_r indicate the separation and reattachment positions along the suction surface, respectively. Due to gravity, the ink has a tendency to fall downward, resulting in dropping streak lines, particularly in regions of low shear stress.

Test 1 (top) and Test 2 (bottom)

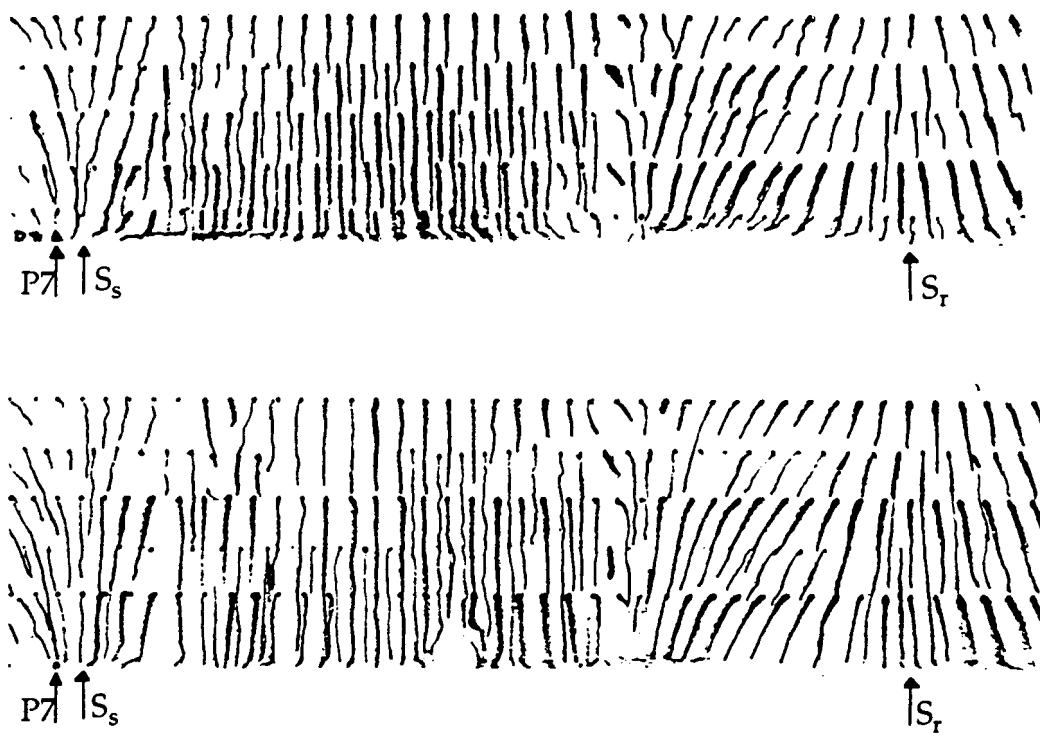

Fig. A.1 Shear stress direction visualization for FSTI = 0.5 %, Re = 50,000

Test 1 (top) and Test 2 (bottom)

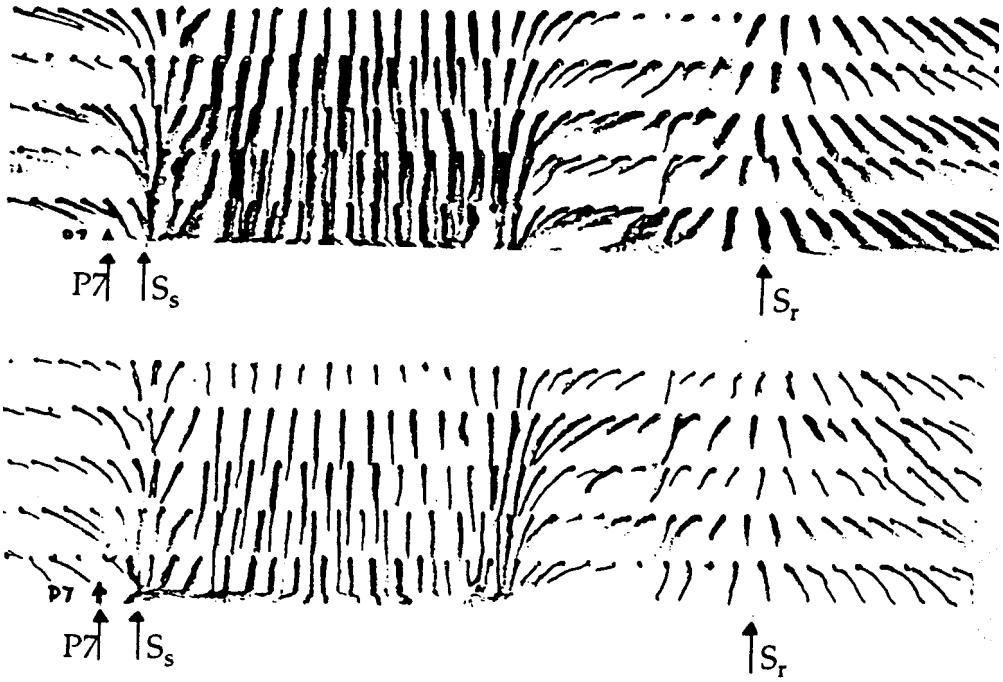

Fig. A.2 Shear stress direction visualization for FSTI = 0.5 %, Re = 100,000

Test 1 (top) and Test 2 (bottom)

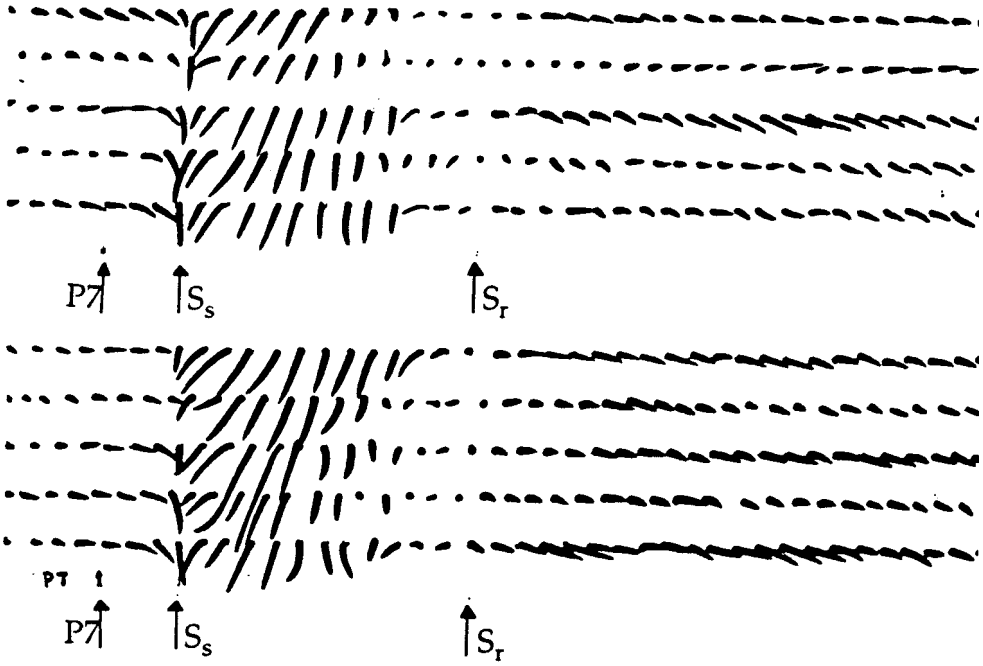

Fig. A.3 Shear stress direction visualization for FSTI = 0.5 %, Re = 200,000

Test 1 (top) and Test 2 (bottom)

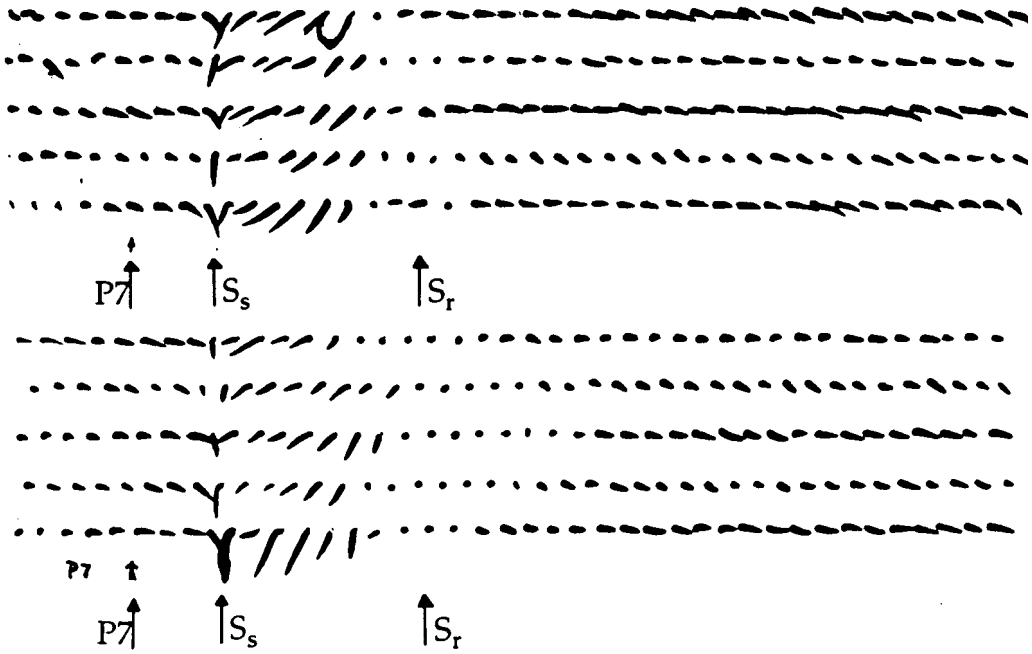

Fig. A.4 Shear stress direction visualization for FSTI = 0.5 %, Re = 300,000

Test 1 (top) and Test 2 (bottom)

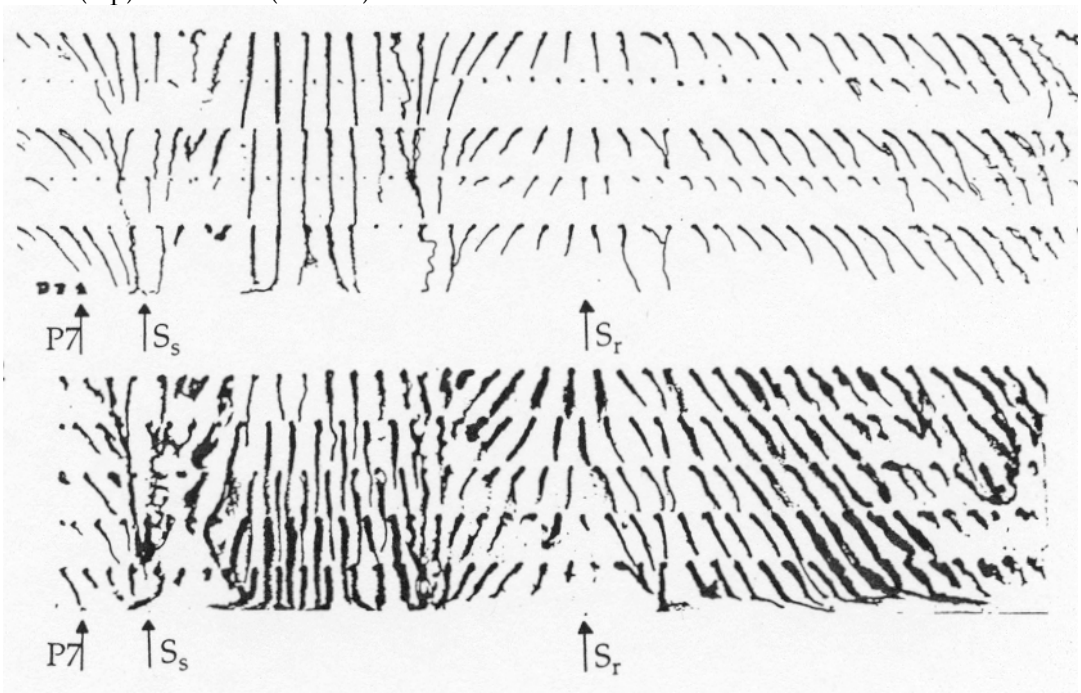

Fig. A.5 Shear stress direction visualization for FSTI = 2.5 %, Re = 500,000

Test 1 (top) and Test 2 (bottom)

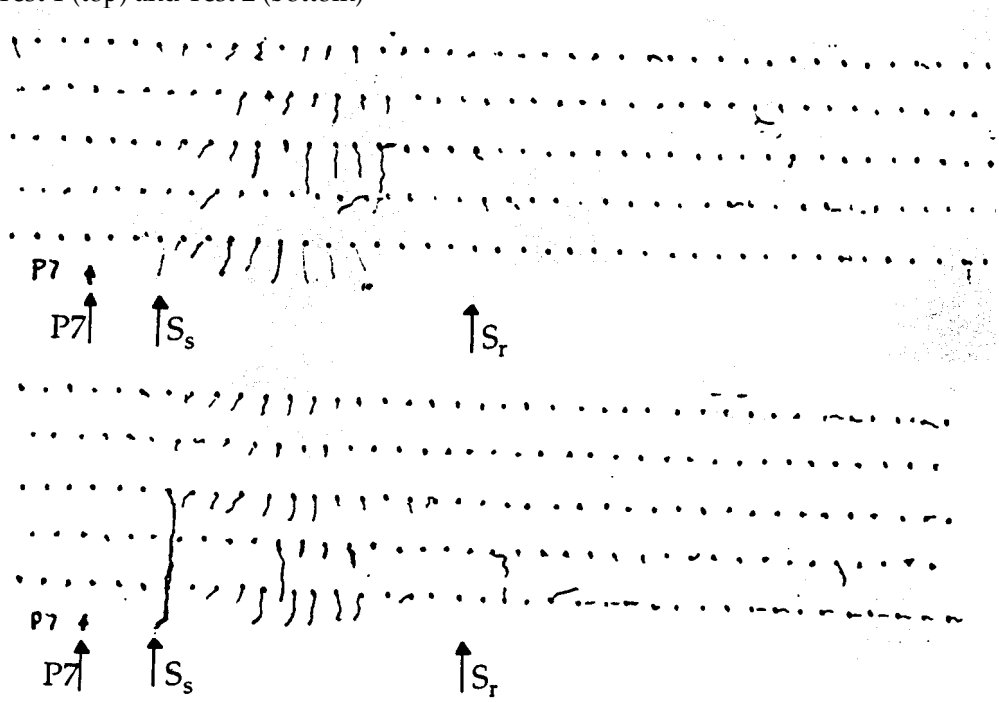

Fig. A.6 Shear stress direction visualization for FSTI = 2.5 %, Re = 100,000

Test 1 (top) and Test 2 (bottom)

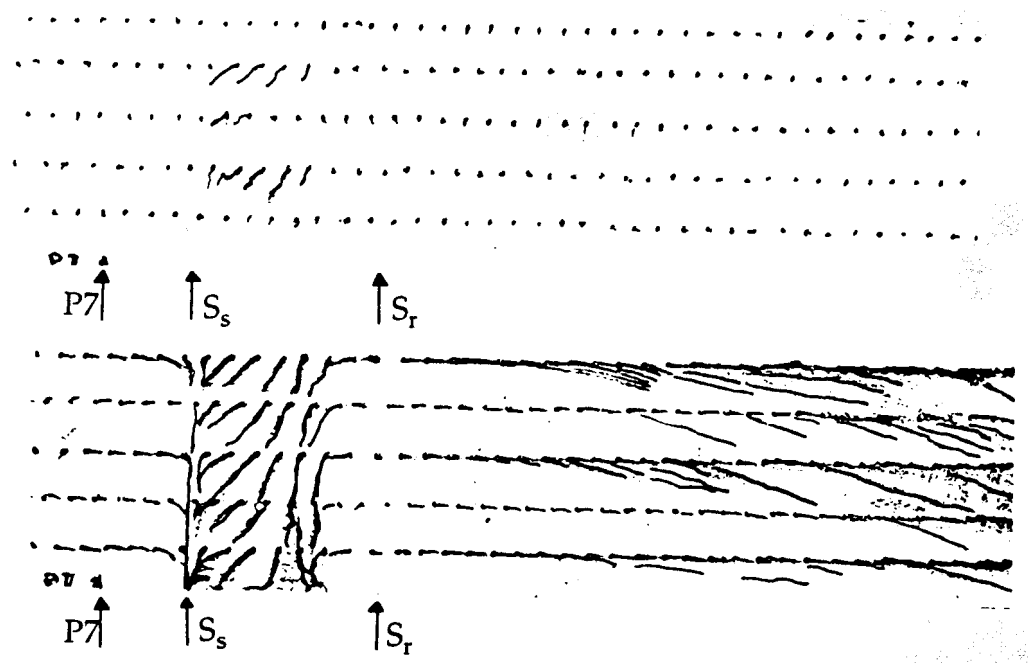

Fig. A.7 Shear stress direction visualization for FSTI = 2.5 %, Re = 200,000

Test 1 (top) and Test 2 (bottom)

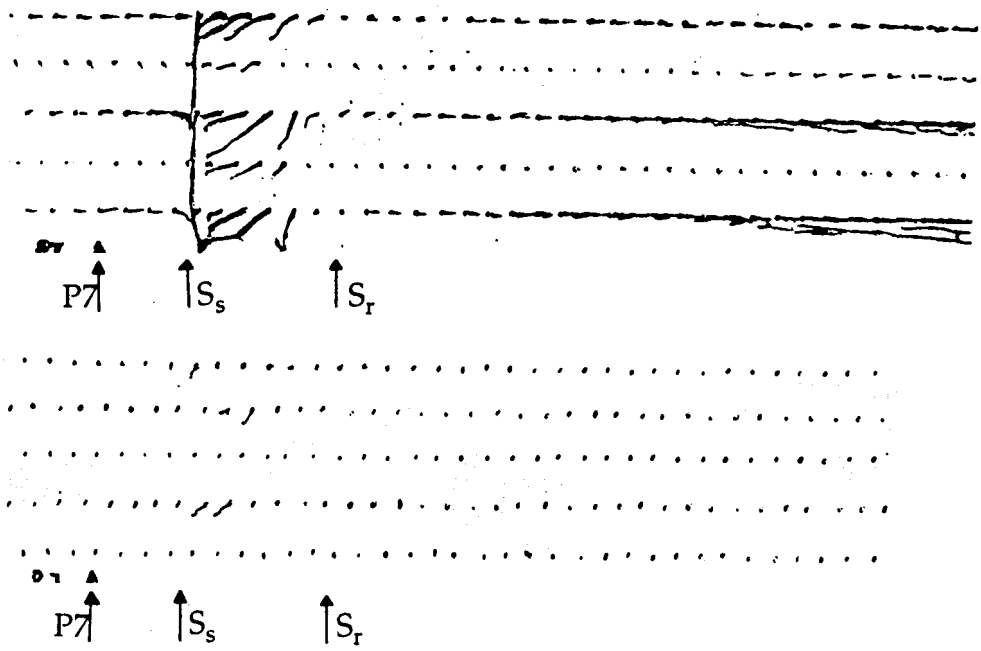

Fig. A.8 Shear stress direction visualization for FSTI = 2.5 %, Re = 300,000

Test 1 (top) and Test 2 (bottom)

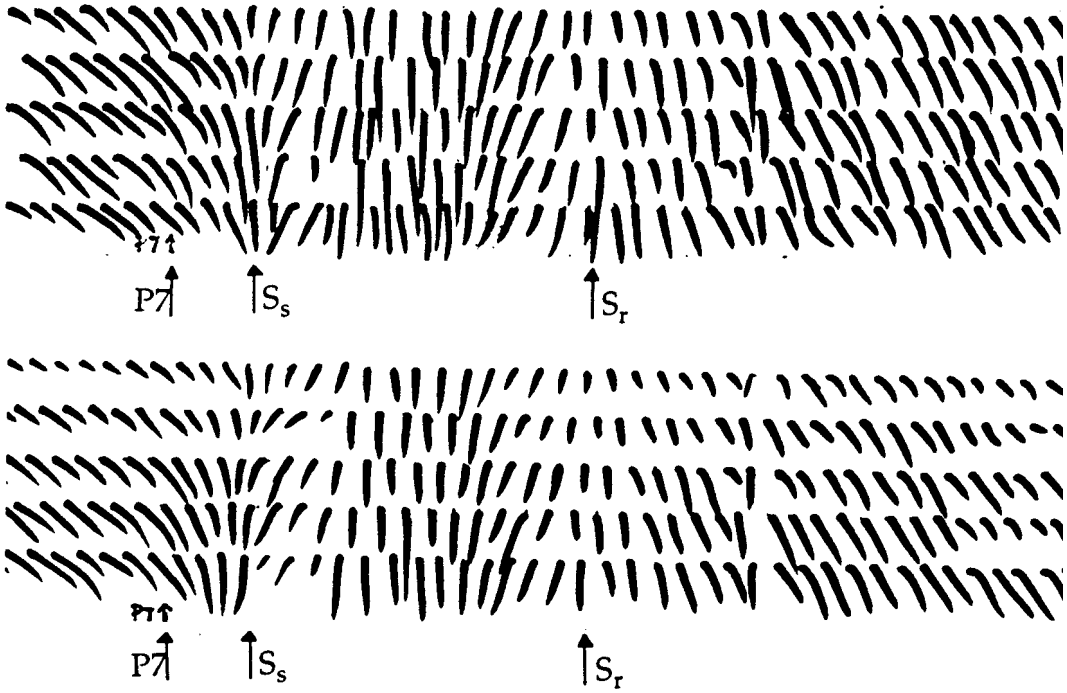

Fig. A.9 Shear stress direction visualization for FSTI = 10 %, Re = 50,000

Test 1 (top) and Test 2 (bottom)

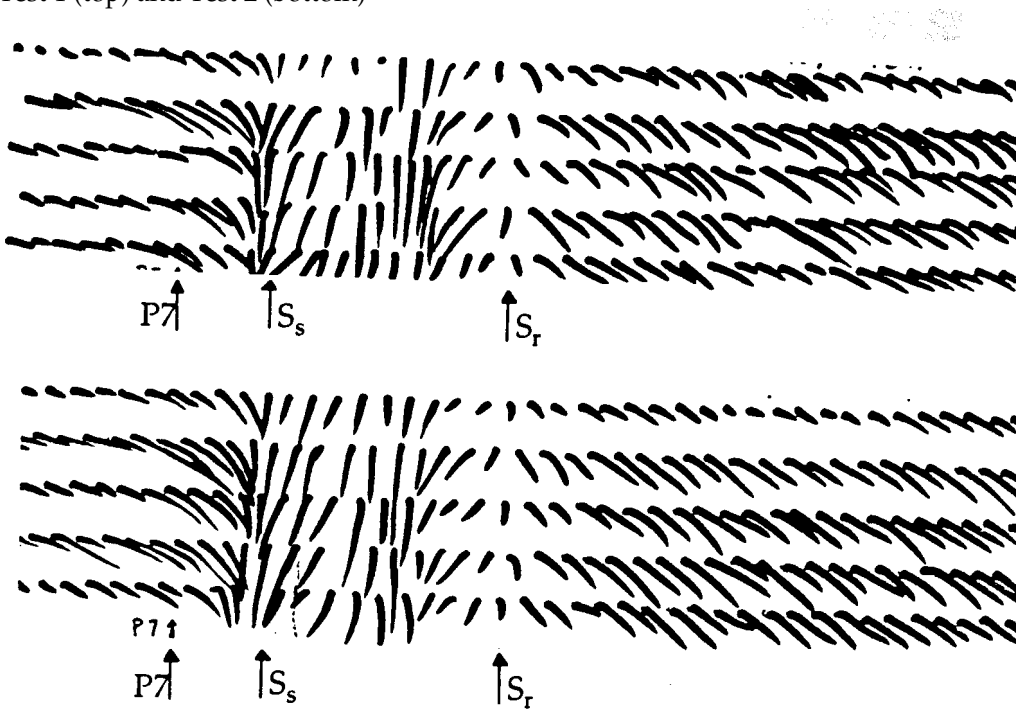

Fig. A.10 Shear stress direction visualization for FSTI = 10 %, Re = 100,000

Test 1 (top) and Test 2 (bottom)

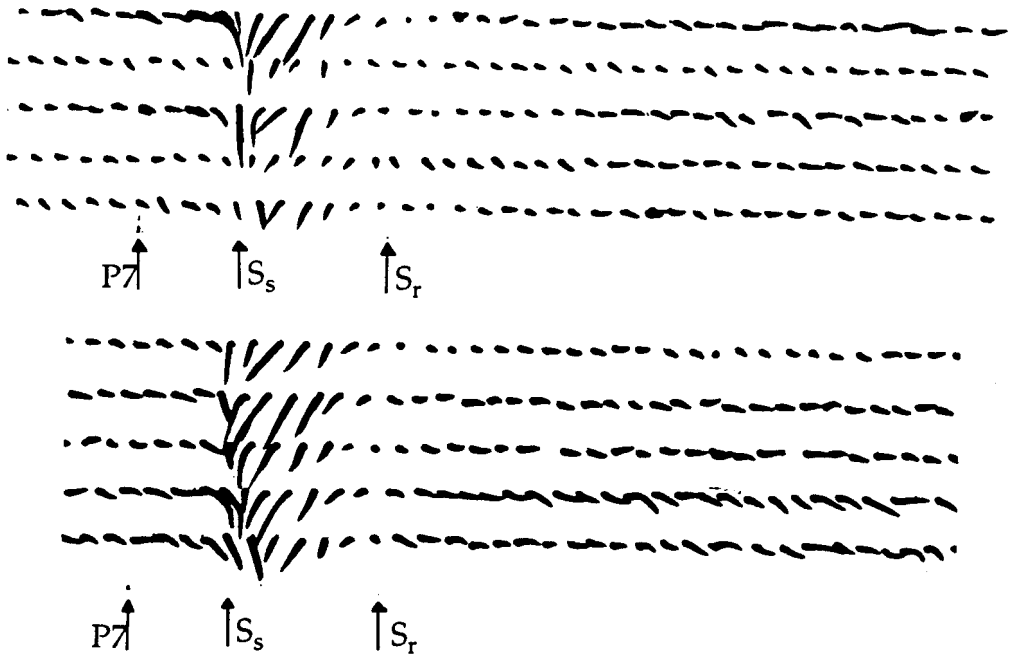

Fig. A.11 Shear stress direction visualization for FSTI = 10 %, Re = 200,000

REPORT DOCUMENTATION PAGE

Form Approved
OMB No. 0704-0188

Public reporting burden for this collection of information is estimated to average 1 hour per response, including the time for reviewing instructions, searching existing data sources, gathering and maintaining the data needed, and completing and reviewing the collection of information. Send comments regarding this burden estimate or any other aspect of this collection of information, including suggestions for reducing this burden, to Washington Headquarters Services, Directorate for Information Operations and Reports, 1215 Jefferson Davis Highway, Suite 1204, Arlington, VA 22202-4302, and to the Office of Management and Budget, Paperwork Reduction Project (0704-0188), Washington, DC 20503.

1. AGENCY USE ONLY (*Leave blank*)

2. REPORT DATE
March 2000

3. REPORT TYPE AND DATES COVERED
Final Contractor Report

4. TITLE AND SUBTITLE
Measurements in a Transitional Boundary Layer Under Low-Pressure Turbine Airfoil Conditions

5. FUNDING NUMBERS
WU–522–31–23–00
NAG3–1249

6. AUTHOR(S)
Terrence W. Simon, Songgang Qiu, and Kebiao Yuan

7. PERFORMING ORGANIZATION NAME(S) AND ADDRESS(ES)
University of Minnesota
Department of Mechanical Engineering
Minneapolis, Minnesota 55455

8. PERFORMING ORGANIZATION REPORT NUMBER
E–12215

9. SPONSORING/MONITORING AGENCY NAME(S) AND ADDRESS(ES)
National Aeronautics and Space Administration
John H. Glenn Research Center at Lewis Field
Cleveland, Ohio 44135–3191

10. SPONSORING/MONITORING AGENCY REPORT NUMBER
NASA CR—2000-209957

11. SUPPLEMENTARY NOTES
Project Manager, David Ashpis, Turbomachinery and Propulsion Systems Division, NASA Glenn Research Center, organization code 5820, (216) 433–8317.

12a. DISTRIBUTION/AVAILABILITY STATEMENT
Unclassified - Unlimited
Subject Categories: 02, 07, and 34 Distribution: Nonstandard

This publication is available from the NASA Center for AeroSpace Information, (301) 621–0390.

12b. DISTRIBUTION CODE

13. ABSTRACT ***(Maximum 200 words)***

This report presents the results of an experimental study of transition from laminar to turbulent flow in boundary layers or in shear layers over separation zones on a convex-curved surface which simulates the suction surface of a low-pressure turbine airfoil. Flows with various free-stream turbulence intensity (FSTI) values (0.5%, 2.5% and 10%), and various Reynolds numbers (50,000, 100,000 200,000 and 300,000) are investigated. Reynold numbers in the present study are based on suction surface length and passage exit mean velocity. Flow separation followed by transition within the separated flow region is observed for the lower-Re cases at each of the FSTI levels. At the highest Reynolds numbers and at elevated FSTI, transition of the attached boundary layer begins before separation, and the separation zone is small. Transition proceeds in the shear layer over the separation bubble. For both the transitional boundary layer and the transitional shear layer, mean velocity, turbulence intensity and intermittency (the fraction of the time the flow is turbulent) distributions are presented. The present data are compared to published distribution models for bypass transition, intermittency distribution through transition, transition start position, and transition length. A model developed for transition of separated flows is shown to adequately predict the location of the beginning of transition, for these cases, and a model developed for transitional boundary layer flows seems to adequately predict the path of intermittency through transition when the transition start and end are known. These results are useful for the design of low-pressure turbine stages which are known to operate under conditions replicated by these tests.

14. SUBJECT TERMS
Boundary layer; Turbulence; Transition; Separation; Modeling; Turbulence modeling; Intermittency; Turbulent spot; Turbine

15. NUMBER OF PAGES
221

16. PRICE CODE
A10

17. SECURITY CLASSIFICATION OF REPORT
Unclassified

18. SECURITY CLASSIFICATION OF THIS PAGE
Unclassified

19. SECURITY CLASSIFICATION OF ABSTRACT
Unclassified

20. LIMITATION OF ABSTRACT